Higher-order phenomena in nanomechanics of two-dimensional material membranes

Siskins, M.

DOI
10.4233/uuid:95293616-4c1d-4e75-ad45-f502a5b5f22a

Publication date
2021

Document Version
Final published version

Citation (APA)
Siskins, M. (2021). *Higher-order phenomena in nanomechanics of two-dimensional material membranes*. [Dissertation (TU Delft), Delft University of Technology]. https://doi.org/10.4233/uuid:95293616-4c1d-4e75-ad45-f502a5b5f22a

HIGHER-ORDER PHENOMENA IN NANOMECHANICS OF TWO-DIMENSIONAL MATERIAL MEMBRANES

HIGHER-ORDER PHENOMENA IN NANOMECHANICS OF TWO-DIMENSIONAL MATERIAL MEMBRANES

Proefschrift

ter verkrijging van de graad van doctor
aan de Technische Universiteit Delft,
op gezag van de Rector Magnificus prof. dr. ir. T. H. J. J. van der Hagen,
voorzitter van het College voor Promoties,
in het openbaar te verdedigen op maandag 1 november 2021 om 15:00 uur

door

Makars ŠIŠKINS

Master of Physics,
The University of Manchester, Manchester, het Verenigd Koninkrijk,
geboren te Riga, Letland.

Dit proefschrift is goedgekeurd door de

promotors: prof. dr. P.G. Steeneken
prof. dr. ir. H.S.J. van der Zant

Samenstelling promotiecommissie:

Rector Magnificus,	voorzitter
Prof. dr. P.G. Steeneken,	Technische Universiteit Delft, promotor
Prof. dr. ir. H.S.J. van der Zant,	Technische Universiteit Delft, promotor
Onafhankelijke leden:	
Prof. dr. A. Mishchenko,	The University of Manchester
Prof. dr. K.F. Mak,	Cornell University
Prof. dr. K.I. Bolotin,	Freie Universität Berlin
Prof. dr. E. Coronado,	Universitat de València
Prof. dr. Y.M. Blanter,	Technische Universiteit Delft
Prof. dr. G.A. Steele,	Technische Universiteit Delft, reserve lid

TUDelft Delft University of Technology
delft leiden Casimir research school
NWO
Nederlandse Organisatie voor Wetenschappelijk Onderzoek
GRAPHENE FLAGSHIP

Keywords: two-dimensional materials, nanomechanics, resonance, NEMS, graphene, pressure sensor, magnetic materials, phase transitions, anisotropy, laser interferometry

Printed by: ProefschriftMaken, De Bilt.

Front: Artist impression of a laser interferometry measurement technique, by Makars Šiškins (human).

Back: Artist impression of a 2D material heterostructure, by "Nikolay Ironov" (neural network, Art.Lebedev studio, http://ironov.artlebedev.ru/en/).

Casimir PhD Series, Delft-Leiden 2021-26
ISBN 978-90-8593-492-9

An electronic version of this dissertation is available at http://repository.tudelft.nl/.
This dissertation has associated numerical data shown in figures in a data repository at https://doi.org/10.5281/zenodo.5498177.

Моей семье посвящается.
To my family.

CONTENTS

SUMMARY

This thesis studies higher-order material properties[*] and effects in van der Waals crystals, such as anisotropic Young's modulus, magnetostriction, and non-trivial thermal expansion effects near magnetic and electronic phase transitions, that can affect the nanomechanical motion of multilayer two-dimensional (2D) material membranes. These couplings make the motion of nanomechanical resonators a useful and universal tool to probe 2D material properties that are often hard to access otherwise. The thesis consists of four parts.

In Part I, the methods to fabricate and probe the nanomechanical properties of van der Waals materials membranes are described. Chapter 2 discusses the typical workflow of the fabrication and characterization of 2D material membranes. Chapter 3 of this part presents experimental techniques for 2D material membranes: the static methods that involve force-indentation Atomic Force Microscopy and pressure-induced membrane deflection methods, and the dynamic methods that involve laser interferometry technique and controllable electrostatic deflection.

In Part II, the experiments focus on probing of elastic properties of 2D materials, such as Young's modulus. In Chapter 4, the fabrication and characterization of membrane arrays made of stacked bilayer graphene are described, together with the application of these for highly sensitive pressure sensors. Chapter 5 presents the isolation and characterization of a new 2D material, orpiment. It also describes methods for mechanically probing its anisotropic Young's modulus.

Part III describes mechanisms of coupling the membrane mechanical motion to the magnetic phase of the material. The mechanism that is mainly responsible for this coupling has a thermodynamic nature and is related to the changes in the material's specific heat and entropy, described in Chapter 6, together with experimental evidence utilizing membranes of $FePS_3$, $MnPS_3$, and $NiPS_3$. In Chapter 7, two spatially separated membranes of $FePS_3$ and $MnPS_3$ are shown to exchange mechanical energy and thus strongly couple. Also, the effect of phase transitions in these compounds on coupling strength is discussed. In Chapter 8, the antiferromagnetic membranes of van der Waals metal-organic frameworks are studied with the laser interferometry nanomechanical technique. Signatures of strong coupling of magnetism to motion are observed in these membranes. Chapter 9 reports the detection and tuning of ferromagnetic Curie temperature in $Cr_2Ge_2Te_6$ heterostructures.

Part IV of the thesis provides an outlook to the experiments that are still in an early stage, yet might potentially have a high impact in the fields of nanomechanics and 2D materials. Chapter 10 reports the large mechanical anisotropy in rectangular membranes of $CoPS_3$ and $FePS_3$ that arises as the material is cooled through the antiferromagnetic Néel temperature. This effect is believed to be present due to the appearance of sponta-

---

[*] Which are variable as a nonlinear function of temperature, crystalline orientation or strain.

neous magnetostriction at the T_N, and related to the magnetic order parameter. This thesis proposes a method of using this effect to study the order parameter, solely by mechanical means. In Chapter 11, the relation between the characteristic thermal relaxation time constant and thermoelastic damping of antiferromagnetic membranes is studied. Finally, in Chapter 12, few examples of applying the laser interferometry method to detect phase transition temperatures in compounds with electronic phase transitions are discussed.

SAMENVATTING

Dit proefschrift behandelt hogere-orde materiaaleigenschappen[†] en effecten in van der Waalskristallen, zoals een anisotrope elasticiteitsmodulus, magnetostrictie en niet-triviale thermische expansie-effecten nabij magnetische en elektronische fase-overgangen, die invloed kunnen hebben op de nanomechanische beweging van meerlaagse membranen vervaardigd van tweedimensionale (2D) materialen. Deze koppelingen maken de beweging van nanomechanische resonatoren tot een praktisch en universeel middel voor het bepalen van 2D materiaaleigenschappen die doorgaans moeilijk te bestuderen zijn op een andere manier. Dit proefschrift bestaat uit vier delen.

In deel I staan methoden beschreven om van der Waals membranen te fabriceren en hun nanomechanische eigenschappen te bepalen. Hoofdstuk 2 bespreekt het typische stappenplan voor fabricatie en karakterisering van membranen vervaardigd van 2D materialen. Hoofdstuk 3 van dit deel beschrijft experimentele technieken voor membranen van 2D materialen: de statische methodes die het membraan indrukken door het uitoefenen van kracht met een atoomkrachtmicroscoop (AFM), of laten doorbuigen onder invloed van een drukverschil, als ook de dynamische methodes die laser interferometrie en gecontroleerde elektrostatische doorbuiging benutten.

In deel II focussen de experimenten op de bepaling van elastische eigenschappen van 2D materialen, zoals de elasticiteitsmodulus. In Hoofdstuk 4 wordt de fabricatie en karakterisering beschreven van reeksen membranen vervaardigd van meerlaags grafeen, en wordt dieper ingegaan op hun toepassing als uitzonderlijk gevoelige druksensoren. Hoofdstuk 5 gaat in op de isolatie en karakterisering van een nieuw 2D materiaal, orpiment. Verder worden methodes beschreven voor het bepalen van zijn anisotrope elasticiteitsmodulus.

Deel III beschrijft koppelingsmechanismen tussen de mechanische beweging van het membraan en de magnetische fase van het materiaal. Het mechanisme dat voornamelijk verantwoordelijk is voor deze koppeling is thermodynamisch van aard en is gerelateerd aan de veranderingen in de specifieke warmte en entropie van het materiaal, en is beschreven in hoofdstuk 6, samen met experimenteel bewijs aan de hand van membranen van $FePS_3$, $MnPS_3$, en $NiPS_3$. In hoofdstuk 7 wordt getoond dat twee ruimtelijk gescheiden antiferromagnetische membranen van $FePS_3$ en $MnPS_3$ mechanische energie uitwisselen en dus sterk koppelen. Daarnaast wordt het effect van fase-overgangen in deze materialen op de sterkte van de koppeling besproken. In hoofdstuk 8 worden antiferromagnetische membranen gemaakt met van der Waals metaal-organische raamwerken bestudeerd door middel van de laser interferometrische nanomechanische techniek. We zien aanwijzingen voor sterke koppeling tussen magnetisme en beweging in deze membranen. Hoofdstuk 9 beschrijft de detectie en afstemming van de ferromagnetische Curie temperatuur in $Cr_2Ge_2Te_6$ heterostructuren.

[†] Dit zijn variabelen als niet-lineaire functie van temperatuur, kristalstructuur en rek.

Deel IV van dit proefschrift geeft een vooruitzicht op experimenten die zich nog in een vroeg stadium bevinden, maar potentieel een grote impact hebben op het gebied van nanomechanica en 2D materialen. Hoofdstuk 10 gaat in op de grote mechanische anisotropie in rechthoekige membranen van $CoPS_3$ en $FePS_3$, die ontstaat wanneer het materiaal gekoeld wordt voorbij de antiferromagnetische Néel temperatuur. Er wordt van uitgegaan dat dit effect ontstaat door spontane megnetostrictie bij T_N, en gerelateerd is aan de magnetische orde parameter. In dit proefschrift wordt een methode voorgesteld om dit effect te gebruiken voor het bestuderen van de orde parameter, uitsluitend door mechanische middelen. In hoofdstuk 11 wordt de relatie tussen de karakteristieke thermische tijdsconstante en thermoelastische demping van antiferromagnetische membranen bestudeerd. Tot slot, worden in hoofdstuk 12, een aantal voorbeelden van het gebruik van de laser interferometrie methode voor het detecteren van fasetransitie temperaturen in materialen met elektronische fasetransities bediscussieerd.

PREFACE

Throughout the history of human development, people seemed to really care about two things when choosing materials: strength and weight. In a nutshell, the idea always was "it must be light, and it must be strong." Indeed, as humanity, we always found ways to decrease weight and increase the strength of our everyday tools. Materials are so historically important that we are even naming ages after them. In the Stone Age, we made wheels and axes out of stone and wood. In the Bronze Age, we made swords and arrows from bronze that were later substituted for Iron and other metal alloys that allowed us to build guns, cannons, and eventually cities, skyscrapers, and spacecrafts.

This has pushed our development further until we reached a new era of high technologies. Then, for the last 40 years, we had something that could be called the Silicon Age. What we care about now is not how to make a better hammer, but rather a better, faster, cheaper *and* smarter phone, of course with the best camera possible. We know exactly what we need to achieve it. Now, we want extremely good sensors and tiny, smart electronics. So small that these should be nano-scale tiny – around one-millionth of a millimeter in size. Moreover, even at this size, they should perform better than electronics that we have now or have some new, unprecedented functionality.

Of course, to make something that small and smart, we want the best materials. Most of the nano-electronics these days are made of silicon. Silicon is good but not good enough to satisfy our contemporary needs. We want a better processor or sensor in our devices so badly that we are already close to reaching the limit of what conventional silicon can do. This is one of the most significant challenges for nanotechnology and scientists working in the field today. That is why it was so important when in 2004, we discovered two-dimensional materials and their first of a kind - graphene.

Graphene is a layer of carbon atoms, one atom thick. It is about 200 000 times thinner than a human hair. It is as thin as it can get for something that we can call "a material." At the same time, graphene is an excellent electrical and heat conductor – much better than copper or silicon. It is also super light, in fact, likely as light it can get. It is lighter than plastic and incredibly strong: graphene is roughly 100x stronger than steel. Just Imagine: "1 m^2 hammock made of graphene could hold a cat and yet weigh as much as one of the cat's whiskers[‡]". And, at the same time, it would also be almost entirely transparent. Crazy.

In some sense, we are lucky that graphene was the first, but not the only 2D material. It came together with a family of hundreds of others. Thanks to that, we now can smartly design stacks of these materials that show properties that are unavailable in these layers individually. We even can look into the thinnest possible magnets that have remarkably complex properties. Can we in the future use these for high-density memory devices? Such questions we still have to answer.

[‡] From Scientifc Background on the Nobel Prize in Physics 2010, by the Class for Physics of the Royal Swedish Academy of Sciences

I was lucky enough to study and work with great scientists at the University of Manchester - the place where graphene was discovered - the “home of graphene.” Now, I am near the end of my doctorate at another renowned place - the Delft University of Technology. Throughout my academic career, I had a chance to observe a small bit of the long way that the material has to go from lab to fab. We see the perspectives of these materials in ultrasensitive sensors, smaller computers, better “hammocks for cats,” and many more. However, even if we say that we understand the material well, the challenge is to get it to the industry. This is indeed a massive challenge since graphene and silicon seem to be quite industrially incompatible. Solving this issue may take tens of years of work. In some sense, graphene and 2D materials can revolutionize our electronics not because they are so good and smart, but also because their integration into production would mean that we would rethink the long-ago established way of building our industrial lines and fabrication processes. Perhaps, because this is what revolutions do: overthrow the old order, in favour of a new system.

Still, the future that new materials like graphene can provide us with is worth it. Progress is unavoidable, and eventually, we will enter a new era with a new phenomenally great material, after which we will be proud to name the age of our history. Even if it will not be Graphene Age in the end but some other great substance we do not know yet. We will continue to search until we find exactly what we need, as we shape these tiny things for our big future.

Makars Šiškins
Delft, June 2021

1

INTRODUCTION

In this introductory chapter we summarize the current status of the research field. We explain the motivation behind studying two-dimensional material membranes and formulate the research questions of this thesis.

IN the drive of technological advancement, we are in constant need of better sensors, smaller electronics, and memory devices. In pursuit of Moore's Law and the growth rate of the electronics market needs, it is increasingly difficult to manufacture functional devices that would be distinguished for their unprecedented performance. To make simultaneously the best and most compact electronics, people in research and development have long been working on technologies with typical features on the nanometer scale - one-millionth of a millimeter. Conventional electronics often stumbles over material's limitations, as going small and thin poses problems for electrical conductors in transistors and chips, and mechanical elements in modern sensors. For example, in membrane sensors, it is challenging to produce a membrane made of silicon or its derivatives so thin and small that it is strong enough under stress and at the same time has the required flexibility, maintaining its conductive and functional properties.

The field of nanomechanics deals with issues of this kind. Anticipating these problems, nanomechanics focuses on describing the mechanical properties of a wide range of nanomaterials - from nanoparticles [1] and ultrathin complex oxides [2] to DNA [3], trying to select those with functionally interesting or fundamentally important properties. As the name suggests, this is also a field that studies fundamental mechanical processes happening at the nanoscale. It concerns not only the motion of nanosize particles or deflections of ultrathin membranes but also physical and mechanical effects in nanoresonators that vibrate with low amplitudes on the scale of nanometers and beyond.

Two-dimensional (2D) crystals are believed to be promising candidate materials to address many material challenges in electronics and sensors due to their atomic thickness. These layers do not possess a third out-of-plane dimension, as their thickness is often defined by a single or only a few atoms. Thus these materials form perfect membranes [4] and nanomechanical systems [5, 6]. This chapter will explore which properties make these 2D membranes so interesting, application-wise promising, and compelling to explore.

1.1. TWO-DIMENSIONAL MATERIALS

1.1.1. GRAPHENE AND TRANSITION METAL COMPOUNDS

Graphene was the first monolayer 2D material isolated in 2004 by the Manchester group [7]. It was obtained using a legendary micromechanical exfoliation or Scotch tape method when the adhesive tape is used to cleave atomically thin hexagonal layers of natural graphite bonded only by weak van der Waals forces. These layers showed many remarkable electronic properties [8]. Graphene is an exception-material - a unique semimetal with linear conduction and valence bands meeting at a Dirac point, ergo having a zero bandgap. The consequence of that is the charge carriers mimic relativistic particles, behaving as massless Dirac fermions [7, 8]. Graphene is also a system of extreme electronic quality at room temperature, that is indicated by high electron mobility ranging from 15 000 to 200 000 $\mathrm{cm^2V^{-1}s^{-1}}$ [7, 9], and even observation of high-temperature quantum Hall effect [10]. Consequently, these discoveries lead to the Nobel prize being awarded to Andre Geim and Konstantin Novoselov for their pioneering work in 2010.

From the perspective of nanomechanics, we are interested in the extraordinary mechanical properties of graphene and other 2D materials (see Fig. 1.1). Interestingly, this

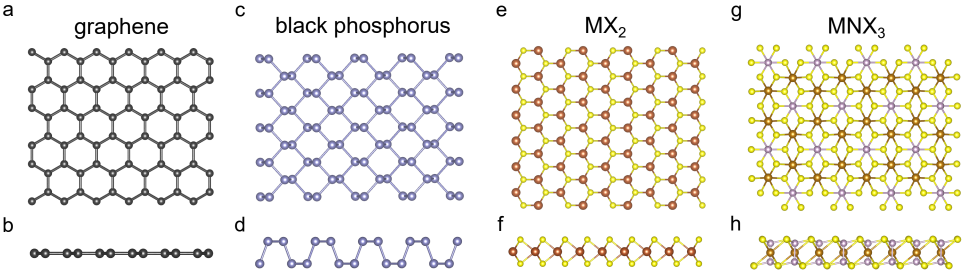

Figure 1.1: Atomic structure of the most common two-dimensional materials. Black circles indicate carbon, blue - phosphorus, yellow - chalcogens, red - transition metals, and violet - p-elements. Plotted using VESTA package [11].

chemically simplest 2D structure of hexagonally arranged carbon atoms (see Fig. 1.1a,b) is held together by exceptionally strong planar bonds. This grants graphene a remarkably high strength with Young's modulus of 1 TPa and high intrinsic tensile breaking strength of 130 GPa [12], and phenomenal thermal stability with melting point around 4000 K [13]. Arguably except for artificial 2D compound borophene (2D layer of boron) [14, 15], this makes graphene the strongest material known in nature. It is also one of the best known thermal conductors with thermal conductivity higher than 1800 $Wm^{-1}K^{-1}$ [16]. All these properties promise graphene wide commercial applicability in electronics [17], batteries [18], mechanical sensors [6, 19], molecular-level precise water filtration membranes [20], high-temperature electronics [21] and hot-electron light emitters [22].

One of the common uses of graphene is to suspend it to form membranes [4, 9, 23, 24]. Mechanically speaking, membranes of graphene are exceptional but reasonably well-understood [19, 23, 24]. These show quite "classical" almost isotropic mechanical behavior. Drawing an understandable and straightforward analogy, one can compare a pristine graphene sheet to an extremely strong flat sheet of thin paper (see Fig. 1.2). Pulling this sheet in one direction or the other will give the same result, i.e., show isotropic Young's modulus. Deflection and resonant motion of membranes made of such isotropic material are then independent of the crystalline orientation. However, complex material effects, such as anisotropic Young's modulus, can introduce such dependence. The well-known 2D material with this property is black phosphorus [25] (see Fig. 1.1c,d). Anisotropic materials, like black phosphorus, often have an armchair-like crystalline structure (see Fig. 1.2c). By a visual assessment of a 2D layer at the atomic scale, an analogy to a zigzag-folded sheet of paper becomes evident (see Fig. 1.2b). Such structures are much easier to stretch in one direction than in the other. The mechanical consequences of such structural anisotropy in these membranes are manifested by the complex dynamics of vibrational modes and their resonance frequency, which now does depend on the membrane geometry and the relative orientation of the crystal [26]. This structural feature, in combination with its electronic properties, makes materials like black phosphorus exciting for flexible optoelectronics [27, 28] and nanomechanical device concepts [26, 29].

The more complicated the 2D material structure gets, the more complicated its properties can become. Many materials from the transition metal dichalcogenide (TMD)

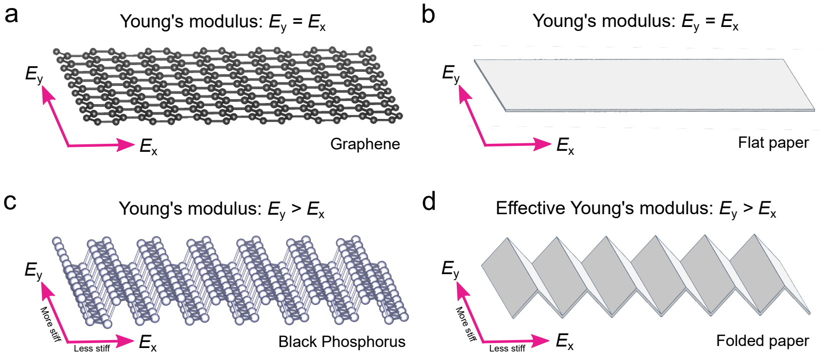

Figure 1.2: Analogy for the (an-)isotropic mechanical behavior. **a** Crystalline structure of a monolayer graphene. **b** Schematic of a flat sheet of paper. **c** Crystalline structure of a monolayer black phosphorus. **d** Schematic of a folded sheet of paper.

family, that adapt general formula MX_2 (M - metal, X - chalcogen), exhibit fascinating optoelectric properties [30, 31]. For instance, monolayers of molybdenum disulfide and diselenide (MoS_2 and $MoSe_2$) have a direct bandgap and can be used in transistors, optical emitters, and detectors [32–34]. In contrast, other 2D TMD crystals, like tantalum disulphide TaS_2, are metallic and exhibit charge density wave phases [35] and low-temperature superconductivity [36]. Mechanical properties of these compounds are mostly isotropic [37, 38] with Young's modulus around 150 – 350 GPa [37–39], although often having elastic anomalies near electronic phase transitions [40, 41].

Perhaps, the most exciting and the least studied 2D material family takes the MNX_3 formula, where M is the metal, N the p-element, such as crystallogen or pnictogen, and X the chalcogen. Metallic atoms that are bonded through neighboring chalcogen atoms in these layers form hexagonal sub-latices. Many representatives of this family have magnetic transition metals (Fe, Mn, Ni, or Co) in these sub-latices and thus are known for their magnetic properties [42].

1.1.2. MAGNETIC 2D MATERIALS

Magnetic compounds are one of the most recent frontiers in research of 2D materials [42]. These atomically thin layers of magnetic van der Waals crystals provide an ideal platform to study magnetism in 2D and open opportunities for spintronics devices, magnetic memory concepts and novel functional sensors [43, 44]. In reduced dimensions long-range isotropic spin order is not stable at a finite temperature, according to the Mermin-Wegner theorem. However, magnetic anisotropy can stabilize a magnetic phase in 2D and protect it from thermal fluctuation [42]. This facilitated recent discovery of stable 2D Ising antiferromagnetic ordering in flakes of $FePS_3$ [45] and ferromagnetisms in atomically thin layers of CrI_3 [46] and $Cr_2Ge_2Te_6$ [47].

As a follow up of these studies, a variety of magnetic van der Waals materials with a different type of magnetism and intra- and interlayer exchange coupling were investigated, leading to a discovery of 2D magnetism in exfoliated layers of many MX_3 and MNX_3 compounds (see Table 1.1) [42–44]. The large anisotropy that stabilizes the mag-

Material	Magnetism	Bulk T_C	Mechanical properties	
			theory	experiments
$Cr_2Ge_2Te_6$	↑↑↑↑↑↑ ↑↑↑↑↑↑	61 – 68 K [47]	[48]	this thesis
Fe_3GeTe_2	↑↑↑↑↑↑ ↑↑↑↑↑↑	205 K [49, 50]	[51]	—
$CrBr_3$	↑↑↑↑↑↑ ↑↑↑↑↑↑	35 K [52]	[53]	—
$CrCl_3$	↑↑↑↑↑↑ ↓↓↓↓↓↓	14 K [54]	[53]	[55]
CrI_3	↑↑↑↑↑↑ ↓↓↓↓↓↓	61 K [46]	[53, 56]	[55, 57]
$MnPS_3$	↓↑↓↑↓↑ ↓↑↓↑↓↑	78 K [58]	[59, 60]	this thesis
$NiPS_3$	↓↑↓↑↓↑ ↓↑↓↑↓↑	155 K [58]	[59, 60]	this thesis
$CoPS_3$	↓↑↓↑↓↑ ↓↑↓↑↓↑	118 K [61, 62]	[63]	this thesis
$FePS_3$	↓↑↓↑↓↑ ↑↓↑↓↑↓	114 K [58]	[59, 60]	this thesis
Magnetic MOFs	↓↑↓↑↓↑ ↑↓↑↓↑↓	10 – 20 K [64]	—	[64], this thesis

Table 1.1: List of magnetic van der Waals materials with indicated inter- and intralayer type of magnetism, transition temperature T_C in bulk crystals, and literature references regarding their mechanical properties.

netic ground state in these layers often results from the low-symmetry nature of van der Waals crystals and coupling between electronic orbitals and spins [42, 46, 61, 65]. In some cases, these 2D compounds contain transition metal ions with the unquenched orbital moment, bounded to the specific oxidation state of the ion, e.g., Fe^{2+} and Co^{2+}, that can facilitate the anisotropy [42] as well as coupling of its magnetic properties to lattice [61]. In other materials with a quenched orbital moment in their ground state, like those containing Ni^{2+}, Mn^{2+} and Cr^{3+}, the anisotropy originates from more intricate effects, like mixing of the magnetic ground state with higher-energy orbital states [65] and anisotropic super-exchange interactions [42, 66].

Many challenges related to specific properties of these materials and their chemical stability in ambient conditions limit available fabrication and experimental methods [42]. In addition to that, the majority of the most studied magnetic 2D materials have an (anti-)ferromagnetic transition Curie temperature T_C well below that of room conditions (see Table 1.1). Typical experimental methods for studying the magnetic ordering in these crystals are cryogenic optical probes, like Raman spectroscopy [45], magneto-optic Kerr effect [46, 47], magnetic circular dichroism [57], and low-temperature charge carrier transport techniques, like magnon-assisted tunneling [52]. However, some materials couple weakly to magnetic, optic, and electronic probes, making it challenging to study magnetism in particular in ultrathin insulating antiferromagnets [42].

The novel approach to probing magnetic properties of 2D materials is to utilize these as suspended membranes that form nanomechanical resonators [5, 57, 67]. This way, the resonant motion of such membranes could be studied using nanomechanical methods as a function of temperature, which allows relating changes in its motion near the phase transition to the T_C. The challenges here are related to the fact that knowledge on mechanical properties of these materials, such as it Young's modulus, is very limited, as many of these compounds will be utilized as nanomechanical systems for the first time in this thesis (see Table 1.1).

1.2. NANOMECHANICAL MEMBRANE RESONATORS

Nano-electromechanical systems (NEMS), as a smaller-scale successor of micro-electro-mechanical systems (MEMS), are known as a useful tool for their potential to study novel quantum, and electromagnetic effects at the nanoscale [68–70]. Along with that, these are used for various applications, including ultra-sensitive mass detection [71, 72], bandpass filters with variable properties [73], logic gates [74–76] and signal amplifiers [77]. Many of these applications of NEMS can be enhanced by using freestanding membranes of 2D materials suspended over a cavity that form nanomechanical membrane resonators [5, 6]. Due to the combination of low mass, high strength, and their unique properties, these 2D membranes find their use in several lines of research:

- **Thermodynamics**
  Thermodynamic processes and heat diffusion in 2D can be supported by phononic, electronic, and magnetic means [5]. Membranes of 2D materials help to neglect substrate contributions to heat transport and study pure thermodynamic processes. Understanding of these processes is needed to fully explain energy dissipation, heat transport phenomena, and condensed matter effects in 2D [16, 78–80];

- **Dynamics and nonlinear mechanics**
  Due to their atomic thickness, the 2D membranes in motion show signatures of nonlinearities even at picoNewton-scale forces [81]. This results in large vibration amplitudes [82] with a dynamic strain modulation [83], that is used for studies of parametric excitation mechanisms, (negative) nonlinear damping [84] and mode coupling as well as the study of material parameters such as Young's modulus and nonlinear spring constant [5, 81, 82, 85];

- **Sensors and functional devices**
  Atomic thickness together with smart fabrication methodologies allows the integration of 2D materials and their heterostructures, with a wide range of magnetic, optical, and electrical properties on the same chip [30], to novel sensors and functional devices that include pressure sensors, microphones, accelerometers, and mass and gas sensors[6];

- **Condensed matter physics**
  Sensitivity of the resonant motion of 2D material membrane to both external and internal forces facilitates its use as probes of phase transitions [41, 57, 67], as well as condensed matter [5] and quantum phenomena in 2D [86].

Emerging nanomechanical methods allow to study these research questions by utilizing membrane deflection and its mechanical resonance[*] [5, 6]. Perhaps, the most important advantage of these techniques is an opportunity for high-precision strain manipulation and control. Strain, and thus the resonance frequency, of these 2D membranes, can be tuned over an extensive range both statically [12] and dynamically [83, 89]. This facilitates control options unavailable in many other NEMS in favor of strain engineering of different material phases and phenomena [90], and new functionalities of 2D material sensors [6].

1.2.1. SENSORS AND FUNCTIONAL DEVICES

Unique properties of 2D materials open up broad sensing possibilities in these layers [6]. Suspending these materials as membranes, ribbons, or bridges can double the active surface area of the sensor, eliminate substrate interactions, utilize their thermal properties, and importantly provide the readout mechanism through its resonant motion [5, 6]. Additional processing of such membranes by various fabrication methods can allow novel functionality. For example, with the controlled creation of nanoscale pores in graphene membranes, noble gases, like helium, argon, or krypton, can be distinguished at the molecular level by measuring their permeation rate of several tens of nanoseconds using the membrane motion (Fig. 1.3) [91].

Without pores, graphene membranes are nearly impermeable for gases [92, 93], and thus their deflection is very susceptible to changes in atmospheric gas pressure [23]. In fact, its deflection sensitivity[†] is one of the largest possible due to graphene thickness. This facilitates the creation of pressure sensors from such membranes [6, 94–97]. However, the sensitivity of a single membrane graphene sensor is not sufficient for practical applications [97]. Therefore, production methods are desired to fabricate nearly 10 000 membrane sensors operating in parallel, which would show a sensitivity comparable to commercial chips [97]. This work will discuss the fabrication method for such graphene membrane arrays and probe their elastic properties using nanomechanical methods to ensure sufficient quality and functionality.

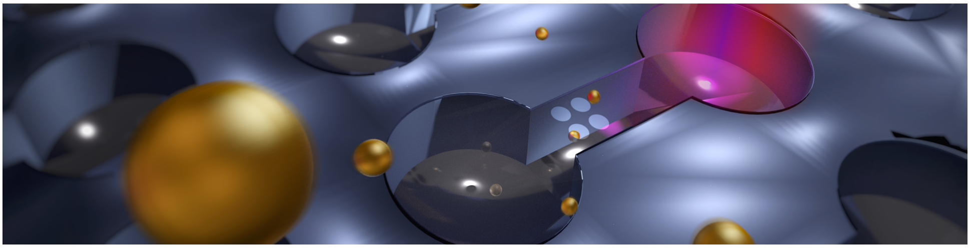

Figure 1.3: Molecules permeating through nanopores in laser-driven dumbbell shaped graphene membranes [91], artistic impression.

---

[*] As also comprehensively discussed in Ph.D. theses of Dolleman, R.J. [87] and Davidovikj, D. [88]

[†] In nanometers per Pascal

1.2.2. RESONATORS AS PROBES

Nanomechanical resonators are used as probes for high-frequency gas dynamics [91], adsorption mechanisms of gases superfluids [98], quantum processes in coupled systems [69, 70, 99] and fundamental forces of nature [100]. However, all these processes that affect the motion of the resonators are external. An interesting situation arises when nanomechanical resonators become self-sensitive devices. Thus, observing the change in the oscillation frequency of such resonator, one can draw conclusions about the processes and physical phenomena occurring inside the material this resonator was made of.

Several examples of nanomechanical resonators used as probes for condensed matter physics are found in the literature that utilize the coupling of the resonance frequency with the elastic properties of the material [41] or with the electric field effect [86]. Thus, it is possible to study phase transitions in charge density waves systems by exploiting anomalies in Young's modulus near the phase transition [41, 101], which is essentially a nanoscale analogue of the vibrating reed method [102, 103]. In addition, by applying a small electric field to the resonator, one can observe quantum effects [86] as well as topological phases [104] through the resonance frequency due to the modulation of chemical potential in the low-dimensional material.

This work considers another meaningful connection between the higher-order phenomena in the resonance of 2D material nanomechanical membranes and their material properties. It can be shown that the membrane frequency depends on the phase of the substance, for example, its magnetic state. Interestingly, this relation is a direct consequence of Landau's theory of second-order phase transitions [105, 106]. Before the phase transition, in the disordered state, the order parameter is zero. In the ordered phase, the order parameter takes a non-zero value, which changes the free energy, entropy and, as a consequence, leads to a rapid rise in the specific heat at the transition temperature. This jump affects the thermal expansion coefficient through thermodynamic relations, reflected in the membrane's strain and characteristically changing its resonance frequency with the temperature change, as schematically depicted in Fig. 1.5. It allows us to assess the applicability of this fundamental relationship between the resonance frequency and order parameter, allowing studies of phase transitions in material systems that are challenging to characterize otherwise, like electrically insulating 2D layered antiferromagnets (Fig. 1.4).

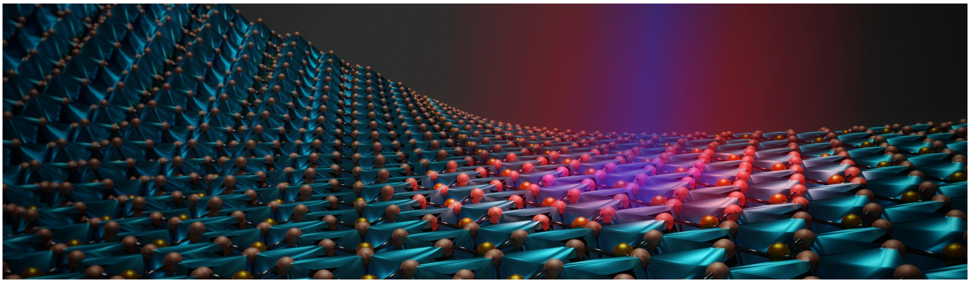

Figure 1.4: Nanomechanical probe of vibrating antiferromagnetic $FePS_3$ membrane [67], artistic impression.

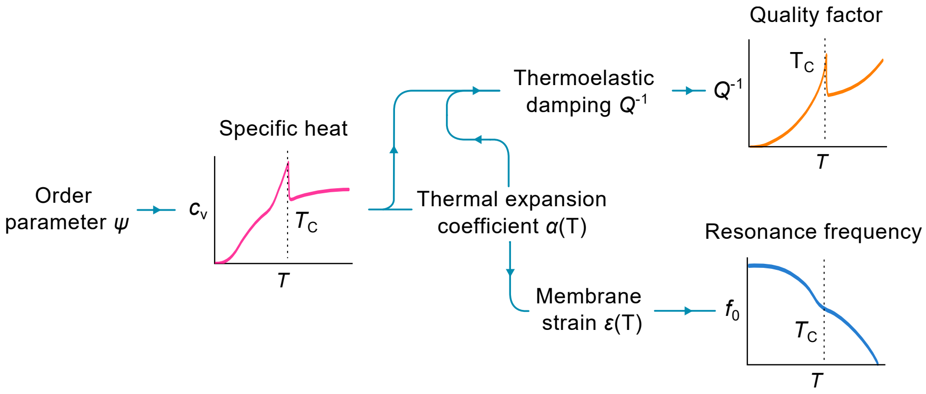

Figure 1.5: Schematic diagram indicating interrelations between mechanical and thermodynamic parameters.

1.3. DICTUM FACTUM

This thesis consists of four parts. Part I explains the fabrication of 2D material membranes and formulates the nanomechanical techniques used to probe these. In Part II we discuss 2D materials with rather notable elastic effects in mechanical properties of their membranes. We fabricate stacked double-layer graphene membranes and probe their superior elastic properties. We further utilize these membranes in capacitive pressure sensors, showing their promising perspectives for commercialization. We also introduce a new anisotropic 2D material - arsenic sulfide As_2S_3, which is significantly more stable in air than black phosphorus [107, 108] and makes it possible to study its anisotropic elastic properties in detail by using angle-resolved nanomechanical probes.

In Part III, we look at membranes with more complex, higher-order effects in their nanomechanical motion. These effects arise when material parameters, such as thermal expansion coefficient, cannot be taken as constant[‡] to describe the experimental observations since these are affected by phenomena that are complicated functions of temperature and strain. In particular, we investigate the influence of second-order phase transitions on the mechanical properties of 2D material membranes. First, we formulate a direct connection between the free energy, the order parameter, and the membrane tension. Then, we theoretically substantiate this connection and also experimentally verify it for various phase transitions in materials of different types and origins, such as 2D layered antiferromagnets, ferromagnets, and their heterostructures. Finally, we also discuss how mechanical dissipation, driven by thermoelastic damping mechanisms, can affect the operation of more complex mechanical systems, such as coupled membrane resonator pairs made of antiferromagnetic transition metal phosphor sulfides.

In Part IV, we provide an outlook for future experiments that become possible based on our results. We discuss the preliminary experimental evidence that suggests that these methods that can bridge many other condensed matter physics phenomena and nanomechanical experiments: i) studies of critical behavior via spontaneous magnetostriction; ii) studies of thermodynamics near phase transitions in thin layers through

---

[‡] Zero-order approximation.

the mechanism of thermoelastic damping and membrane quality factor (see Fig. 1.5); iii) and importantly, application of the methodology to electronic second-order phase transition systems, like charge density waves materials.

I

Part One

Methods

Chapters 2 and 3

2

FABRICATION

In this chapter, we discuss the typical workflow of the fabrication and characterization of 2D material membranes. We first present the process for fabricating the substrates with the arrays of cavities to support freestanding membranes. Then, the 2D material mechanical exfoliation and transfer are discussed. Lastly, we describe the characterization procedures of suspended membranes.

MEMBRANES of 2D materials are used in various applications [5], such as gas sensing [91], molecular sieving [109], water filtration [20], resonant and physical sensors [94, 97, 110]. Of course, the quality of the material that is forming membranes in these cases and the corresponding fabrication workflow radically variates. For instance, porous, rich of defects graphene oxide membranes are promising for gas sieving and filtration [20, 109]. In some works, to get that functionality pristine graphene membranes are treated with invasive tools, such as heavy-ion bombardment to distort perfect long-range crystallinity and controllably establish pores [91]. In contrast, the same distorted membrane then cannot be used for other applications, like pressure sensing [94, 97, 110], or fundamental studies, like observing quantum phenomena through mechanical resonance [86].

One requires fabricating pristine, flat, single-crystal membranes - as free of defects, contamination, and irregularities as possible - to study purely mechanical phenomena and higher-order condensed matter effects in mechanical resonance. For this reason, some conventional methods to handle and transfer 2D materials, such as the hot pick-up technique [111], cannot be applied to suspend any material of arbitrary choice due to the often found high reactivity of these in air, even at relatively small temperatures above ambient room conditions [47].

Here, we will discuss the all-dry viscoelastic method for transferring 2D materials [112] and suspending these to form membrane resonators. This is a bottom-up fabrication technique that allows the fast and deterministic transfer of 2D material flakes at room temperature in the absence of liquids. We find this method to be the least invasive and the most suitable to create pristine, high-quality membranes of the materials discussed in this thesis.

2.1. SUBSTRATE FABRICATION

Most of the membranes discussed in this thesis are suspended and supported by silicon dioxide (SiO_2) on p++ doped silicon (Si) substrate with an array of holes of either circular or rectangular shape etched through the SiO_2. To fabricate these, we first dice a Si/SiO_2 (oxide thickness: 285 nm) wafer into square pieces of about 2×2 cm^2 in lateral size (unless specified otherwise). We then clean these chips in nitric acid (HNO_3). The process flow differs for the samples where the deposition of electrical contacts is desired to contact the flake of 2D material. This feature requires additional fabrication steps that are skipped for chips with cavities only.

To pattern the desired metallic leads for electrical contact to the sample on the chip, we spin-coat two subsequent layers of poly(methyl methacrylate) (PMMA): 495 and 950 kDa for the bottom and the top layer, respectively. We use these layers as a mask to pattern a specific design using electron-beam (e-beam) lithography at a dose ranging at $900 - 1100$ μc/cm^2. We then develop a resist for 90 seconds in a 1:3 solution of methyl isobutyl ketone (MIBK) and isopropyl alcohol (IPA). To ensure complete removal of the resist, we rinse the chips for additional 90 seconds in IPA. After the development, exposed substrate areas are etched using by using a reactive ion etcher (RIE) with CHF_3 (50 sccm) and Ar (2.5 sccm) plasma, removing 100 nm of the 285 nm of exposed SiO_2. Then, using an electron beam evaporator, we evaporate 5 nm of titanium (Ti) and 95 nm of either gold (Au), palladium (Pd) or gold-palladium (Au-Pd) into the etched structure.

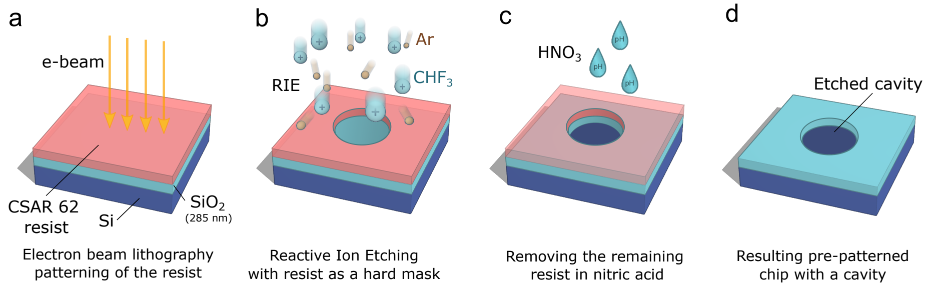

Electron beam lithography patterning of the resist

Reactive Ion Etching with resist as a hard mask

Removing the remaining resist in nitric acid

Resulting pre-patterned chip with a cavity

Figure 2.1: Schematic of the process flow for patterning Si/SiO_2 substrates without electrodes. **a** Electron beam (e-beam) lithography step. **b** Reactive ion etching (RIE) step. **c** Resist stripping step. **d** Resulting substrate.

This way, we embed the electrodes into the SiO_2, minimizing the step height between the surface of SiO_2 and metal contact. The chips are then submerged in 45°C warm acetone for about 45 minutes for a lift-off process and rinsed in IPA.

In the consequent step, we etch holes through the 285 nm thin SiO_2 layer to define the desired array of cavities. The process for samples without electrodes typically starts from this step. The main stages of the process are schematically depicted in Fig. 2.1. To pattern an array of cavities in SiO_2 layer of a substrate, we spin-coat CSAR 62 (AR-P 6200) resist. We pattern it using e-beam lithography with doses ranging 300-350 $\mu C/cm^2$ (Fig. 2.1a). Resist is then developed, following by the etching of exposed SiO_2 areas in RIE (Fig. 2.1b). Resist is utilized as a hard mask, as the etching rate ratio between CSAR 62 and SiO_2 is about 1:2. After the process, the remaining resist is stripped in HNO_3 (Fig. 2.1c) or, in some cases, in PRS-3000. The resulting chips (Fig. 2.1d) are diced into smaller 4×4 mm^2 substrates (unless specified otherwise), which are then plasma-cleaned in O_2 barrel asher and prepared for 2D material transfer.

In some experiments in Chapter 7, we used a different process flow to fabricate more intricate sample designs that involved an additional electrically insulating layer of spin-on glass. The specific fabrication details, in this case, are explained accordingly in Chapter 7 and could also be found in previous works [97, 113].

2.2. 2D MATERIAL PREPARATION

To create suspended membranes, thin pieces of van der Waals material are transferred on a pre-patterned Si/SiO_2 chip. SiO_2 provides mechanical support and electrical insulation between the transferred 2D material membranes and the bottom Si plate. We use mechanical exfoliation from bulk crystals to reliably produce few-nanometer thin monocrystalline layers of 2D materials[*] [114], and deterministic all-dry viscoelastic stamping to transfer these to the substrate [112]. This method is noninvasive [112] and clean of residue (comparably to alternative techniques [111, 115]). It allows performing the 2D material transfer at room temperature without additional chemicals and liquids, which helps to maintain the pristine quality of fragile or chemically sensitive materials. The absence of contact with liquids also helps to leave the suspended membranes intact,

---

[*] Apart from the fabrication of stacked double-layer graphene membranes, described Chapter 4.

Material	Crystal	Origin	Notable property
graphene	CVD[†]-grown monolayers	Applied Nanolayers B.V.[‡]	High Young's modulus and tensile strength [116]
As_2S_3	Natural bulk; Synthetic bulk	Senduchen, Russia; 2D Semiconductors[‡]	Anisotropic Young's modulus [108, 117]
WSe_2	Synthetic bulk	2D Semiconductors[‡]	High thermal expansion coefficient [118]
$FePS_3$, $MnPS_3$, $NiPS_3$, $CoPS_3$	Synthetic bulk	University of Valencia	Antiferromagnets [58, 62]
MUVs[§]	Synthetic bulk	University of Valencia	Antiferromagnets [64]
$Cr_2Ge_2Te_6$	Synthetic bulk	Peking University	Ferromagnet [47]
TaS_2, $TaSe_2$	Synthetic bulk	University of Valencia	Charge density waves [35, 119]

Table 2.1: List of van der Waals crystals used to fabricate 2D material membranes in this thesis.

as capillary forces often delaminate the transferred flakes, create cracks or collapse the membranes to the bottom of the cavity.

In fabricating samples, we use several bulk van der Waals crystals described in Table 2.1. Thin flakes of these materials are exfoliated using an adhesive tape method [7, 114]. We use "Nitto" and "Scotch Magic" tapes to exfoliate from natural or high-quality synthetically grown crystals (see Table 2.1 and Fig. 2.2a) with known stoichiometry. After few iterations, the exfoliated 2D material is transferred from the adhesive tape (Fig. 2.2b) to the optically transparent and chemically inert polydimethylsiloxane (PDMS) stamp on top of the microscope glass slide, which serves as rigid support (Fig. 2.2c). The tape is then gently pressed into the PDMS stamp to release any air pockets between the two surfaces and sharply peeled off. Viscoelastic forces between the PDMS stamp and 2D material result in some of the thin 2D material flakes staying on the surface of the stamp (Fig. 2.2d).

Using the reverse procedure, the PDMS stamp with the flake on its surface is turned upside down and brought in contact with the pre-patterned substrate to transfer the flake (Fig. 2.3a). We use micromanipulators to control the distance between the stamp and the surface of the substrate. We also exploit the optical transparency of both the stamp and thin 2D material flakes [112] to control the positioning of the flake over the

---

[†] Chemical Vapour Deposition [120]

[‡] Commercial company

[§] Materials of the University of Valencia, a layered coordination polymer family [64]

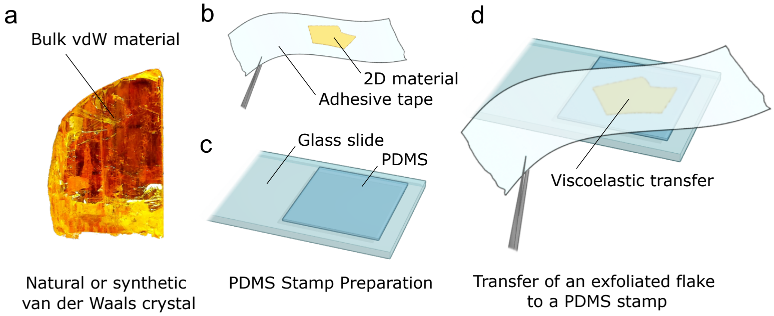

Figure 2.2: Schematic of exfoliation steps and stamp preparation. **a** Image of the As_2S_3 bulk crystal. **b** Mechanical exfoliation step. **c** Polydimethylsiloxane (PDMS) stamp preparation step. **d** Viscoelastic transfer of the flake to the stamp.

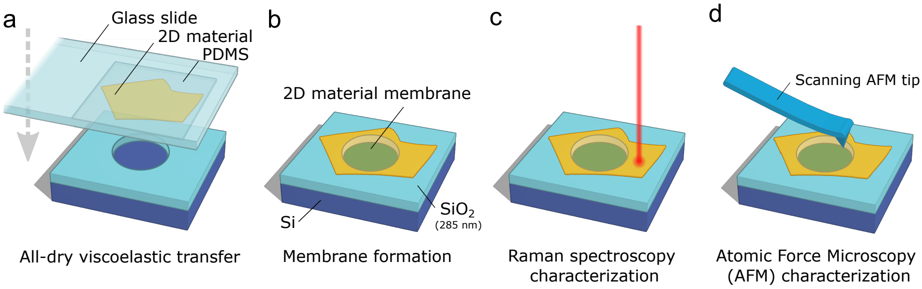

Figure 2.3: Schematic of the all-dry viscoelastic transfer and characterization of the sample. **a** Viscoelastic transfer step. Grey arrow indicates the axis of motion. **b** 2D material membrane suspended over a cavity in the Si/SiO_2 substrate. **b** Raman spectroscopy characterization step. Red ray indicates the laser beam. **d** Atomic Force Microscopy (AFM) tapping mode imaging step.

etched cavities in the substrate to cover these fully and create suspended membranes (Fig. 2.3b). The delamination of the flake is performed at a slow rate to avoid any damage to the membrane. Using the same method, flakes can also be deterministically stacked on top of each other forming heterostructures.

2.3. SAMPLE CHARACTERIZATION

After the membrane is fabricated, we characterize some samples using the Raman spectroscopy technique to confirm the quality and crystallinity of the material (Fig. 2.3c). Raman spectroscopy studies are performed using a Horiba Scientific LabRAM HR system at an excitation of either $\lambda_{\text{red}} = 632$ nm, $\lambda_{\text{green}} = 514$ nm, or $\lambda_{\text{blue}} = 488$ nm in a backscattering geometry in parallel-polarized configuration of incident and scattered light field ($e_i || e_s$) with a 360° rotational sample stage. We also perform an additional characterization step for some samples by imaging these using scanning electron microscopy (SEM) in an FEI Nova NanoSEM 450 system.

For the last step, we inspect the membranes using atomic force microscopy (AFM)

(Fig. 2.3d). Inspection and height profile scans are performed in tapping mode on a Bruker Dimension FastScan AFM. We typically use cantilevers with spring constants of $k_c = 30 - 40\ \mathrm{Nm}^{-1}$. The flake thickness with a corresponding uncertainty is determined by measuring multiple profile scans of the same flake. In Fig. 2.4, we show examples of AFM tapping-mode images for membranes of several materials studied. As a result of all-dry viscoelastic stamping, the suspended region of the flake is typically pristine and free of polymer residues. Depending on various factors, such as the thickness of the membrane, flow of the fabrication process, and the material used, these membranes can be found sagged down, as shown in Fig. 2.4a with profile scans indicated with solid magenta lines. In some cases, it also facilitates the adhesion to the sidewalls of the cavity, shown in Fig. 2.4b, which can affect the thermal properties of the membrane [78]. However, when the fabrication nuances are optimized for the particular material, flat and homogeneous membranes can be fabricated, similar to those shown in Fig. 2.4c and d.

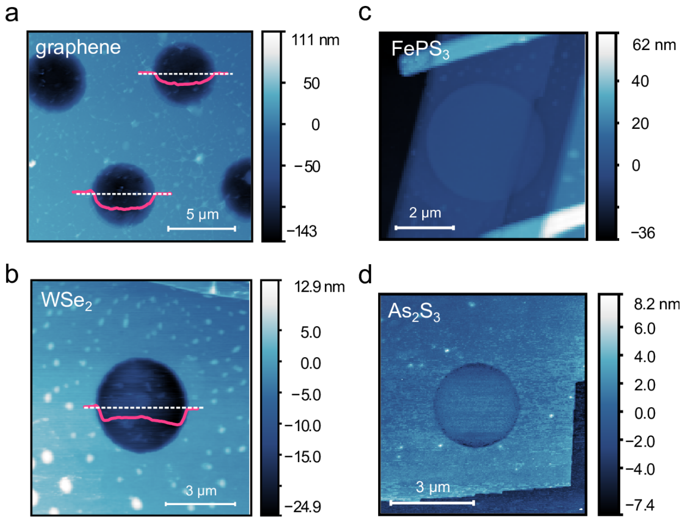

Figure 2.4: Suspended membranes of **a** stacked double-layer graphene (see Chapter 4), **b** tungsten diselenide (see Chapter 9), **c** iron phosphor trisulfide (see Chapter 6), and **d** arsenic trisulfide (see Chapter 5). Solid magenta lines in (a) and (b) indicate the profile of line scans (dashed lines).

2.4. MATERIAL SELECTION

It is essential to mention the reasons why the choice of material is crucial when fabricating the samples. The materials discussed in this thesis are notable for their properties (see Table 2.1). For example, in Chapters 6, 7, 8, 10 and 11 we discuss membranes made from different kinds of van der Waals antiferromagnets. Each of these materials has its characteristic fabrication subtleties that determine the quality of membranes produced, which is important for studying high-order properties in these membrane resonators.

Different materials exfoliate in different ways, giving a characteristic geometry for the flakes depending on the symmetry of the crystal and interlayer bonding. For ex-

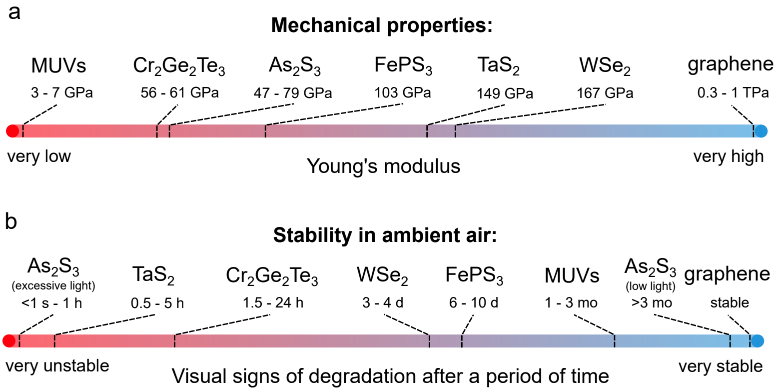

Figure 2.5: Properties of the materials from Table 2.1. **a** Mechanical properties of the materials [48, 59, 64, 108, 117, 121–123]. **b** Average degradation time of few-layer samples as determined by the appearance of visually notable signatures of decomposition [45, 47, 64, 108]. s indicates seconds, h - hours, d - days and mo - months.

ample, the cubic lattice of the metal-organic MUV layers in Chapter 8 produces strictly rectangular-shaped flakes of rather homogeneous thickness [64]. However, crystals such as As_2S_3 and $Cr_2Ge_2Te_6$ in Chapters 5 and 9, respectively, are often found in sawtooth-shaped flakes with numerous terraces on the material's surface [47, 108]. The mechanical properties of these materials also should be taken into account. We present these properties for the key materials used in this thesis in Fig. 2.5a. Graphene, being an atomically thin 2D material, has remarkable strength and an extremely high Young's modulus [116], which allows it to be easily obtained and suspended as a membrane. On the other hand, metal-organic layers of MUVs are much more flexible and brittle, which makes it much more difficult to suspend and characterize [64].

In addition, the presented materials have very different chemical stability in the air, as shown in Fig. 2.5b. While the $FePS_3$ membranes in Chapter 6 can be exposed to air atmosphere for several days [45], the TaS_2 membranes in Chapter 12 degrade within a few hours [124]. One shall take all these parameters into account in the manufacture of 2D material membranes and, subsequently, store these in an oxygen-free low-light environment to avoid degradation and surface oxidation.

3

EXPERIMENTAL TECHNIQUES

In this chapter, the static and dynamic methods of mechanical characterization of 2D material membranes are described. The chapter provides basic principles of the techniques used in this thesis, explaining which material parameters or phenomena could be probed with each method. We discuss static deflection of membranes by point-force applied with Atomic Force Microscopy tip and by gas pressure difference. We also describe the laser interferometry technique that is used to probe membrane resonance frequencies at an extended temperature range.

Nanomechanical methods [5] provide various mechanisms where two-dimensional (2D) material membranes are used as probes for ultra-small change of mass [125, 126], thermodynamic [78, 79, 127] and electromagnetic [128] interactions, nonlinear dynamics [81, 85] and quantum phenomena [86]. Several readout methods, incl. transconductive [89], capacitive [97], and optical [24] mechanisms exist to probe a change in static or dynamic deflection of the membrane arising from the interaction of this membrane with internal or external effects [5]. The deflection for a unit of applied force is mainly defined by the elastic properties of the membrane material, such as Young's modulus and Poisson's ratio and its strain [37]. At first assessment, this dependence looks solely mechanical. However, thermodynamic interactions in the material and coupling of physical phenomena to strain make nanomechanical membrane resonators a powerful tool to characterize condensed matter phenomena in a wide variety of materials [41, 57, 67, 124], including ultra-low in volume, atomically thin or electrically insulating so that conventional bulk characterization methods become unsuitable [57, 67].

Several methods are used in this thesis as a tool to probe mechanical properties of the membranes and to unambiguously relate these to material properties, such as anisotropic stiffness, and higher-order effects, such as second-order phase transitions, magnetostriction and thermoelastic dissipation. We group these experimental techniques into static and dynamic nanomechanical methods, indicating whether the membrane is probed in motion or at rest. Here, we discuss the basic principles behind each of these methods and demonstrate their applicability in experiments. Static methods are applied at room temperature and are mainly used to either assess or utilize the elastic properties of the membranes in Part II and III. Dynamic methods are applied at cryogenic temperatures down to $T = 4$ K, allowing to probe strain in the membrane as a function of temperature and electrostatic force. This way, we use thermal strain to assess second-order phase transitions, such as from paramagnetic to (anti-)ferromagnetic in suspended van der Waals crystals in Part III and IV.

3.1. STATIC NANOMECHANICAL METHODS

3.1.1. FORCE-INDENTATION ATOMIC FORCE MICROSCOPY

Force-indention Atomic Force Microscopy (AFM) method is a reliable mechanical probe of 2D material membrane defection in response to a force applied at its center by an AFM cantilever tip [12, 37, 129]. In our AFM setup, we fix the sample on xy piezoelectric positioning stage, as we show in Fig. 3.1a. We use AFM cantilevers of typical stiffness ranging $k_c = 1-32$ Nm^{-1} in force-indentation experiments, that are placed directly above the membrane on z-axis close-loop piezoelectric nanopositioner. We use cantilever tips with a tip radius of $\sim 7-10$ nm, as confirmed by scanning electron microscope imaging. Upon the contact with the sample the deflection of AFM cantilever is recorded in real time by measuring reflected laser intensity from its top surface by the four-quadrant photodiode. The generated photodiode voltage is then calibrated with the deflection of the cantilever against the solid surface to get the deflection sensitivity in Vm^{-1}. This way the deflection of the cantilever Δz_c can be measured in nanometers in real time and the cantilever stiffness k_c can be calibrated from the thermal tuning procedure [130].

We characterize the suspended membranes by deflecting these from the position of

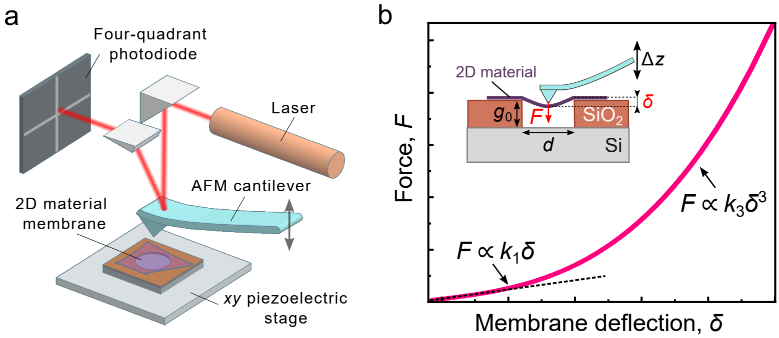

Figure 3.1: Schematic of the force-indentation Atomic Force Microscopy (AFM) technique. **a** Schematic of the AFM measurement setup. Grey arrow indicate the AFM tip movement by z-axis piezoelectric positioner. **b** Trend of the force-deflection curve of Eq. 3.1. Linear and cubic part is indicated. Inset: Schematic of the experimental principle. Δz is the motion of the z-axis piezoelectric positioner, δ the membrane deflection, d the membrane diameter, F the applied force, g_0 the cavity depth, and $k_{1,3}$ the linear and cubic spring constant.

rest, applying a force $F = k_c \Delta z_c$ at its centre with the tip of the AFM cantilever. The elastic deformation of the membrane $\delta = \Delta z - \Delta z_c$ during the loading cycle is measured as a difference between the motion of the z-axis piezo-positioner Δz and the cantilever deflection Δz_c, as shown in the inset of Fig. 3.1b. Small applied force F causes the linearly proportional membrane deflection δ as $F \propto k_1\delta$. The linear spring constant of the membrane k_1 then is related to both its pre-tension and elastic material parameters. However, at large F it is cubic in δ, as shown in Fig. 3.1b. The complete equation for a circular membrane deflection with a point-force applied at its centre reads [12, 129]:

$$F = k_1\delta + k_3\delta^3 = \left(\frac{4\pi E}{3(1-\nu^2)}\,\frac{h^3}{r^2}\right)\delta + (\pi n_0)\,\delta + \left(\frac{q^3 E h}{r^2}\right)\delta^3, \tag{3.1}$$

where E is the Young's modulus, ν the Poisson's ratio and n_0 the pre-tension, h the thickness, r the radius, and $q = 1/(1.05 - 0.15\nu - 0.16\nu^2)$ the geometry-related parameter [129]. Three terms are noted in Eq. 3.1. The first term is related to the bending stiffness and is negligible in atomically thin membranes [12, 129]. The second term is dominated by membrane pre-tension, that accumulates during the fabrication. The third therm is related to nonlinear membrane stiffness. It is notable that only cubic terms are independent on pre-tension in membranes, thus the elastic material parameters can be extracted from the nonlinear part of the experimentally measured δ, given that ν of the material is known or calculated separately [12, 129], as we discuss in Part II of this thesis.

3.1.2. GAS PRESSURE MEMBRANE DEFLECTION

Another technique to control the static membrane deflection and probe its elastic properties is the gas pressure deflection method [6, 19, 23, 110], often referred to as a bulge test [131]. When a membrane of 2D material fully covers a circular cavity, the gas trapped inside of this cavity is effectively sealed at atmospheric pressure during the fabrication [19, 23, 92, 93, 110]. Thus, when the external gas pressure outside the cavity is changed and the gas escape time is long enough, the membrane will deflect either up or down,

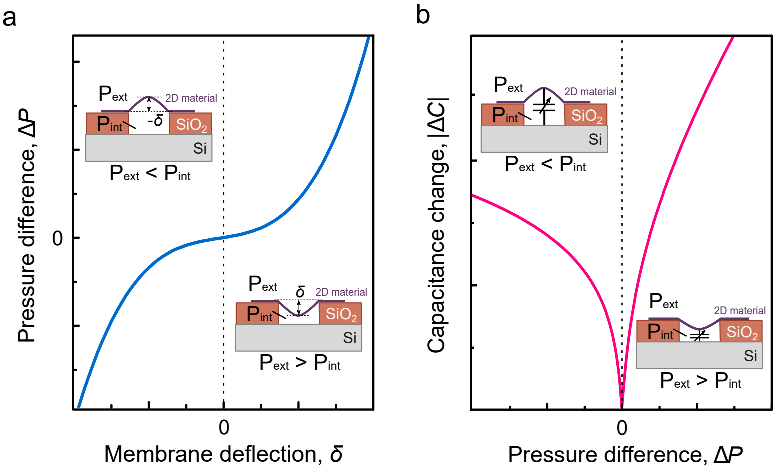

Figure 3.2: Gas pressure membrane deflection principle. **a** Dependence between the pressure difference ΔP and the membrane deflection δ. Insets: Schematics of the membrane deflection at corresponding external P_{ext} and internal P_{int} gas pressure. **b** Trend of the capacitance change ΔC per ΔP. Insets: Schematics of the capacitance change due to membrane deflection. Vertical dashed lines in both panels indicate reference at zero.

depending on the expansion or contraction of the volume of the trapped gas inside the cavity [19, 23].

This principle is also applicable for practical purposes. Graphene membranes are intrinsically impermeable for gases [23, 93], making circular graphene membranes effectively vacuum-proof sealed nanodrums [23, 92, 93]. In combination with large membrane deflections in response to the slightest changes in external pressure, this property makes them promising for applications in gas pressure sensing [95, 97, 110, 132], as demonstrated in Chapter 4. Conducting properties of graphene at the same time allow to capacitively read out the deflection with sensitivity compatible with state-of-the-art commercial pressure sensors [95–97, 110, 132].

The pressure difference $\Delta P = P_{\text{int}} - P_{\text{ext}}$ established between the internal pressure of a gas trapped inside of a cavity P_{int} and the external atmospheric gas pressure P_{ext} corresponds to the circular membrane deflection that it causes at its centre δ [19, 97] as:

$$\Delta P = \frac{4n_0}{r^2}\delta + \frac{8Eh}{3r^4(1-\nu)}\delta^3. \tag{3.2}$$

In Fig. 3.2a, we show the trend of Eq. 3.2 in abstract units. For $P_{\text{int}} \gg P_{\text{ext}}$, the membrane bulges up establishing negative δ and deflecting the membrane away from Si back-plate. Symmetrically, for $P_{\text{int}} \ll P_{\text{ext}}$ the membrane deflects down minimising the separation between membrane and Si electrode. The deformation shape $\xi(r')$ at an arbitrary radial distance from the centre r' is assumed to be hemi-spheric [133]:

$$\xi(r',\delta) = \delta\left(1 - \frac{r'^2}{r^2}\right). \tag{3.3}$$

Thus, the membrane deflection shape affects the capacitance of the device as:

$$C(\delta) = 2\pi\varepsilon_0 \int_0^r \frac{r'}{g_0 - \xi(r',\delta)} \mathrm{d}r', \tag{3.4}$$

where ε_0 is the vacuum permittivity. The capacitance change $\Delta C(\delta) = C(\delta) - C_0$ to that capacitance C_0 at $\Delta P = 0$ as a result is asymmetric around zero, as we show in Fig. 3.2b. The shape of the curve in Fig. 3.2b depends strongly on membrane and material parameters given by Eq. 3.2. Therefore, as discussed in Chapter 4, production of a high-sensitivity gas pressure sensor requires optimization of all parameters in Eq. 3.2.

3.2. DYNAMIC NANOMECHANICAL METHODS

3.2.1. LASER INTERFEROMETRY AND RESONANT MEMBRANE MOTION

The most commonly used experimental technique in this thesis is laser interferometry [24]. We use it to bring 2D material membranes to motion and measure their vibration using a homodyne detection scheme [134]. In the laser interferometer setup (see Fig. 3.3a), a power-modulated blue diode laser (λ = 405 nm) is used to excite and optothermally drive into motion the membrane, that is placed inside of a low-temperature vacuum chamber. The blue laser beam is emitted by a laser diode and then guided to the sample chamber using a cold mirror. When the membrane is in motion, an interferometric displacement detection is obtained by focusing a He-Ne laser beam (λ = 632 nm) on the suspended membrane centre. Coupling of the membrane deflection to the optical field is accomplished by a combination of absorption of the membrane and reflection from its surface. The interfering reflections from the membrane and the Si substrate underneath are then guided to a photodiode using a combination of quarter-wave plate ($\lambda/4$) and polarizing beam splitter cube. The modulation of the photodiode signal, that is a measure of the displacement of the membrane, is processed by a vector network analyzer (VNA).

The sample under test is mounted on a xyz piezopositioning stage inside a closed-cycle optical 4 K cryostat Montana Instruments Cryostation s50, as shown in Fig. 3.3b. The membranes are measured with a spacial resolution by moving the sample with respect to lasers with nanopositioners [134]. The laser spot size that we achieve with this setup is in the order of $\sim 1-2$ μm depending on the objective used (50x/100x), allowing to measure membranes > 2 μm in lateral size. A local sample heater is used to perform temperature sweeps at a rate of ~ 3 K per minute, while keeping the pressure in the chamber below 10^{-6} mbar. However, during data acquisition the temperature is kept constant with ~ 10 mK stability by the heater and a closed feedback loop temperature controller Lakeshore 335.

Using the laser interferometry technique, we acquire the amplitude data near the fundamental resonance frequency of the mechanical resonator $f_0(T)$ at a set temperature T. At f_0 a characteristic resonance peak in amplitude A is found together with a corresponding $\Delta\phi = 90°$ phase shift between force and displacement, that can be described by linear harmonic oscillator model [135, 136], as shown in Fig. 3.3c. The quality factor Q for a membrane in motion is defined as the ratio of the energy stored in the resonator to the energy lost per one radian of the oscillation cycle, and is calculated from

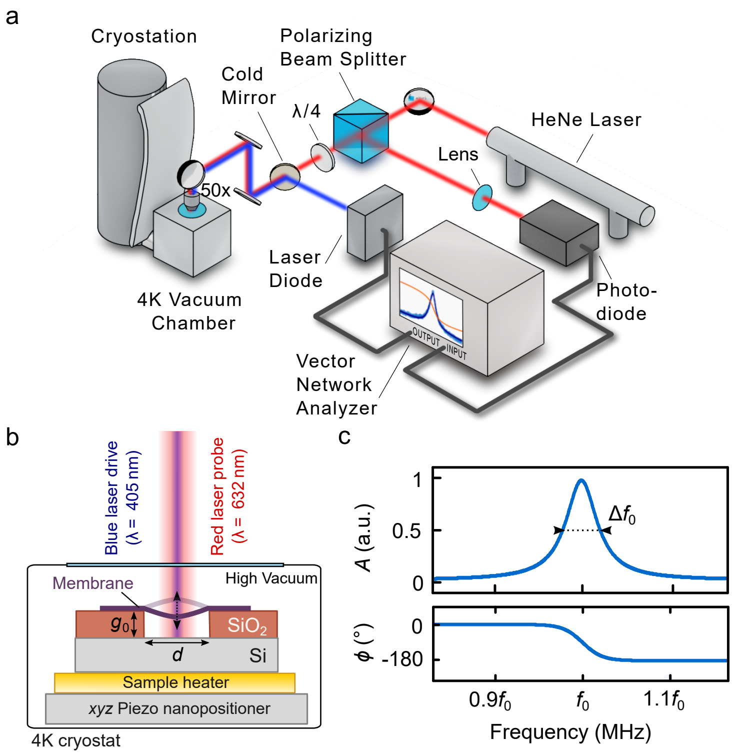

Figure 3.3: Laser interferometry technique. **a** Schematic of the laser interferometry setup. **b** Schematic of the vacuum chamber cross-section with the device mounted. Vertical black arrow indicates the motion of the membrane in the optical field. **c** Amplitude A of the resonance peak of the fundamental membrane mode and corresponding phase ϕ. f_0 is the resonance frequency and Δf_0 the full width at half maximum of the peak.

the full width at half maximum of the peak Δf_0 as $Q = \frac{f_0}{\Delta f_0}$.

The resonance frequency of the membrane resonator, f_{membrane}, is dictated by its tension $n(T)$ [136]:

$$f_{\text{membrane}} = \frac{2.4048}{\pi d}\sqrt{\frac{n(T)}{\rho h}}. \tag{3.5}$$

where d is the diameter of the membrane, and ρ the mass density. However, often the membranes discussed in this thesis are made of many-layer 2D material flakes and also have a small bending rigidity contribution. In the crossover membrane-plate regime f_0 can be approximated as [136, 137]:

$$\begin{aligned} f_0(T) \approx \sqrt{f^2_{\text{membrane}} + f^2_{\text{plate}}} = \\ \sqrt{\left(\frac{2.4048}{\pi d}\right)^2 \frac{n(T)}{\rho h} + \left(\frac{10.21 h}{\pi d^2}\right)^2 \frac{E}{3\rho\left(1-\nu^2\right)}}. \end{aligned} \tag{3.6}$$

For the thicker plate-like resonators $f_{\text{plate}} \propto h$, for small and linear deflection [136–138].

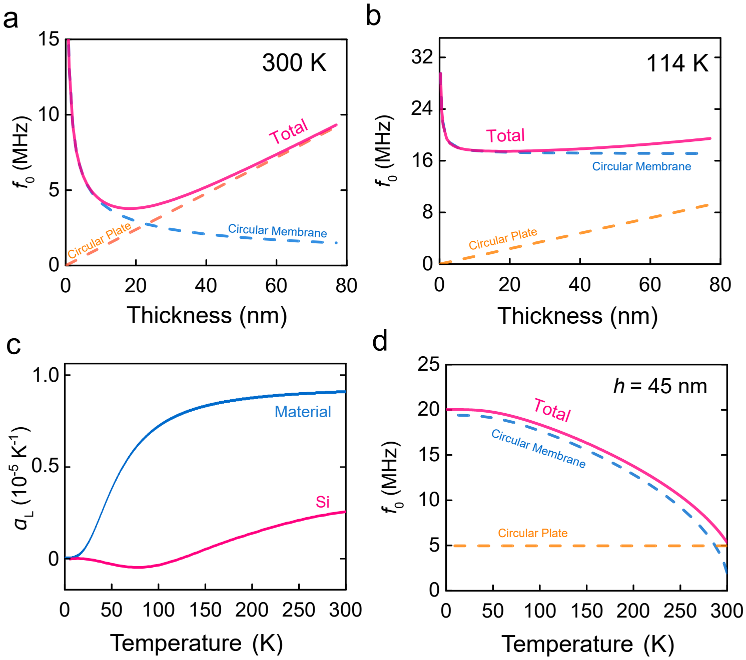

Figure 3.4: Resonance frequency of a membrane resonator as a function of thickness for **a** 300 K and **b** 114 K. **c** Comparison of thermal expansion coefficients of the material as predicted from the Debye model (solid blue line) to that of the Si substrate (solid magenta line). **d** Calculated resonance frequency of the membrane using Eq. 3.6 with a diameter of 10 μm taking into account the thermal expansion coefficient of the material form (c).

For thin membranes, however, Eq. 3.5 yields $f_{\text{membrane}} \propto h^{-0.5}$. When the membrane is subjected to temperature changes, the total tension is dominated by thermal strains ϵ_{th}. Thermal strains are of dilatational nature and do not cause any shear, thus, these can be written as: $\epsilon_{\text{th}} = -\alpha\Delta T$, where α is the thermal expansion coefficient. In-plane thermal strain is then related to tension according to the Hooke's law as $n(T) = n_0 + \frac{Eh\epsilon_{\text{th}}(T)}{(1-\nu)}$, where n_0 the intrinsic pre-tension introduced during the fabrication process. Thus, according to the Eq. 3.6 the membranes under study of a range of thicknesses can be found in the plate or in the membrane limit at a given temperature.

We use Eq. 3.6 to plot f_0 of the circular resonator in the membrane-plate crossover regime as a function of its thickness. For practical reasons, we use material parameters $E = 103$ GPa, $\nu = 0.304$ and $\rho = 3375$ kg m^{-3}, that are close to that of FePS$_3$ [59], which is used in Chapters 6, 7, 9, 10 and 11 of this thesis. The relative contribution of the plate term to the frequency of the resonator is largest at room temperature because the membrane tension is the lowest. As shown in Fig. 3.4a at $T = 300$ K and $n_0 = 0.1$ N m^{-1}, thicker resonators ($h > 40$ nm) behave as circular plates. However, as shown in Fig. 3.4b, at lower temperature ($T \approx 114$ K) due to temperature-induced strain $\epsilon(T)$ the resonator behaves closer to the membrane limit over a thickness range from that of a single-layer to ~ 60 nm.

The total strain in such membrane is found using $\epsilon(T) = \epsilon_0 - \int_{300\mathrm{K}}^{T} (\alpha_{\mathrm{material}}(T) - \alpha_{\mathrm{Si}}(T))\mathrm{d}T$, where ϵ_0 is the intrinsic pre-strain at $T = 300$ K [139, 140]. Because $\alpha_{\mathrm{SiO_2}} \ll \alpha_{\mathrm{Si}}$ [141, 142], the effect of the thin $\mathrm{SiO_2}$ layer in the substrate can be neglected. As shown in Fig. 3.4c, the thermal expansion coefficient of the silicon substrate (solid magenta line) is substantially smaller as compared to that of the membrane (solid blue line), as estimated from the thermodynamic relations and the Debye model of specific heat [67] (see Chapter 6). Therefore, the total strain in the membrane will mainly build up due to $\alpha_{\mathrm{material}}$, and this term dominates the change in resonance frequency $f_0(T)$, even for the membrane as thick as $h = 45$ nm, as depicted in Fig. 3.4d.

Variations in the thermal expansion coefficient that affect the strain of the membrane can be probed via its resonance frequency (see Eq. 3.6). This is an important direct link that couples mechanical degrees of freedom to thermodynamic quantities of the membrane's material, providing a possibility to probe condensed matter physics using mechanical resonators [41, 57, 67, 124]. According to thermodynamic models, the thermal expansion coefficient is proportional to a fundamental material parameter - the specific heat. As near a phase transition it is expected to exhibit a discontinuity, the temperature-dependent resonance frequency of a suspended membrane can thus be used to probe the phase change, as we discuss in Parts III and IV.

3.2.2. ELECTROSTATIC DEFLECTION OF CIRCULAR MEMBRANE

In addition to the thermal tension in response to the change of the membrane temperature, strain in the 2D material membrane at motion can be controlled also utilizing electrostatic deflection. A membrane suspended over a circular cavity forms a capacitor C_{g} with a bottom Si gate electrode underneath. The change in gate voltage V_{g} causes the membrane to deflect, tuning the tension and producing a shift in the resonance frequency.

Chen, C. [143] has derived the spring constant k of the membrane resonator under electrostatic strain from continuum mechanics model by analysing a minimum of the total energy [144], given as sum of elastic and electrostatic components $U_{\mathrm{e}} + U_{\mathrm{el}}$:

$$\frac{\partial (U_{\mathrm{e}} + U_{\mathrm{el}})}{\partial z} = \frac{8\pi E h}{3(1-\nu^2) r^2} z^3 + \left(\frac{2\pi E h \epsilon(T)}{1-\nu^2} - \frac{1}{2} C_{\mathrm{g}}'' V_{\mathrm{g}}^2\right) z - \frac{1}{2} C_{\mathrm{g}}' V_{\mathrm{g}}^2 = 0, \tag{3.7}$$

where z is the out-of-plane position of the membrane, and taking the deflection shape ξ under a uniformly distributed electrostatic force from Eq. 3.3 [133, 143]. Thus, the spring constant k of the membrane is found as:

$$k = \left.\frac{\partial^2 (U_{\mathrm{e}} + U_{\mathrm{el}})}{\partial z^2}\right|_{\delta} = \frac{2\pi E h \epsilon(T)}{1-\nu^2} + \frac{8\pi E h}{\left(1-\nu^2\right) r^2}\delta^2 - \frac{1}{2} C_{\mathrm{g}}'' V_{\mathrm{g}}^2, \tag{3.8}$$

where δ is the maximal deflection at the membrane centre and $C_{\mathrm{g}}'' = \frac{\partial^2 C_{\mathrm{g}}}{\partial z^2}$. The resonance frequency of the fundamental vibration mode of the drum as a function of gate voltage is described using Eq. 3.5 and 3.8 as:

$$f_0(V_{\mathrm{g}}) = \frac{1}{2\pi}\sqrt{\frac{1}{m_{\mathrm{eff}}}\left[\frac{2\pi E h \epsilon(T)}{1-\nu^2} + \frac{8\pi E h}{\left(1-\nu^2\right) r^2}\delta^2 - \frac{1}{2}\frac{\partial^2 C_{\mathrm{g}}}{\partial z^2} V_{\mathrm{g}}^2\right]}, \tag{3.9}$$

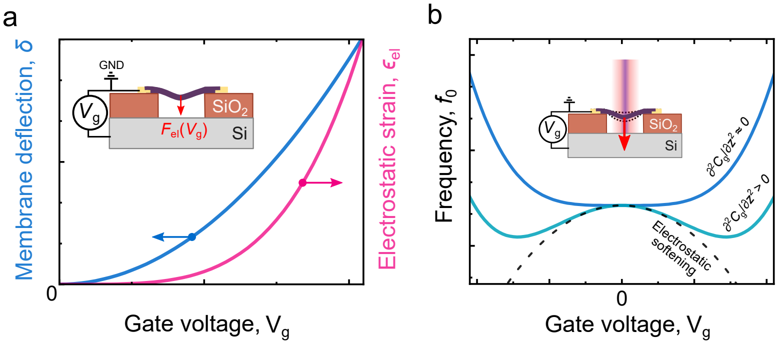

Figure 3.5: Electrostatic deflection of circular membrane. **a** Trend of the membrane deflection and corresponding strain due to an electrostatic force F_{el} applied at the gate voltage V_{g}. Inset: Schematic of the electrostatic membrane deflection. **b** Resonance frequency as a function of V_{g} for different contribution of capacitive term. Grey dashed line indicates the contribution from the electrostatic capacitive softening. Inset: Schematic of the membrane pulling down under F_{el} as it vibrates in the optical field.

where $\frac{\partial^2 C_{\text{g}}}{\partial z^2} \approx \frac{0.542\varepsilon_0 \pi r^2}{g_0^3}$ is the second derivative of capacitance [128, 145], and $m_{\text{eff}} = 0.27\rho h \pi r^2$ the effective mass. The exact solution of Eq. 3.9 for δ at the equilibrium position of the membrane centre due to the electrostatic deflection is rather complex [143]. However, following the approach in Ref. [145] one can approximate δ as:

$$\delta \approx \frac{\varepsilon_0 r^2}{8 g_0^2 n(T)} V_{\text{g}}^2, \tag{3.10}$$

where $n(T) = Eh\frac{\epsilon(T)}{1-\nu}$ is the membrane tension at temperature T. We plot the qualitative trend of the Eq. 3.10 in Fig. 3.5a with a solid blue line. The electrostatic strain ϵ_{el} that corresponds to the deformation of the membrane can be estimated from the the arc length of the deflection [19, 145, 146]: $\epsilon_{\text{el}} \approx \frac{2\delta^2}{3r^2}$, which we plot with a solid magenta line. The alternative derivation is also discussed in Chapter 6, yet quantitatively the resulting equations produce similar values of $\epsilon_{\text{el}}(V_{\text{g}})$. As a result, by combining Eq. 3.10 and 3.9 we show $f_0(V_{\text{g}})$ in Fig. 3.5b.

The Eq. 3.9 consists of three additive terms under the square root. The first term is the elastic contribution. The second term is given by the electrostatic straining. The last term is related to electrostatic capacitive softening of the membrane [128, 145]. When the capacitive softening term is negligible, $f_0 \propto \sqrt{V_{\text{g}}^4}$ that produces U-shaped curve, as shown in Fig. 3.5b with solid blue line. When the term is significant, $f_0 \propto \sqrt{V_{\text{g}}^4 - V_{\text{g}}^2}$ and the curve takes the W-shape, as plotted in Fig. 3.5b with solid green line. Thus, by analyzing measured $f_0(V_{\text{g}})$ using Eq. 3.9 and 3.10, it is possible to quantitatively estimate strain in the membrane under the electrostatic deflection. In addition, since Eq. 3.9 also depends on thermal strain ϵ, this method can be used to probe higher-order phenomena such as second-order phase transitions as a function of electrostatic tension, which we discuss in Part III of the thesis.

II

Part Two

Nanomechanical probe of elastic properties

Chapters 4 and 5

4

GRAPHENE MEMBRANES FOR CAPACITIVE PRESSURE SENSING

The high flexibility, impermeability and strength of graphene membranes are key properties that can enable the next generation of nanomechanical sensors. However, for capacitive pressure sensors the sensitivity offered by a single suspended graphene membrane is too small to compete with commercial sensors. In this chapter, we realize highly sensitive capacitive pressure sensors consisting of arrays of nearly ten thousand small, freestanding double-layer graphene membranes. We fabricate large arrays of small diameter membranes using a procedure that maintains the superior material and mechanical properties of graphene, even after high-temperature anneals. These sensors are readout using a low cost battery-powered circuit board, with a responsivity of up to $47.8\ aF\,Pa^{-1}\,mm^{-2}$*, thereby outperforming commercial sensors.*

Parts of this chapter have been published in *Microsystems* & *Nanoengineering* **6**, 102 (2020) by Makars Šiškins, Martin Lee, Dominique Wehenkel, Richard van Rijn, Tijmen W. de Jong, Johannes R. Renshof, Berend C. Hopman, Willemijn S. J. M. Peters, Dejan Davidovikj, Herre S. J. van der Zant & Peter G. Steeneken

GRAPHENE grown by chemical vapour deposition (CVD) is a strong candidate for realizing next-generation sensor devices [147]. Its hermeticity [23, 92, 93], and superior mechanical [12, 116, 148] and electrical [149] properties, have enabled various types of gas pressure sensors. In most conventional pressure sensors, the pressure is determined from the deflection of a membrane due to the pressure difference between ambient gas and gas in a hermetically sealed reference cavity. There are different ways to readout the deflection of the membrane and thereby quantify the pressure difference. In capacitive graphene pressure sensors, the deflection is readout by measuring the capacitance between the graphene membrane and a reference electrode [95–97, 132]. As the pressure induced deflection increases the mechanical stress and tension in the membrane, it can be measured using the piezoresistive effect [150–152] and can also be probed via the mechanical resonance frequency [23, 92, 153]. In contrast, graphene squeeze-film pressure sensors [94] and Pirani pressure sensors [154] do not require a hermetic reference cavity and operate at small deflection, which can be beneficial for their operation range.

Resonant sensors are conceptually attractive because they potentially offer both gas sensing [91, 155] and pressure sensing [92, 94] functionality within a single device. However, accurate readout of resonance frequencies with low-power electronics is challenging, requires elimination of mass loading and can not be easily scaled up to many devices in parallel. In piezoresistive and Pirani sensors, it is a challenge to eliminate non-pressure related effects of the surrounding gas on the graphene resistance. In contrast, capacitive pressure sensors have the advantage that the membrane capacitance is rather insensitive to gas induced changes in its mass and electrical resistance, and thus depends mainly on geometry and membrane deflection. However, it was found that a single graphene membrane with a diameter of 5 μm has a too small responsivity (< 0.1 aF Pa^{-1}) to be competitive with commercial sensors [97].

In this work, we counter this drawback by creating arrays with a large number of membranes connected in parallel to increase the responsivity [97]. We present few-atom thick pressure sensors that can compete with commercial capacitive pressure sensors using arrays of nearly 10000 double-layer graphene (DLG) membranes. We optimize the design of the sensor elements, the chip layout and the readout electronics to attain a handheld, low-cost, battery-powered electrical readout circuit capable of detecting pressure changes via the static deflection of graphene nanodrums.

4.1. MATERIALS AND METHODS

4.1.1. CHIP DESIGN AND GRAPHENE TRANSFER

Simulations [97] show that to achieve the commercially competitive sensitivity, an array of around 10000 circular graphene drums is needed, each with a diameter of 5 micron. When the drums are placed on a hexagonal grid with a pitch of 10 micron between their centers, they fit on a 1×1 mm^2 chip as shown in Fig. 4.1a. To fabricate this design, Ti/Au electrodes (5 nm/60 nm), for contacting the graphene top electrode, are patterned on a silicon chip with a 285 nm SiO_2 layer. Then the pattern of circular holes with a depth of 240 nm is reactive ion etched into the SiO_2. As shown in the cross-section in Fig. 4.1b, the cavity depth of the holes is less than the SiO_2 layer thickness to prevent the graphene from touching the silicon bottom electrode, and thereby creating an electrical

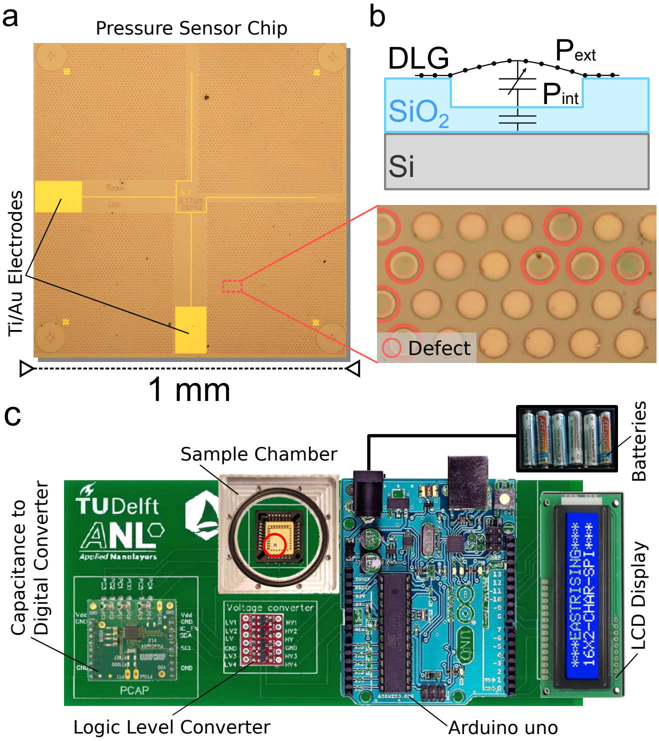

Figure 4.1: Pressure sensor and readout circuitry. **a** Optical image of the sensor chip with 10000 circular holes, a DLG/PMMA membrane and Ti/Au electrodes. Close-up image shows the difference in contrast between intact and defect drums with red circles indicating collapsed membranes. **b** Schematic device cross-section and capacitive pressure readout principle. **c** Read-out circuitry PCB board with the elements labeled. The total size of the PCB board is 6.9 × 17.5 cm^2. The red circle indicates the pressure sensor chip.

short-circuit between the electrodes, when one of the membranes collapses. As a last step the graphene is transferred over the cavities. We use two layers of graphene and small membrane diameter to improve the yield [156] and the mechanical strength [116, 157]. Since the probability that 2 pore defects align is low, the impermeability of DLG is also much higher than that of single layer graphene [23].

To fabricate the double layer graphene (DLG), two sheets of CVD graphene are synthesized and then stacked on top of each other maintaining a pristine quality interface between the sheets. Using Polymethyl Methacrylate (PMMA) as a support layer of 800 nm thickness, DLG is suspended over the pre-patterned circular holes in the SiO_2/Si chip with Ti/Au electrodes (Fig. 4.1a). DLG was produced and transferred in ambient pressure by Applied Nanolayers*. From the differences in contrast between suspended, broken and collapsed drums [156, 158] we estimate that the dry transfer technique results in a yield of 95 – 99% of freely suspended DLG/PMMA membranes. The red circles in the inset of Fig. 4.1a indicate defect drums in a damaged region of the sample and

---

*Commercial company Applied Nanolayers B.V., Delft, NL.

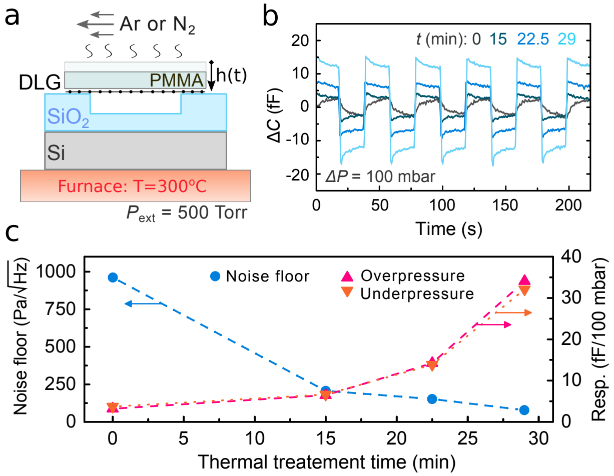

Figure 4.2: Thermal removal of the polymer and its effect on the capacitive response of the sensor. **a** Schematic explanation of the thermal annealing principle that reduces the PMMA thickness $h(t)$. **b** Change in capacitance of a single chip as a function of measurement in response to time dependent pressure changes, ΔP, for samples that have been annealed for different times t (line colors corresponds to color of the corresponding anneal times indicated in the legend). The gas pressure is changed at a rate of 175.4 mbar s^{-1}. **c** Responsivity and noise floor extracted from the data in **b** calculated using Eq. 4.1.

show this difference in contrast.

4.1.2. SENSOR READOUT CIRCUIT BOARD

The graphene capacitive pressure sensor responds to the difference established between the internal pressure of the reference cavity, P_{int} and the external pressure of the environment, P_{ext}. This pressure difference results in a deflection of the atomically thin membrane and a corresponding change in capacitance [97] of the drum, ΔC as schematically depicted in Fig. 4.1b. We wedge bond a 25 μm AlSi 1% wire to Ti/Au pads on a chip for electrical contact to graphene and use a conductive silver-paste to contact the Si substrate. The response of the graphene capacitive pressure sensor is high enough to be read-out by chip-scale commercial electronic components as is demonstrated using the battery-powered circuit shown in Fig. 4.1c. Here, the sample under test is kept in a small on-board vacuum chamber that allows local control over the external gas pressure while preventing the pressure to affect electrical read-out elements. A commercial capacitance to digital converter (AMS PCap04) is then used to record and digitize the capacitance of the sample measured at a peak-to-peak voltage $V_{\text{pp}} = 1.5$ V with a hundred of charge and discharge cycles of 5.73 ms each. After voltage level adjustment by a logic level converter, an Arduino Uno board converts the measured capacitance into pressure using a predetermined calibration curve and displays it on an LCD screen. The circuit board is capable of measuring a change in the chip's capacitance down to ~10 aF on top of a background capacitance of a few tens of picofarads.

4.1.3. EFFECT OF PMMA REMOVAL

After chip fabrication and transfer, the PMMA transfer polymer still covers the DLG sheets. In a number of previous studies protective polymer layers were used to support the graphene to increase the yield, mechanical performance, hermeticity and durability of the devices, in both suspended [132, 159] and touch-mode operation [95]. However, the bending rigidity of the polymer layers reduces the deflection and responsivity of the membranes and sensor. To improve the sensor performance we therefore gradually remove the transfer polymer by annealing it in dry gas [160–163], as shown in Fig. 4.2. PMMA removal mechanisms are mostly related to removing pendant functional groups in the polymer at high temperatures [160, 162]. However, this can trigger the reaction between the graphene and the carbon by-products from the residual polymer and produce amorphous carbon [160, 161]. Lower temperatures of the process and an atmosphere of inert gas, like argon, are needed to prevent the production of amorphous carbon and to maintain a good quality of graphene during the thermal annealing [161].

The sample is put inside a furnace and left at a pressure of 500 Torr with a constant flow of 0.5 SLPM of an inert dry gas (Ar or N_2) at a temperature of 300°C as schematically depicted in Fig. 4.2a. We found no notable difference between the use of Ar or N_2 gas flow in terms of the end quality of DLG layers or PMMA removal rate. The average thickness of the transfer PMMA reduces with annealing time at an estimated rate of ~ 27 nm/minute with only minor residues left on and in-between the graphene layers. For some samples, small regions of local PMMA residue accumulation are still present after the annealing procedure. They accumulate on the surface of a DLG layer that has a thickness of 1.4 – 2.2 nm, as measured by tapping mode atomic force microscopy (AFM) (see Appendix, Fig. 4.7). The PMMA thickness reduction by thermal treatment is found to substantially improve the responsivity of the sensors. Figure 4.2b shows the capacitance change ΔC of a single chip to external pressure changes between 1000 and 900 mbar with a period of 40 seconds as measured after 0, 15, 22.5 and 29 minutes of annealing. Figure 4.2c shows that by following the thermal anneal procedure, an increase in responsivity of almost an order of magnitude was achieved for this particular sample, while in the best case an increase in responsivity of nearly two orders of magnitude was observed after a 30 minute continuous thermal anneal treatment. Further annealing the sample for longer times does not significantly affect the capacitance response (see Appendix, Fig. 4.8). The detection noise floor also decreases substantially as a result of the process. The noise floor, NF, in Pa/$\sqrt{\text{Hz}}$ is defined as:

$$NF = \frac{C_{\text{RMS}}}{\frac{dC}{dP}\sqrt{f_{\text{meas}}}}, \tag{4.1}$$

where C_{RMS} is the root mean squared (RMS) noise in the capacitance measurement, $\frac{dC}{dP}$ the responsivity of the sensor and $f_{\text{meas}} = 1.745$ Hz, the frequency at which the measurements are acquired. The decrease in NF as shown in Fig. 4.2c qualitatively follows from Eq. 4.1 considering the measured increase in responsivity.

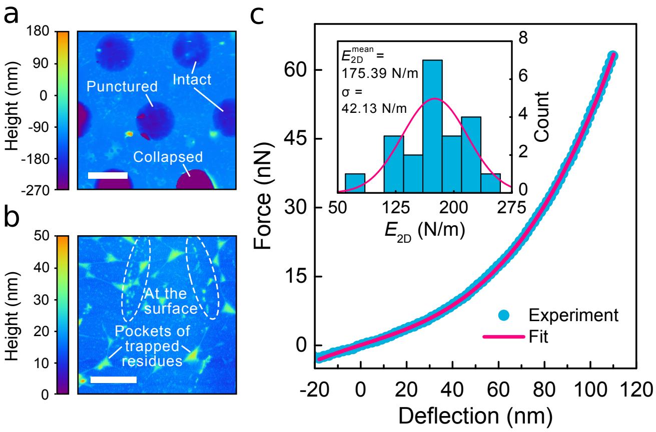

Figure 4.3: Atomic force microscopy (AFM) characterisation of membranes. **a** AFM tapping mode image of DLG drums. State of the drum is labeled. Scale bar: 5 μm. **b** AFM tapping mode image of a supported region of DLG. Residue types are indicated. Scale bar: 1 μm. **c** Force versus membrane deflection curve. Experimental data (blue dots) are fit by the membrane model of Eq. 4.2. Inset: statistics over 21 membranes with corresponding mean values for the extracted two-dimensional Young's modulus, E_{2D}, with a mean pre-tension $n_0 = 0.04 \pm 0.02$ N/m.

4.2. RESULTS AND DISCUSSION

4.2.1. SAMPLE CHARACTERIZATION

After thermal treatment for 30 minutes at 300°C, we inspect the samples for damage. In Fig. 4.3a a tapping mode Atomic Force Microscopy (AFM) image of the sample is shown. Three types of drums can be distinguished visually: intact, ruptured and collapsed drums. Collapsed drums are in contact with the bottom of the cavity and probably do not significantly contribute to the response [95] because they are predominantly damaged and thus not airtight. The ruptured drums are also expected to leak fast [94] and therefore have a negligible contribution to the static capacitance response to gradual pressure changes. Intact drums, however, show a full coverage of the cavity. These drums can hermetically seal the cavity with a constant internal pressure exploiting the extremely low permeability of graphene [23, 92, 93], although in part of these membranes small pores can be present that are too small to be visually detected. A lower height of some drums visible in Fig. 4.3a can be caused by small downward pressure or $P_{\text{int}} < 1$ bar established during the fabrication process. As shown in the AFM measurements in Fig. 4.3b, after the anneal, a substantial number of residues are observed on and below the DLG. The residues form pockets and are also observed in the suspended regions of the device, which suggests that part of the residues is trapped in-between the graphene layers, where they cannot be easily removed [115].

During the fabrication, the capability of graphene to withstand high strains [12, 148, 164] facilitates damage-free transfer, while the thickness of only a few atoms favours higher membrane deflections and thus higher responsivity to pressure changes of the sensor. In order to test the elasticity and mechanical properties of the drums after ther-

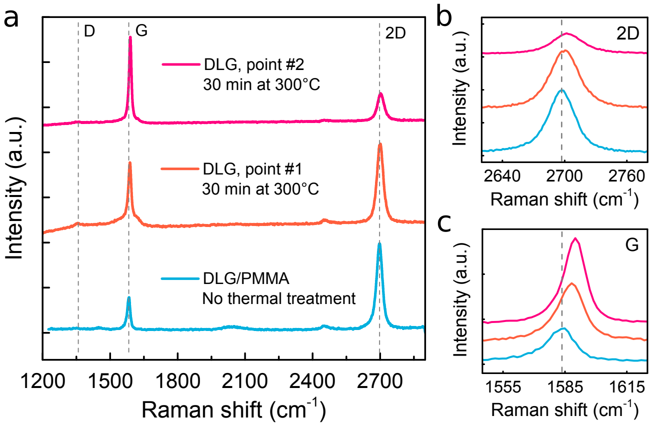

Figure 4.4: Raman spectroscopy of supported DLG. **a** Raman spectra of the DLG/PMMA layer before and after the polymer removal. **b** Close-up of a blue-shift in the 2D peak and **c** the G peaks of graphene.

mal treatment, we use force-indention AFM to apply a point-force in the centre of a single membrane while measuring its deflection [12]. The applied force, F, is proportional to the stiffness of a cantilever k_c and its deflection Δz_c as $F = k_c \Delta z_c$. We use two cantilevers of $k_c = 1.25 \pm 0.12$ N/m and 1.48 ± 0.05 for two separate sets of measurements in two distant places on the chip. We record a force versus membrane deflection curve at the centre of each drum, as depicted in Fig. 4.3c, and fit it to a model for point deflection of a circular membrane [12, 129]:

$$F = n_0 \pi \delta + E_{2\mathrm{D}} R q^3 \left(\frac{\delta}{R}\right)^3, \tag{4.2}$$

where n_0 is the pre-tension, $E_{2\mathrm{D}}$ the two dimensional Young's modulus of the layer, $\nu = 0.16$ the Poisson's ratio [116], δ the resulting deflection, R the radius and a geometrical factor $q = 1/\left(1.05 - 0.15\nu - 0.16\nu^2\right)$ [12, 129]. We use the two dimensional Young's modulus, $E_{2\mathrm{D}} = E_{3\mathrm{D}} h$ for the stacked DLG sheet since the thickness, h, of the layer after the thermal treatment is not well defined. Such an effective quasi-2D Young's modulus provides a more realistic estimate for the mechanical elasticity of the layer and can be directly compared to that of a pristine single layer graphene [12]. In the inset of Fig. 4.3c, the statistics over 21 different drums are shown that yield a mean value of $E_{2\mathrm{D}} = 175$ N/m. This is substantially lower than reported values for both exfoliated and pristine CVD single-layer graphene [12, 116], but comparable to other CVD graphene membranes [159, 164–166], high-quality oxidized graphene sheets [167, 168] and other 2D materials like single-layer MoS_2 [129].

We also examined the sheets of DLG by using Raman spectroscopy, as displayed in Fig. 4.4. Figure 4.4a shows Raman spectra of DLG acquired before the removal of the PMMA layer (blue line) and after the processing at an elevated temperature (orange and magenta line). Before the thermal treatment, the Raman spectrum of DLG is reasonably homogeneous across the chip, showing a Lorenzian-shaped 2D peak of graphene and a

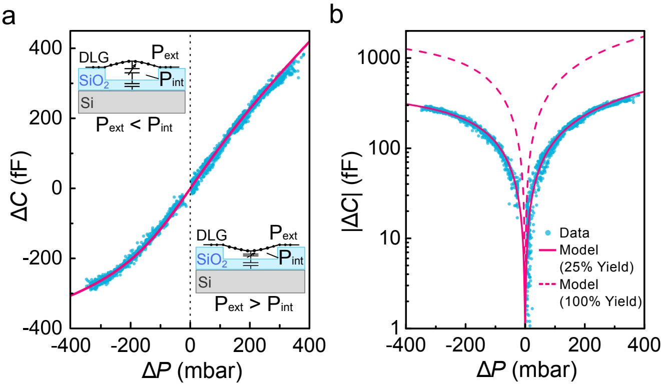

Figure 4.5: Capacitance-pressure curves of the DLG pressure sensor. **a** Measured capacitance-pressure curve (blue points); solid magenta line is a fit of Eq. 4.5 to the data with P_{int} = 0.933 bar, N/N_{tot}=0.25, $E_{2\text{D}}$=175 N/m and n_0 = 0.45 N/m. Insets: schematic images of the effect of membrane deflection. **b** Comparison, on log-scale, of the measured data (blue points) to the model with 100% (magenta dashed line) and 25% (solid magenta line) yield of the hermetic drums using the 2D Young's modulus from Fig. 4.3. All data is acquired during a continuous measurement within a total time of 1 hour at $P_{\text{ext}} \neq P_{\text{int}}$ with a maximal rate of change of the gas pressure of 3.3 mbar s^{-1}.

well-defined G peak [169]. Full width at half maximum (FWHM) of the 2D peak is around ~ 30 cm^{-1} and a high intensity ratio of 2D to G peaks resemble typical features of pristine graphene [169]. In the case of DLG, this indicates that the two layers in the stack are well decoupled and/or have on average a twist-angle [170] larger than 15°. After processing at a high temperature, the width of the 2D peak remains the same (see Fig. 4.4b) while the ratio between 2D to G peaks changes drastically depending on the chosen location of the measurement on the chip (see Fig. 4.4a, orange and magenta lines). Also, a notable blue-shift of both 2D and G peaks is observed, as shown in Fig. 4.4b,c. These observations are attributed to a substantial difference in twist-angle across the DLG sheet [170] as well as local changes in strain as a result of annealing of the graphene layers [171].

We also note the almost complete absence of the D peak in all Raman spectra as shown in Fig. 4.4a, indicating a very low amount of defects in the stacked graphene layers even after exposure to high temperatures [172]. This result is in agreement with the outstanding high-temperature stability of graphene when encapsulated by protective layers [21, 22], and provides evidence that damage, caused by the removal of polymer from suspended graphene, is minimal [160–163].

4.2.2. ANALYSIS OF THE SENSOR RESPONSE

A pressure difference ΔP results in a deflection δ of a circular graphene membrane with radius R, given by:

$$\Delta P = \frac{4n_0}{R^2}\delta + \frac{8E_{2\text{D}}}{3R^4(1-\nu)}\delta^3, \tag{4.3}$$

where the graphene membrane takes the shape of the section of a sphere [19, 97]. Since the pressure inside the reference cavity is about $P_{\text{int}} \approx 1$ bar (the pressure during transfer), at $P_{\text{ext}} = 1$ bar atmospheric pressure $\Delta P \approx 0$ and according to Eq. 4.3 the sensors are expected to have a linear response at small $\Delta\delta$. However, at larger deflections nonlinear mechanical and capacitance effects start to result in non-linearities in the capacitance $C_{\text{d}}(\Delta P)$ curve that can be calculated using the parallel-plate approximation [97] as:

$$C_{\text{d}}(\Delta P) = 2\pi\epsilon_0 \int_0^R \frac{r}{g_0 - \delta(\Delta P)\left(1 - \frac{r^2}{R^2}\right)} \text{dr}, \tag{4.4}$$

where ϵ_0 is the vacuum permittivity, g_0 the gap size between the membrane and bottom electrode for $\Delta P = 0$. The contribution of quantum capacitance of graphene is small [173, 174] and is neglected. The total capacitance change of the sensor can be modeled from Eq. 4.3 and 4.4 as:

$$\Delta C_{\text{total}} = N \times \Delta C_{\text{d}}(\Delta P), \tag{4.5}$$

where N is the number of intact, hermetic drums after both fabrication and thermal treatment. We experimentally test if Eq. 4.4 and 4.5 can model the graphene pressure sensor by applying both substantial negative and positive pressure differences while measuring its capacitance. Figure 4.5a shows the response of the same sensor that was characterized in Figs. 4.3 and 4.4.

The maximal responsivity of the sensor is achieved near ambient pressure in the linear regime, while a notable nonlinear response occurs for $|\Delta P| > 200$ mbar. A number of design factors, such as the drum diameter, the number of drums and the pitch between the drums influence the sensor performance [97]. Importantly, the pressure dependence of ΔC can be well reproduced by the model of Eq. 4.5 using a Young's modulus of $E_{\text{2D}} = 175$ N/m, estimated by an AFM probe for this particular sample, and a pretension $n_0 = 0.45$ N/m as shown by the magenta line in Fig. 4.5a. The model follows the measurement closely when we use a fitted value of N/N_{tot}=0.25 as shown in Fig. 4.5b (solid magenta line), where $N_{\text{tot}} \approx 10000$ is the total number of drums. This indicates that the yield of intact hermetic drums is 25%, and suggests that a large number of drums that look visually intact do not remain hermetic after polymer removal. The theoretical maximum response at a perfect yield of 100% is also shown (dashed magenta line).

Many other factors can influence the responsivity. Since the device capacitance has a strong dependence on the distance between the plates of the pressure sensor, the cavity depth has a large influence on the performance of the sensor. In Fig. 4.6 we demonstrate the performance of two of the best samples with a SiO_2 thickness of 285 nm and 2.17 μm respectively. Both chips have circular holes with a depth of 240 nm fabricated as described previously. Figure 4.6a shows the triangular wave response of both 285 nm (orange line) and 2.17 μm (blue line) chips. As shown in Fig. 4.6b, the difference in responsivity for the two oxide thicknesses as a function of pressure can be more than an order of magnitude. Using Eq. 4.1, we calculate the noise floor to be 34.2 Pa/$\sqrt{\text{Hz}}$ for the 285 nm thick SiO_2 sample and 43.4 Pa/$\sqrt{\text{Hz}}$ for the 2.17 μm one. The measured responsivity of the 285 nm gap device is significantly higher than that of the 2.17 μm one, in qualitative accordance with Eq. 4.1.

There is a notable scatter in the measured capacitance values as seen in Fig. 4.6b that is attributed to the effect of gas escaping the cavities for part of the drums, thus causing $|\Delta P|$ to decrease with measurement time. It has been reported before that when

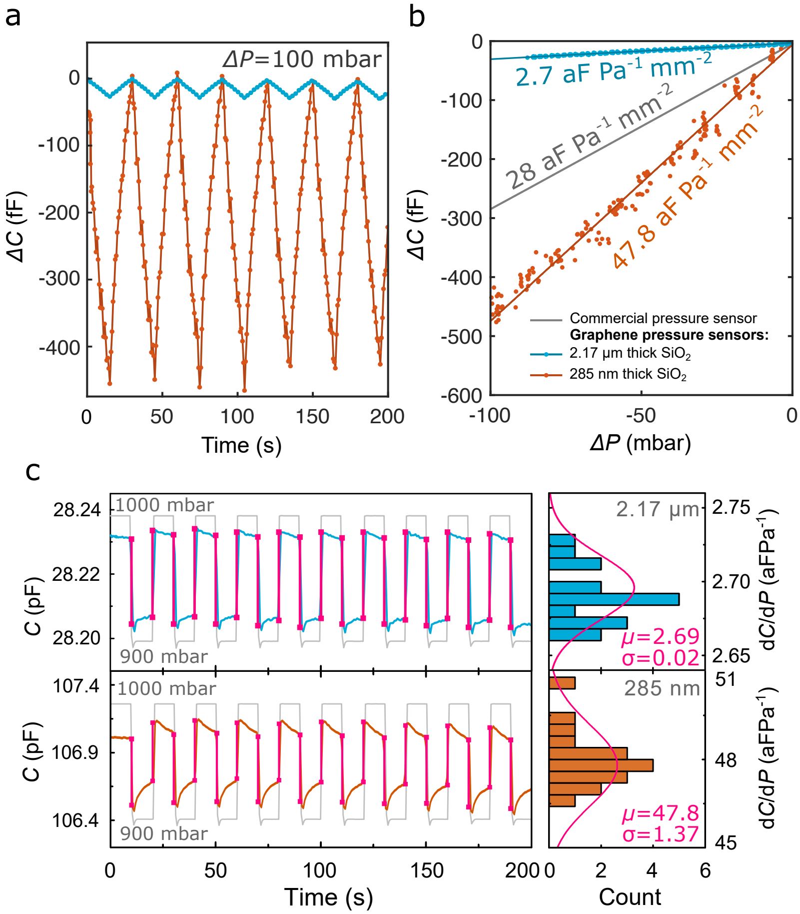

Figure 4.6: Comparison of different capacitive pressure sensors. **a** Triangular pressure wave applied to two graphene sensors with 285 nm and 2.17 μm of oxide thickness showing the measured change in capacitance. The gas pressure is changed at a rate of 6.25 mbar s^{-1}. **b** Responsivity analysis of the chips at small ΔP using multiple periods of measured data from **a** as a function of pressure change and the comparison to a commercial capacitive pressure sensor (Murata SCB10H). **c** Analysis of the responsivity of the chips as determined from periodic pressure steps between 1000 and 900 mbar. The gas pressure is changed at a rate of 175.4 mbar s^{-1}. Panels on the left: Blue line - measured capacitance of a graphene sensor with $h_{\mathrm{SiO_2}}$ = 2.17 μm. Orange line - measured capacitance of a sensor with $h_{\mathrm{SiO_2}}$ = 285 nm. Thin grey line - applied time-dependent pressure profile. Magenta lines - extracted capacitance response of the sensors. Panels on the right: statistics over a number of cycles for both oxide thicknesses. The higher responsivity and larger gas leak rate of the 285 nm device can account for the larger variations. Magenta lines - fit to a normal distribution with corresponding mean values μ and standard deviations σ in aF Pa^{-1} indicated.

graphene is suspended over a SiO_2/Si cavity, it does not always form a perfect hermetic seal[23, 92]. As recently shown by Lee et al., most of the gas permeation in graphene drums occurs along the van der Waals interface between the 2D material and the substrate [92]. As a result of the contribution of this effect, an exponential decrease of C with measurement time is visible in Fig. 4.6c, in response to periodic pressure steps of $\Delta P = 100$ mbar. However, if a good graphene crystallinity is preserved over large areas, the mean path that the gas needs to travel to escape the cavities becomes large, and this will increase the flow resistance of the gas channel and the permeation time constant [92, 155]. This condition seems to be achieved across part of the sample, because no significant hysteresis was observed during the slow pressure sweeps (> 10 minutes per sweep) in Fig. 4.5a and b, suggesting that of the order of 25 % of the drums maintain a constant internal pressure P_{int} for $\Delta P \neq 0$, as supported by the fits in Fig. 4.5a and b.

Optimization of all parameters is required to achieve the best sensor performance for detecting very small pressure differences over an extended range of pressure. DLG pressure sensors show reproducible operation over a pressure range of 65 – 138 kPa (see Fig. 4.5a). In terms of responsivity our best sensor with 285 nm of SiO_2 oxide (orange dots in Fig. 4.6a and b), with a responsivity of 47.8 aF $\text{Pa}^{-1}\text{mm}^{-2}$ over the range of 90 – 100 kPa, already outperforms the commercially available state-of-the-art Murata SCB10H sensor with a responsivity of 28 aF $\text{Pa}^{-1}\text{mm}^{-2}$ in the same range, as shown in Fig. 4.6b. This is comparably larger than what was previously achieved with capacitive sensors based on atomically thin 2D membranes [96, 97], yet competitive with a thicker suspended graphene-covered 140 nm PMMA sheets [132] with a reported responsivity of 123 aF $\text{Pa}^{-1}\text{mm}^{-2}$ over 0 – 80 kPa, using an area of 210 μm^2 of tightly-packed hexagonal membranes. However, if yields close to 100% and hermetic sealing of all drums is realized and the pre-tension is lowered down to ~ 0.04 N/m, the presented graphene-based 2D devices are expected to achieve a theoretical maximum responsivity of ~ 450 aF $\text{Pa}^{-1}\text{mm}^{-2}$ near ambient pressure of 90 – 100 kPa. Further design improvement might even be possible if the gap is reduced, the unsuspended area is minimised and the packing density of the membranes is increased. Using three or five layers of stacked graphene instead of two might help to improve the hermetic sealing issue but would result in a lower sensitivity (see Appendix, Fig. 4.9). Increasing the diameter of drums, on the other hand, could compensate this and produce an increase in responsivity (see Appendix, Fig. 4.10), however, also decrease the yield [156]. We demonstrate the proof-of-the-concept operation of graphene pressure sensors at room temperature conditions (~ 23°C). Eventually, also the temperature-related effects, such as expansion of the gas inside of cavities, small variations in dielectric constant of gas as a function of temperature, as well as thermal expansion of DLG and Si/SiO_2 substrate, can potentially affect the capacitance-to-pressure conversion. For the operation over an extended temperature range, these need to be excluded by combining the pressure sensor with a temperature sensor[175], using appropriate calibration and by sealing the drums under vacuum conditions.

4.3. CONCLUSIONS

Where previous studies had addressed part of the challenges related to realizing portable graphene gas pressure sensors, like the pressure sensitivity, impermeability to gasses and electrical readout, here we bridged these studies by constructing a portable, battery powered functional graphene pressure sensor that outperforms commercial devices. Using off-the-shelf systems for electronic readout and data processing, we enable capacitive readout of a 1×1 mm^2 array of DLG graphene pressure sensors. We realize sensor chips with a high yield of suspended membranes, resulting in a sensor responsivity of 47.8 aF Pa^{-1}mm^{-2}. We demonstrate that thermal treatment is an effective measure for controllable thickness reduction of the support polymer layer, that leads to a significant performance improvement because the thin 2D material membranes are much more flexible than with the support polymer. It is anticipated that further design and fabrication improvements and better control over the device yield can increase the responsivity by a factor 10, thus enabling improvements in applications like indoor navigation, altitude monitoring and activity monitoring, and can enable new applications like presence detection.

4.4. APPENDIX

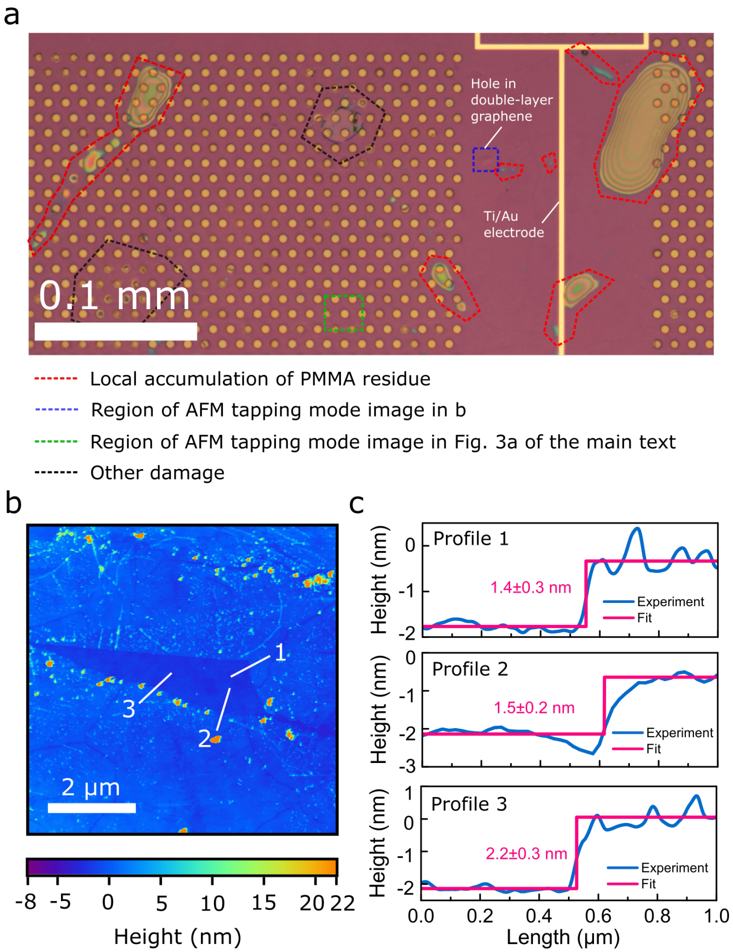

Figure 4.7: Detailed characterization of annealed double-layer graphene in a region where PMMA residues were observed. **a** Optical image of a thermally annealed graphene sample with a 285 nm thickness of SiO_2, results of which are also presented in Fig. 3 of the main text. **b** Tapping mode AFM image of the area indicated with a dashed blue line in **a**. Numbered white lines indicate corresponding height profiles in **c**. The extracted thickness of DLG is indicated for each case.

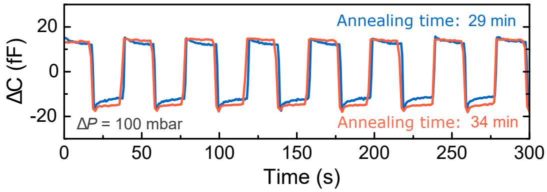

Figure 4.8: Capacitance response of a DLG sample to pressure step-changes after thermal annealing. Coloured lines - change in capacitance of a single chip as a function of measurement time in response to ΔP, annealed for a time indicated in the legend.

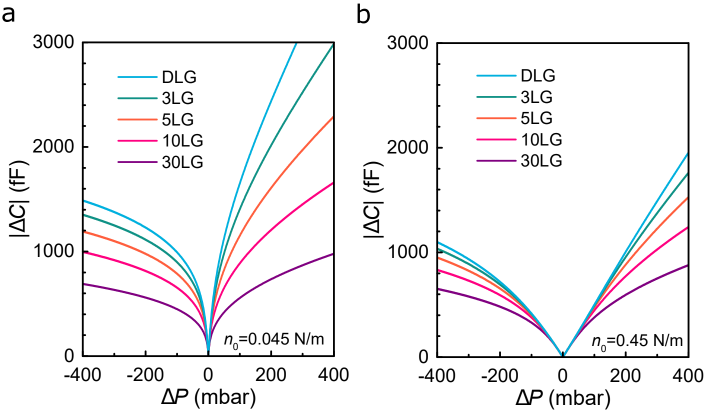

Figure 4.9: Simulated capacitance-pressure curves of the graphene pressure sensor with a different number of layers and pre-tension of **a** 0.045 N/m and **b** 0.45 N/m.

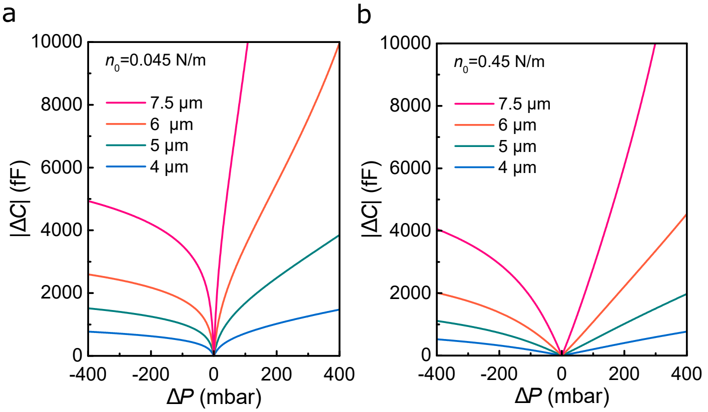

Figure 4.10: Simulated capacitance-pressure curves of the graphene pressure sensor with a different diameter of drums and pre-tension of **a** 0.045 N/m and **b** 0.45 N/m.

5

MECHANICALLY ANISOTROPIC MEMBRANES OF As_2S_3

2D materials with strong in-plane anisotropy are of interest for enabling orientation dependent, frequency tunable, optomechanical devices. However, black phosphorous (bP), the 2D material with the largest anisotropy up to date, is unstable as it degrades in air. In this work we show that As_2S_3 *is an interesting alternative, with a similar anisotropy as bP, while at the same time having a much higher chemical stability. In this chapter, we probe the mechanical and optical anisotropy in* As_2S_3 *by three distinct angular resolved experimental methods: Raman spectroscopy, atomic force microscopy (AFM) and resonance frequency analysis. Using a dedicated angle-resolved AFM force-deflection method, an in-plane anisotropy factor of* $\frac{E_a}{E_c} = 1.7$ *is found in the Young's modulus of* As_2S_3 *with* $E_{a\text{-axis}} = 79.1 \pm 10.1$ *GPa and* $E_{c\text{-axis}} = 47.2 \pm 7.9$ *GPa. The high mechanical anisotropy is also shown to cause up to* 65% *difference in the resonance frequency, depending on crystal orientation and aspect ratio of membranes.*

Parts of this chapter have been published in *ACS Nano* **13**, 9, 10845–10851 (2019) by Makars Šiškins, Martin Lee, Farbod Alijani, Mark R. van Blankenstein, Dejan Davidovikj, Herre S. J. van der Zant and Peter G. Steeneken

AFTER the first exfoliation and characterization of graphene in 2004 [7], 2D crystals have attracted much interest as suspended membranes in mechanical systems due to their unprecedented high elastic moduli and strength [12, 24, 38, 39]. Although resonators of many 2D materials, such as graphene and MoS_2, have been widely studied [24, 89, 97, 112], there are only a few 2D crystals known that exhibit large in-plane anisotropy [176–181]. Black phosphorus (bP) shows the largest known anisotropy in Young's modulus among 2D materials [25, 182] with a ratio of $\frac{E_b}{E_a} = 2$ along the in-plane axes (b and a). However, few-layer bP is only stable in air for several minutes [107], which severely affects its mechanical properties after oxidation [183] and complicates its application and integration into complex nanomechanical systems (NEMS).

Here, we discuss the exfoliation of As_2S_3 including in its monolayer form and the fabrication of suspended membranes of this material. Although As_2S_3 has been studied and applied in its bulk and amorphous form, it has not received much attention in its ultrathin exfoliated form. The anisotropy in the Raman spectrum of As_2S_3 is compared to the mechanical anisotropy in its static deflection, probed by atomic force microscopy (AFM), and in its dynamic deflection, probed by a change in the resonance frequency of mechanical modes. We show that thin layers of As_2S_3 have a mechanical anisotropy comparable to that of black phosphorus while their stability against degradation in ambient air facilitates integration and study of few-layer As_2S_3 resonators in complex mechanical devices. In addition to that, the material has perspectives to become an important member of the class of 2D-materials due to a unique combination of properties: As_2S_3 is known to transmit infrared well [184], has an optical indirect band gap of ~ 2.6 eV [185, 186], shows photoconductivity [187, 188] and has a large acousto-optical figure of merit [189]. This combination of properties make it of interest for fundamental studies of anisotropic phenomena in 2D materials, but can also enable new type of applications like acousto-optic modulators [190].

5.1. RESULTS AND DISCUSSION

5.1.1. STRUCTURE AND CHARACTERIZATION

Arsenic trisulfide, also known as orpiment [191], is a naturally occurring layered crystal. The unit cell of the As_2S_3 lattice consists of two layers inverted through a symmetry center located in a van der Waals gap (Fig. 5.1b). From the crystallographical point of view, a unit cell of arsenic trisulfide is defined by 20 atoms (10 atoms for a monolayer) [186] compared to 2 for graphene, 3 for MoS_2, and 8 for black phosphorus, which makes it one of the most structurally complex 2D materials known. Natural As_2S_3 crystals are of a high purity (see Appendix A1), have low interlayer binding energy [186, 192] and have an exfoliation energy comparable to graphite [185]. These properties enable the use of conventional methods for exfoliation and transfer of flakes [111, 112], when additional safety precautions are applied due to the toxicity of the material [193–195]. Natural crystals of As_2S_3 can be well exfoliated as indicated by the tapping mode AFM measurements in Fig. 5.1d, that show flakes as thin as 0.83 nm with consecutive step heights ranging from 0.7 – 0.8 nm. The monolayer thickness is expected to be a half of the unitcell along b-axis, $h_{As_2S_3} = 0.5 \times 0.96$ nm $= 0.48$ nm [191]. Since the step height observed in AFM

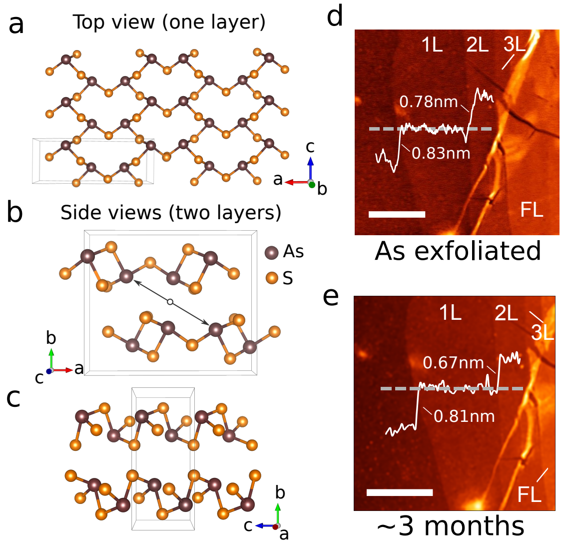

Figure 5.1: Crystal structure and atomic force microscopy (AFM) images of As_2S_3. **a** The crystal lattice of a single-layer As_2S_3. Projection along b-axis. Gray box indicates a single unit cell. **b** Projection along a-axis. Inversion center is indicated. **c** Projection along c-axis. **d-e** AFM images of a nm-thin exfoliated layer of As_2S_3 on SiO_2/Si as fabricated and after ~ 3 months in air. Scale bars: 1 μm.

is less than twice the layer thickness, we conclude that we have exfoliated a monolayer of As_2S_3. A similar 40 – 60% difference between the measured AFM stepheight and expected thickness of a single layer has been also observed in AFM studies of other 2D materials and might be related to intercalation effects [196]. As shown in the AFM image in Fig. 5.1e, the thickness of As_2S_3 monolayer remains virtually unchanged after three months in air under ambient light. The multilayer flakes of As_2S_3, that were exfoliated from the same crystal as the monolayer, are stable for hours at low or ambient light conditions (see Appendix A1), such that it is likely that no degradation occurs in the absence of light. This stability is an important advantage over other strongly anisotropic 2D materials like black phosphorous that decompose rapidly in air [107] as can be seen in AFM measurements [197]. The stability in ambient conditions of As_2S_3 can be attributed to its low solubility in water [195, 198] and low oxidation rate in air in the absence of excessive exposure to light [199, 200].

We fabricated a number of samples with flake thicknesses, h varying from 0.8 to 129 nm. Flakes were transferred on top of a pre-patterned SiO_2/Si chip with 12 rectangular cavities by an all-dry viscoelastic stamping method [112]. Each subsequent rectangle is rotated by a 30° angle with respect to the previous one and has a length of the longest side, b considerably larger than its width, a. We estimate the orientation of the optical axes of each flake using polarized light microscopy [177], thus taking advantage of the transcendent in-plane birefringence of the crystal: $\Delta n_{As_2S_3}$ measures ~ 0.35 around visible frequencies [201], which is ~ 1.4× higher than of black phosphorus and ~ 10× that

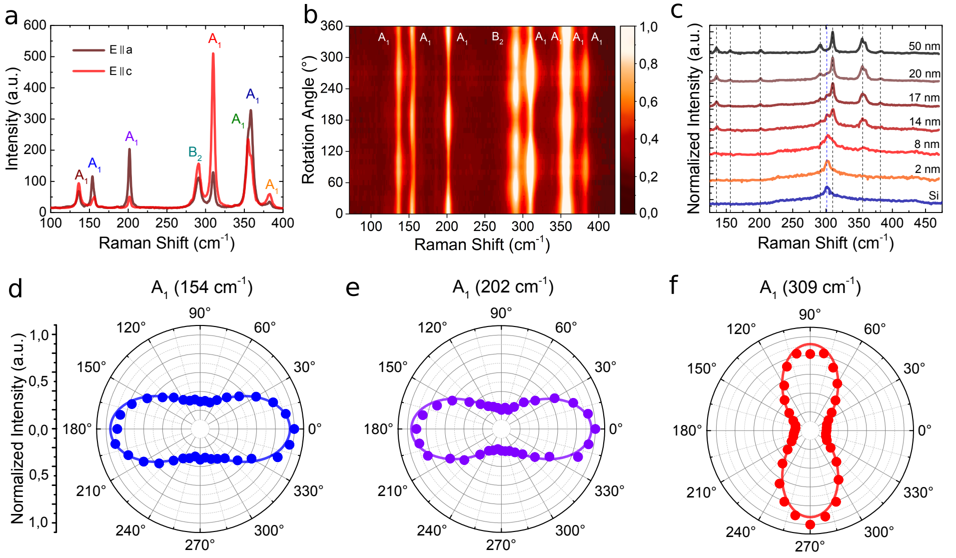

Figure 5.2: **a** Raman spectra of a bulk As_2S_3 crystal (thickness, $h \sim 50$ nm) for a polarization of incident red laser light ($\lambda = 632$ nm) along two crystalline axis (a and c). **b** Polarization-dependent Raman intensity spectra obtained by sample rotation with normal incident light (along the b-axis of a crystal). **c** Thickness-dependent Raman spectra under $\lambda = 632$ nm excitation. **d-f** Polarization-dependence for three Raman-active modes. Vibrational modes in a, b and d-f are labelled in accordance to previous works [202–207] on As_2S_3.

of ReS_2 [179]. This allows us to coarse-align the optical axes of the flakes to one of the cavities (see Appendix A2). A flake transferred on top of this pre-patterned array of cavities forms a star-shaped mechanical resonator, such that the stiffness of each membrane in the structure is dominated by the mechanical properties along the shorter side of the rectangle.

5.1.2. POLARIZATION-DEPENDENT RAMAN SPECTROSCOPY

We have studied the anisotropy of arsenic trisulfide in detail by polarization-dependent Raman Spectroscopy [208] at $\lambda = 488$, 514 and 632 nm of a laser excitation (see Appendix A7). At $\lambda = 632$ nm the measured Raman spectrum shows at least 8 vibrational modes: 7 symmetric (A_1) and 1 asymmetric (B_2) (Fig. 5.2a) with respect to rotations around the principal axis, corresponding to a C_{2v}^7 point group symmetry of a single As_2S_3 layer [202, 203]. These could be related to a C_{2h} point group symmetry of the bulk crystal through a correlation table [202, 203, 206, 207]. The intensity of Raman modes depends on the linear polarization angle of incident light in a backscattering Raman setup. As shown in Fig. 5.2d-f, A_1 (154 cm^{-1} and 202 cm^{-1}) Raman modes have the largest intensity when the light polarization is aligned along the a–axis, while A_1 (309 cm^{-1}) mode has the maximum intensity along the c-axis [202, 203, 206, 207]. We explain this behavior using group theory and Raman tensor calculations, assuming Placzek approximation (see Appendix

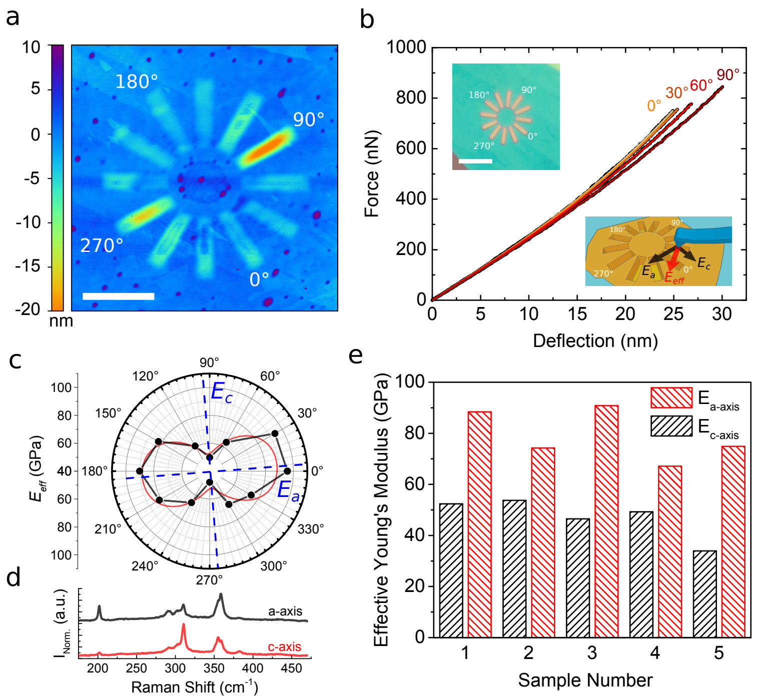

Figure 5.3: Detailed angle-resolved study of the Young's modulus of As_2S_3. **a** Tapping mode AFM image of the sample. Scale bar: 4 μm. **b** Typical force-deflection curve obtained at different angles of a rectangular cavity with respect to crystalline axes. Top inset: optical image of the sample. Scale bar: 8 μm. Bottom inset: a principle of the measurement. **c** Angle-resolved effective Young's modulus of the membrane. Red line - fit to Eq. 5.2. Young's moduli for in-plane crystalline directions (E_a and E_c) are indicated. **d** Raman spectra along each axis. **e** Effective Young's modulus along *a* and *c* crystalline axes measured for the best 5 samples of various thickness (from 9 to 25 nm).

A3), which produces a good fit to the measured data (Fig. 5.2d-f). The frequency of Raman phonons did not depend on the measured flake thickness, although the intensity of the signal decreased accordingly (Fig. 5.2c).

We used this polarization dependent Raman modes to determine the exact crystalline orientation for flakes of thicknesses down to 8 nm. At a smaller number of layers (*e.g.* 2 nm of thickness) the signal of the Si from the substrate starts to dominate the spectra. We have also performed photodegradation tests by analysing the Raman spectrum of the 354 – 358 cm^{-1} modes under a set of laser powers. Although As_2S_3 is known to transmit infrared well [184], approaching the band-gap of the material (~ 2.6 eV [186, 209]) with excessive light can convert the crystal to its amorphous state [210] thus locally destroying the crystallinity of the flake (see Appendix A1). Taking this into account, we further used flakes of thicknesses, $h > 8$ nm and a corresponding low power of the incident laser light to minimise damage to the suspended As_2S_3 membranes.

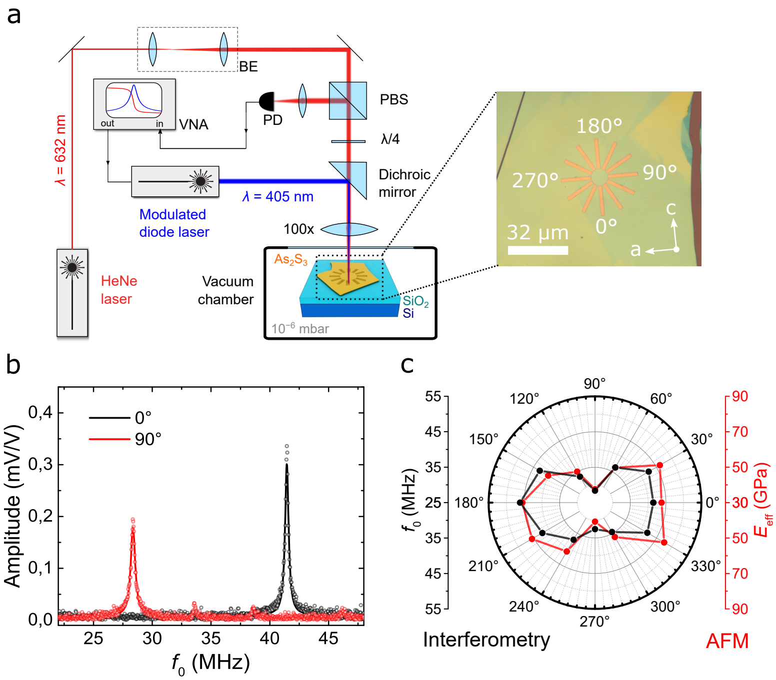

Figure 5.4: Measurement setup and measured angle-resolved frequency response of the device. **a** Schematic of the measurement setup. **b** Angle-dependent frequency response of rectangular resonators rotated by 90° with respect to the a-axis. **c** Comparison of anisotropic response observed in motion (laser interferometry, black) and statics (AFM force-indention, red).

5.1.3. ANISOTROPY IN THE STATIC MECHANICAL PROPERTIES

The strong asymmetry of the crystalline structure of As_2S_3 along the a- and c-axes (Fig. 5.1b,c) is also expected to cause a large anisotropy in the Young's modulus of the material [117]. We have studied the mechanical anisotropy in the Young's modulus as a function of angle by AFM using the star-shaped configuration shown in Fig. 5.3a. With an AFM tip of calibrated stiffness we indent the As_2S_3 membranes suspended over star-shaped trenches and record the force-deflection curve at the center of each of the 12 membranes of the same flake. We use cantilevers with spring constants between $k_c = 30-40$ N/m for thicker flakes (> 12 nm) and $k_c = 8-9$ N/m for thinner ones (< 12 nm). Each data point on the polar diagram in Fig. 5.3a is an averaged value from fitting 3 – 5 force-deflection curves obtained at the same position.

The high aspect ratio of the rectangular membranes, $b \gg a$ is chosen such that the slope of the force-deflection curve is dominated by the effective Young's modulus, E_{eff} along the shortest side of the rectangle. As shown in Fig. 5.3b, a difference in deflection, δ, was achieved for an equal force applied, F. Assuming a point force deflection at the center of the cavity, we obtain the following equation for the force-distance relation of

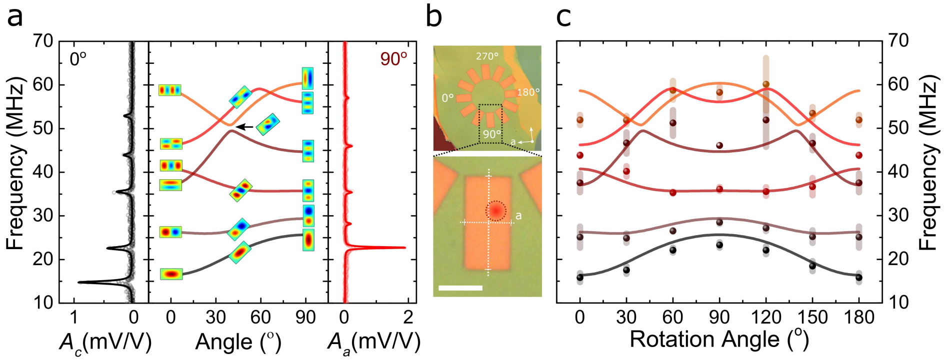

Figure 5.5: Change in resonance frequency of vibrational modes of an As_2S_3 plate. **a** Finite element model (FEM) for the first 6 modes of a resonator compared to the measured amplitude (A_c, A_a) of resonance peaks at 0° and 90° rotation of the rectangular membrane with respect to the c-axis of the crystal. **b** Optical image of a device with orientation and scales indicated. Dimensions are $a = 5$ μm and $b = 10$ μm. Scale bar: 5 μm. Both blue and red lasers are focused at the position indicated by the red circle in the lower panel. **c** Vibrational mode frequencies with corresponding errors compared to the FEM model.

the rectangular membrane (see Appendix A4):

$$F = \frac{E_{\text{eff}} h^3}{12\alpha(1-\nu^2)a^2}\delta + C_2 N_0 \delta + \frac{c_0}{(1-\nu^2)^{0.85}} \frac{E_{\text{eff}} h}{a^2}\delta^3 , \tag{5.1}$$

where $\alpha(a,b)$, $C_2(a,b)$ and $c_0(a,b)$ are geometry-dependent factors and N_0 is the intrinsic pre-tension. Using Poisson's ratio $\nu^2 = 0.094$ [211, 212], we fit Eq. 5.1 to the data and extract effective Young's moduli along the set of angles to the crystalline axes. We take into account measured thickness variations as determined by AFM, which are found to be at most 1-2 single layers (as seen on Fig. 5.3a), to extract correct values of E_{eff}. Figure 5.3c shows the characteristic dumbbell shape of angle-resolved effective Young's moduli, which is a typical example of mechanical anisotropy in layered materials [182]. We also measure Raman spectra along the hard and soft axis of the crystal to connect the observed anisotropy in mechanical properties to the crystalline orientation (Fig. 5.3d). The dependence of E_{eff} on the rotation angle, θ in a particular direction is defined from Hooke's law, taking into the account E_a, E_c and an effective shear, G_{eff} (see Appendix A5) [182]:

$$E_{\text{eff}}(\theta) = \frac{1}{\frac{1}{E_a}\cos^4\theta + (\frac{1}{G_{\text{eff}}} - \frac{2\nu}{E_a})\sin^2\theta\cos^2\theta + \frac{1}{E_c}\sin^4\theta} . \tag{5.2}$$

From the fits of Eq. 5.2 to the data in Fig. 5.3c,e we obtain $E_a = 79.1 \pm 10.1$ GPa, $E_c = 47.2 \pm 7.9$ GPa and $G_{\text{eff}} = 28.0 \pm 2.5$ GPa, so that the ratio of the mechanical anisotropy, $\frac{E_a}{E_c} \sim 1.7$ (Fig. 5.3e). These values are also consistent with additional measurements done on synthetically grown As_2S_3 showing that effect of possible defects and stacking faults on mechanical anisotropy in natural As_2S_3 crystals is insignificant (see Appendix A6).

5.1.4. DYNAMIC MECHANICAL PROPERTIES

When As_2S_3 is suspended over a rectangular hole made in a SiO_2/Si substrate it forms a resonator. We use the light intensity modulation by the motion of the membrane to measure the resonance frequencies in a laser interferometer. A schematic of the setup is shown in Fig. 5.4a. Here, the modulated blue diode laser is used to opto-thermally drive the As_2S_3 membrane, and the red laser to read out its motion [134]. This allowed us to observe a significant shift in the resonance frequency of the fundamental mode, $f_0(\theta)$ at $\theta = 90^\circ$ to the hard axis (a-axis) of the crystal (Fig. 5.4b). We were also able to resolve the natural mode frequency as a function of crystalline orientation of a membrane and compare it to the effective Young's modulus extracted for the same flake with the force-deflection AFM measurements. As shown in Fig. 5.4c, the ratio of anisotropy measures $\frac{E_a}{E_c} = \left(\frac{f_0(0^\circ)}{f_0(90^\circ)}\right)^2 = 2.0\pm0.3$ in the dynamic experiment which is comparable to $\frac{E_a}{E_c} = 1.8\pm0.1$ found from the static deflection of the same flake. This confirms the significant effect of anisotropy in the Young's modulus on the mechanical response of the membranes.

We further investigated the evolution of higher modes of thick rectangular As_2S_3 resonators as a function of the angle to the crystalline axis. We transferred a 129 ± 3 nm thick flake, as measured by tapping mode AFM, over a set of rectangular cavities with a $b : a = 2 : 1$ side ratio (Fig. 5.5b). This aspect ratio results in mode crossings [213] at certain angles, θ and a more complex frequency dependence on angle for higher modes [26]. In Fig. 5.5a,c the solid lines show the results of Finite Element Method (FEM) model obtained using COMSOL Multiphysics package of the first 6 modes of a clamped As_2S_3 plate resonator. The model matches experimental data well (Fig. 5.5a and 5.5c) for the first 4 modes. Note that no fitting parameters were used with only the thickness measured from AFM and elastic constants [117] of As_2S_3 added as an input to the FEM simulations. For higher modes we observe a discrepancy between the measured position of the resonance peak and the model, which could be due to a larger sensitivity of higher modes to perturbations and imperfections of the system [134]. We show 6 modes obtained from FEM simulation together with 5 experimentally detected modes in Fig. 5.5c to emphasize that the highest measured mode could not be precisely identified but is likely to be related to either the 5th or 6th mode of the resonator. Interestingly, as can be seen in Fig. 5.5a, an avoided crossing is expected when the long side of the rectangular membrane with $b/a = 2$ aspect ratio makes an angle of 40° with respect to the c-axis of the crystal. This unique feature could be potentially used in further studies of strong intrinsic coupling and internal resonances between modes in rectangular resonators of different ratio of sides [213].

5.2. CONCLUSIONS

In conclusion, we combined optical and mechanical characterisation techniques to obtain a comprehensive picture of the in-plane anisotropy in arsenic trisulfide. Using polarization-dependent Raman spectroscopy and force-deflection AFM in a star-shaped geometry of rectangular cavities, we systematically characterized the mechanical anisotropy in few-layers of this van der Waals crystal and relate that to its crystalline structure and orientation. We showed quantitatively that the anisotropy in the Young's modulus of As_2S_3 is close to that of black phosphorus, which is currently known to have the largest in-plane $\frac{E_a}{E_b}$ ratio among 2D crystals [25]. We also demonstrated that this results in a large orientation-specific change in the resonance frequency of higher vibrational modes in As_2S_3 resonators. These mechanical properties make As_2S_3 an interesting alternative to black phosphorus for applications in flexible strain-dependent optoelectronical devices [185], while stability in air makes it a promising material for further integration into optomechanical nanodevices as well as for research of anisotropic nonlinear mechanics in the 2D limit. We also believe that, due to its high flexibility [117, 211, 212] and pronounced optoelectronic properties [201, 209], As_2S_3 has perspectives to find applications in atomically thin optical waveplates [179], and to become an interesting candidate material for polarization-sensitive flexible photoconductors [187, 188] and acousto-optic modulators [189].

5.3. APPENDIX

A1: STABILITY AND PHOTODEGRADATION OF As_2S_3

Photodegradation is a significant problem in the study of As_2S_3, since the band-gap of 2.6 eV [185] lies in the visible range of frequencies - in the blue part of a spectrum. We found out that the process of photodegradation depends both on the power of irradiation and on the wavelength. When the sample was exposed to radiation for a long period of time it turned into an amorphous form (Fig. 5.6a), thus destroying the lattice of the crystalline As_2S_3. Figure 5.6 shows the degradation of the crystal in time with the corresponding time constants, τ that are determined by fitting the exponential decay of the Raman peak intensity. One may notice that τ depends linearly on $\log P$ for the red laser used in this experiment. A similar situation was observed for the blue laser with much shorter time constants. Thus, we conclude that the photodegradation has a trend towards speeding up when approaching the band gap of a material.

It is interesting that this process, in fact, cannot be called photo-decomposition, since we did not observe any traces of separate arsenic/sulfur components or oxides in SEM and EDX (Fig. 5.7). This effect could be compared with a study carried out by Frumar et al. [210], who showed that under radiation As_2S_3 did not decompose, but turned into an amorphous form according to a mechanism, where the kinetic barrier between the crystalline and amorphous form was significantly lowered under the influence of visible light. Perhaps, this process can be slowed down when encapsulating As_2S_3 in hBN (as in the case of black phosphorus [214]); however, this question is outside the scope of this work. Nevertheless, at sufficiently low red laser intensities it is possible to stay in a relatively stable crystal configuration for hours.

A2: POLARIZED LIGHT MICROSCOPY

As_2S_3 is potentially one of the most birefringent 2D layered crystals known, with $\Delta n \approx 0.35$: $n_\gamma \approx 3.0$ $(E||a)$, $n_\beta \approx 2.6$ $(E||c)$ for visible light frequencies [201]. We can use this property to find the crystalline orientation of a particular flake by means of Polarized Light Microscopy (PLM) by observing the intensity change due to conversion of linear to circular/elliptical polarization on a sample between crossed polarizers. When linearly polarized light is incident in parallel to one of the optical axes of the crystal, the polar-

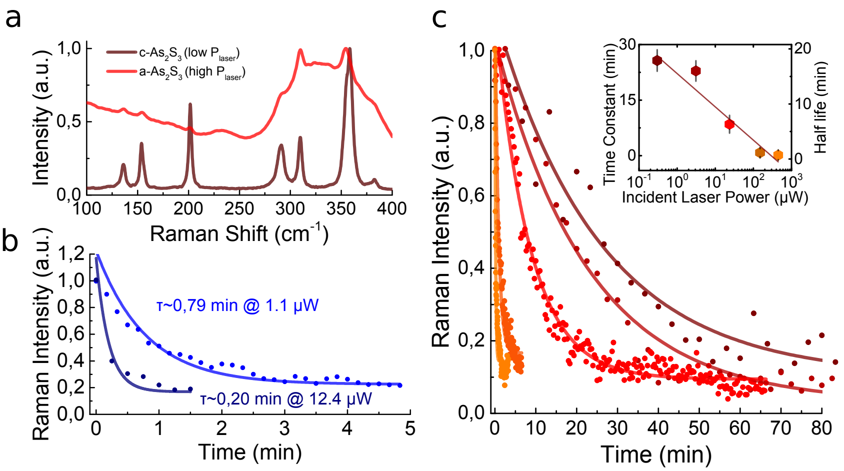

Figure 5.6: Stability of crystalline As_2S_3 in air. **a** Raman spectrum of a crystal measured at different red laser power. At a high power, the Raman spectrum of amorphous-As_2S_3 is dominating the response. **b** Power-dependent photodegradation of a crystal ($h \approx 20$ nm) at $\lambda_{\text{blue}} = 488$ nm excitation. **c** Power-dependent photodegradation of a crystal ($h \approx 20$ nm) at $\lambda_{\text{red}} = 632$ nm excitation. Inset: time constant of degradation as a function of laser power.

ization of incident light is not modified due to interaction with only one ray component of the biaxial birefringent material ($\boldsymbol{\beta}$ or $\boldsymbol{\gamma}$). At other angles, polarization is rotated such that it can pass through the crossed polarizer on the way back. As shown in Fig. 5.8, four intensity minima are observed when a polarization of incident light matches one of the optical axes in a crossed polarizer configuration.

The intensity profile can be described as [177]:

$$\Delta I_{\text{refl}}(\theta) \propto [I_{45^\circ} - I_{\text{sub}}] \sin 2\theta \,,$$

where I_{45° is reflected intensity at $\theta = 45°$ between a crystal axis and the polarizer, and I_{sub} the reflected intensity form a substrate. This way we deduct directions of the optical axes from a PLM polar diagram (Fig. 5.8) and correlate these to other properties of the material.

A3: POLARIZATION-DEPENDENT RAMAN SPECTROSCOPY

Arsenic trisulfide exhibits a strong optical in-plane anisotropy. Such a strong anisotropy proceeds directly from the symmetry of a single layer. Interestingly, the symmetry of a bulk As_2S_3 crystal is different from a monolayer. A monolayer is assigned to the Pnm21 space-group or C_{2v}^7 point-group symmetry. In the bulk case, the three-periodic crystalline symmetry should become P21/n (C_{2h}^5) with 2 layers contained in a unit cell. These are related through a correlation table [202–204, 207]. It has been experimentally shown [202–204, 206] that the layer symmetry, C_{2v}, rather than the three-dimensional symmetry, dictates the Raman spectrum of the material. We therefore further label these modes

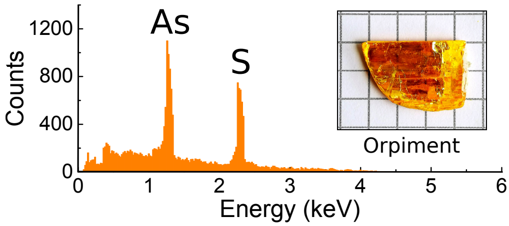

Figure 5.7: Typical energy-dispersive X-ray spectrum (EDX) of a As_2S_3 mineral. Inset: photo of an orpiment crystal. Scale: 0.5 cm.

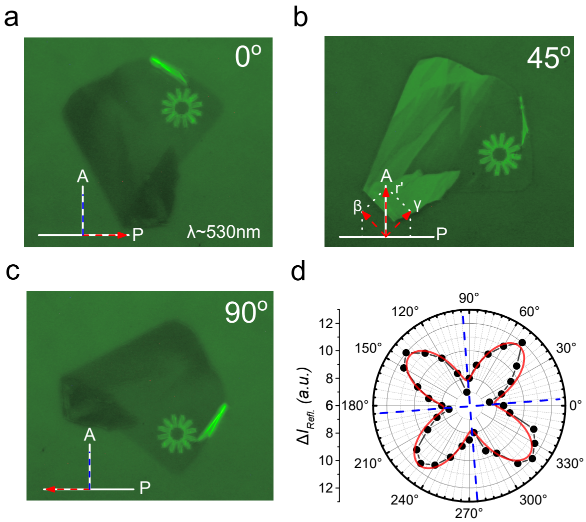

Figure 5.8: Sample viewed in a polarized light microscope. Example of the determination of crystallographic axes of a particular flake.

according to the layer symmetry which is consistent with the assignment broadly discussed and proposed in early works [202–207].

Looking from the molecular perspective [204, 215, 216], the layers of As_2S_3 are formed by AsS_3 pyramids that are linked by As-S bonds producing As-S-As chains. Modes that are associated with stretching vibration of AsS_3 pyramids are expected at ~ 310 cm^{-1} and near ~ 345 cm^{-1}. Modes near ~ 130 and ~ 160 cm^{-1} are also related to vibrations of AsS_3 pyramids. Higher modes around 380-430 cm^{-1} are likely to be associated with stretching of As-S-As bridges. Also, additional bands are expected at ~ 55 and ~ 218 cm^{-1} that are the modes associated with As-S-As vibrations. Intensity of many of these were observed to be dependent on the polarization configuration of the experiment [202, 203, 206, 207]. Thus, most of the Raman modes (excl. Rigid Layer modes [217]) could be explained by taking into account the polarization of incoming and scattered waves relative to crystal axes ($E||a$ and $E||c$). This property makes it possible to observe a strong dependence on the polarization angle in the intensity of Raman modes for any number of layers.

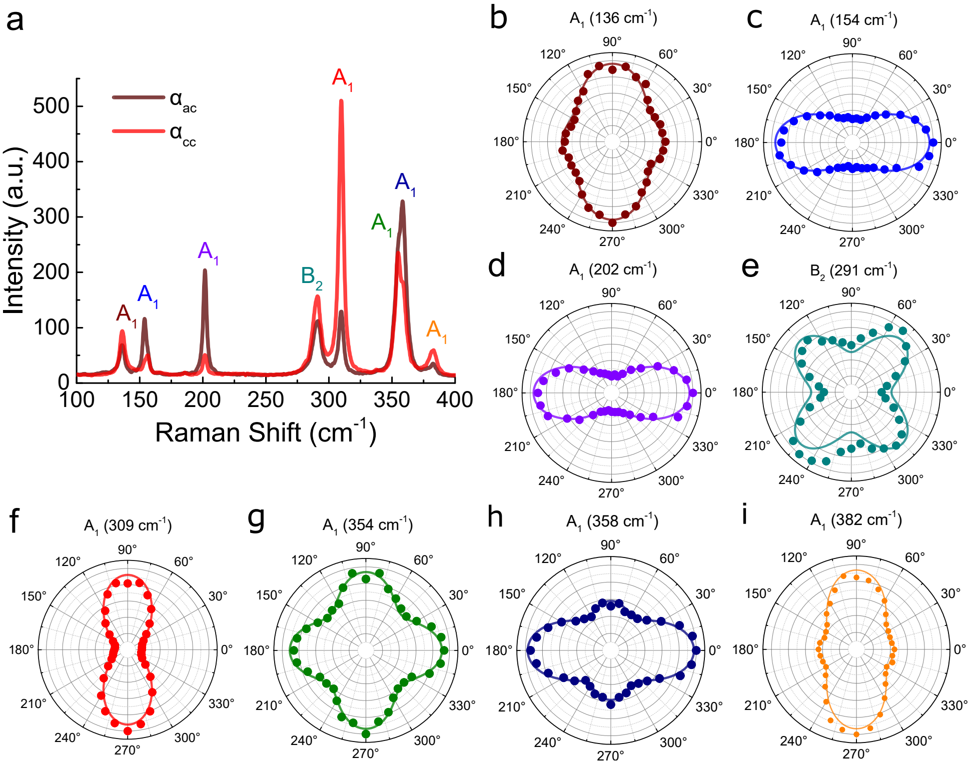

Figure 5.9: Angle-dependant Raman spectra. **a** Typical Raman spectra of a bulk As_2S_3 crystal ($h > 50$ nm) for a polarization of incident red laser light ($\lambda = 632$ nm) along the two crystalline axes (a and c). **b-i** Polarization-dependence of the normalized Raman intensity spectra for eight Raman active modes. Vibrational modes are colour-coded.

We investigated the Raman spectrum of As_2S_3 as a function of incident polarization angle, under an intrinsic linear polarization of the laser in a Raman setup. In Fig. 5.9 a typical Raman spectrum with the polarization oriented in the plane of the two crystalline axes (a and c) is shown. A similar picture is observed for samples with different layer thicknesses; however, when attempting to measure thin flakes (< 5 nm), the Raman signal was found to be too low to distinguish it from Si spectrum arising from a SiO_2/Si substrate.

For a thicker crystal (> 50 nm), we measured the spectrum as a function of a polarization angle. The observed anisotropy in the Raman signal can be analyzed from the point of view of group theory. For Pnm21 (C_{2v}^7) there should be 27 optical phonon modes in the Γ-point of the Brillouin Zone, which gives an irreducible representation: $\Gamma - P = 7A_1 + 7A_2 + 7B_1 + 6B_2$. All modes are Raman active. A_1 and B_2 modes are both Raman and infrared active. Taking into account the Placzek approximation [218], the Raman intensity of each such phonon mode should be described as:

$$I \propto |e_i \cdot \tilde{\mathscr{R}} \cdot e_s|^2, \tag{5.3}$$

where $e_{i,s}$ is the electric polarization of the unitary vectors of the incident and scattered light and $\tilde{\mathscr{R}}$ is the Raman tensor. Raman tensors of all active modes in As_2S_3 are given by:

$$\tilde{\mathscr{R}}(A_1) = \begin{bmatrix} |a|e^{i\phi_a} & 0 & 0 \\ 0 & |b|e^{i\phi_b} & 0 \\ 0 & 0 & |c|e^{i\phi_c} \end{bmatrix} \quad \tilde{\mathscr{R}}(A_2) = \begin{bmatrix} 0 & |d|e^{i\phi_d} & 0 \\ |d|e^{i\phi_d} & 0 & 0 \\ 0 & 0 & 0 \end{bmatrix}$$

$$\tilde{\mathscr{R}}(B_1) = \begin{bmatrix} 0 & 0 & 0 \\ 0 & 0 & |e|e^{i\phi_e} \\ 0 & |e|e^{i\phi_e} & 0 \end{bmatrix} \quad \tilde{\mathscr{R}}(B_2) = \begin{bmatrix} 0 & 0 & |f|e^{i\phi_f} \\ 0 & 0 & 0 \\ |f|e^{i\phi_f} & 0 & 0 \end{bmatrix}.$$

It should be noted that elements of the Raman tensor are written taking into account a complex phase, as a result of the fact that under red light absorption still plays a role [209]. Thus, for the backscattering geometry and taking into account the axes of the crystal: $e_{i,s} = (\cos\theta, 0, \sin\theta)$. Since only non-zero solutions give a contribution to Raman spectra, only the modes A_1 and B_2 are active in the given experimental configuration. Using the Raman tensors mentioned above, we obtain the following equations for the Raman intensity of each mode:

$$I_{A_1} \propto |a|^2 \left[\left| 1 + \left(\frac{|b|}{|a|} - 1 \right) \sin^2\theta \right|^2 + \frac{1}{2} \frac{|b|}{|a|} \sin^2 2\theta (\cos\phi_{ba} - 1) \right], \tag{5.4}$$

$$I_{B_2} \propto |f|^2 \sin(2\theta)^2 + r^2. \tag{5.5}$$

It is worth noting that the complex phase does not contribute to the mode B_2; however, at $\theta \sim 0°$, we do not observe a zero of intensity. This means that for this mode it is necessary to make a correction to account for non-ideal analyzer extinction ratio to efficiently cut off components other than the original incident linear polarization. This approach makes it possible to obtain a decent fit of data and to show that Raman modes active in this configuration are only A_1 and B_2, which correlates well with the interpretation proposed by Zallen et al. [202].

A4: DERIVATION OF FORCE-DEFLECTION EQUATION FOR A RECTANGULAR PLATE WITH PRE-TENSION

A rectangular plate with in-plane dimensions a and b and thickness h is considered in an orthogonal coordinate system $(O; x, y, z)$ (Fig. 5.10).

Three displacements u, v, and w, are used to describe the plate middle surface deformation. Based on classical plate theory, the displacements u_1, u_2, u_3 in x, y, z directions, respectively, of an arbitrary point of the plate are given by:

$$u_1 = u - z\frac{\partial w}{\partial x}, \quad u_2 = v - z\frac{\partial w}{\partial y}, \quad u_3 = w. \tag{5.6}$$

The strain-displacement relations can be written as:

$$\epsilon_x = \epsilon_{x,0} + zk_x, \quad \epsilon_y = \epsilon_{y,0} + zk_y, \quad \gamma_{xy} = \gamma_{xy,0} + zk_{xy}, \tag{5.7}$$

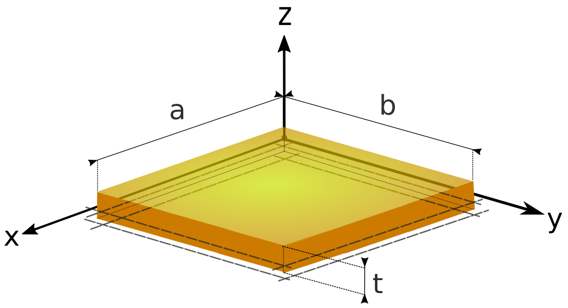

Figure 5.10: Schematics of a thin plate model.

where by considering non-linear terms of the von Kármán type:

$$\epsilon_{x,0} = \frac{\partial u}{\partial x} + \frac{1}{2}\left(\frac{\partial w}{\partial x}\right)^2, \quad \epsilon_{y,0} = \frac{\partial v}{\partial y} + \frac{1}{2}\left(\frac{\partial w}{\partial y}\right)^2, \quad \gamma_{xy,0} = \frac{\partial v}{\partial x} + \frac{\partial u}{\partial y} + \frac{\partial w}{\partial x}\frac{\partial w}{\partial y}, \tag{5.8}$$

$$k_x = -\frac{\partial^2 w}{\partial x^2}, \quad k_y = -\frac{\partial^2 w}{\partial y^2}, \quad k_{xy} = -2\frac{\partial^2 w}{\partial x \partial y}. \tag{5.9}$$

The elastic strain energy of a thin rectangular plate is given by [219]:

$$\begin{aligned} U_p = & \frac{1}{2}\frac{Eh}{1-\nu^2}\int_0^a\int_0^b \left\{\epsilon_{x,0}^2 + \epsilon_{y,0}^2 + 2\nu\epsilon_{x,0}\epsilon_{y,0} + \frac{1-\nu}{2}\gamma_{xy,0}^2\right\}\mathrm{d}x\mathrm{d}y \\ + & \frac{1}{2}\frac{Eh^3}{12(1-\nu^2)}\int_0^a\int_0^b \left\{k_x^2 + k_y^2 + 2\nu k_x k_y + \frac{1-\nu}{2}k_{xy}^2\right\}\mathrm{d}x\mathrm{d}y \\ + & \frac{1}{2}N_0\int_0^a\int_0^b \left\{\left(\frac{\partial w}{\partial x}\right)^2 + \left(\frac{\partial w}{\partial y}\right)^2\right\}\mathrm{d}x\mathrm{d}y, \end{aligned} \tag{5.10}$$

where E is the Young's modulus, ν is the Poisson's ratio and N_0 is a uniform pre-tension. The virtual work done by a concentrated transverse force at $(\tilde{x} = a/2, \tilde{y} = b/2)$ is given by [219]

$$W = \int_0^a\int_0^b \tilde{f} w \delta(x-\tilde{x})\delta(y-\tilde{y})\mathrm{d}x\mathrm{d}y = \tilde{f} w|_{x=\tilde{x},y=\tilde{y}}, \tag{5.11}$$

where $\tilde{f}$ is the force amplitude and δ is the Dirac delta function.

It is assumed that the plate is simply supported and the edges can move only in the direction orthogonal to the edge (simply supported movable edges). The boundary conditions are [219]:

$$\begin{aligned} &v = 0, \quad w = 0, \quad N_x = 0, \quad M_x = 0, \quad \text{at } x = 0,\ a, \\ &u = 0, \quad w = 0, \quad N_y = 0, \quad M_y = 0, \quad \text{at } y = 0,\ b, \end{aligned} \tag{5.12}$$

where N_x, N_y are the in-plane force resultants and M_x, M_y are the moment resultants. They can be obtained in terms of middle-surface strains as:

$$N_x = \frac{Eh}{1-\nu^2}\left(\epsilon_{x,0} + \nu\epsilon_{y,0}\right), \quad N_y = \frac{Eh}{1-\nu^2}\left(\epsilon_{y,0} + \nu\epsilon_{x,0}\right), \tag{5.13}$$

$$M_x = -D\left(k_x + \nu k_y\right), \quad M_y = -D\left(k_y + \nu k_x\right),$$

where D is the bending rigidity of the plate defined as: $D = \dfrac{Eh^3}{12(1-\nu^2)}$. The suitable eigenfunctions that satisfy the geometric boundary conditions 5.12 are:

$$u\left(x,y\right) = \sum_{m=1}^{\tilde{M}} \sum_{n=1}^{\tilde{N}} u_{m,n} \cos(m\pi x/a)\sin(n\pi y/b), \tag{5.14}$$

$$v\left(x,y\right) = \sum_{m=1}^{\tilde{M}} \sum_{n=1}^{\tilde{N}} v_{m,n} \sin(m\pi x/a)\cos(n\pi y/b),$$

$$w\left(x,y\right) = \sum_{m=1}^{M} \sum_{n=1}^{N} w_{m,n} \sin(m\pi x/a)\sin(n\pi y/b),$$

where m and n are the number of half-waves in the x and y directions, respectively; $u_{m,n}$, $v_{m,n}$, $w_{m,n}$, are the generalized coordinates. $\tilde{M}$ and $\tilde{N}$ indicate terms in the expansion of the in-plane displacements and are usually larger than M and N, which are the necessary terms in the expansion of transverse deflection. The convergence and accuracy of the solution can be examined by using different number of terms in the expansions 5.14.

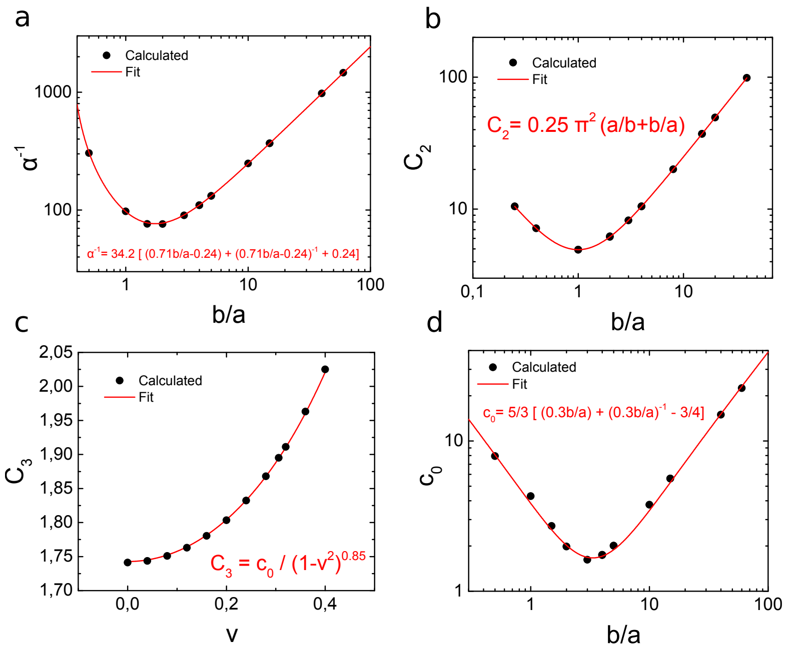

Figure 5.11: Coefficients obtained from calculations and corresponding equations of the best fit.

The discretized equilibrium equations can then be obtained as:

$$\frac{\partial U}{\partial q_j} = \frac{\partial W}{\partial q_j}, \quad j = 1, \ldots, \bar{N}, \tag{5.15}$$

where q_j are the degrees-of-freedom (DoF) which are elements of the generalized coordinates vector $\mathbf{q} = \{u_{m,n}\ v_{m,n}\ w_{m,n}\}^T$ and $\bar{N}$ is the total number of DoF. In our study, in order to obtain good convergence, $\bar{N} = 201$ yielding the same number of algebraic equations, obtained by setting $\tilde{N} = \tilde{M} = 19$, $M = N = 1$, and neglecting even number of half-waves. The reason for including only odd half-waves in the solution is because the concentrated force is acting at the center of the plate and thus, even half-waves do not contribute to the response. The final equation of motion can be simplified to:

$$c_1 E w_{1,1} + c_2 N_0 w_{1,1} + c_3 E w_{1,1}^3 = \tilde{f} w_{1,1}, \tag{5.16}$$

in which c_i ($i = 1,2,3$) are constants that are determined by solving the 200 equations governing the in-plane motion, in terms of $w_{1,1}$, and inserting the outcome in the sole non-linear equation governing the motion in transverse direction.

Following previous works on isotropic rectangular plates and membranes [131, 220] and setting $w_{1,1} = \delta$, Eq. 5.16 can be rewritten as follows:

$$\begin{aligned} F &= c_1 E_{\text{eff}}\delta + c_2 N_0 \delta + c_3 E_{\text{eff}}\delta^3 \\ &= \frac{E_{\text{eff}} h^3}{12\,\alpha(a,b)\,(1-\nu^2)a^2}\delta + C_2(a,b) N_0 \delta + C_3(\nu,a,b)\frac{E_{\text{eff}} h}{a^2}\delta^3. \end{aligned} \tag{5.17}$$

From the calculations we empirically deducted the geometry correction factor $\alpha(a,b)$ and coefficients $C_2(a,b)$ and $C_3(\nu,a,b)$ as a function of b/a ratio (Fig. 5.11). We approximate [131, 220] $C_3(\nu)$ as $C_3(\nu,a,b) = \frac{c_0(a,b)}{(1-\nu^2)^n}$, which gives a reasonable fit to the calculated C_3 values.

A5: FIT OF THE EFFECTIVE YOUNG'S MODULUS

Mechanical response of As_2S_3 is a typical example of deflection of a highly anisotropic thin plate [182, 221]. Since this system is of a quasi-2D structure for orthogonal deflections, the elastic constants and moduli can be written from the Hooke's law under plane-stress condition with respect to the crystalline axes (abc):

$$\begin{bmatrix} \sigma_{aa} \\ \sigma_{cc} \\ \sigma_{ac} \end{bmatrix} = \frac{1}{1-\nu_{ac}\nu_{ca}} \begin{bmatrix} E_a & \nu_{ca}E_a & 0 \\ \nu_{ac}E_c & E_c & 0 \\ 0 & 0 & G_{ac}(1-\nu_{ac}\nu_{ca}) \end{bmatrix} \begin{bmatrix} \epsilon_{aa} \\ \epsilon_{cc} \\ 2\epsilon_{ac} \end{bmatrix},$$

where $E_i = \frac{\sigma_i}{\epsilon_i}$ is the Young's modulus along the axis of i, $\nu_{ij} = -\frac{d\epsilon_j}{d\epsilon_i}$ is the Poisson's ratio with tensile strain applied in the direction i and the response strain in the direction j, and G_{ac} is the shear modulus on the ac plane of a crystal. For a quasi-2D system, the Young's modulus along an arbitrary direction at angle θ to the a-axis of a crystal can be derived using the following equation [182]:

$$E_{\text{eff}}(\theta) = \frac{1}{\frac{1}{E_a}\cos^4\theta + \left(\frac{1}{G_{ac}} - \frac{2\nu_{ac}}{E_a}\right)\sin^2\theta\cos^2\theta + \frac{1}{E_c}\sin^4\theta}. \tag{5.18}$$

Note that this direction-specific effective Young's modulus, $E_{\text{eff}}(\theta)$ is pronounced at large aspect ratio of sides (a and b), so that Eq. 5.17 and 5.18 can be only applied when $b \gg$

a. When extracting an effective Young's modulus from force-deflection AFM curves, $\nu = 0.306$ [211, 212] was used, which is a good approximation for $\nu^2 = \nu_{ac}\nu_{ca}$ considering $C_{11} = 99.6 \pm 1.0$ GPa, $C_{33} = 21.9 \pm 1.4$ GPa and $C_{13,31} = 20.6 \pm 1.9$ GPa found for c-As_2S_3 in literature [117]. Using the same approximation, $\nu = 0.306 \approx \nu_{ac}$ to fit the angle-dependant effective Young's modulus, G_{ac} should be now written as an effective shear modulus G_{eff}.

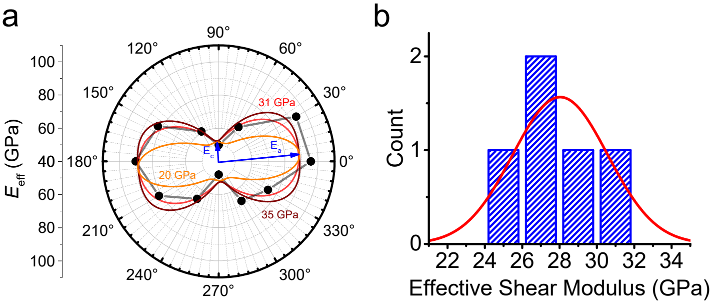

Figure 5.12: G_{eff} estimation. **a** Fit for different values of the effective shear. **b** Statistics of extracted effective shear modulus for flakes ranging from 9 to 25 nm in thickness.

We now rewrite equation 5.18 as:

$$E_{\text{eff}}(\theta) = \frac{1}{\frac{1}{E_a}\cos^4\theta + (\frac{1}{G_{\text{eff}}} - \frac{2\nu}{E_a})\sin^2\theta\cos^2\theta + \frac{1}{E_c}\sin^4\theta}, \tag{5.19}$$

and fit this equation to the measured data. For As_2S_3 we experimentally found $G_{\text{eff}} = 28.0 \pm 2.5$ GPa, which is close to the typical value found in literature [117]: $C_{55} = G_{ac} = 24.0 \pm 0.8$ GPa for bulk As_2S_3.

A6: MECHANICAL PROPERTIES OF THE SYNTHETIC LAB-GROWN As_2S_3

In natural van der Waals crystals the number of defects, as well as the interlayer stacking faults, can potentially affect the mechanical properties and anisotropy of a crystal. Since for the natural As_2S_3 crystal these properties are unknown, to confirm our findings we have performed an additional study on the commercially purchased synthetic lab-grown crystal. According to the information provided by a manufacturer, these crystals have perfect stoichiometry, large domain size, minimal defect density (1 part in 100,000 unit cells), and perfected purity level (99.9998%).

Using mechanical exfoliation and all-dry viscoelastic stamping, we fabricated the suspended sample of 15.7 ± 0.4 nm thickness as measured by tapping mode AFM (see Fig. 5.13a, inset). Using the force-deflection AFM technique and the experimental procedure described in Fig. 5.3, we have obtained corresponding force-deflection curves for each of 12 rectangular membranes (see Fig. 5.13). We fit the data using Eq. 5.17 to extract effective Young's Modulus for each orientation. The obtained E_{eff} is shown in Fig. 5.13b and fitted using Eq. 5.18. The crystalline orientation was then found using Raman spectroscopy as described in Fig. 5.13c. For synthetic As_2S_3, we experimentally found $E_\text{a} = 67.7 \pm 4.7$ GPa, $E_\text{c} = 38.9 \pm 3.5$ GPa, and $G_{\text{eff}} = 22.8 \pm 2.8$ GPa and thus anisotropy factor of 1.74. These values are consistent with E_a and E_c found for the natural crystal within the range of statistical uncertainty.

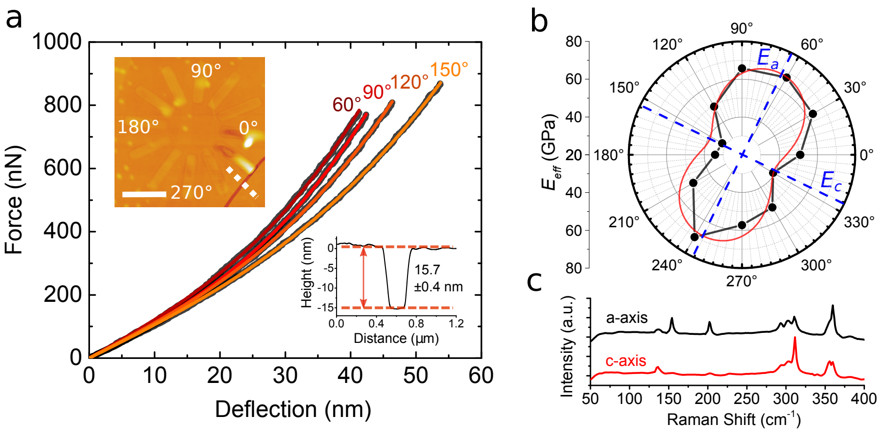

Figure 5.13: Detailed angle-resolved study of the Young's modulus of synthetic As_2S_3. **a** Force-deflection curves obtained at different angles of a rectangular cavity with respect to crystalline axes. Top inset: Tapping mode AFM image of the sample. Scale bar: 3 μm. Bottom inset: Tapping mode AFM height profile along the dashed line. **b** Angle-resolved effective Young's modulus of the membrane. Red line - fit to Eq. 5.18. Young's moduli for in-plane crystalline directions (E_a and E_c) are indicated. **c** Raman spectra along each axis.

A7: WAVELENGTH- AND POLARIZATION-DEPENDENT RAMAN SPECTROSCOPY OF SYNTHETIC AND NATURAL As_2S_3 CRYSTALS

In order to check impact of laser excitation wavelength on the Raman anisotropy for both natural and synthetic crystal, we have performed additional detailed angle-resolved polarization dependent studies. Following the approach described in Appendix A3, we use the backscattering geometry in the parallel-polarized ($e_i||e_s$) configuration. Figure 5.14 shows the measured data for each combination of crystal origin and wavelength. As expected, considering what was previously found in similar systems [222, 223], there was a certain change of parameters a, b and ϕ_{ba} (see Eq. 5.4 and Appendix A3) for symmetry of Raman modes at each particular wavelength. The origin of this change is unknown, but the symmetry and orientation of the modes used to determine the crystalline axis in this work remains the same.

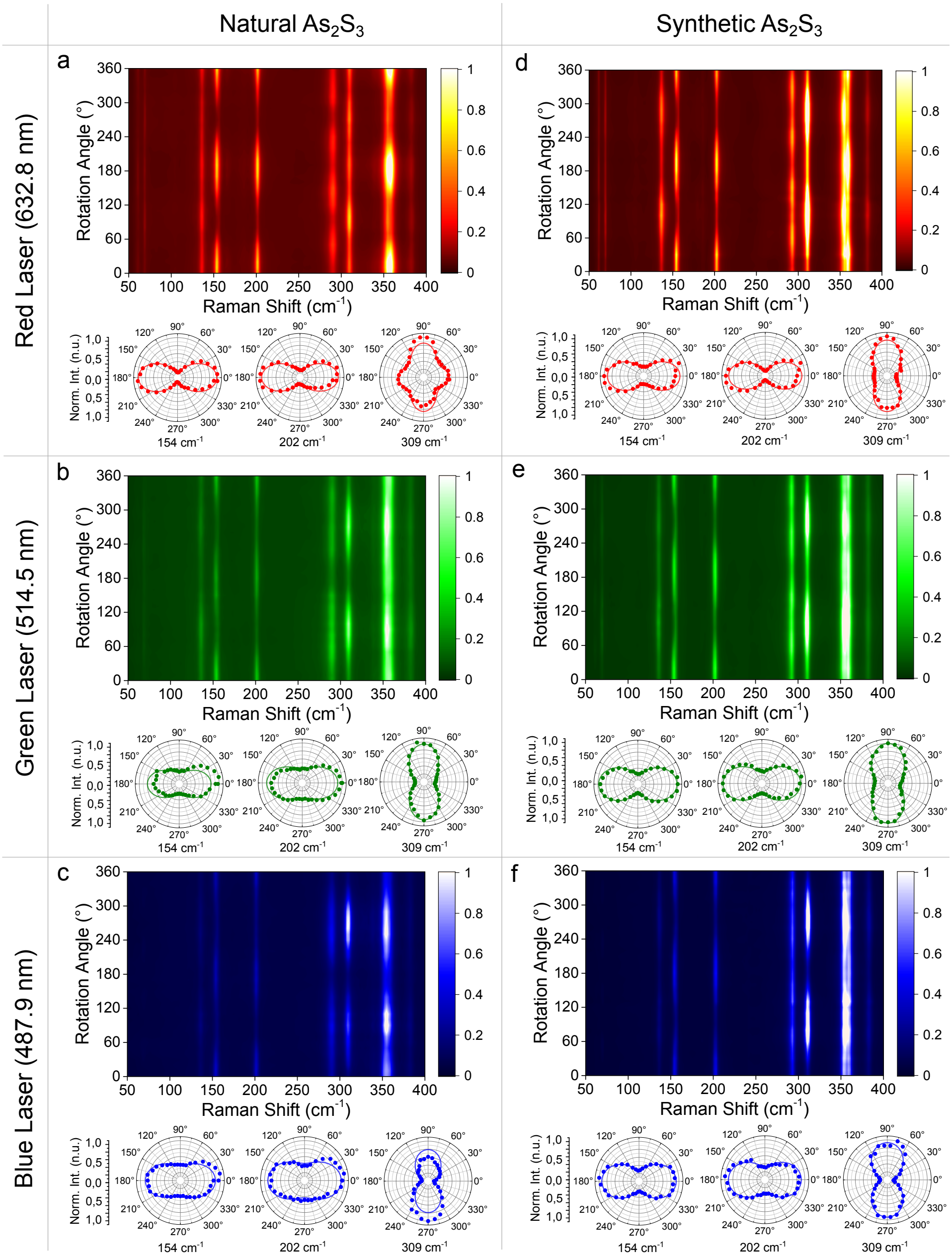

Figure 5.14: Wavelength- and polarization-dependant Raman spectra measured at 3 different excitation wavelength. **a-f** Top: Polarization-dependence of the normalized Raman intensity spectra. Bottom: Normalized intensity of vibrational modes 154, 202 and 309 cm^{-1} as a function of polarization and wavelength of excitation. Left column **a-c** - natural As_2S_3 and right column **d-f** - synthetic As_2S_3.

III

Part Three

Nanomechanical probe of phase transitions

Chapters 6, 7, 8 and 9

6

NANOMECHANICS OF ANTIFERROMAGNETS NEAR THE PHASE TRANSITION

The reduced dimensionality of two-dimensional (2D) materials results in characteristic types of magnetically and electronically ordered phases. However, only few methods are available to study this order, in particular in ultrathin insulating antiferromagnets that couple weakly to magnetic and electronic probes. In this chapter, we demonstrate that phase transitions in thin membranes of 2D antiferromagnetic $FePS_3$, $MnPS_3$ *and* $NiPS_3$ *can be probed mechanically via the temperature-dependent resonance frequency and quality factor. The observed relation between mechanical motion and antiferromagnetic order is shown to be mediated by the specific heat and reveals a strong dependence of the Néel temperature of* $FePS_3$ *on electrostatically induced strain. It thus offers the potential to characterize phase transitions in a wide variety of materials, including those that are antiferromagnetic, insulating or so thin that conventional bulk characterization methods become unsuitable.*

Parts of this chapter have been published in *Nature Communications* **11**, 2698 (2020) by Makars Šiškins, Martin Lee, Samuel Mañas-Valero, Eugenio Coronado, Yaroslav M. Blanter, Herre S. J. van der Zant and Peter G. Steeneken

NANOMECHANICAL resonators made of two-dimensional (2D) materials offer interesting pathways for realizing high-performance devices [89, 224]. Unique functionalities and phenomena emerge when combining nanomechanics with the types of magnetic and electronic phases that have recently been uncovered in 2D materials like magic-angle induced phase transitions [225, 226], 2D Ising antiferromagnets [45] and ferromagnetism in 2D atomic layers [46, 47] and heterostructures [42]. Only a few methods are available to study these phases in 2D materials [30, 42, 45–47]. A universal method to characterize phase transitions in bulk crystals is via anomalies in the specific heat, that are present at the transition temperature according to Landau's theory [106]. However, specific heat is difficult to measure in thin micron-sized samples with a mass of less than a picogram [79, 127].

We demonstrate that these phases are strongly coupled to mechanical motion: the temperature dependent resonance frequency and quality factor of multilayer 2D material membranes show anomalies near the phase transition temperature. Although coupling between mechanical and electronic/magnetic degrees of freedom might not seem obvious, the intuitive picture behind this coupling is that changes in the electronic/magnetic order and entropy in a material are reflected in its specific heat, which in turn results in variations in the thermal expansion coefficient that affect the tension and resonance frequency. As the specific heat near a phase transition is expected to exhibit a discontinuity [106], the temperature dependent resonance frequency of a suspended membrane can thus be used to probe this transition.

The coupling of mechanical degrees of freedom to magnetic and electronic order is attributed to thermodynamic relations. Nanomechanical resonators, therefore, offer the potential to characterize phase transitions and realize device concepts in a wide variety of systems, not restricted only to van der Waals materials but including those that are ultrathin, antiferromagnetic or insulating [42]. Here, we use nanomechanical motion to investigate magnetic order in membranes of semiconducting $\mathrm{FePS_3}$, and subsequently discuss $\mathrm{NiPS_3}$ and insulating $\mathrm{MnPS_3}$ - antiferromagnetic members of the transition-metal phosphor trisulphides ($\mathrm{MPS_3}$) [58].

6.1. RESULTS

6.1.1. ANTIFERROMAGNETIC MECHANICAL RESONATORS

$\mathrm{FePS_3}$ is an Ising-type antiferromagnet with a Néel temperature in bulk in the range of $T_\mathrm{N} \sim 118-123$ K [45, 58, 227], exhibiting a distinct feature in its specific heat near T_N [227]. Ionic layers in $\mathrm{FePS_3}$ are stacked in van der Waals planes, that can be exfoliated to thin the crystal down with atomic precision [45]. Using mechanical exfoliation and all-dry viscoelastic stamping [112], we transfer thin flakes of $\mathrm{FePS_3}$ over circular cavities etched in an oxidised Si wafer, to form membranes (see the inset in Fig. 6.1a). Suspended $\mathrm{FePS_3}$ devices with thicknesses ranging from 8 to 45 nm are placed in a cryostat and cooled down to a temperature of 4 K. The resonance frequency of the nanodrums is then characterized using a laser interferometry technique [136] (see Fig. 6.1a and Chapter 3).

The resonance frequency of the fundamental membrane mode, $f_0(T)$, is measured in the temperature range from 4 to 200 K. Typical resonances are shown in Fig. 6.1b-d in the antiferromagnetic phase (80 K), near the transition (114 K) and in the paramagnetic

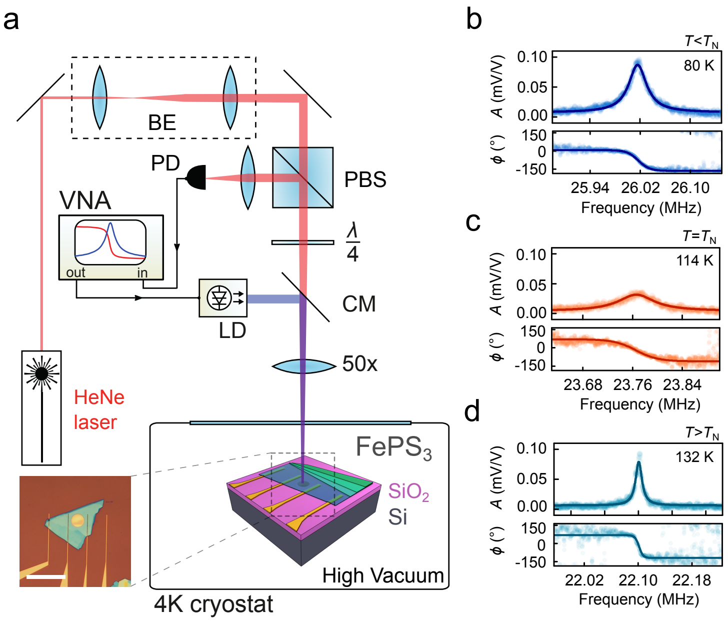

Figure 6.1: Characterisation of mechanical resonances in a thin antiferromagnetic FePS_3 membrane. **a** Laser interferometry setup. Red interferometric detection laser: $\lambda_{\text{red}} = 632$ nm. Blue actuation laser diode: $\lambda_{\text{blue}} = 405$ nm. VNA - Vector Network Analyzer, CM - Cold Mirror, PBS - Polarizing Beam Splitter, PD - Photodiode, LD - Laser Diode. All measurements are performed at incident laser powers of $P_{\text{red}} < 10$ μW and $P_{\text{blue}} < 0.6$ μW. It is checked for all membranes that the resonance frequency changes due to laser heating are insignificant. Inset: optical image of a FePS_3 membrane, including electrodes introducing an option for electrostatic control of strain in the membrane. Flake thickness: 45.2 ± 0.6 nm; membrane diameter: $d = 10$ μm. Scale bar: 30 μm. **b-d** Amplitude (A) and phase (ϕ) of the fundamental resonance at three different temperatures for the device shown in **a**. Filled dots - measured data; solid lines - fit of the mechanical resonance used to determine f_0 and Q [136].

phase (132 K), respectively. Figure 6.2a shows $f_0(T)$ of the same FePS_3 membrane (solid blue curve). Near the phase transition, significant changes in amplitude, resonance frequency and quality factor are observed.

6.1.2. RESONANCE AND SPECIFIC HEAT

To analyze the data further, we first analyze the relation between f_0 and the specific heat. The decrease in resonance frequency with increasing temperature in Fig. 6.2a is indicative of a reduction in strain due to thermal expansion of the membrane. The observed changes can be understood by considering the resonance frequency of a bi-axially tensile strained circular membrane:

$$f_0(T) = \frac{2.4048}{\pi d}\sqrt{\frac{E}{\rho}\frac{\epsilon(T)}{(1-\nu)}}, \tag{6.1}$$

where E is the Young's modulus of the material, ν its Poisson's ratio, ρ its mass density, $\epsilon(T)$ the strain and T the temperature. The linear thermal expansion coefficient of the

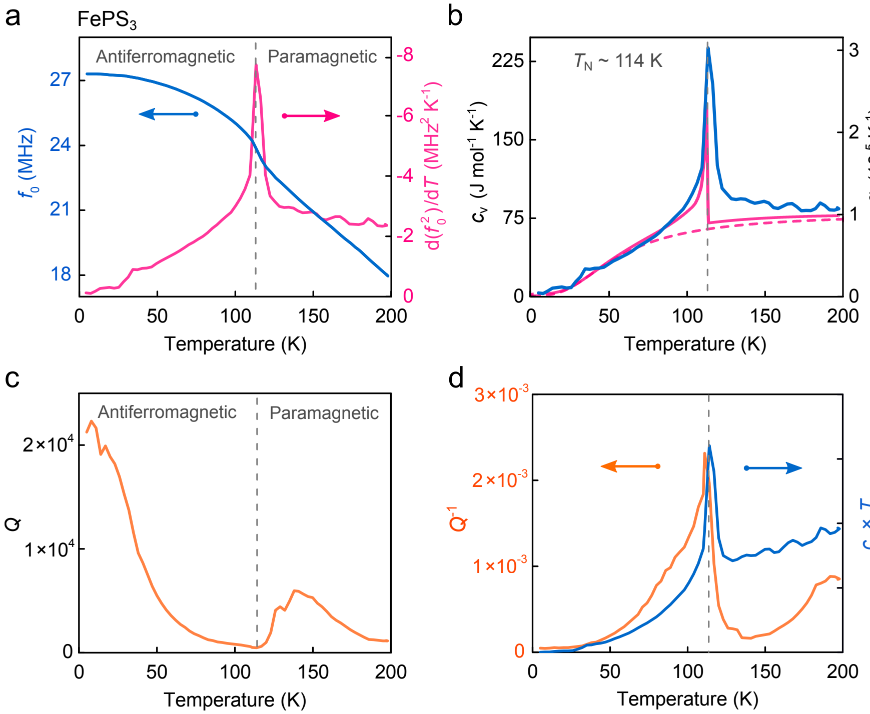

Figure 6.2: Mechanical and thermal properties properties of a FePS$_3$ resonator with membrane thickness of 45.2 ± 0.6 nm. In all panels, dashed vertical lines indicate the detected transition temperature, $T_N = 114 \pm 3$ K as determined from the peak in the temperature derivative of f_0^2. **a** Solid blue line - measured resonance frequency as a function of temperature. Solid magenta line - temperature derivative of f_0^2. **b** Solid blue line - experimentally derived specific heat and corresponding thermal expansion coefficient. Solid magenta line - the theoretical calculation of the magnetic specific heat as reported in Takano et al. [227] added to the phononic specific heat from Debye model (dashed magenta line) with a Debye temperature of $\Theta_D = 236$ K [227]. **c** Mechanical quality factor $Q(T)$ of the membrane fundamental resonance. **d** Solid orange line - measured mechanical damping $Q^{-1}(T)$ as a function temperature. Solid blue line - normalized $c_v(T)\,T$ term [228, 229] (see Appendix A3), with $c_v(T)$ taken from **b**.

membrane, $\alpha_L(T)$, and silicon substrate, $\alpha_{Si}(T)$, are related to the strain in the membrane [140] as $\frac{d\epsilon(T)}{dT} \approx -(\alpha_L(T) - \alpha_{Si}(T))$, using the approximation $\alpha_{SiO_2} \ll \alpha_{Si}$ (see Appendix A1). By combining the given expression for $\frac{d\epsilon(T)}{dT}$ with Eq. 6.1 and by using the thermodynamic relation $\alpha_L(T) \simeq \gamma c_v(T)/(3KV_M)$ [230] between $\alpha_L(T)$ and the specific heat (molar heat capacity) at constant volume, $c_v(T)$, we obtain:

$$c_v(T) \simeq 3\alpha_L(T)\frac{KV_M}{\gamma} = 3\left(\alpha_{Si} - \frac{1}{\mu^2}\frac{d[f_0^2(T)]}{dT}\right)\frac{KV_M}{\gamma}. \tag{6.2}$$

Here, K is the bulk modulus, γ the Grüneisen parameter, $V_M = M/\rho$ the molar volume of the membrane and $\mu = \frac{2.4048}{\pi d}\sqrt{\frac{E}{\rho(1-\nu)}}$, that are assumed to be only weakly temperature dependent. The small effect of non-constant volume ($\nu \neq 0.5$) on c_v is neglected.

We use Eq. 6.2 to analyze $f_0(T)$ and compare it to the calculated specific heat for

$FePS_3$ from literature [227]. In doing so, we estimate the Grüneisen parameter following the Belomestnykh–Tesleva relation $\gamma \approx \frac{3}{2}\left(\frac{1+\nu}{2-3\nu}\right)$ [230, 231]. This is an approximation to Leont'ev's formula [232], which is a good estimation of γ for bulk isotropic crystalline solids within ~ 10% of uncertainty [230]. Furthermore, we use literature values for the elastic parameters of $FePS_3$ as obtained from first-principles theoretical calculations [59] to derive $E = 103$ GPa, $\nu = 0.304$ and $\rho = 3375\ \mathrm{kg\,m^{-3}}$.

6.1.3. DETECTING PHASE TRANSITIONS

In Fig. 6.2a, the steepest part of the negative slope of $f_0(T)$ (solid blue curve) leads to a large peak in $\frac{\mathrm{d}(f_0^2(T))}{\mathrm{d}T}$ (solid magenta curve) near 114 K, the temperature which we define as T_N and indicate by the vertical dashed lines. In Fig. 6.2b the specific heat curve of $FePS_3$ (blue solid line) as estimated from the data in Fig. 6.2a and Eq. 6.2 is displayed. The results are compared to a theoretical model for the specific heat of $FePS_3$ (magenta solid line in Fig. 6.2b), which is the sum of a phononic contribution from the Debye model (magenta dashed line) and a magnetic contribution as calculated by Takano et al. [227]. It is noted that other, e.g. electronic contributions to $c_\mathrm{v}(T)$ are small and can be neglected in this comparison, as is supported by experiments on the specific heat in bulk $FePS_3$ crystals [227]. The close correspondence in Fig. 6.2b between the experimental and theoretical data for $c_\mathrm{v}(T)$ supports the applicability of Eq. 6.2. It also indicates that changes in the Young's modulus near the phase transition, that can be of the order of a couple of percent [40, 41], are insignificant and that it is the anomaly in c_v of $FePS_3$ which produces the observed changes in resonance frequency and the large peak in $\frac{\mathrm{d}(f_0^2)}{\mathrm{d}T}$ visible in Fig. 6.2a.

6.1.4. EFFECT OF STRAIN

The abrupt change in $c_\mathrm{v}(T)$ of the membrane can be understood from Landau's theory of phase transitions [106]. To illustrate this, we consider a simplified model for an antiferromagnetic system, like $FePS_3$, with free energy, F, which includes a strain-dependent magnetostriction contribution (see Appendix A2). Near the transition temperature and in the absence of a magnetic field it holds that:

$$F = F_0 + [a(T - T_\mathrm{N}) + \zeta(\epsilon)]L_z^2 + BL_z^4. \tag{6.3}$$

Here, a and B are phenomenological positive constants, L_z is the order parameter in the out-of-plane direction and $\zeta(\epsilon) = \eta_{ij}\epsilon_{ij}$, a strain-dependent parameter with η_{ij} a material-dependent tensor, that includes the strain and distance dependent magnetic exchange interactions between neighbouring magnetic moments. By minimizing Eq. 6.3 with respect to L_z, the equilibrium free energy, F_min, and order parameter are obtained (see Appendix A2). Two important observations can be made. Firstly, strain shifts the transition temperature according to:

$$T_\mathrm{N}^*(\epsilon) = T_\mathrm{N} - \frac{\zeta(\epsilon)}{a}, \tag{6.4}$$

where T_N^* is the Néel temperature, below which free energy minima F_min with finite order ($L_z \neq 0$) appear. Secondly, since close to the transition the specific heat follows

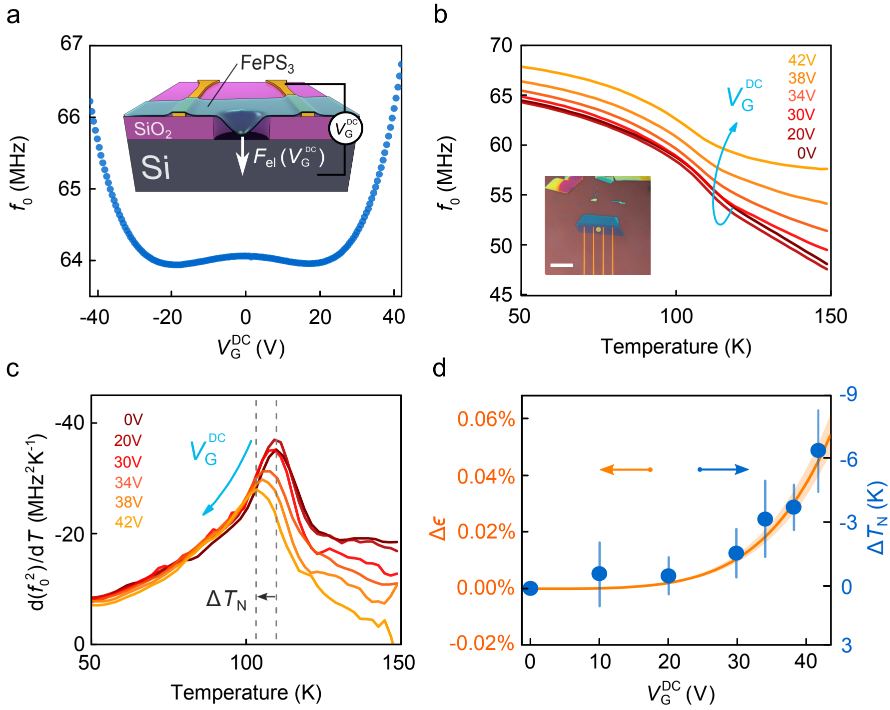

Figure 6.3: Resonance frequency and transition temperature tuning with a gate voltage. **a** Resonance frequency as a function of gate voltage at 50 K. Inset - schematics of the electrostatic tuning principle. **b** Resonance frequency as a function of temperature for six different voltages. Inset: optical image of the sample, $h = 8 \pm 0.5$ nm. Scale bar: 16 μm. **c** Derivative of f_0^2 as a function of gate voltage and temperature. Blue arrow, line colors and legend indicate the values of V_G^{DC}. Dashed grey lines indicate the decrease in transition temperature $\Delta T_N = T_N^*(V_G^{DC}) - T_N(0\,V)$ with increasing V_G^{DC}. **d** Blue solid dots - shift in T_N as a function of V_G^{DC} extracted from the peak position in **c**. Vertical blue bars - error bar in ΔT_N estimated from determining the peak position in **c** within 2% accuracy in the measured maximum. Orange solid line - model of electrostatically induced strain $\Delta\epsilon$ as a function of V_G^{DC} (see Appendix A4).

$c_v(T) = -T\frac{\partial^2 F_{min}}{\partial T^2}$, this general model predicts a discontinuity in c_v of magnitude $T_N^*\frac{a^2}{2B}$ at the transition temperature T_N^*, in accordance with the experimental jump in $c_v(T)$ and $\frac{d(f_0^2(T))}{dT}$ observed in Fig. 6.2a and b.

6.1.5. TEMPERATURE DEPENDENT Q-FACTOR

We now analyze the quality factor data shown in Fig. 6.2c,d. Just above T_N, the quality factor of the resonance (Fig. 6.2c) shows a significant increase as the temperature is increased from 114 to 140 K. The resonance frequency and quality factor are related via causality: $f(T) = f_0(T)\sqrt{1-\frac{1}{4Q(T)^2}}$. However, for a quantitative change in the Q-factor next to the phase transition in samples presented in Fig. 6.2c, we expect the effect on $f_0(T)$ to be of the order of kHz, which is insignificant compared to the change in frequency up to ~ 2 MHz. Thus, the observed minimum in the quality factor near the phase transition, suggests that dissipation in the material is linked to the thermodynamics and can be related to thermoelastic damping. We model the thermoelastic damping according to Zener [228] and Lifshitz-Roukes [229] that report dissipation of the form $Q^{-1} \propto \frac{\alpha_L^2(T)}{c_V(T)}\, T \propto c_V(T)\, T$ (see Appendix A3). Since we have obtained an estimate of $c_V(T)$ from the resonance frequency analysis (Fig. 6.2b), we use this relation to compare the experimental dissipation $Q^{-1}(T)$ (orange solid line) to a curve proportional to $c_V(T)\, T$ (blue solid line) in Fig. 6.2d. Both the measured dissipation and the thermoelastic term display a peak near $T_N \sim 114$ K. The close qualitative correspondence between the two quantities is an indication that the thermoelastic damping related term indeed can account for the temperature dependence of $Q(T)$ near the phase transition. We note that the temperature dependent dissipation in thin membranes is still not well understood, and that more intricate effects might play a role in the observed temperature dependence, as we discuss in Chapter 11.

6.1.6. ELECTROSTATIC STRAIN

Eq. 6.4 predicts that the transition temperature is strain-dependent due to the distance dependent interaction coefficient $\zeta(\epsilon)$ between magnetic moments. To verify this effect, we use an 8 ± 0.5 nm thin sample of $FePS_3$ suspended over a cavity of 4 μm in diameter. A gate voltage V_G^{DC} is applied between the flake and the doped bottom Si substrate to introduce an electrostatic force that pulls the membrane down and thus strains it (see Appendix Fig. 6.6 and 6.7). As shown in Fig. 6.3a, the resonance frequency of the membrane follows a W-shaped curve as a function of gate voltage. This is due to two counteracting effects [233]: at small gate voltages capacitive softening of the membrane occurs, while at higher voltages the membrane tension increases due to the applied electrostatic force, which causes the resonance frequency to increase.

Figure 6.3b shows $f_0(T)$ for six different gate voltages. The shift of the point of steepest slope of $f_0(T)$ with increasing V_G^{DC} is well visible in Fig. 6.3b and even more clear in Fig. 6.3c, where the peak in $\frac{\mathrm{d}(f_0^2)}{\mathrm{d}T}$ shifts 6 K downward by electrostatic force induced strain. The observed reduction in T_N^* as determined by the peak position in $\frac{\mathrm{d}(f_0^2)}{\mathrm{d}T}$ qualitatively agrees with the presented model and its strain dependence from Eq. 6.4, as shown in Fig. 6.3d indicative of a reduced coupling of magnetic moments with increasing distance between them due to tensile strain.

6.2. DISCUSSION

Since the coupling between specific heat and the order parameter in materials is of a general thermodynamic nature, the presented methodology is applicable to a wide variety of materials provided that elastic properties of the material and Grüneisen parameter are weakly temperature dependent, the substrate satisfies the condition $\alpha_{\text{substrate}} \ll \alpha_{\text{material}}$ and that the frequency shifts and changes in Q are large enough to be resolved (also see Chapter 12 for discussion on electronic phase transitions). We further demonstrate the method by detecting magnetic phase transitions in $NiPS_3$ and $MnPS_3$.

We measure $MnPS_3$ and $NiPS_3$ membranes with a 10 μm diameter and thicknesses of 31.8 ± 1.2 and 35.7 ± 1.1 nm, respectively (see Appendix A5). Comparative study of these

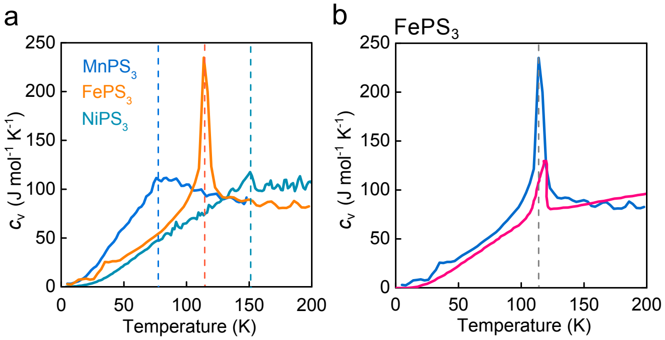

Figure 6.4: Estimated specific heat (c_V) for **a** MPS$_3$ (M=Fe, Mn, Ni) membranes of $h = 45.2 \pm 0.6$ nm, 31.8 ± 1.2 nm and 35.7 ± 1.1 nm, respectively. Dashed lines indicate the corresponding transition temperatures (T_N): $T_N = 76 \pm 5$ K for MnPS$_3$, $T_N = 114 \pm 3$ K for FePS$_3$ and $T_N = 151 \pm 5$ K for NiPS$_3$. **b** Specific heat of ultrathin FePS$_3$ membrane compared to that of its bulk form. Solid blue line - measured c_V of the FePS$_3$ ultrathin membrane. Solid magenta line - c_V reported by Takano et al. [227] for a bulk crystal.

is particularly interesting since FePS$_3$ is an Ising antiferromagnet, while the other two are Heisenberg (MnPS$_3$) and XY (NiPS$_3$) antiferromagnets [58]. We use the measured temperature dependence of the fundamental membrane mode resonance frequency, $f_0(T)$, to estimate specific heat of these compounds using analysis described above and compare it to the case of FePS$_3$.

In Fig. 6.4a the estimated specific heat for the three MPS$_3$ compounds are displayed, as determined from the data in Fig. 6.2a and Appendix Fig. 6.8 using Eq. 6.2. Detected temperatures are indicated by dashed lines and found to be $T_N = 76 \pm 5$ K for MnPS$_3$, $T_N = 114 \pm 3$ K for FePS$_3$ and $T_N = 151 \pm 5$ K for NiPS$_3$, which are in agreement with experiments on bulk crystals [58, 227]. Compared to FePS$_3$, the specific heat anomaly near the phase transitions in MnPS$_3$ and NiPS$_3$ is more gradual with both materials showing broader maxima in $c_V(T)$ near the T_N. This suggests weaker magnetoelastic coupling in these compounds in comparison to FePS$_3$ [61]. As shown in Fig. 6.4b, for FePS$_3$ we obtain a good correspondence to bulk literature values [227] (solid magenta curve) without fitting parameters. The transition related peak in c_V, however, is more pronounced in the case of the ultrathin membrane (solid blue curve) than in the bulk. Since the effect is reproducible (see Appendix A6), it may indicate an additional contribution to the thermal expansion coefficient near T_N in FePS$_3$ membranes related to spontaneous magnetostriction effect [61] (see Chapter 10 for a detailed discussion).

6.3. CONCLUSION

In conclusion, we have demonstrated that there exist a strong coupling between mechanical motion and order in ultrathin membranes of 2D materials. An analytical equation for the relation between the specific heat of the material and the temperature dependent resonance frequency is derived and shown to be in good agreement with experimental results. Since the materials are utilized in a suspended state, substrate effects on the electronic and magnetic properties of the thin materials are excluded. The technique is not only appealing for the characterisation of ultrathin membranes of antiferromagnetic and insulating materials that are difficult to characterize otherwise, but also for the development of device concepts exploiting the unique properties of the materials involved. It is anticipated that it can be applied to a large range of van der Waals materials [30, 42], 2D ferromagnets [57], thin 2D complex oxide sheets [2, 234] and organic antiferromagnets [64].

6.4. APPENDIX

A1: FUNDAMENTAL RESONANCE FREQUENCY OF A CIRCULAR PLATE AND MEMBRANE

In this section we briefly analyze the resonance frequency of the $FePS_3$ resonators and show that near the phase transition these are close to the membrane limit. The relative contribution of the plate term to the frequency of the resonator is largest at room temperature because the membrane tension is the lowest. As shown in Fig. 3.4a of Chapter 3, at $T = 300$ K and $n_0 = 0.1$ N m^{-1} thicker $FePS_3$ samples ($h > 40$ nm) behave as circular plates. However, as shown in Fig. 3.4b of the same chapter, in proximity of $T_N \approx 114$ K due to temperature-induced strain $\epsilon(T)$, the resonator behaves close to the membrane limit over a thickness range from a monolayer to 60 nm, also covering the thickness of the resonator in Fig. 6.2.

As also shown in Chapter 3, the total strain in the membrane is estimated using $\epsilon(T) = \epsilon_0 - \int_{300\mathrm{K}}^{T}(\alpha_{\mathrm{material}}(T) - \alpha_{\mathrm{Si}}(T))\mathrm{d}T$, where ϵ_0 is the intrinsic pre-strain at $T = 300$ K [139, 140]. In Fig. 6.5 we show that the thermal expansion coefficient of the silicon substrate [141, 142] (solid magenta line) is small compared to that of $FePS_3$. Therefore, the total strain in the membrane will mainly build up due to α_{FePS_3}, and this term dominates the change in resonance frequency, $f_0(T)$ as depicted in Fig. 6.2.

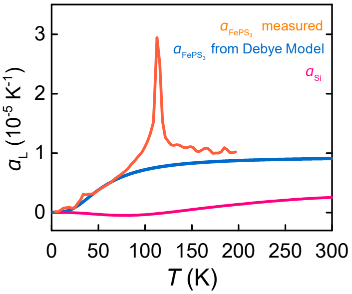

Figure 6.5: Comparison of thermal expansion coefficients of $FePS_3$ as measured (solid orange line) and as predicted from the Debye model (solid blue line) to that of the Si substrate (solid magenta line).

A2: ENTROPY IN A SUSPENDED ANTIFERROMAGNET

A uniaxial antiferromagnet with two antiparallel magnetic sub-lattices close to the phase transition can be modeled by the Landau theory of phase transitions [105, 106]. In this theory, the vector order parameter **L** is defined as the difference between the magnetizations of the two sublattices, $\mathbf{M}_1$ and $\mathbf{M}_2$ (thus, the antiferromagnetic vector $\mathbf{L} = \mathbf{M}_1 - \mathbf{M}_2$).

This order parameter is zero in the paramagnetic phase and is finite in the antiferromagnetic phase. The magnetization, $\mathbf{M}$, is the sum of both magnetizations ($\mathbf{M} = \mathbf{M}_1 + \mathbf{M}_2$) and equals to zero in the absence of an external magnetic field, $\mathbf{H}$.

For a uniaxial crystal antiferromagnet, the transition temperature is commonly known as Néel temperature, T_N, but, as conveyed by Landau et al. [105, 106], it is also referred to as the antiferromagnetic Curie temperature and denoted as T_C. Note that further we will consider the Néel temperature, denoted as T_N, as the temperature where the transition from a paramagnetic to an antiferromagnetic phase takes place. Near T_N, $\mathbf{L}$ is small and the free energy, F, can be expanded in terms of $\mathbf{L}$ and $\mathbf{H}$, since the magnetization is only non-zero when an external field $\mathbf{H}$ is present (i.e. a spin-flop transition). Following Landau formalism and considering z-axis as the main axis of symmetry, we write (see e.g. Ref. [106]):

$$\begin{aligned} F = F_0 + AL^2 + BL^4 + D\,(\mathbf{H}\cdot\mathbf{L})^2 + D' H^2 L^2 \\ -\frac{1}{2}\chi_\mathrm{p} H^2 + \frac{1}{2}\beta\left(L_x^2 + L_y^2\right) - \frac{1}{2}\mu_\mathrm{M}\left(H_x^2 + H_y^2\right) - \frac{H^2}{8\pi}\,, \end{aligned} \tag{6.5}$$

where $A = a(T - T_\mathrm{N})$, D, D', a and B are phenomenological positive constants which are taken temperature independent, χ_p the isotropic susceptibility for $T > T_\mathrm{N}$, β the index that describes the temperature dependence of the spontaneous magnetization below T_N ($\beta > 0$ for $\mathbf{L}$ directed out-of-plane) and μ_M the magnetic susceptibility in the paramagnetic phase. The minimization of Eq. 6.5, where the vector $\mathbf{L}$ is along the z-axis (thus, $L_x = L_y = 0$ and $\beta > 0$) and in the absence of field ($H = 0$), gives $L_x = L_y = 0$ and $L_z = 0$ for $T > T_\mathrm{N}$ (paramagnetic phase) and $L_z = \sqrt{a(T_\mathrm{N} - T)/(2B)}$ for $T < T_\mathrm{N}$ (antiferromagnetic phase).

Now we introduce strain. For an easy-axis antiferromagnet near T_N with the vector $\mathbf{L}$ along the z-axis and in the absence of field, we can write Eq. 6.5 as:

$$F = F_0 + AL^2 + BL^4 + \frac{1}{2}\beta\left(L_x^2 + L_y^2\right) + \zeta L_z^2 + \zeta_x L_x^2 + \zeta_y L_y^2\,, \tag{6.6}$$

where the last three added terms describe the magnetostriction effects, i.e., the coupling of magnetic moments to strain; the coefficients ζ, $\zeta_{x,y}$ are linear combinations of the components of the strain tensor. We assume that the strain is determined by the deformation of the membrane, and that the back-action exerted by the magnetization on the strain is negligible. In that case, for the calculation of the order parameter, ζ and $\zeta_{x,y}$ can be treated as temperature-independent constants. We also assume that $|\zeta|, |\zeta_{x,y}| \ll \beta$, so that even the strained antiferromagnet exhibits an easy-axis. The minimization of Eq. 6.6 gives $L_x = L_y = 0$, leading to a free energy which only depends on L_z,

$$F = F_0 + \left[a\,(T - T_\mathrm{N}) + \zeta\right] L_z^2 + BL_z^4. \tag{6.7}$$

The first observation is that the magnetostriction effects shift the antiferromagnetic phase transition point. Indeed, the phase transition occurs at the temperature T_N^* at which the coefficient multiplying L_z^2 in Eq. 6.7 vanishes. This gives $T_\mathrm{N}^* = T_\mathrm{N} - \zeta/a$.

Second, we calculate the behavior of the specific heat close to the phase transition. Minimizing Eq. 6.7 with respect to L_z, we find the equilibrium free energy, $F_\mathrm{min} = F_0 -$

$a^2(T-T_N^*)^2/(4B)$ in the antiferromagnetic phase, where F_0 is the free energy of the paramagnetic phase. We proceed by calculating the entropy $S_{\rm min} = -\partial F_{\rm min}/\partial T$,

$$S_{\rm min} - S_0 = \begin{cases} -a^2(T_N^* - T)/(2B) & T < T_N^* \\ 0 & T > T_N^* \end{cases}, \tag{6.8}$$

where $S_0 = -\partial F_0/\partial T$ is the entropy of the paramagnet with S_0 the non-magnetic contribution to the entropy. Since the renormalized transition temperature T_N^* is strain-dependent, the entropy of the antiferromagnet contains an additional (as compared to the paramagnetic phase) strain-dependent term. The specific heat near T_N^*, $c_{\rm v,min} = T\partial S_{\rm min}/\partial T$, reads

$$c_{\rm v,min} - c_{\rm v,0} = \begin{cases} T_N^* a^2/(2B) & T < T_N^* \\ 0 & T > T_N^* \end{cases}, \tag{6.9}$$

where $c_{\rm v,0}$ is the non-magnetic contribution to the specific heat. This derivation shows, in line with Landau theory [105, 106], that the specific heat has a jump at the transition temperature, T_N^*.

A3: DISSIPATION AND THERMOELASTIC DAMPING IN VIBRATING MEMBRANES

For a membrane in motion the dissipation Q^{-1} is defined as the ratio of the energy lost per cycle to 2π times the stored energy. The total dissipation in a membrane is given by the sum of all contributing dissipation mechanisms [135]:

$$Q^{-1} = Q^{-1}_{\rm medium} + Q^{-1}_{\rm clamping} + Q^{-1}_{\rm intrinsic} + Q^{-1}_{\rm other}. \tag{6.10}$$

$Q^{-1}_{\rm medium}$ is related to losses due to the interaction with a fluid medium or gas and can thus be neglected in high vacuum. $Q^{-1}_{\rm clamping}$ is related to the transfer of mechanical energy to the anchoring substrate, which has a small temperature dependence [135]. $Q^{-1}_{\rm intrinsic}$ quantifies all intrinsic damping mechanisms of the material, such as thermoelastic damping, internal and surface friction, and phonon-phonon interaction loss. $Q^{-1}_{\rm other}$ relates all other possible damping mechanisms, such as electrical charge damping and magneto-motive damping. In this section we focus on deriving the expression for the thermoelastic damping. Further derivation in this section follows Zener's standard linear solid model [228, 235].

The dissipation is equal to the ratio between the imaginary and real parts of the complex elastic modulus $E^*(\omega) = E'(\omega) + {\rm i}E''(\omega)$:

$$Q^{-1} = \frac{E''}{E'}. \tag{6.11}$$

For a standard linear solid with a single relaxation mechanism, real and imaginary parts of the complex elastic modulus are given by:

$$E'(\omega) = E_{\rm r} + (E_{\rm u} - E_{\rm r})\frac{\omega^2\tau^2}{1+(\omega\tau)^2},\; E''(\omega) = (E_{\rm u} - E_{\rm r})\frac{\omega\tau}{1+(\omega\tau)^2}, \tag{6.12}$$

where ω is the resonance eigenfrequency, τ the thermal relaxation time, E_r and E_u are the relaxed (or isothermal) and unrelaxed (or adiabatic) Young's moduli, respectively (see Ref. [135, 235] for more details). From Eq. 6.11, the dissipation is then:

$$Q^{-1} = (E_u - E_r)\frac{\omega\tau}{E_r + E_u(\omega\tau)^2} \approx \frac{E_u - E_r}{E_r}\frac{\omega\tau}{1+(\omega\tau)^2}, \tag{6.13}$$

for $(E_u - E_r) \ll E_r \approx E_u$. For a standard thermoelastic solid and in the case of thermoelastic damping Q^{-1}_{TED}, Eq. 6.13 can be rewritten as [228, 229, 235]:

$$Q^{-1}_{\text{TED}} = \frac{E_u - E_r}{E_r}\beta = \frac{E\alpha^2 T}{c_v}\beta, \tag{6.14}$$

where α is the thermal expansion coefficient, c_v the specific heat and β the thermomechanical parameter, that in Zener's model is $\beta_Z = \frac{\omega\tau}{1+(\omega\tau)^2}$. The exact expression for thermoelastic damping and its relation to the thermal properties of solids was found by Lifshitz and Roukes [229] with $\beta_{LR} = \frac{6}{\xi^2} - \frac{6}{\xi^3}\frac{\sinh(\xi)+\sin(\xi)}{\cosh(\xi)+\cos(\xi)}$, where $\xi = \frac{\pi}{\sqrt{2}}\sqrt{\omega\tau}$. Under the assumption that the temperature dependence of $\omega\tau$ is small (see Chapter 11 for further discussions), Eq. 6.14 can be written as:

$$Q^{-1}_{\text{TED}} \propto \frac{E\alpha^2 T}{c_v}. \tag{6.15}$$

The close correspondence between this expression and the data in Fig. 6.2d indicates that this assumption is reasonable.

As could be noted from Eq. 6.2 and assuming the elastic properties of the material and its Grüneisen parameter to have a negligible temperature dependence at low temperatures, the thermoelastic damping Q^{-1}_{TED} is related to the frequency f_0 of the resonator as:

$$Q^{-1}_{\text{TED}}(T) \propto \frac{E\alpha^2(T)T}{c_v(T)} \propto c_v(T)\,T \propto -T\frac{\mathrm{d}[f_0^2(T)]}{\mathrm{d}T}, \tag{6.16}$$

where we use $\alpha(T) \propto c_v(T)$ and $c_v(T) \propto \frac{\mathrm{d}[f_0^2(T)]}{\mathrm{d}T}$ according to Eq. 6.2. Therefore, in accordance with our observations, an anomaly (a jump) in the specific heat at the transition temperature will be visible in both $\frac{\mathrm{d}[f_0^2(T)]}{\mathrm{d}T}$ and $Q^{-1}(T)$ if the thermoelastic damping is the dominating dissipation mechanism near T_N.

A4: ELECTRIC FIELD INDUCED STRAIN IN A CIRCULAR FePS$_3$ MEMBRANE

A constant electrostatic load is applied to the circular membrane with a radius a (see Fig. 6.6). This results in a uniform curvature R with a maximum deflection δ.

In this system, the electrostatic load is balanced by the total tension n_{total}:

$$\frac{\varepsilon_0 (V_G^{\text{DC}})^2}{2(g_0-\delta)^2}\pi R^2 = 2\pi n_{\text{total}} R, \tag{6.17}$$

where ε_0 is the vacuum permittivity, V_G^{DC} the applied voltage, g_0 the gap size between the membrane and the bottom silicon plate. For small deflections the radius of curvature can be approximated as:

$$R \approx \frac{a^2}{2\delta}, \tag{6.18}$$

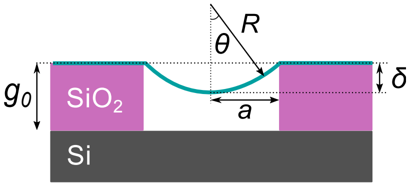

Figure 6.6: Schematic of the membrane deformation, cross-section view.

so that the tension n_{total} becomes:

$$n_{\text{total}} = \frac{\varepsilon_0 (V_G^{DC})^2}{2(g_0-\delta)^2}\frac{a^2}{4\delta}. \tag{6.19}$$

The radial strain in such a membrane can be estimated from the arc length [145, 146]:

$$\epsilon = \frac{R\theta - a}{a} \approx \frac{a^2}{6R^2}. \tag{6.20}$$

Combining this result with Eq. 6.18 yields:

$$\epsilon \approx \frac{2\delta^2}{3a^2}. \tag{6.21}$$

From Hooke's law and including Eq. 6.21, one can write the strain due to deformation as:

$$n = \frac{Eh}{1-\nu}\epsilon = \frac{2Eh\delta^2}{3a^2(1-\nu)}, \tag{6.22}$$

Therefore, the total tension in the membrane, including the thermal expansion induced tension $n_0(T)$ at a certain temperature T, can be written as:

$$n_{\text{total}} = n_0(T) + n = n_0(T) + \frac{2Eh\delta^2}{3a^2(1-\nu)} = \frac{\varepsilon_0 (V_G^{DC})^2}{2(g_0-\delta)^2}\frac{a^2}{4\delta}, \tag{6.23}$$

which also can be rewritten as:

$$V_G^{DC} = \sqrt{\frac{2(g_0-\delta)^2}{\varepsilon_0}\left(\frac{4\delta n_0(T)}{a^2} + \frac{8Eh\delta^3}{3a^4(1-\nu)}\right)}. \tag{6.24}$$

As shown in Fig. 6.7a, Eq. 6.24 in combination with 6.21 and 3.6 fits the experimental data well and is used to provide an estimate of the electrostatically induced strain in the membrane (see Fig. 6.7b).

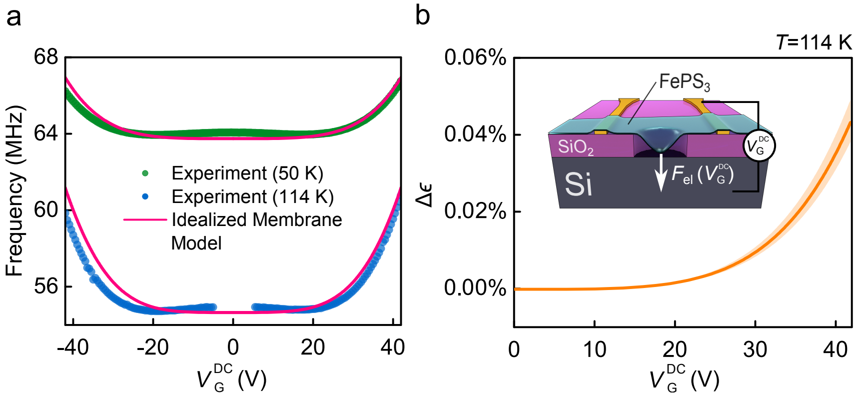

Figure 6.7: **a** Idealized electrostatically strained membrane model for $n_0 = 0.01$ N m^{-1}, $g_0 = 285$ nm, $a = 2$ μm, $h = 8$ nm, $E = 103$ GPa and $\nu = 0.304$; superimposed with corresponding experimental data. **b** Estimate of added radial strain at $T = 114$ K. The shaded orange region represents an estimated uncertainty from the accuracy in determining the temperature induced strain (±0.015%) at $T = 114$ K. Inset - schematics of the experiment.

A5: MECHANICAL RESONANCES AND SPECIFIC HEAT OF MPS$_3$ (M=FE, NI, MN)

In addition to FePS$_3$, we measure MnPS$_3$ and NiPS$_3$ membranes with a 10 μm diameter and thicknesses of 31.8 ± 1.2 and 35.7 ± 1.1 nm, respectively. At the phase transition, significant changes in both the resonance frequency (Fig. 6.8a) and quality factor (Fig. 6.8b) of the MnPS$_3$ membrane are observed. Figure 6.8a shows the resonance frequency (solid blue line) and the corresponding $\frac{\mathrm{d}(f_0^2)}{\mathrm{d}T}$ (solid magenta line) with a peak that occurs at a temperature similar to the transition temperature from the antiferromagnetic phase (< 78 K) to the paramagnetic phase (> 78 K) in the bulk material [227] and is thus attributed as T_N. The temperature dependence of $\frac{\mathrm{d}(f_0^2)}{\mathrm{d}T}$ shows a broad hump with a smeared peak at T_N, which resembles the temperature dependent specific heat $c_\mathrm{v}(T)$ of this material in bulk form [227]. Figure 6.8b shows the mechanical dissipation, Q^{-1}, that exhibits a local minimum close to T_N as well as a local maximum at $T \sim 36$ K.

In Fig. 6.8c the resonance frequency of the NiPS$_3$ membrane (solid blue line) is shown with the corresponding $\frac{\mathrm{d}(f_0^2)}{\mathrm{d}T}$ (solid magenta line). A small peak is noticeable in $\frac{\mathrm{d}(f_0^2)}{\mathrm{d}T}$ near bulk $T_\mathrm{N} \sim 155$ K indicating the phase transition [236]. However, as shown in Fig. 6.8d, no significant anomalies in the Q-factor were observed in the case of NiPS$_3$. Compared to FePS$_3$, the effect of the phase transitions in MnPS$_3$ and NiPS$_3$ on the resonances is more gradual (see Fig. 6.8a-d) with both materials showing broader maxima in $\frac{\mathrm{d}(f_0^2(T))}{\mathrm{d}T}$ near their T_N at 76 K and 151 K, respectively, which is consistent with measurements of bulk crystals [58, 227]. Dissipation measurements, however, do not show a clear peak at T_N like in the case of FePS$_3$.

We calculate the corresponding temperature dependent specific heat $c_\mathrm{v}(T)$ for the three MPS$_3$ samples. Following the methodology described above, we estimate the Grüneisen parameter following the Belomestnykh–Tesleva relation [231, 237]: $\gamma \approx \frac{3}{2}\left(\frac{1+\nu}{2-3\nu}\right)$. We use

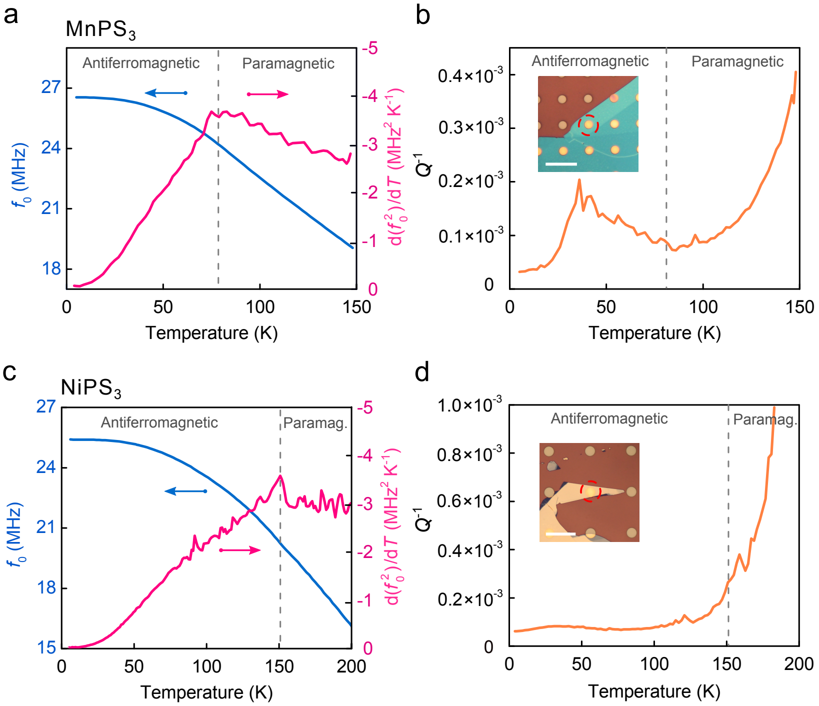

Figure 6.8: Mechanical properties of $MnPS_3$ and $NiPS_3$ membranes. Dashed vertical lines indicate transition temperatures, T_N. **a** Solid blue line - Measured resonance frequency of $MnPS_3$ membrane as a function of temperature. Solid magenta line - Temperature derivative of f_0^2. **b** Measured mechanical damping (Q^{-1}) as a function temperature. Inset: Optical image of the sample, $h = 32.3 \pm 0.4$ nm. Scale bar: 40 μm. **c** Solid blue line - Measured resonance frequency of $NiPS_3$ membrane as a function of temperature. Solid magenta line - Temperature derivative of f_0^2. **b** Measured mechanical damping (Q^{-1}) as a function temperature. Inset: Optical image of the sample, $h = 35.7 \pm 0.5$ nm. Scale bar: 30 μm.

reported values for monolayers of $FePS_3$ ($C_{11} = 72.7$ N m^{-1}, $C_{12} = 22.1$ N m^{-1} and $\rho_{2D} = 2.16 \times 10^{-6}$ kg m^{-2}), $MnPS_3$ ($C_{11} = 61.7$ N m^{-1}, $C_{12} = 20.2$ N m^{-1} and $\rho_{2D} = 2.00 \times 10^{-6}$ kg m^{-2}) and $NiPS_3$ ($C_{11} = 87.0$ N m^{-1}, $C_{12} = 23.1$ N m^{-1} and $\rho_{2D} = 2.15 \times 10^{-6}$ kg m^{-2}) as obtained from first-principles calculations [59, 60]. We convert these to three-dimentional Young's modulus E, mass density ρ and Poisson's ratio ν using $E = \frac{C_{11}^2 - C_{12}^2}{C_{11}} \frac{1}{h}$, $\rho = \frac{\rho_{2D}}{h}$ and $\nu = \frac{C_{12}}{C_{11}}$, taking the interlayer distance for the compounds $h_{FePS_3} = 0.64$ nm, $h_{MnPS_3} = 0.65$ nm and $h_{NiPS_3} = 0.64$ nm [67]. The resulting values are $E = 103$ GPa, $\nu = 0.304$ and $\rho = 3375$ kg m^{-3} for $FePS_3$, $E = 85$ GPa, $\nu = 0.327$ and $\rho = 3076$ kg m^{-3} for $MnPS_3$ and $E = 126$ GPa, $\nu = 0.265$ and $\rho = 3359$ kg m^{-3} for $NiPS_3$. The resulting calculated specific heat for the three MPS_3 membranes is displayed in Fig. 6.4.

A6: REPRODUCIBILITY OF MEASUREMENTS

In order to assess reproducibility of the measured effect between the samples, we show the Q^{-1} data for the $FePS_3$ sample from Fig. 6.2 (Drum 1) compared with the data for one additional sample (Drum 2) in Fig. 6.9.

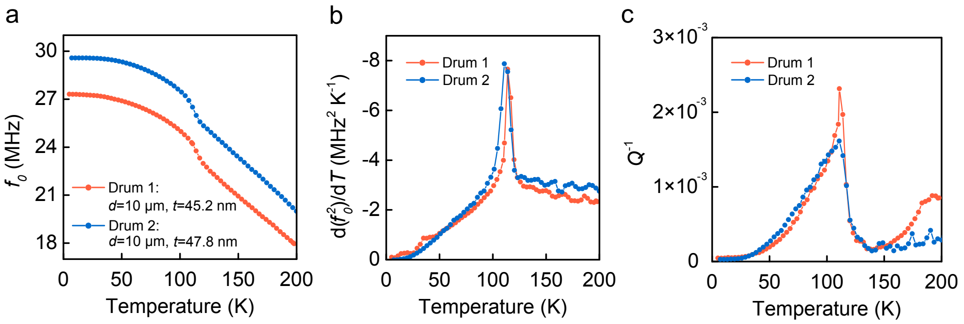

Figure 6.9: Mechanical properties of a $FePS_3$ resonators with membrane thicknesses indicated in a legend. **a** Resonance frequency as a function of temperature. **b** Temperature derivative of f_0^2 for both samples. **c** Measured mechanical damping Q^{-1} as a function temperature.

We choose the sample parameters (i.e., thickness, h, and drum diameter, d) to be similar for a fair comparison. The features related to phase transition in both frequency (Fig. 6.9b) and quality factor (Fig. 6.9c) are present in both cases. The drum 2, however, has a higher pre-stress accumulated in a result of the fabrication, which is concluded from a notable frequency mismatch in Fig. 6.9a. Some variation in T_N of around $2-3$ K can be noted between the samples in Fig. 6.9b, which we attribute to the pre-strain variation in a result of fabrication since, as we report in Fig. 6.3, T_N^* of $FePS_3$ is very sensitive to strain. In Fig. 6.10, the Q^{-1} terms from Fig. 6.9c are displayed and compared to $c_V \times T$ terms for both drums. We note that the position of the peak for Q^{-1} and $c_V \times T$ corresponds to each other up to the resolution of the measurement.

The results for $FePS_3$ are also well reproducible within a single device (Drum 2) with no hysteresis observed in both frequency and Q-factor for multiple temperature sweeps, as shown in Fig. 6.11.

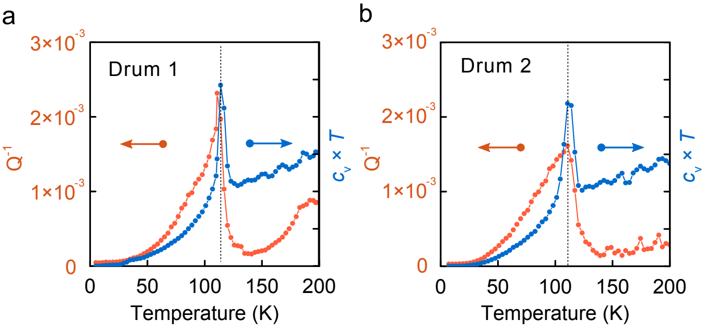

Figure 6.10: Measured mechanical damping $Q^{-1}(T)$ as a function temperature in filled orange dots in both panels for samples form Fig. 6.9. Filled blue dots in both panels - normalized $c_V(T)\ T$ term (see Appendix A3).

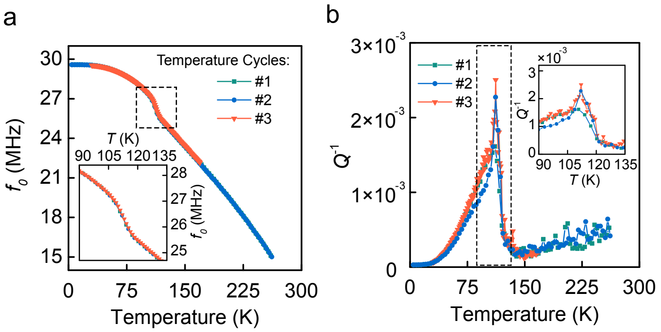

Figure 6.11: Multiple temperature cycles for Drum 2 from Fig. 6.9. **a** Filled dots - resonance frequency as a function of temperature. Inset: a close-up of the region indicated with dashed line box. **b** Filled dots - measured mechanical damping Q^{-1} as a function temperature. Inset: a close-up of the region indicated with dashed line box.

7

TUNABLE STRONG COUPLING BETWEEN SPATIALLY SEPARATED $FePS_3$ NANODRUMS

Coupled nanomechanical resonators made of two-dimensional materials are promising for processing information with mechanical modes. However, the challenge for these types of systems is to control the coupling. Here, we demonstrate strong coupling of motion between two suspended membranes of the magnetic 2D material $FePS_3$. *We describe a tunable electromechanical mechanism for control over both the resonance frequency and the coupling strength using a gate voltage electrode under each membrane. We show that the coupling can be utilized for transferring data from one drum to the other by amplitude modulation. Finally, we also study the temperature dependence of the coupling, and in particular how it is affected by the antiferromagnetic phase transition characteristic of this material. The presented electrical coupling of resonant magnetic 2D membranes holds promise of transferring mechanical energy over a distance at low electrical power, thus enabling novel data readout and information processing technologies.*

NANO-ELECTROMECHANICAL systems (NEMS) are attracting attention of the scientific community for their potential to study novel quantum and electromagnetic effects at the nanoscale [68–70]. Along with that, micro- and nanoresonators have been studied for various applications, including sensitive mass detection [71, 72], bandpass filters with variable properties [73], logic gates [74–76] and signal amplifiers [77]. For instance, arrays of coupled highly-cooperative NEMS and oscillators are already utilized for the coherent manipulation of phonon populations [238–240], and for data processing and storage [70, 241]. Recently, NEMS made out of two-dimensional (2D) materials have also gained interest due to perspectives for realizing high-performance oscillators [89, 224] and novel sensor concepts [6]. This is not only due to the atomic thinness of these devices, but also because the fabrication methodology allows the integration of a range of materials and their heterostructures, with a wide range of magnetic, optical and electrical properties, on the same chip [30]. Hence, coupling NEMS resonators made of 2D materials and heterostructures promises even more interesting implementation possibilities.

Various studies have reported mechanical coupling between different resonance modes of the same 2D membrane by mechanical, optical and electronic means [85, 242–244]. However, realisation of coupling between resonances of spatially separated 2D membranes has appeared to be more difficult and was only recently achieved via a mechanical phononic transduction mechanism [245, 246]. A mechanically mediated coupling mechanism via a phonon bath was demonstrated [245, 246], but although the coupling could be adjusted via the individual resonance frequencies of the resonators, the coupling strength itself is fixed by the mechanical geometry of the structure that determined the phonon bath. In order to achieve full control over the coupling, a tunable transduction mechanism is needed which not only adjusts the degree of coupling between the resonators, but also regulates their resonance frequencies.

Here, we demonstrate an electrical transduction mechanism for coupling mechanical resonances of two spatially separated membranes made of van der Waals material, allowing control over both the resonance frequency and the coupling strength via gate electrodes. We use the mechanism to strongly couple the fundamental mechanical modes of two suspended circular antiferromagnetic $FePS_3$ membranes that are separated by an edge-to-edge distance of 2 microns. We show that the coupling mechanism can be utilized for transferring data from one drum to the other, a feature that is useful in data processing and storage systems. Coupling of magnetic materials like $FePS_3$ is of interest, since their mechanical resonances can be sensitive to both the magnetic phase [67] and the magnetisation of that phase [57]. To investigate this, we study the temperature dependence of the coupling strength, and in particular how it is affected by the antiferromagnetic phase transition at the Néel temperature, $T_N \sim 114$ K [45, 227].

7.1. RESULTS AND DISCUSSION

7.1.1. SAMPLE FABRICATION

We fabricate two circular suspended $FePS_3$ resonators on top of a Si/SiO_2 substrate on which we define an array of Au bottom gate electrodes. We first patterned the bottom Au electrodes with a Ti adhesive layer on top of Si/SiO_2 substrate using positive resist

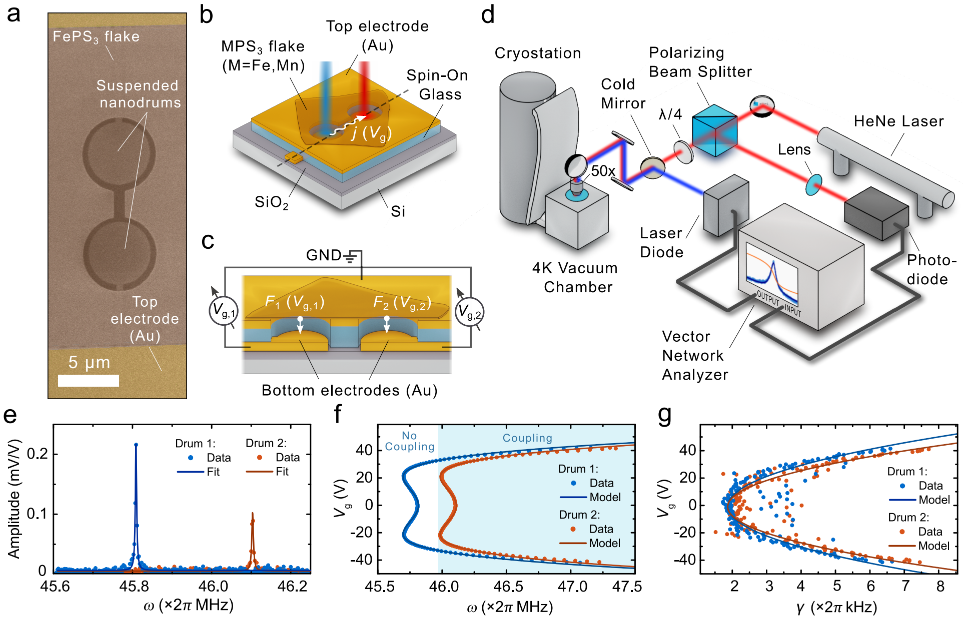

Figure 7.1: Measurement principle and setup. **a** False-coloured SEM image of the sample. Flake thickness: 25.6 ± 0.4 nm. **b** Schematics of device and optical measurement principle; $j(V_g)$ is the voltage-dependent coupling parameter. **c** Schematics of cross-section of the device, electrically induced force $F_{1,2}$ and gate voltage V_g. **d** Laser interferometry setup. Red laser: $\lambda_{red} = 632$ nm. Blue laser: $\lambda_{blue} = 405$ nm. All measurements were performed at incident laser powers of $P_{red} \leq 100$ μW and $P_{blue} \leq 1.5$ μW, unless stated otherwise. **e** Detected resonance peaks for the two suspended drums. Filled dots - measured data, Solid lines - linear harmonic oscillator fits. **f** Resonance frequencies $\omega(V_g)$ of drums 1 and 2, extracted from fits similar to **e**. Filled dots - measured data, Solid lines - continuum mechanics model [143, 145] (see Appendix A1). Blue region indicates the parameter-space where $\omega_1 = \omega_2$ condition can be met. **g** Dissipation rate $\gamma(V_g)$ for two drums extracted from fits similar as shown in **e**. Filled dots - measured data; Solid lines - Joule dissipation model [128, 140, 247] (see Appendix A2).

e-beam lithography. Following that, a layer of HSQ FOX-12 spin-on glass (SOG) are spin-coated on top of the chip [97]. Subsequently, we anneal the chips in a furnace at 500 °C in Ar gas for 50 minutes. This cures the spin-on-glass, hardens it and improves the surface smoothness. This also provides an electrical insulation between subsequently deposited top layers and the bottom electrode, as indicated in Fig. 7.1. In the following step, we deposit the top An electrode layer with a Ti adhesive layer by evaporation. Using an additional Cr layer as a hard mask, we define circular cavities of $r = 3$ μm in radius and $x_c = 220$ nm in depth by e-beam lithography and reactive ion etching through the SOG. This exposes the circular bottom An electrode of $r_g = 2.5$ μm in radius on the bottom of the cavity. The chip fabrication is also described in detail in the previous work [97].

7.1.2. LASER INTERFEROMETRY OF FePS$_3$ RESONATORS

We transfer a flake of few-layer FePS$_3$ exfoliated from a synthetically grown bulk crystal [67] over these cavities by a dry transfer technique [112] to create two separated circular membranes of the same flake as depicted in Fig. 7.1a-c. As shown in Fig. 7.1b, we

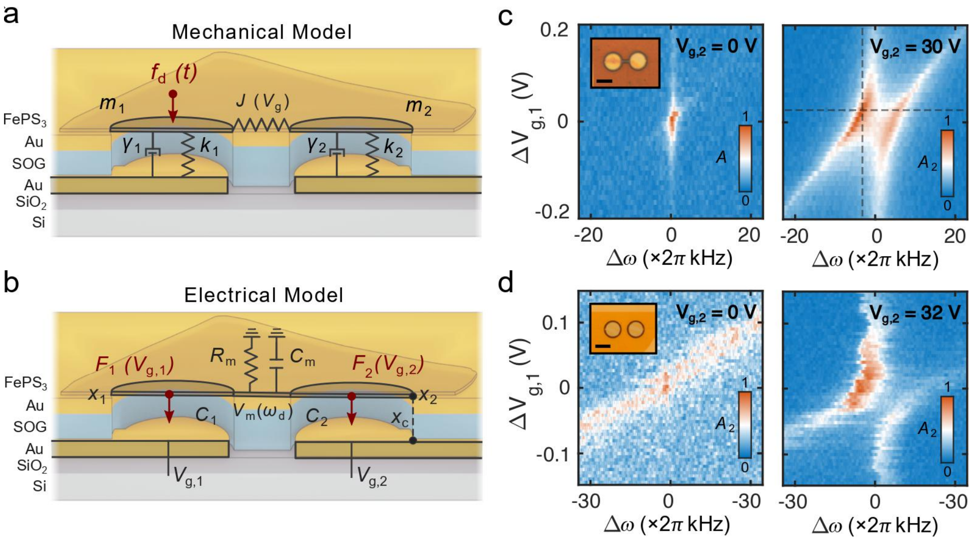

Figure 7.2: Strong coupling of spatially separated FePS$_3$ membrane resonators. Schematics of coupled membrane oscillators: **a** Mechanical model: $m_{1,2}$ is the effective mass, $k_{1,2}$ the effective stiffness, and $J(V_g)$ the gate voltage dependent coupling parameter. **b** Electrical model: $C_{1,2}$ is the capacitance of each drum towards the gate electrode that is kept at a voltage V_g, R_m the resistance to ground, C_m the capacitance to ground, and $V_m(\omega_d)$ the voltage between the membranes. **c** Sample with a suspended channel between the drums. Left panel: Weak coupling of motion between spatially separated drums at $V_{g,1}$ = 36.9 V and $V_{g,2}$ = 0 V and $\Delta\omega = \omega_d - \omega_2$. Inset: Optical image of the sample. Thickness: 25.6±0.4 nm. Scale bar: 6 μm. Right panel: Strong coupling of motion between spatially separated drums at $V_{g,1}$ = 37.2 V and $V_{g,2}$ = 30 V. **d** Sample without a suspended channel between the drums (see Appendix A7). Left panel: Weak coupling of motion at $V_{g,1}$ = 32.4 V and $V_{g,2}$ = 0 V. Inset: Optical image of the sample. Thickness: 14.5 ± 0.3 nm. Scale bar: 6 μm. Right panel: Strong coupling of motion at $V_{g,1}$ = 34.5 V and $V_{g,2}$ = 32 V.

focus red and blue lasers on these drums to excite the motion of one and measure the displacement of the other using a laser interferometry technique, thus probing the coupling between fundamental vibration modes of these membranes. To realize the study as a function of gate voltage and corresponding electrostatically induced strain for both drums, we use local electrodes that allow us to individually adjust the gate voltage, V_g, for each of the resonators (see Fig. 7.1c). The single FePS$_3$ flake, out of which the resonators are formed, is contacted via a top metal electrode to ground. A false-coloured scanning electron microscopy (SEM) image in Fig. 7.1a shows a 25.6 ± 0.4 nm FePS$_3$ flake suspended over the electrodes forming two separated membrane resonators. The resonators are placed in a closed-cycle cryostat with optical access that is connected to a laser interferometry setup, as shown in Fig. 7.1d.

When operating the laser interferomery technique with both lasers focused at the same position on the same membrane, we independently characterize the resonance spectra of the fundamental membrane modes of drums 1 and 2 at a temperature of 4 K as shown in Fig. 7.1e. We fit these spectra to a harmonic oscillator model and extract the resonance frequencies $\omega_{1,2}$ as a function of V_g, which are displayed with filled blue and orange dots in Fig. 7.1f. The resonances $\omega_{1,2}(V_g)$ of both drums closely follow the continuum mechanics model [143, 145], as shown by the solid blue and orange lines in Fig. 7.1f (see Appendix A1). At certain values of $V_{g,1}$ and $V_{g,2}$, the frequencies ω_1 and ω_2 of the corresponding resonance peaks match at $\omega_1 = \omega_2$, as indicated by the light blue region in Fig. 7.1f. In this regime we can expect an avoided frequency crossing if the exchange of the excitation energy between the drums is sufficiently large and the drums are strongly coupled [70]. The coupling strength is also related to the dissipation $\frac{1}{Q_{1,2}}$ of the resonators involved [238, 242]. Hence, we plot the corresponding mechanical energy dissipation rates $\gamma_{1,2} = \frac{\omega_{1,2}}{Q_{1,2}}$ of the FePS$_3$ membranes in Fig. 7.1g. Measured $\gamma_{1,2}(V_g)$ follow a parabolic behavior, in accordance with a Joule dissipation model (solid blue and orange lines, see Appendix A2), which can be attributed to capacitive displacement currents in the suspended region of the flake [128, 140, 247].

7.1.3. ELECTROMECHANICAL COUPLING MODEL

The mechanical behavior of coupled membrane resonators can be modeled by two coupled resonators, schematically depicted in Fig. 7.2a. The motion of coupled resonators is described by:

$$\begin{cases} \ddot{x}_1 + \gamma_1 \dot{x}_1 + \omega_1^2 x_1 = j x_2 + f_d \cos \omega_d t \\ \ddot{x}_2 + \gamma_2 \dot{x}_2 + \omega_2^2 x_2 = j x_1 \end{cases}, \tag{7.1}$$

where $x_{1,2}$ are the membrane displacements and f_d is the force at a drive frequency ω_d. The coupling parameter $j = \frac{J}{\sqrt{m_1 m_2}}$, where $m_{1,2}$ is the effective mass, is responsible for the transfer of energy between the two resonators and thus coupling of the mechanical motion. Several coupling mechanisms can contribute to J (see Appendix A3). In this work, we present evidence for an electromechanical coupling mechanism for adjusting the coupling strength between two 2D material resonators.

Figure 7.2b shows the schematic of the electrical circuit that mediates the coupling (see Appendix A4). The suspended part of the thin FePS$_3$ flake, that covers the two cavities, is both resistively and capacitively connected to ground via the interface between the flake and the Au top electrode. We assume that the voltage $V_{m,DC}$ that is established between drum 1 to drum 2 is zero since the Au top electrode effectively shunts potential differences between the drums. However, since the capacitance C_m between the FePS$_3$ flake and Au top electrode is large, it dominates the electrical coupling of the flake to ground ($\frac{1}{\omega_d C_m} \ll R_m$, where R_m is the resistance to ground). As is outlined in Appendix A4, the optothermal drive of the first drum at non-zero $V_{g,1}$ then results in a non-zero flake voltage $V_{m,AC}$ that causes an electrostatic force on the second drum, $F_{2,AC} = -J_{el} x_{10} \sin(\omega_d t)$, where x_{10} is the amplitude of periodic displacement and the electrical coupling parameter J_{el} is given by:

$$J_{el} \cong \frac{\left(\varepsilon_0 \pi r_g^2\right)^2}{C_m} \frac{V_{g,1} V_{g,2}}{(x_c - x_{g,1})^2 (x_c - x_{g,2})^2}, \tag{7.2}$$

where ε_0 is the dielectric permitivity of vacuum, $x_g(V_g)$ the static deflection at the centre of membrane (see Appendix A1) and x_c the separation between the membrane and the bottom electrode. By combining equations 7.1 and 7.2, it is seen that J_{el} results in a transfer of mechanical energy via electromechanical coupling between the spatially separated

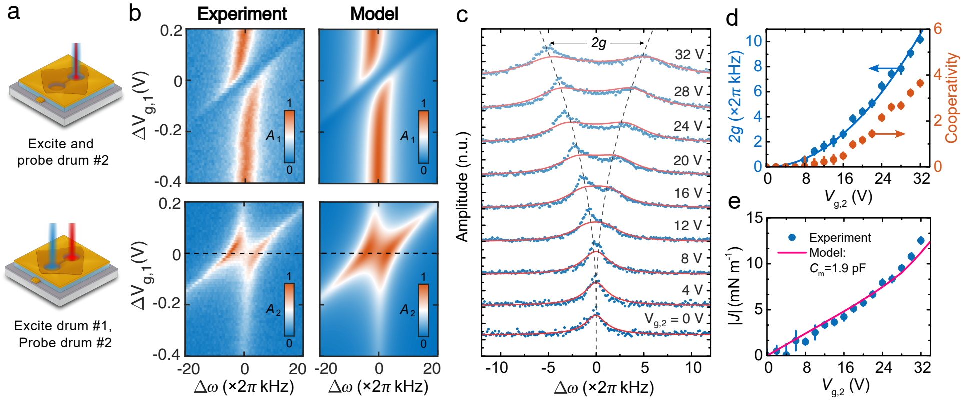

Figure 7.3: Comparison between the coupled oscillators model and experiments. **a** Schematic indication of the position of lasers for each row of data in **b**. **b** Measured normalized amplitudes $A_{1,2}$ of the resonance peaks at $V_{g,1} = 37.2$ V and $V_{g,2} = 30$ V compared with the model of Eq. 7.1 and Eq. 7.2 (see Appendix A1-4). Dashed horizontal line examples the extraction of data shown in **c** at $\Delta\omega = \omega_d - \omega_2$. **c** Amplitude A_2 of the resonance peak splitting of drum 2 at different $V_{g,2}$. Filled blue dots - measured data. Solid red lines - fit to the model of Eq. 7.3. Dashed black line - positions of peak maxima used to extract $2g$. **d** Splitting $2g$ and cooperativity plotted against V_g. Filled blue dots - measured $2g$ obtained from **c**. Solid blue line - fit to a parabola used as a guide to the eye. Filled orange dots - cooperativity calculated from $2g$ and corresponding $\gamma_{1,2}$ from Fig. 7.1g. **e** Measured and modeled coupling constant $J(V_g)$. Filled blue dots - J extracted from the fit in **c**. Solid magenta line - comparison to the model of Eq. 7.2. Error bars in **d** and **e** are indicated with vertical colored lines.

FePS$_3$ drums. It is notable that the driving force on the second drum $F_{2,\mathrm{AC}}$ is proportional to the product of the individual gate voltages applied to each of the drums. This means that at $V_g = 0$ V on either drum, the electrical coupling parameter $J_{\mathrm{el}} = 0$ even if $\omega_1 = \omega_2$ and $f_d > 0$. This property distinguishes the expected behavior of this mechanism from phonon- or tension-mediated coupling [242, 244–246], where frequency matching and a non-zero driving force acting on one of the drums are sufficient conditions for coupling and thus splitting of the resonance frequency to occur.

We use this characteristic to provide evidence for the proposed mechanism, by first matching the resonance frequencies of the drums by tuning $\omega_{1,2}$ such that $\omega_1 = \omega_2$ using electrostatic pulling, as shown in Fig. 7.1f. Then we alter $V_{g,1}$ of the drum that we drive with the modulated blue laser, while measuring the amplitude of motion of the other drum that is probed with the red laser at a constant $V_{g,2}$. Figure 7.2c shows the resonance peak splitting for different V_g applied to both membranes. Two distinct regimes are visible: one that corresponds to weak coupling at $V_{g,2} = 0$ V (and $J_{\mathrm{el}} = 0$) and the other to strong coupling with the avoided frequency crossing visible at $V_{g,2} = 30$ V (and $J_{\mathrm{el}} \neq 0$). We did not observe any change to the avoided crossing related to the change of laser intensity or its modulation amplitude (see Appendix A5). Also, resonance peaks disappear when the blue laser drive is focused on the unsuspended region of FePS$_3$ (see Appendix A6). These observations show that neither a periodic heating from the laser beam, nor other parasitic electrical actuation mechanisms are responsible for the transfer of mechanical energy and strong coupling between the drums. Moreover, we observed the same behaviour in a test sample without a suspended channel connecting the two membranes, as shown in Fig. 7.2d (see Appendix A7), thus providing additional evidence ruling out the possibility of strong tension-mediated direct mechanical coupling. We note that the non-zero amplitudes in weak coupling regime at $V_{g,2} = 0$ V in both Fig. 7.2c and d indicate the presence of some other, much less pronounced, mechanisms of weak coupling (see Appendix A3). However, the evidence above suggests that the contribution of these mechanisms, that can couple the motion of two spatially separated FePS$_3$ resonators under our experimental conditions, is negligible in comparison to the dominant mechanism that we propose in Fig. 7.2b and Eq. 7.2 with $J \approx J_{\mathrm{el}}$.

7.1.4. STRONG COUPLING BETWEEN SPATIALLY SEPARATED NANODRUMS

Using the setup described above, we focus red and blue laser either on separate drums to excite one membrane and measure the motion of the other, or on the same drum to excite and measure a single one (see Fig. 7.3a). We apply corresponding V_g to the drums in order to match their $\omega_{1,2}$ and measure the avoided crossing of the resonance frequencies in both configurations of lasers. By solving Eq. 7.1, we find amplitudes for the two configurations of lasers as [248]:

$$\begin{aligned} A_1 &= \frac{f_{\mathrm{d}}}{\gamma_1\omega_{\mathrm{d}}}\frac{\sqrt{\delta_2^2+1}}{\triangle}, \\ A_2 &= \frac{f_{\mathrm{d}}}{\gamma_1\gamma_2\omega_{\mathrm{d}}^2}\frac{|j|}{\triangle}, \end{aligned} \tag{7.3}$$

where A_1 is the oscillation amplitude with lasers on the same drum, A_2 the amplitude with lasers on different drums, $\triangle = \sqrt{(\Lambda+1-\delta_1\delta_2)^2+(\delta_1+\delta_2)^2}$, $\Lambda = \frac{j^2}{\gamma_1\gamma_2\omega_{\mathrm{d}}^2}$ the coupling strength coefficient, and $\delta_{1,2} = \frac{\omega_{1,2}^2-\omega_{\mathrm{d}}^2}{\gamma_{1,2}\omega_{\mathrm{d}}}$ the detuning. In Fig. 7.3b the measured amplitudes $A_{1,2}$ at $V_{g,2} = 30$ V are compared to simulations based on the continuum mechanics model (see Appendix A1) as well as Eq. 7.1 and 7.2. The model is in good agreement with the experimental data (see Appendix A1-4).

We now investigate the gate voltage dependence of strong coupling between the separated FePS$_3$ membrane resonators. In Fig. 7.3c we show the resonance peak splitting $2g$ with increasing $V_{g,2}$. We extract $2g$ from peak maxima of the measured data in Fig. 7.3c, which we plot together with the cooperativity calculated [242, 245] as $\frac{(2g)^2}{\gamma_1\gamma_2}$. A strong coupling regime and an avoided crossing is reached when the figure of merit of the coupling, the cooperativity, is above 1, which is achieved for $V_{g,2} > 16$ V. We also fit A_2 of the same data set in Fig. 7.3c to Eq. 7.3 to extract j. Figure 7.3e displays the measured coupling constant $J(V_g)$ (filled blue dots), compared to the electrical coupling model of Eq. 7.2 (solid magenta line). The model follows the experiment closely for $C_m = 1.9$ pF, reproducing both the quasi-linear part of the data at $V_{g,2} < 24$ V and the nonlinear part at $V_{g,2} > 24$ V that appears due to the deflection of the membrane x_g at larger V_g.

7.1.5. AMPLITUDE MODULATED TRANSMISSION OF INFORMATION

In the strong coupling regime the excitation energy is transferred between the resonators. In Fig. 7.4 we demonstrate that this channel of energy exchange can be amplitude-modulated to transfer binary data from one drum to another. We lock the gate voltage V_g of both drums and lock the excitation frequency at ω_d as indicated with dashed lines in Fig. 7.2c.

Then, we modulate the drive power of the blue laser between 2.5 and 5 dBm with a step function, and thus the amplitude of excitation force f_d of drum 1, while measuring the motion of drum 2 using the red laser. The peak value in the measured spectral density corresponds to resonant motion of drum 2 at the excitation frequency ω_d as shown in Fig. 7.4a. The lower maximum of measured spectral peak density corresponds to a bit with a value 0, while the larger maximum to 1. Using this approach, we send a binary image to drum 1 and read it out on drum 2. The result is plotted in Fig. 7.4b as a map of the maximum spectral density of the detected resonance peak on drum 2. The received picture is clearly distinguishable with no bits lost during the transfer.

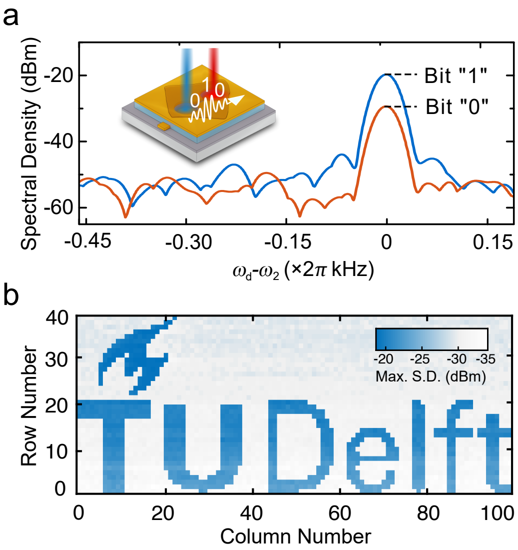

Figure 7.4: Information transfer between drums. **a** Measured spectral density near ω_2 at 0 and 1 bit of amplitude modulated excitation. Inset: schematics of the experiment. **b** Map of the maximum of the spectral density showing a binary picture that was sent to drum 1 and received at drum 2 at a bit rate of 4 bit/s.

7.1.6. COUPLING NEAR THE ANTIFERROMAGNETIC NÉEL TEMPERATURE

$FePS_3$ is an antiferromagnetic semiconductor at low temperature [249, 250] with a Néel temperature $T_N \sim 114$ K [45, 227], where it exhibits a phase transition to a paramagnetic phase. The phase change in $FePS_3$ is accompanied by a large anomaly in the thermal expansion coefficient that produces an accumulation of substantial tensile strain in the membrane [67] as it is cooled down from room temperature to 4 K. As a consequence, at cryogenic temperatures membranes of $FePS_3$, even tens of nanometers thick [67], have large quality factors of $2-6\times10^4$ that are comparable to high-Q membranes made of strained monolayers of WSe_2 and $MoSe_2$ [140]. In earlier works it was shown that the mechanical resonances of magnetic membranes can be sensitive to both the magnetic phase [67] and the magnetisation of that phase [57]. Therefore, when strongly coupled, small differences in magnetization can result in large differences in the resonance frequencies and the mechanical damping of the membranes and thus the coupling strength, making such coupled resonators very sensitive to small changes in the magnetic state of the material.

In Fig. 7.5a-e, we study a sample of $FePS_3$ to assess the temperature dependence of the coupling strength near the T_N. Following the experimental organisation and analysis from above, we fix $V_{g,2}$ of the drum 2 at 29 V and measure the resonance frequency, coupling parameter and cooperativity as a function of temperature. As shown in Fig. 7.5b, when the sample is heated up from 4 to 135 K, $\omega_{1,2}$ soften near the T_N of 107 K. This also appears as a characteristic peak in $\frac{\mathrm{d}(f_0^2)}{\mathrm{d}T} = \frac{1}{4\pi^2}\frac{\mathrm{d}(\omega_2^2)}{\mathrm{d}T}$ in Fig. 7.5d and originates from the anomaly in the specific heat of the material at T_N [67, 227]. Interestingly, with the temperature approaching T_N, the splitting of the resonance peak disappears, as shown in Fig. 7.5c. However, as follows from Eq. 7.2, J_{el} is not expected to have a strong temperature dependence or abrupt drop to zero near T_N, which is also notable from Fig. 7.5d, where we plot the experimentally obtained $J(T)$. Instead, this switch from strong to weak coupling regime is related to a continuous decrease of the cooperativity due to an increasing $\gamma_{1,2}$ as it approaches the transition temperature, as shown in Fig. 7.5e. This behavior of $\gamma_{1,2}(T)$ can be attributed to the increasing contribution of thermoelastic dissipation to the nanomechanical motion of drums near phase transitions [67].

To support the hypothesis that the temperature dependent spectral changes are related to the temperature dependence of the dissipative terms in the equation of motion, we fabricated a sample of $MnPS_3$ that exhibits the antiferromagnetic to paramagnetic phase transition at $T_N \sim 78$ K [227]. In Fig. 7.5f-j, we show the experimental data for $MnPS_3$ that revealed a behavior similar to $FePS_3$. As shown in Fig. 7.5g, ω_2 softens near $T = 77$ K which is close to T_N. We observe the splitting disappearing next to 75 ± 10 K, as displayed in Fig. 7.5h. As expected, J does not show any systematic change near T_N, which is depicted in Fig. 7.5i. However, in Fig. 7.5j the cooperativity has a sharper drop in value as the sample goes from strong to weak coupling regime with increasing temperature. This coincides with a broad kink in $\gamma_{1,2}$ that is visible near T_N of $MnPS_3$, providing evidence for the hypothesis.

7.2. CONCLUSIONS

In conclusion, we have demonstrated a mechanism that mediates strong coupling between spatially separated membranes made of antiferromagnetic materials $FePS_3$ and $MnPS_3$. This coupling mechanism can be switched on and tuned by an electrostatic gate. In addition, the electromechanical transfer of energy can be amplitude modulated and is shown to be capable of performing bit-by-bit communication. This provides control advantages that can find the use in the development of new device concepts, such as nanomechanical logic gates [74–76] and hybrid systems combining magnetic mechanical oscillators and qubits [99]. We have further shown that the magneto-mechanical properties of antiferromagnetic materials also can affect the coupling strength and cooperativity between the membranes next to the phase transition. For example, we have shown that the increasing mechanical dissipation [67] near T_N of $FePS_3$ and $MnPS_3$ diminishes the cooperativity of such coupled membrane systems as T approaches T_N. Therefore, coupled NEMS made of magnetic membrane resonators can provide a deeper

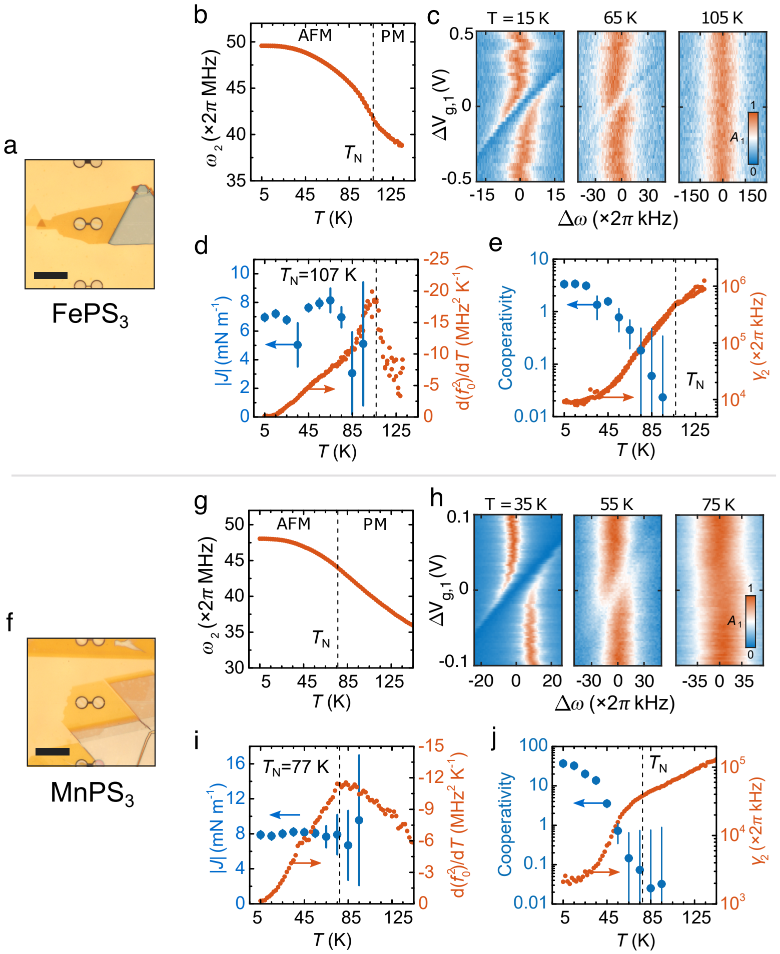

Figure 7.5: Temperature dependence of the coupling between antiferromagnetic membranes. **a** Optical image of the FePS$_3$ sample. Thickness: 13.9 ± 0.3 nm. Scale bar: 18 μm. **b** Resonance frequency ω_2 of the FePS$_3$ drum as a function of temperature. **c** Normalized amplitude A_1 of the resonance peak splitting at $\Delta\omega = \omega_d - \omega_2$ plotted for three different temperatures. **d** Filled blue dots - measured coupling constant J. Filled orange dots - $\frac{\mathrm{d}(f_0^2)}{\mathrm{d}T}$ of the data in **b**. **e** Filled blue dots - cooperativity, filled orange dots - dissipation rate γ_2. The bottom panel **f-j** follows the same structure as the top panel **a-e** with the data shown for a MnPS$_3$ sample. **f** Optical image of the MnPS$_3$ sample. Thickness: 10.5 ± 0.4 nm. Scale bar: 18 μm. Vertical dashed lines in all panels indicate the detected T_N. Error bars in **d**, **e**, **i** and **j** are indicated with vertical blue lines.

insight into coupling of magnetic properties to the nanomechanical motion. We also anticipate that in the future antiferromagnetic NEMS of this type can be useful to study more intricate magnetic phenomena, like a magnetostriction in ultrathin layers [57], and the emission of spin currents by mechanical deformations - the piezospintronic effect [251].

7.3. APPENDIX

A1: CONTINUUM MECHANICS MODEL OF THE CIRCULAR MEMBRANE RESONATORS OF FePS3

A flake, which is suspended over a circular cavity with a bottom gate electrode underneath, forms a capacitor-like structure. The mechanical response of the drum can be altered by applying a gate voltage. The change in the gate potential causes the flake to deflect, thereby producing a shift in the resonance frequency [143], as described in Chapter 3. This method is used to tune the resonance frequency of the oscillators such that the frequency matching condition $\omega_1 = \omega_2$ and the avoided crossing are established.

The spring constant k of the membrane is given by (see Chapter 3):

$$k = \frac{2\pi E h \epsilon_0}{1-\nu^2} + \frac{8\pi E h}{\left(1-\nu^2\right) r^2} x_{\mathrm{g}}^2 - \frac{1}{2} C_{\mathrm{g}}'' V_{\mathrm{g}}^2, \tag{7.4}$$

where $C_{\mathrm{g}}'' = \frac{\partial^2 C_{\mathrm{g}}}{\partial x^2}$ and x_{g} the maximal deflection at the membrane centre. The electrostatic deflection is approximated [145] as:

$$x_{\mathrm{g}} \approx \frac{\varepsilon_0 r_{\mathrm{g}}^2}{8 x_{\mathrm{c}}^2 T} V_{\mathrm{g}}^2, \tag{7.5}$$

where $x_{\mathrm{c}} = 220$ nm is the cavity gap size, $r_{\mathrm{g}} = 2.5$ μm the radius of the bottom gate electrode, and $T = Eh\frac{\epsilon}{1-\nu}$ the membrane tension. Using eq. 7.4, we find the resonance frequency of the fundamental vibration mode of the drum, ω_0, by including both membrane and plate contributions [37]:

$$\omega_0 \approx \sqrt{\omega_{\mathrm{membrane}}^2 + \omega_{\mathrm{plate}}^2} = \sqrt{\frac{k}{m_{1,2}} + \left(\frac{10.21 h}{2r^2}\right)^2 \frac{E}{3\rho(1-\nu^2)}}, \tag{7.6}$$

where $m_{1,2}$ is the effective mass and $\rho = 3375$ kg/m^3 the mass density of FePS$_3$.

We use a combination of Eq. 7.4, 7.5 and 7.6 to model $\omega(V_{\mathrm{g}})$ of both drums. As shown in Fig. 7.6, the model describes closely the experiment for both membranes. For drum 1, we used $\epsilon = 0.274\%$, which is within expected values [67] at $T = 4$ K, an effective mass of $m_1 = 620$ fg, which is close to the theoretical value of $m_{\mathrm{eff}} = 0.27\rho h \pi r^2 = 659.58$ fg, and $C_{\mathrm{g},1}'' = 2.66$ mF/m^2, which is slightly smaller than the estimate [128, 145] $C_{\mathrm{g}}'' \approx \frac{0.542\varepsilon_0 \pi r_{\mathrm{g}}^2}{x_{\mathrm{c}}^3} = 8.85$ mF/m^2. For drum 2, we used $\epsilon = 0.279\%$, an effective mass of $m_2 = 624.6$ fg, and $C_{\mathrm{g},2}'' = 2.6$ mF/m^2.

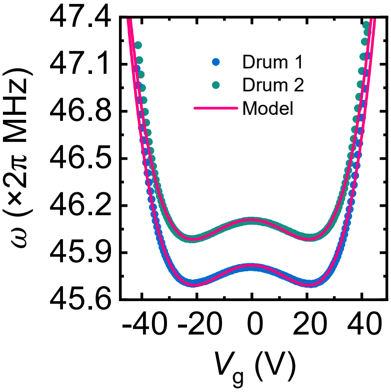

Figure 7.6: Frequency $\omega(V_g)$ of the resonance peaks for two drums (the same as in Fig. 7.1.) at 4 K. Filled dots - measured data, Solid lines - continuum mechanics model of Eq. 7.4, 7.5 and 7.6.

A2: JOULE DISSIPATION MODEL

An applied gate voltage, V_g, to the membrane can induce capacitive displacement currents due to the periodic change of capacitance induced by the mechanical motion [128, 247]. These currents consequently can decrease the quality factor via Joule dissipation [128]. We derive the equation for the Joule dissipation model for a circular membrane of $FePS_3$ closely following the approach from Ref. [128] and [247].

Membrane oscillations cause its periodic deflection and thus variations in the distance between the membrane and the gate electrode. This gives rise to a time-varying capacitance $C(t) = C_{eq} + \delta C \cos(\omega_d t)$, where C_{eq} is the geometrical capacitance at equilibrium position of the membrane, δC the capacitance oscillation amplitude, and ω_d the drive frequency of the membrane. The induced displacement currents, I_d, in the membrane generated by V_g and time- varying capacitance $C(t)$ are described by $I_d(V_g) = \omega_d V_g \delta C \sin(\omega_d t)$. Assuming that the effective resistance of $FePS_3$ membranes $R_{1,2}$ does not change significantly with V_g, the energy dissipated per period by the displacement current U_d is:

$$U_d(V_g) \approx R_{1,2} \int_0^{2\pi/\omega_d} I_d^2 \mathrm{d}t = \pi R_{1,2}\, \omega_d\, (\delta \mathrm{C})^2\, V_g^2. \tag{7.7}$$

The dissipation due to displacement currents is found as $\frac{1}{Q_d(V_g)} = \frac{U_d(V_g)}{2\pi U_t}$, where U_t is the total energy stored in the resonator. The total dissipation $\frac{1}{Q_{1,2}}$ is:

$$\frac{1}{Q_{1,2}} = \frac{1}{Q_0} + \frac{1}{Q_d(V_g)} = \frac{1}{Q_0} + \frac{R_{1,2}\,\omega_d}{2U_t} (\delta C)^2\, V_g^2. \tag{7.8}$$

Considering the corresponding mechanical energy dissipation rates $\gamma_{1,2} = \frac{\omega_{1,2}}{Q_{1,2}}$ of $FePS_3$ membranes at a resonance frequency $\omega_d = \omega_{1,2}$, Eq. 7.8 can be rewritten in terms of $\gamma_{1,2}$:

$$\gamma_{1,2} = \frac{\omega_{1,2}}{Q_0} + \frac{\omega_{1,2}}{Q_d(V_g)} = \gamma_0 + \frac{R_{1,2}\,\omega_{1,2}^2}{2U_t} (\delta C)^2\, V_g^2 = \gamma_0 + \frac{R_{1,2}}{m_{1,2}} \left(\frac{\partial C_g}{\partial x}\right)^2 V_g^2, \tag{7.9}$$

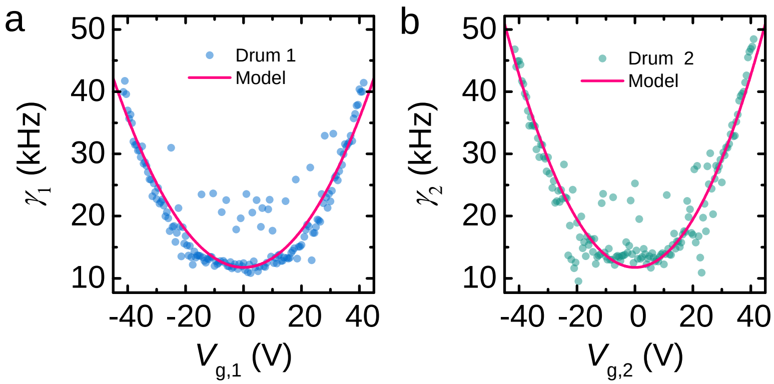

Figure 7.7: Dissipation rate $\gamma_{1,2}(V_g)$ of the resonance peaks for two drums (the same as in the main text Fig. 1.) at 4 K. **a,b** Filled dots - measured data, Solid lines - Joule dissipation model of Eq. 7.9.

where $\frac{\partial C_g}{\partial x} \approx \frac{\varepsilon_0 \pi r_g^2}{x_c^2}$. We use $m_{1,2}$ for each resonator from Appendix A1 and plot the model of Eq. 7.9 versus the measured $\gamma_{1,2}$. As shown in Fig. 7.7a, model describes the experiment well in case of drum 1 with $\gamma_0 = 11.76$ kHz and $R_1 = 721.4\ \Omega$. In Fig. 7.7b, the model is also shown for drum 2 following the experiment closely with $\gamma_0 = 11.75$ kHz and $R_2 = 937.1\ \Omega$.

A3: LINEAR COUPLED OSCILLATORS MODEL

In order to predict the measured response, we describe our system as a pair of damped resonators characterized with their effective masses m_1 and m_2 and corresponding positions $x_1(t)$, $x_2(t)$ (depicted in Figure 7.8). The derivation closely follows the one from Ref. [248]. The coupling potential between the oscillators is defined in a bi-linear form $V_{int} = -Jx_1x_2$, where J is the coupling parameter. In an experiment, multiple mechanisms can contribute to J, such that it is approximately equal to the sum of individual contributions:

$$J \approx J_{\text{mech}} + J_{\text{el}} + J_{\text{ph}} + J_{\text{other}}, \tag{7.10}$$

where J_{mech} is the direct mechanical contribution to coupling, J_{el} the electrical coupling parameter, J_{ph} is the coupling via a phonon bath in the material, and J_{other} accounts for other possible mechanisms of coupling. In our case, the electrical coupling parameter J_{el}, that is related to the capacitive ground between the flake and the top electrode as will be described in Appendix A4, is $J_{\text{el}} \gg J_{\text{mech}}, J_{\text{ph}}, J_{\text{other}}$ and acts as the dominant coupling mechanism, so $J \approx J_{\text{el}}$.

Let us assume that an external force of amplitude F and drive frequency ω_d is applied to one of the resonators resulting in motion that is described as:

$$\begin{cases} m_1\ddot{x}_1 + \Gamma_1\dot{x}_1 + k_1x_1 = Jx_2 + F\cos\omega_d t, \\ m_2\ddot{x}_2 + \Gamma_2\dot{x}_2 + k_2x_2 = Jx_1, \end{cases} \tag{7.11}$$

where $\Gamma_{1,2}$ is the damping coefficient, $k_{1,2}$ the stiffness of the corresponding oscillator.

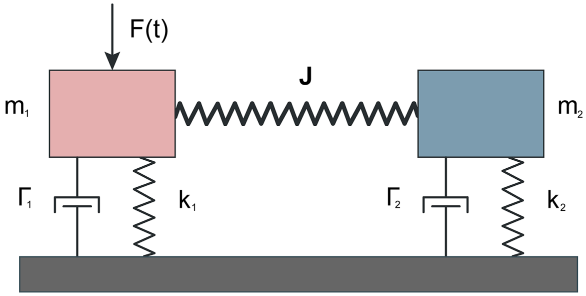

Figure 7.8: Schematic drawing of two linearly coupled damped resonators. $\Gamma_{1,2}$ is the damping parameter, $F(t)$ the driving force, $k_{1,2}$ the spring constant.

The same equation can be presented in a different form:

$$\begin{cases} \ddot{x}_1 + \gamma_1 \dot{x}_1 + \omega_1^2 x_1 = \frac{J}{m_1} x_2 + f_\mathrm{d} \cos \omega_\mathrm{d} t, \\ \ddot{x}_2 + \gamma_2 \dot{x}_2 + \omega_2^2 x_2 = \frac{J}{m_2} x_1, \end{cases} \tag{7.12}$$

where $\gamma_{1,2}$ is the dissipation ratio, $\omega_{1,2} = \sqrt{\frac{k_{1,2}}{m_{1,2}}}$ the natural frequency, and $f_\mathrm{d} = F/m_1$ the re-scaled force. When two resonators are of a similar effective mass $m_1 \approx m_2$, the coupling coefficient J can be expressed as $j = \frac{J}{\sqrt{m_1 m_2}} \approx \frac{J}{m_{1,2}}$, which further simplifies the equation to:

$$\begin{cases} \ddot{x}_1 + \gamma_1 \dot{x}_1 + \omega_1^2 x_1 = j x_2 + f_\mathrm{d} \cos \Omega t, \\ \ddot{x}_2 + \gamma_2 \dot{x}_2 + \omega_2^2 x_2 = j x_1. \end{cases} \tag{7.13}$$

At some point in time, the system of Eq. 7.13 attains a steady-state motion with two resonators developing synchronized motion at a drive frequency ω_d. This stationary state can be described by:

$$\begin{cases} x_1(t) = A_1 \cos(\omega_\mathrm{d} t + \phi_1) = \mathrm{Re}[A_1 e^{i(\omega_\mathrm{d} t + \phi_1)}], \\ x_2(t) = A_2 \cos(\omega_\mathrm{d} t + \phi_2) = \mathrm{Re}[A_2 e^{i(\omega_\mathrm{d} t + \phi_2)}]. \end{cases} \tag{7.14}$$

We now introduce non-dimensional rescaled detuning $\delta_{1,2} = \frac{\omega_{1,2}^2 - \omega_\mathrm{d}^2}{\gamma_{1,2}\, \omega_\mathrm{d}}$ which captures the difference between the driving frequency ω_d and natural frequencies $\omega_{1,2}$ of corresponding resonators. With this substitution, $x_{1,2}(t)$ is a solution [248] to Eq. 7.13 if amplitudes $A_{1,2}$ are equal to:

$$\begin{cases} A_1 = \frac{f_\mathrm{d}}{\gamma_1 \omega_\mathrm{d}} \frac{\sqrt{\delta_2^2 + 1}}{\triangle}, \\ A_2 = \frac{f_\mathrm{d}}{\gamma_1 \gamma_2 \omega_\mathrm{d}^2} \frac{|j|}{\triangle}, \end{cases} \tag{7.15}$$

where $\triangle = \sqrt{(\Lambda + 1 - \delta_1 \delta_2)^2 + (\delta_1 + \delta_2)^2}$, and $\Lambda = \frac{j^2}{\gamma_1 \gamma_2 \omega_\mathrm{d}^2}$ the coupling strength coefficient. Due to the symmetry between equations in Eq. 7.13, A_1 describes the amplitude of the driven resonator and A_2 the amplitude of the non-driven one. In Fig. 7.9 we show an example of a fit of the measured data at 4 K, $V_{\mathrm{g},1} = 37.21$ V and $V_{\mathrm{g},2} = 30$ V to the model

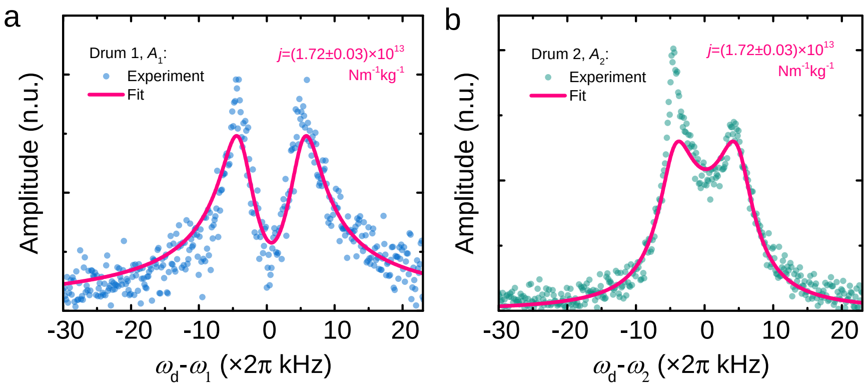

Figure 7.9: Amplitudes of a resonance frequency splitting $A_{1,2}$ for two drums (the same as in the main text Fig. 1 and 3.) at 4 K. **a,b** Filled dots - measured data, Solid lines - fit to the coupled oscillators model of Eq. 7.15.

of Eq. 7.15. We use $\gamma_{1,2}(V_\mathrm{g})$ and $\omega_{1,2}(V_\mathrm{g})$ from the data in Fig. 1f,g and leave f_d and j as fitting parameters. We fit to measured amplitudes normalised as $\frac{A_{1,2}}{\max[A_{1,2}]}$, so only the fit value of j has a physical meaning. The model of Eq. 7.15 describes the experiment well for $j = 1.72 \times 10^{13}$ Nm^{-1}kg^{-1} with only a small amplitude excess in A_2 which likely originates from some higher-order nonlinear effect.

A4: ELECTROMECHANICAL COUPLING MODEL

Suspended parts of a flake act as circular membrane capacitors $C_{1,2}$ together with the bottom gate electrodes of radius r_g. The unsuspended region of the flake is situated on top of the grounded gold electrode. Ideally, if the material would be a good conductor, the DC resistance to grounded metal, R_m, should drain all currents that are induced as a result of the motion. However, in the case of a poorly conducting material like $FePS_3$ and $MnPS_3$, the capacitance between flake and metal electrode can dominate the AC electrical coupling to ground, which mediates an electromechanical coupling between the membranes. We model this electrical coupling mechanism for $FePS_3$ and $MnPS_3$ by considering electrical equivalent DC and AC circuits of the membrane system, as shown in Fig. 7.10a. In doing so, we assume that the contact between the top gold electrode and the flake is ohmic for DC signals, such that the DC voltage established on the flake is $V_\mathrm{m,DC} \approx 0$ V, as shown in Fig. 7.10b. However, for the AC circuit shown in Fig. 7.10c, for which the AC impedance $\frac{1}{\omega_\mathrm{d} C_\mathrm{m}}$ is significantly lower than R_m, C_m acts as a capacitive coupling element and produces an equivalent of a capacitive divider for the AC signal, that results in a time dependent voltage across both flakes (Fig. 7.10c).

As shown in Fig. 7.10, the time-varying capacitance $C_1(t)$ of the drum 1 and its time-

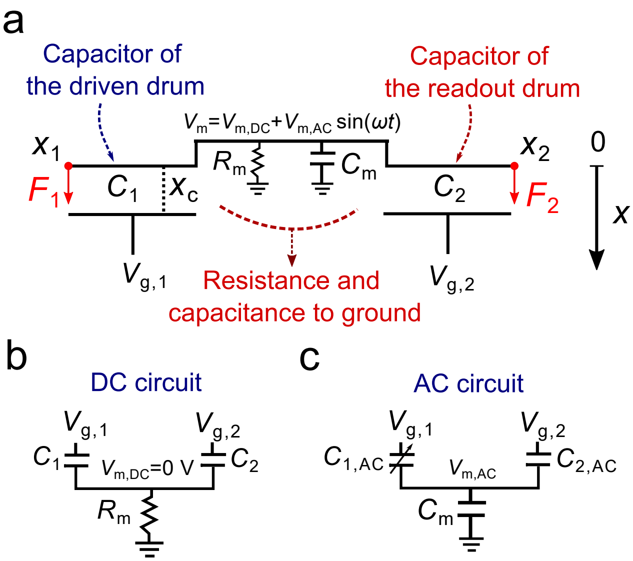

Figure 7.10: Schematic drawing of equivalent electrical circuit of two membrane capacitors. V_m is the voltage established between the membranes, R_m and C_m, respectively, the resistance and capacitance between the ground electrode and the suspended flake, $F_{1,2}$ the force acting on the membrane, $C_{1,2}$ the capacitance between the membrane and bottom gate electrode separated by cavity distance x_c.

dependent term $C_{1,\mathrm{AC}}(t)$ can be written as:

$$C_1(t) = \frac{\varepsilon_0 \pi r_\mathrm{g}^2}{x_\mathrm{c} - x_1(t)} \approx \frac{\varepsilon_0 \pi r_\mathrm{g}^2}{x_\mathrm{c}} \left(1 + \frac{x_1(t)}{x_\mathrm{c}}\right), \tag{7.16}$$

$$C_{1,\mathrm{AC}}(t) = \frac{\varepsilon_0 \pi r_\mathrm{g}^2}{x_\mathrm{c}^2} x_{10} \sin(\omega_\mathrm{d} t), \tag{7.17}$$

where x_{10} is the periodic displacement amplitude. We now consider the AC voltage between the flake and ground, $V_{\mathrm{m,AC}}$ and write the charge conservation equation of the system in Fig. 7.10c in the following form:

$$-\left(V_{\mathrm{g},1} - V_{\mathrm{m,AC}}\right) C_{1,\mathrm{AC}}(t) + C_\mathrm{m} V_{\mathrm{m,AC}} = 0. \tag{7.18}$$

To further simplify the derivation of corresponding forces acting on membranes, we use $C_\mathrm{m} >> C_{1,2}$ and that $x_1 >> x_2$ when driving the drum 1. Then, from the Eq. 7.18, $V_{\mathrm{m,AC}}$ becomes:

$$V_{\mathrm{m,AC}}(t) = \frac{V_{\mathrm{g},1} C_{1,\mathrm{AC}}(t)}{C_{1,\mathrm{AC}}(t) + C_\mathrm{m}} \approx V_{\mathrm{g},1} \frac{C_{1,\mathrm{AC}}(t)}{C_\mathrm{m}} \approx \frac{V_{\mathrm{g},1}}{C_\mathrm{m}} \frac{\varepsilon_0 \pi r_\mathrm{g}^2}{x_\mathrm{c}^2} x_{10} \sin(\omega_\mathrm{d} t). \tag{7.19}$$

The voltage oscillation of $V_\mathrm{m}(\omega_\mathrm{d}, t)$ affects the potential between the membrane of drum 2 and its gate electrode and results in a oscillating force $F_2(t)$ acting on this membrane. This force can be described as:

$$F_2(t) = \frac{1}{2} \frac{\varepsilon_0 \pi r_\mathrm{g}^2}{(x_\mathrm{c} - x_2(t))^2} \left(V_{\mathrm{g},2} - V_{\mathrm{m,AC}}\right)^2. \tag{7.20}$$

Using that $V_{\mathrm{m,AC}} << V_{\mathrm{g},2}$ and $x_2 << x_{\mathrm{c}}$, this can be written as:

$$F_2(t) \approx \frac{1}{2}\frac{\varepsilon_0 \pi r_{\mathrm{g}}^2}{x_{\mathrm{c}}^2} V_{\mathrm{g},2}^2 - \frac{\varepsilon_0 \pi r_{\mathrm{g}}^2}{x_{\mathrm{c}}^2} V_{\mathrm{g},2} V_{\mathrm{m,AC}}(t). \tag{7.21}$$

By substituting $V_{\mathrm{m,AC}}$ from Eq. 7.19 and taking only the time-dependent part of the Eq. 7.21, the force $F_{2,\mathrm{AC}}$ that drives the readout drum at $V_{\mathrm{g}} < 0$ V is:

$$F_{2,\mathrm{AC}}(t) = -\frac{\epsilon_0 \pi r_{\mathrm{g}}^2}{x_{\mathrm{c}}^2} V_{\mathrm{g},2} V_{\mathrm{m,AC}}(t) \cong -\frac{\left(\epsilon_0 \pi r_{\mathrm{g}}^2\right)^2}{C_{\mathrm{m}}} \frac{V_{\mathrm{g},1} V_{\mathrm{g},2}}{x_{\mathrm{c}}^4} x_{10} \sin(\omega_{\mathrm{d}} t). \tag{7.22}$$

However, at large V_{g} the membrane deflects down due to the introduced electrostatic force (see Appendix A1). The solution that accounts for the exact deflection shape would be rather complex [143]. However, one can substitute x_{c} in Eq. 7.22 for corresponding $x_{\mathrm{c}} - x_{\mathrm{g}}(V_{\mathrm{g}})$ for each membrane, under the assumption that the central part of the membrane is what contributes the most to the resultant change in $F_{2,\mathrm{AC}}$ due to deflection. This results in the final equation for the electrostatic force on drum 2, $F_{2,\mathrm{AC}}$, that is caused by the motion of drum 1 and its effect on the flake voltage $V_{\mathrm{m,AC}}$:

$$F_{2,\mathrm{AC}}(t) \cong -\left[\frac{\left(\epsilon_0 \pi r_{\mathrm{g}}^2\right)^2}{C_{\mathrm{m}}} \frac{V_{\mathrm{g},1}\, V_{\mathrm{g},2}}{(x_{\mathrm{c}} - x_{\mathrm{g},1})^2 (x_{\mathrm{c}} - x_{\mathrm{g},2})^2}\right] x_{10} \sin(\omega_{\mathrm{d}} t) = -J_{\mathrm{el}} x_{10} \sin(\omega_{\mathrm{d}} t), \tag{7.23}$$

where J_{el} is the electrical coupling parameter from Eq. 7.10.

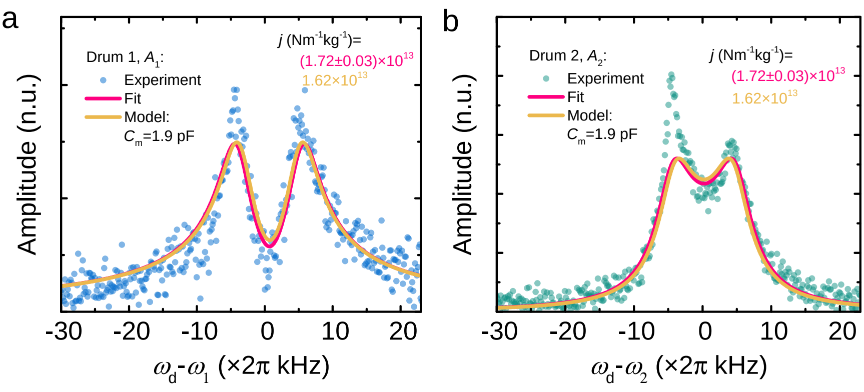

Figure 7.11: Normalized amplitudes of a resonance frequency splitting $A_{1,2}$ for two drums (the same as in the main text Fig. 7.1 and 7.3.) at 4 K. **a,b** Filled dots - measured data, Solid magenta lines - fit to the coupled oscillators model of Eq. 7.15 from Fig. 7.9, Solid orange lines - model of electrically coupled FePS$_3$ membranes described in Appendix A4 calculated using Eq. 7.15 and 7.23.

We now use Eq. 7.15 from Appendix A3, together with the coupling parameter $J \approx J_{\mathrm{el}}$ from Eq. 7.23 to calculate the amplitudes $A_{1,2}$ as a function of frequency, showing the resonance peak splitting. In Fig. 7.11 we plot the measured data at 4 K fitted with Eq. 7.15, together with the model of Eq. 7.15 and 7.23 for $V_{\mathrm{g},1} = 37.21$ V, $V_{\mathrm{g},2} = 30$ V and $C_{\mathrm{m}} = 1.9$ pF. We use $\gamma_{1,2}(V_{\mathrm{g}})$ and $\omega_{1,2}(V_{\mathrm{g}})$ from the data in Fig. 1f,g and leave f_{d} in Eq. 7.15 as scaling factor. The $j = \frac{J}{\sqrt{m_1 m_2}} = 1.62 \times 10^{13}$ Nm^{-1}kg^{-1}, that we calculate using Eq. 7.23, describes the experiment well and is quantitatively close to $j = 1.72 \times 10^{13}$ Nm^{-1}kg^{-1} that is extracted from the fit of the same experimental data to Eq. 7.15. This confirms that, even though quite simplified, our model explains the mechanism of strong coupling between distant membrane resonators.

A5: LASER INTENSITY AND DRIVING POWER DEPENDENCE

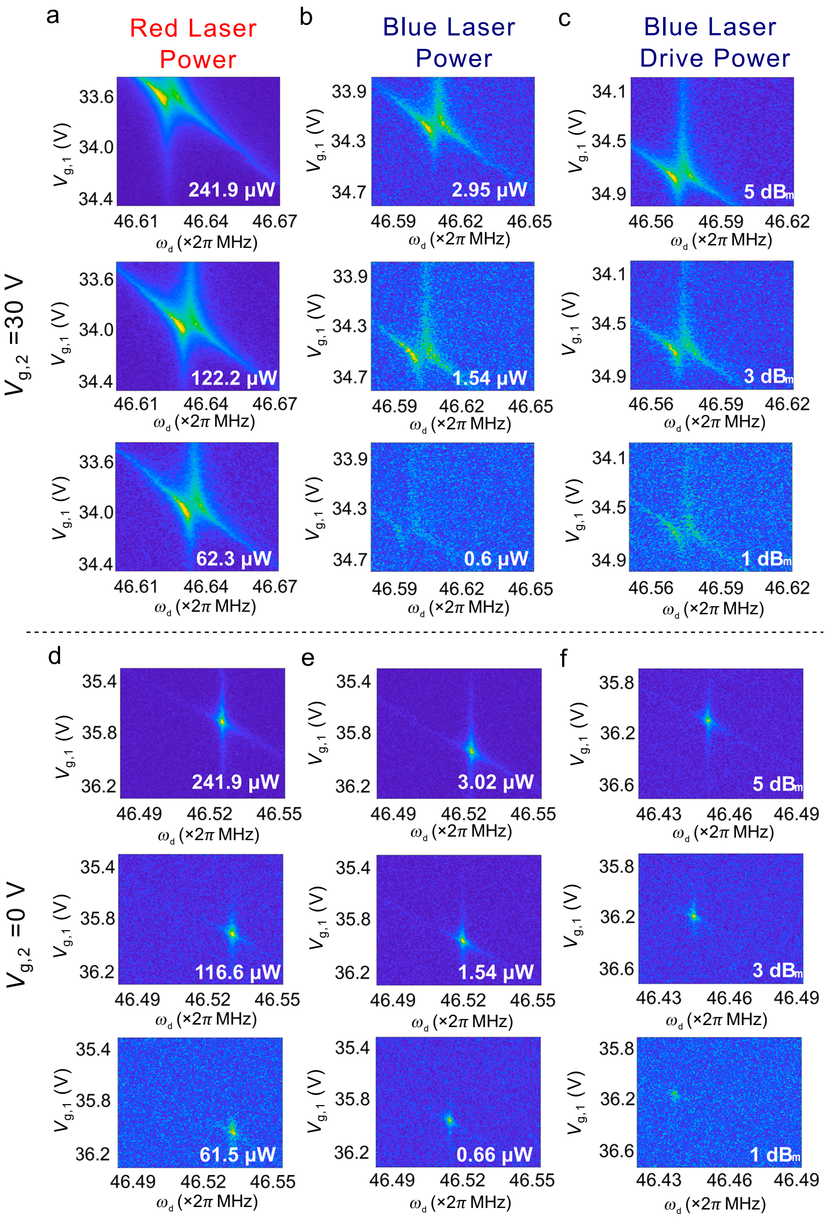

Figure 7.12: Normalized amplitudes of the resonance frequency splitting A_2 for different power and drive of lasers at $T = 4$ K. **a-c** Measured A_2 at $V_{g,2} = 30$ V. **d-f** Measured A_2 at $V_{g,2} = 0$ V. Respective laser power or drive power is labeled in all panels. **a**, **d**, **c** and **f** is measured at $P_{\text{blue}} \approx 1.5$ μW. **b**, **e**, **c** and **f** is measured at $P_{\text{red}} \approx 100$ μW. **a**, **b**, **d** and **e** is measured at $P_d \approx 5$ dBm. Within all figures of top and bottom panels no substantial change in the splitting $2g$ was observed.

A6: LASER POSITION DEPENDENCE

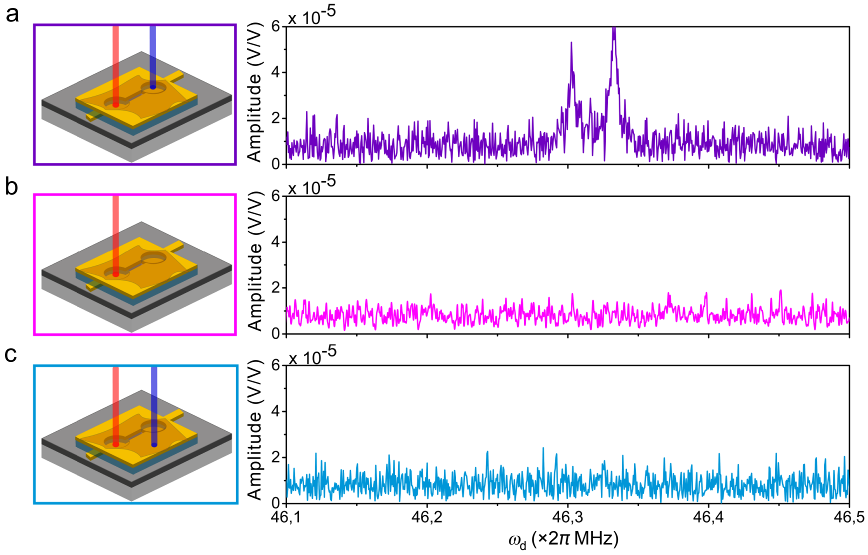

Figure 7.13: Measured amplitudes of the resonance frequency splitting A_2 at blue laser drive power P_d = 1 dBm and 4 K. Blue laser is optothermally actuating the motion of the drum which in turn through electrical coupling (described in Appendix A3 and 4) put the other drum in motion, that is probed by the red laser. **a-c** Left panels: Schematics of the laser position. Right panel: measured resonance peak splitting or its absence at respective laser position.

A7: TEST SAMPLE WITHOUT A MICRO-CHANNEL CONNECTING TWO SUSPENDED DRUMS

It is important to check the possible contribution of other tension-related coupling effects in our experiments. Also, an informative test is required for understanding if the ground capacitor C_m described in Appendix A4 is possibly formed because of the non-grounded part of the flake that is suspended over the channel connecting two circular membranes. To do so, we fabricate an additional test sample without this channel, now having a top ground electrode electrically grounding the area between suspended drums, mechanically supported as shown in Fig. 7.14a.

Following the methodology from Appendix A1 and the one described in the main text, we measure $\omega(V_\mathrm{g})$ for each membrane and plot it in Fig. 7.14b. Although ω_2 is notably larger than ω_1 at V_g = 0 V, we are able to match these frequencies to establish $\omega_1 = \omega_2$ condition with non-zero $V_{\mathrm{g},1}$ and $V_{\mathrm{g},2}$. We now sweep $V_{\mathrm{g},2}$ from 0 to 32 V and measure the amplitude A_2 of the avoided crossing by driving drum 1 and measuring drum 2, as shown in Fig. 7.15. The splitting of the resonance peak occurs only at large $V_{\mathrm{g},2}$ with a $2g$ value similar to the case described in Fig. 2 and 3. Thus, other effects arising due to the channel connecting the drums, like tension- or phonon-mediated coupling as well as its effect on C_m, do not contribute significantly to the coupling mechanism and thus can be neglected.

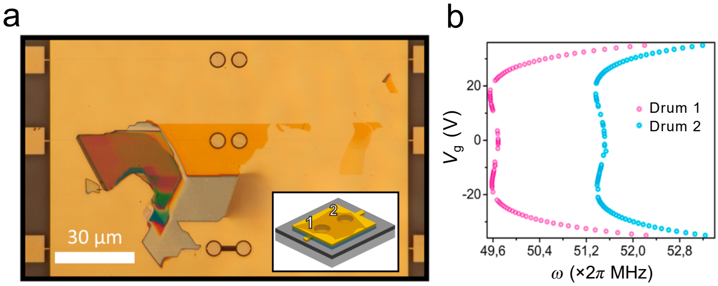

Figure 7.14: Sample of 14.5 ± 0.3 nm thin FePS$_3$ without a channel connecting the two membranes. **a** Optical image of the sample. Inset: Schematics of the sample. Cavity depth x_c = 220 nm, drum radius r = 3 μm, bottom gate electrode radius r_g = 2.5 μm. **b** Frequency $\omega(V_g)$ of the resonance peaks for the two drums (the same as in Fig. 7.2d) at 4 K.

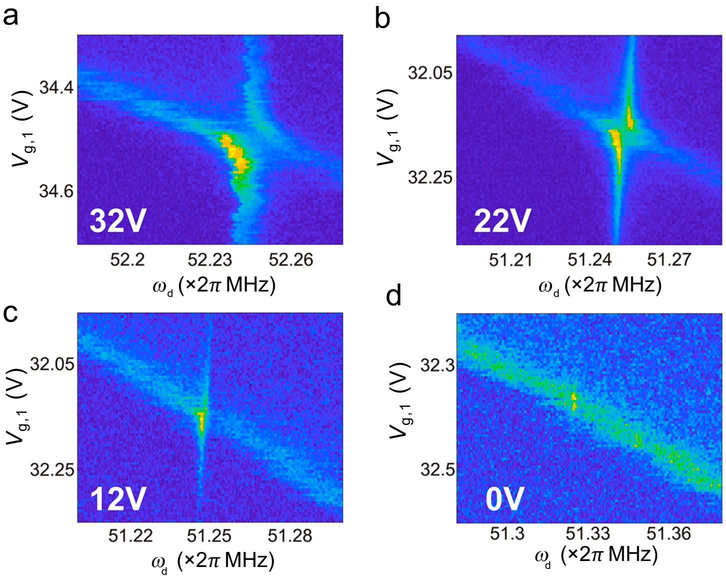

Figure 7.15: Normalized amplitudes of the resonance frequency splitting A_2 for two drums from Fig. 7.14 at 4 K. $V_{g,2}$ is labeled in all panels.

8

MECHANICAL PROBE OF MAGNETIC PHASE TRANSITIONS IN LAYERED METAL-ORGANIC FRAMEWORKS

Coupling of the magnetic phase change to mechanical properties of resonating membranes of two-dimensional (2D) materials can be used to study phase transition temperatures in the compounds where it is challenging to do so otherwise, e.g., ultrathin electrically insulating magnets. This chapter explores the coupling of antiferromagnetic phase change in van der Waals metal-organic framework (MOF) materials to the mechanical resonance of their membranes. We use this phenomenon to mechanically probe phase transition temperatures, T_N*, in three 2D layered MOFs in the absence of an external magnetic field. We observe a change in detected* T_N *depending on the type of metallic centres in these compounds and their arrangement in a crystalline lattice. We also observed a colossal negative thermal expansion coefficient in one layered MOF compound at temperatures* $T < 7$ *K. We anticipate that these methods and observations, combined with the possibility of artificially designing magnetic order in synthetic layered MOFs, in the future can help to manipulate and understand magnetic ordering and magnetoelastic interactions in 2D.*

MAGNETIC two-dimensional (2D) materials provide a platform to study magnetic ordering in reduced dimensions [42]. Experimental exploration of these compounds is often complicated by their instability in ambient air and the difficulty of detecting magnetism in the 2D layers using conventional methods [42, 46, 47]. This limitation narrows the scientific attention to systems like $FePS_3$, $Cr_2Ge_2Te_6$ or CrI_3 [45–47], which are usually hexagonal magnets and do not cover the whole symmetry and spin-ordering options possible theoretically [42]. To extend the range of magnetic materials beyond ionically bound inorganic compounds, here we study metal-organic frameworks that offer more freedom to design and synthesize magnetic 2D layered crystals of desired magnetic centres and symmetry.

Several methods are available to artificially induce magnetic order in van der Waals crystals and 2D materials. Chemical functionalization of van der Waals crystals and 2D materials by ion intercalation [252] or anchoring of molecules on the surface [253, 254] can induce magnetic phenomena. However, preservation of the long-range order in these systems remains a challenge. Alternatively, a new field of synthetic 2D polymers, that include metal-organic framework (MOF) 2D materials [64, 255], has recently emerged, showing isolation of crystalline layers with a stable structural long-range order, as well as robust magnetism in these layers. These properties, together with the possibility of the additional functionalization of their surface, make them promising candidates for fabricating membranes [64, 256] for gas separation [257] and sensing concepts [64].

In this work, we explore the coupling of magnetic properties to the nanomechanical motion of membranes made of magnetic coordination polymers [64] to study phase transitions in layers that are so thin that it is challenging to investigate these using conventional methods. These layers are MOFs with the general formula $[M(bimX)_2]$, where HbimX is the benzimidazole functionalized in the 5-position with X=H or Cl with the metallic centre M=Fe or Co. We use naming nomenclature of the form MUV-N-X (M), where MUV is the Material of the University of Valencia, N the crystalline structure type (see Fig. 8.1), X the functionalization molecule, and M the metallic centre. These crystals are formed from defect-free functionalized 2D layers translated along *c*-axis with the van der Waals gap forming between the layers, as shown in Fig. 8.1a-c. Since the MUV membranes are grown synthetically, it is possible to control the symmetry of the crystal and thus its magnetic structure by a specific choice of metallic centres, coordination compounds, and ligand molecules in the crystal grow recipe [64].

8.1. RESULTS AND DISCUSSION

8.1.1. MAGNETIC LAYERED MOFS

We direct our attention to three types of magnetic MOF crystals: MUV-1-Cl (Fe), MUV-8-Cl_2 (Fe), and MUV-1-H (Co). As shown in Fig. 8.1a-c, the thickness of a single-layer 2D MUV varies with the corresponding number and arrangement of magnetic metal centres. In the case of MUV-1-Cl (Fe) and MUV-1-H (Co), each separate 2D layer consists of a single sub-lattice of metallic centres, that result in a thickness of a single-layer ~ 1 nm. However, MUV-8-Cl_2 (Fe) packs two sublattices of metallic centres within a single layer, making the thickness of a single-layer 2D MUV ~ 1.5 nm in this case. The crystalline symmetry and the arrangement of magnetic atoms within a 2D layer are also different

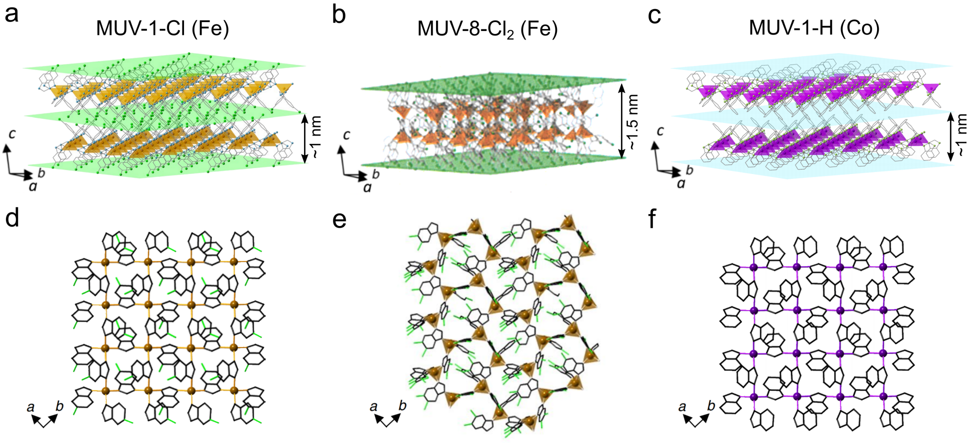

Figure 8.1: Crystalline structure of layered van der Waals MOFs. **a-b** In-plane view to the layered structure of MUV-N-X (M). Cl and H atoms located at the surface of the layers, represented as green and cyan planes, respectively. **d-f** Out-of-plane view to the single-layer of corresponding MUV-N-X (M). In all panels iron centres are shown in orange, cobalt centres in violet (incl. polyhedral representation), nitrogen atoms in blue, carbon atoms in black, chlorine atoms in green, and hydrogen atoms in cyan. Reproduced with permission [64]. Copyright 2018, Springer Nature.

in the case of MUV-8-Cl_2 (Fe), as we show in Fig. 8.1d-f. While MUV-1 compounds have metallic centres arranged in a cubic array, in MUV-8-Cl_2 (Fe) compound, these are found in distorted hexagons.

The layered structure of MUVs described in Fig. 8.1 and Fig. 8.2a is also well-visible upon the close-up view with a scanning electron microscope of MUV-1-Cl (Fe) bulk crystals, as shown in Fig. 8.2b. In this case, metallic centers of Fe^{2+}, that are located in the nearly-cubic arrangement within a single 2D layer, facilitate the presence of intralayer antiferromagnetic exchange coupling [64], as displayed in Fig. 8.2c. The antiferromagnetic coupling is also found for interlayer spin arrangement, as shown in Fig. 8.2d. This magnetic order results in a phase transition towards a canted spin structure below the Néel temperature $T_N = 20$ K, which is experimentally determined in previous works [64]. It is also notable that the terminating functionalization molecule lies in the van der Waals gap, enabling only weak interactions (e.g., Cl...Cl) between the layers and modifying its surface.

8.1.2. MEMBRANES OF MAGNETIC MOFS IN MOTION

We utilize weak interlayer interactions in these van der Waals crystals and thin them down to nanoscale thicknesses using mechanical exfoliation (see Chapter 2). These thin flakes then are suspended over pre-defined 285 nm deep cavities in SiO_2/Si chip, forming membrane resonators, as shown in Fig. 8.2e. The motion of these membranes is measured using a laser interferometry set-up, described in Chapter 3. A power-modulated blue diode laser ($\lambda = 405$ nm) is focused at the centre of the membrane and used to optothermally excite the membrane into motion at a given frequency. A red He-Ne laser

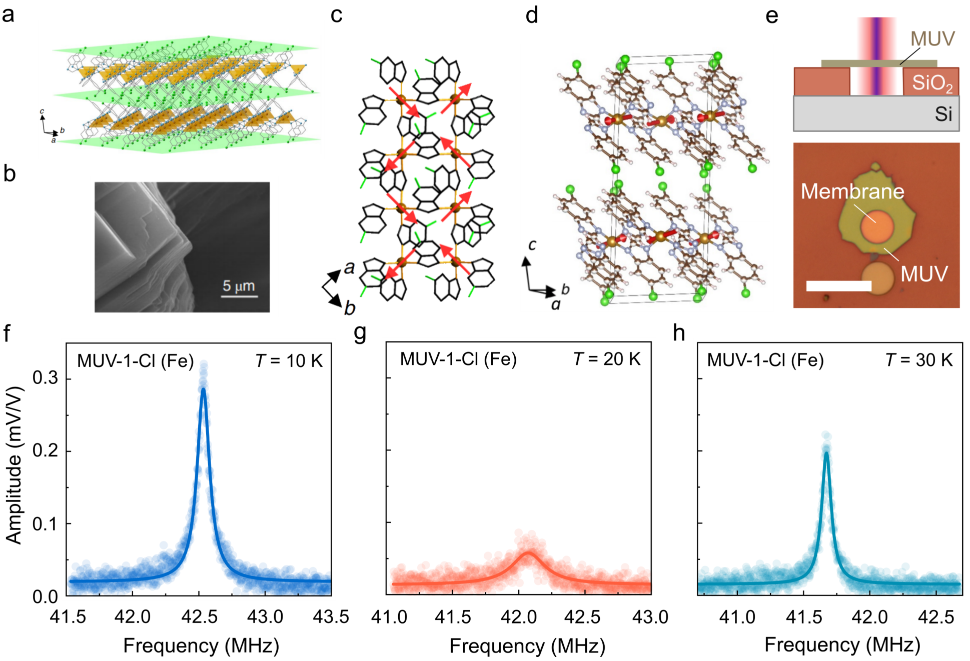

Figure 8.2: Characterization of MUV-1-Cl (Fe) crystals and membranes. **a** Crystalline structure the compound similar to Fig. 8.1a and d. **b** Scanning election microscope image of the bulk crystal. **c** Spin magnetic moment orientation in plane of the layer. **d** Interlayer magnetic moment orientation. Color scheme analogous to Fig. 8.1. Red arrows indicate spin magnetic moment orientation in (c) and (d). **e** Suspended membrane of MUV-1-Cl (Fe). Top panel: Schematic of the sample. Blue and red rays indicate laser interferometer probe and drive. Bottom panel: Optical image of the sample. Scale bar: 10 μm. **f-h** Measured resonance peak of the fundamental membrane mode of the sample in (e) at the indicated temperatures T = 10 K, T = 20 K and T = 30 K. Colored dots - measured amplitude of the peak. Solid colored lines - fit to the linear harmonic oscillator model. Panels (a-d) are reproduced with permission [64]. Copyright 2018, Springer Nature.

(λ = 632 nm) then is used to read out membrane vibrations, which is analyzed using a homodyne detection scheme and processed by a Vector Network Analyser. As the example of the detected membrane motion, we show the measured resonance frequency of the fundamental membrane mode f_0 of MUV-1-Cl (Fe) membrane below T_N at T = 10 K, at the T_N = 20 K, and above the T_N at T = 30 K, as shown in Fig. 8.2f-h. A significant drop in the peak amplitude is observed at T = 20 K with a notable broadening of the resonance peak. This behaviour is attributed to increased thermoelastic damping near T_N, that was previously observed in other antiferromagnetic membranes of van der Waals materials [67].

As notable from Fig. 8.2f-h, f_0 decreases with increasing temperature, which indicates that the strain in the membrane reduces. The temperature dependence of f_0 is caused by the thermal expansion coefficient of the material, which is mainly defined by the specific heat. The anomaly in the resonance frequency and the quality factor is expected in the vicinity of the T_N due to the change in the specific heat of the material

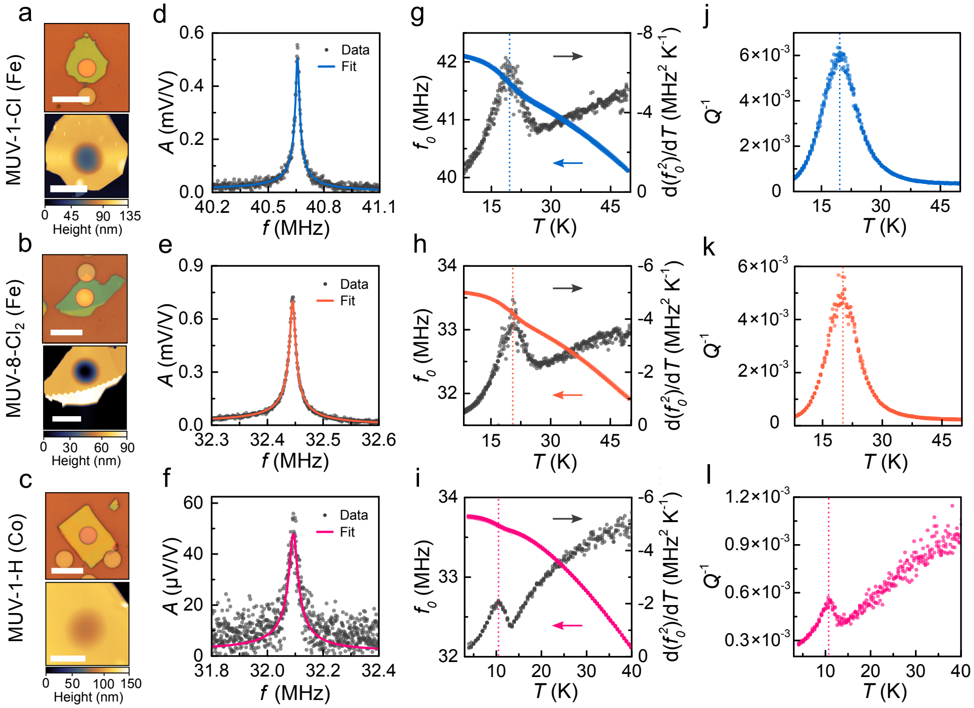

Figure 8.3: Mechanical resonances of thin metal-organic framework membranes. **a-c** MUV-1-CL (Fe), MUV-8-Cl$_2$ (Fe) and MUV-1-H (Co) membranes, respectively, subsequent panels **d-l** in the same rows belong to the same devices. Top panels: Optical images. Bottom panels: Peak-force atomic force microscopy (AFM) images. **a** Scale bars: Top panel - 10 μm. Bottom panel - 10 μm. Membrane thickness $h = 87.7 \pm 0.7$ nm and diameter $d = 5$ μm. **b** Scale bars: Top panel - 12 μm. Bottom panel - 6 μm. Membrane thickness $h = 65.2 \pm 1.3$ nm and diameter $d = 6$ μm. **c** Scale bars: Top panel - 12 μm. Bottom panel - 6 μm. Membrane thickness $h = 116.4 \pm 1.4$ nm and diameter $d = 6$ μm. **d-f** Resonance peaks of the fundamental membrane mode at 40 K. Colored lines - standard harmonic oscillator fit, black dots - measured data. **g-i** Colored dots - resonance frequency f_0 as a function of temperature, black dots - temperature derivative of $f_0^2(T)$ as a function of temperature. Dashed colored lines - peak position at the phase transition temperature, T_N [67, 106]. **j-l** Mechanical dissipation Q^{-1} as a function of temperature.

at the magnetic phase transition [67]. The characteristic transition temperature T_{N} in these compounds is defined by the exchange between magnetic metallic centres in a lattice [64]. The change in the position of magnetic atoms in the lattice then produces a different exchange between them that affects the antiferromagnetic ordering, the corresponding transition temperature and magnetoelastic effects.

To study this effect, we exfoliate flakes of MUV-1-Cl (Fe), MUV-8-Cl$_2$ (Fe) and MUV-1-H (Co) and transfer these over circular cavities (diameter $d = 5-6$ μm) etched in a SiO$_2$/Si substrate using deterministic dry viscoelastic stamping to form freestanding membranes (see Fig. 8.3a-c). Due to the large flexibility, low Young's modulus $E = 3-7$ GPa [64] and thus low bending rigidity of metal-organic framework sheets [64, 256, 258], suspended flakes behave as tension-dominated membranes even at relatively large thicknesses for a given range of cavity diameters [64]. Samples are placed on a cold finger

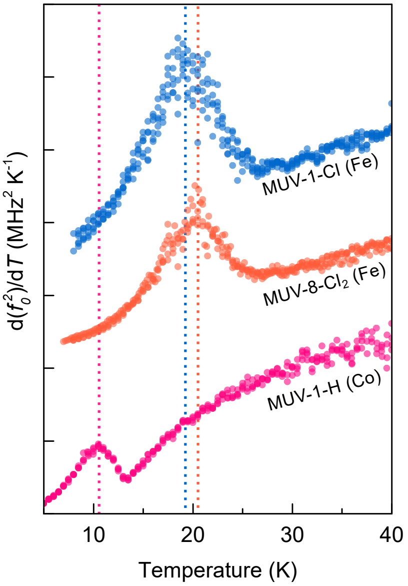

Figure 8.4: Comparison of the temperature derivative of f_0 for all three compounds from Fig. 8.3. Dashed colored lines - peak positions at the phase transition temperature, T_N [67, 106].

in a closed cycle cryostat and cooled down to a temperature of 4 K at a pressure below 10^{-6} mbar. Temperature-dependent mechanical properties of the membranes are then investigated using a laser interferometry technique [67] from 4 to 50 K in the absence of a magnetic field. Figures 8.3d-f show resonances of a fundamental membrane mode at 40 K for MUV-1-Cl (Fe), MUV-8-Cl$_2$ (Fe) and MUV-1-H (Co) as indicated by the panels in top, middle and bottom row, respectively (filled black dots). We fit the measured resonance peaks to a linear harmonic oscillator (colored solid lines) to extract the fundamental mode resonance frequency f_0 and mechanical quality factor Q. When reducing temperature to 40 K, the increased Q-factors ranging from 1000 to 3500 and high resonance frequencies of 32.1 – 40.67 MHz at 40 K indicate a high tension in the membranes due to a build-up of the thermal expansion induced strain. This strain in the membranes is caused by a difference in thermal expansion between the membrane material and the substrate (see Chapter 3). The material thermal expansion coefficient is then related to its specific heat, c_v. This interrelation allows to observe phase transition-related anomalies in $c_v(T)$ reflected in $f_0(T)$, since $c_v(T) \propto -\frac{\mathrm{d}(f_0^2(T))}{\mathrm{d}T}$ [67].

In Fig. 8.3g-i, we plot measured f_0 (colored filled dots) and corresponding temperature derivative of f_0^2 (black filled dots) for all three compounds. The phase transition-related anomaly is well visible as a kink in $f_0(T)$ and is even more pronounced in $\frac{\mathrm{d}(f_0^2(T))}{\mathrm{d}T}$, which can be attributed to the discontinuity in the specific heat of the compounds at T_N according to the Landau theory of phase transitions [67, 106]. Mechanical dissipation $Q^{-1}(T)$ also exhibits a local maximum near T_N, as displayed in Fig. 8.3j-l, that can be related to thermoelastic damping [67], although also the more intricate magnetomotive damping mechanism might contribute [135].

In Fig. 8.4, we also plot $\frac{\mathrm{d}(f_0^2(T))}{\mathrm{d}T}$ of all three studied compounds on a single graph for comparative purpose. Vertical dashed lines at the peak positions in Fig. 8.4 correspond to the detected transition temperature of the corresponding thin MUV compound. The transition temperatures detected in thin membranes using the mechanical resonance correspond well to that measured with magnetic susceptibility as a function of temperature on bulk crystals (see Appendix A1): 19.5 ± 1.0 K, compared to 20.7 K for MUV-1-Cl (Fe); 20.5 ± 1.0 K, compared to 23.2 K for MUV-8-Cl_2 (Fe); and 11.0 ± 1.0 K, compared to 12.4 K for MUV-1-H (Co). The correlation between the observed peak position in Fig. 8.4 using mechanics, and the value of T_{N} measured using magnetic probes, suggests that the magnetic order is strongly coupled to the mechanical motion. This result demonstrates that the change in magnetic order can be studied in nanoscale samples of electrically insulating magnetic MOFs via mechanical probes, which is challenging to do with alternative conventional methods.

The use of this nanomechanical approach for detecting magnetic order in molecular materials is believed to be limited by their inherent instability to the exposure of the laser beam, which can damage the suspended membranes [64]. Still, the layered MOFs with layer thickness down to 65 nm studied in this chapter are shown to be stable enough to be measured using this technique. In the future, we expect to overcome this limitation by fabricating more robust and thinner membranes, combining ultrathin layers of these MOFs with atomically thin layers of an inorganic material (like h-BN layers). We anticipate that this will open possibilities to study the tuning of T_{N} with the dimensionality of the system (number of magnetic layers) or with the strain of the membrane induced by an external stimulus (like an electrostatic gate voltage, see Chapters 6 and 9).

8.1.3. COLOSSAL NEGATIVE THERMAL EXPANSION COEFFICIENT

In the last part of this work, we direct our attention to the thermal expansion coefficient α as determined in membranes of MUV-1-Cl (Fe) and shown in Fig. 8.5. We calculate α of this compound from the measured $f_0(T)$ (see Chapter 6) using $E = 3 - 7$ GPa [64, 256, 258], a Poisson's ratio $\nu = 0.44$ [256, 259, 260], mass density $\rho = 1572$ kg m^{-3} [64] and plot it in Fig. 8.5a, showing the lower and higher boundary of values defined by the uncertainty in E using the shaded blue regions. At the high-temperature region $T \gg T_{\mathrm{N}}$, the thermal expansion component, as determined using a fit of the data by the Debye model (fitted Debye temperature 120.8 ± 0.6 K), is indicated with a solid magenta line. At the T_{N}, a peak is visible, which attributed to the magnetic discontinuity in c_{v} at the phase transition temperature [67, 106].

Unexpectedly, we have observed another anomaly in α of this compound in the low-temperature region at $T \ll T_{\mathrm{N}}$. As shown in Fig. 8.5b, the sign of α changes from positive to negative at ~ 7 K. The negative α then peaks at $T \approx 5$ K. Interestingly, the local minimum $\alpha(5\text{ K}) < -100 \times 10^{-6}$ K^{-1}, which is lower than the limit often referred as colossal negative thermal expansion coefficient [261, 262]. This phenomenon is occasionally found as a property of various metal-organic framework compounds [261–265], but was never previously reported for van der Waals 2D crystals [263–265]. One of the hypothetical explanations for observation of this phenomenon is not related to mag-

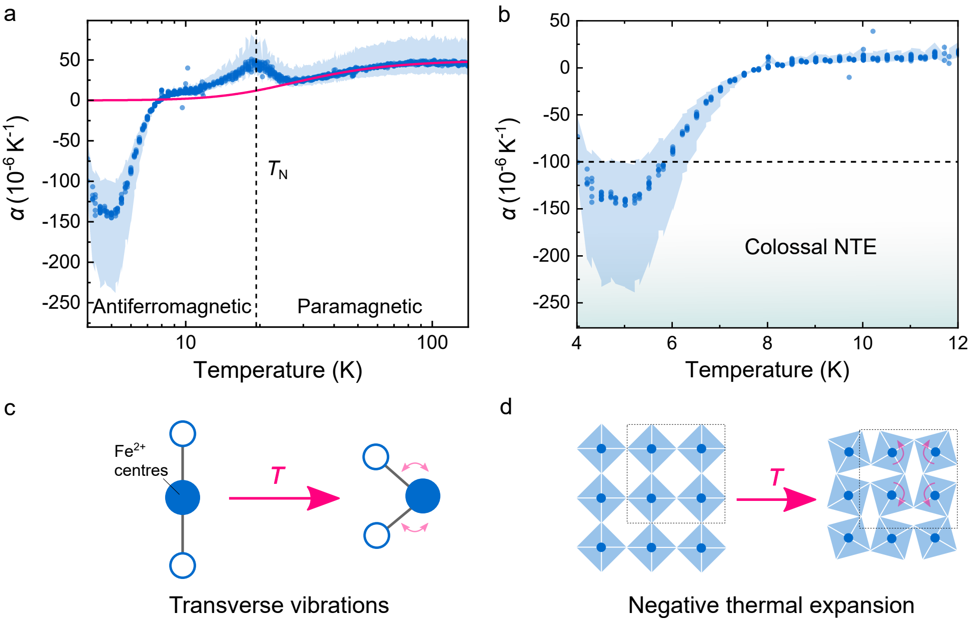

Figure 8.5: The thermal expansion of MUV-1-Cl (Fe). **a** Thermal expansion coefficient α. Filled blue dots - α as extracted from measured $f_0(T)$ using method described in Chapter 3. Solid magenta line - fit to the Debye model. Vertical dashed line indicates the phase transition temperature T_N. **b** Close-up of data in (a). Horizontal dashed line indicates the limit for the colossal negative thermal expansion coefficient (NTE). Blue region in (a) and (b) indicate the region of uncertainty. **c** Schematic of the transverse vibrations around the metallic centre. **d** Schematic of the in-plane rotation of polyhedral units around the metallic centre (filled blue dot). View along the out-of-plane axis. Dashed square indicates the unit of volume before the volume decrease.

netic properties of MUVs, but rather results from transverse vibrations around metallic centres [263, 265], shown in Fig. 8.5c. These vibrational modes have lower excitation energy than longitudinal modes and thus are excited at lower temperatures and often dominate in that temperature range [265]. Consequently, over a particular temperature range, these modes induce rotation around the metallic centre that results in decrease in volume with increasing T, as shown in Fig. 8.5d, and thus produce the observed large negative thermal expansion coefficient [263, 265].

8.2. CONCLUSIONS

In conclusion, we have shown that magnetic order in van der Waals MOF magnets is strongly coupled to the mechanical motion and can be therefore studied via mechanical probes. Using this method, specific heat-related phenomena can be studied for a thin suspended crystal of sub-picogram mass in the absence of external magnetic field [67]. We demonstrated the feasibility of detecting the coupling between mechanical and magnetic properties in these layered MOF magnets by detecting the transition temperature of three compounds of different crystal structures and metallic centers, in a good correspondence with bulk measurements. We anticipate that these nanomechanical methods, in combination with artificially designed and created magnetic order in layered MOFs, can in the future help to better understand fundamental models of magnetism [42], magnetoelastic interactions [57, 67] and thermodynamics in 2D [78, 79, 127]. In addition to that, we used nanomechanics to observe colossal negative thermal expansion in these 2D layered MOFs, which we attribute to transverse vibrations [261–265] in these materials of reduced dimensionality [64, 255]. Perhaps, this notable property can also serve for strain engineering in 2D material heterostructure membranes [30], allowing to apply compressive strain to other 2D materials in the stack at cryogenic temperatures.

8.3. APPENDIX

A1: THERMAL DEPENDENCE OF MAGNETIC SUSCEPTIBILITY.

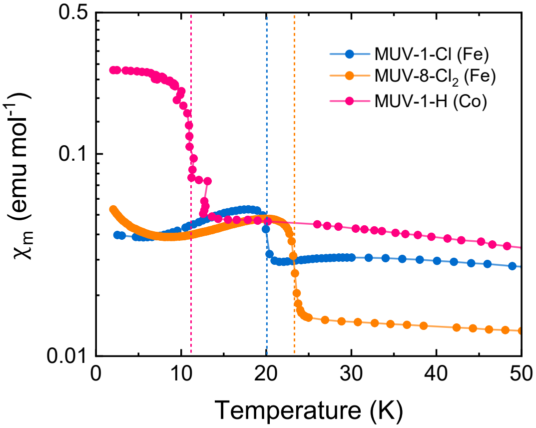

Figure 8.6: Magnetic susceptibility of bulk MUV compounds as a function of temperature. Vertical dashed lines indicate the corresponding phase transition temperature T_N: 20.7 K for MUV-1-Cl (Fe), 23.2 K for MUV-8-Cl$_2$ (Fe), and 12.4 K for MUV-1-H (Co).

9

NANOMECHANICAL PROBE AND TUNING OF CURIE TEMPERATURE OF FERROMAGNETIC $Cr_2Ge_2Te_6$ HETEROSTRUCTURES

Two-dimensional (2D) magnetic materials with strong magnetostriction, like $Cr_2Ge_2Te_6$ *(CGT), provide opportunities for strain tuning of their magnetic state, which offers potential applications in ultrathin spintronic and magneto-mechanical devices. However, realizing this potential requires understanding the coupling between 2D magnetism and mechanical properties, and the ability to controllably strain the magnets and monitor their ferromagnetic Curie temperature* T_C *on a device level. In this work, we suspend thin CGT layers to form nanomechanical membrane resonators. We then probe the mechanical and magnetic properties of CGT as a function of temperature and strain by static and dynamic nanomechanical methods. Pronounced signatures of magneto-elastic coupling are observed in the temperature-dependent resonance frequency of these membranes near* T_C*. We further utilize CGT in heterostructures with thin* WSe_2 *and* $FePS_3$ *layers to control the strain in CGT flakes and quantitatively probe the transition temperatures of all materials involved. In addition, an enhancement of* T_C *by* 2.5 ± 0.6 *K in CGT is realized in the absence of an external magnetic field using electrostatic force to induce a strain of* 0.016% *in the suspended heterostructure. Nanomechanical strain thus offers a compelling degree of freedom to probe and control magnetic phase transitions in 2D layered ferromagnets and heterostructures.*

THE recent discovery of long range order in two-dimensional (2D) (anti)ferromagnets [45–47] has triggered extensive studies of these 2D materials to experimentally probe magnetism of reduced dimensionality [42]. One material of particular interest is $Cr_2Ge_2Te_6$ (CGT) - a semiconducting ferromagnet with a bulk Curie temperature $T_C \sim 60-66$ K [47, 266]. In contrast to many other 2D layered ferromagnetic compounds [42], CGT exhibits inter- and intra-layer ferromagnetic coupling for any number of layers [47]. Recent progress has been made in manipulating the magnetic order of CGT using electrostatic gating [267, 268], magnetic field [47, 269], pressure [270, 271], ion intercalation [272] and via spin-orbit torque [273, 274]. Mechanical strain, offers another degree of freedom for such manipulation as bulk CGT was recently shown to exhibit strong spin-lattice coupling [270, 275] with a corresponding negative thermal expansion coefficient near T_C [266]. Similar phenomena are also found in other bulk chromium-based magnetic van der Waals crystals, like CrI_3, $CrBr_3$ and $Cr_2Si_2Te_6$ [276–278]. However, the coupling between magnetic order and strain in thin CGT has not been studied experimentally, as strain is a difficult parameter to control in ultrathin layers [90, 279].

Emerging nanomechanical methods allow for high-precision strain manipulation and control when 2D materials are suspended forming ultrathin membrane resonators [83, 89]. Due to the combination of low mass with high strength, these membranes find potential use in high-performance devices [89, 224] and in a wide range of sensor applications [6]. The resonance frequency of these membranes can be tuned over a large range by strain [89], which can be controlled both statically [12] and dynamically [83, 89]. Moreover, the difference between the thermal expansion coefficient of suspended 2D material layers and the substrate [67, 140] or other materials in a heterostructure [57, 280] provides additional routes for strain engineering. Nanomechanical strain can also be used to probe magnetic states [67] and switch between these states [57, 281]. It is the relation between strain, a material's thermal expansion coefficient and its magnetic properties which results in the coupling between mechanical and magnetic degrees of freedom, that allows investigation of magnetic phase transitions in 2D layered material membranes [57, 67].

Here, we demonstrate that the magnetic phase transition of suspended thin CGT membranes can be probed mechanically via the temperature-dependent resonance frequency. CGT is known to exhibit high magnetostriction, i.e. a strong magneto-elastic coupling between magnetic order and the lattice [266, 270, 275], that deforms the crystal near T_C [266]. Thus, to control the strain in thin CGT flakes and deterministically probe the transition temperature, we choose other 2D materials layers, WSe_2 and $FePS_3$, with positive thermal expansion coefficient and integrate them to form heterostructure membranes [30, 280, 282, 283] with CGT, which are important to compensate CGT's negative thermal expansion [266]. We then use these heterostructure membranes to probe and analyze the effect of the mutual interaction between the different 2D materials and CGT, and study the effect of electrostatically induced strain on the ferromagnetic order near T_C.

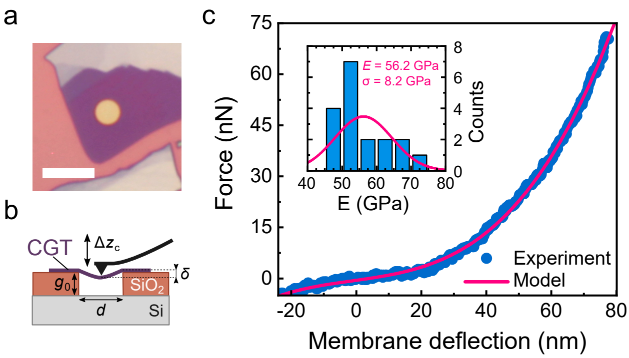

Figure 9.1: Force indentation of suspended membranes of CGT. **a** An optical image of a 9.5 ± 0.3 nm thin CGT membrane with a radius $r = 2$ μm. Scale bar: 8 μm. **b** A schematic of the membrane deflection by a cantilever tip. Δz_c is the cantilever deflection, $g_0 = 285$ nm the separation between the membrane and the bottom Si substrate, d the membrane diameter, and δ the membrane deflection. **c** A force versus membrane deflection plot. Experimental data (filled blue circles) are fit by the point-force deflection of a circular membrane model of Eq. 9.1 (solid magenta line). The inset shows a histogram of the Young's moduli extracted from 18 CGT membranes of 9.5 - 30.1 nm thicknesses, which were used to obtain the mean value of the Young's modulus E and corresponding standard deviation σ.

9.1. RESULTS AND DISCUSSION

9.1.1. ELASTIC PROPERTIES

The force-deflection curve of suspended membranes contains information about mechanical properties of the material. Thus, we first study thin layers of CGT by a static deflection method [12, 129]. We fabricate a freestanding membrane by suspending a mechanically exfoliated thin CGT flake over a circular hole by the all-dry viscoelastic stamping method [112] (Fig. 9.1a). We then apply the Atomic Force Microscopy (AFM) force nanoindentation method [12, 129] to indent the centre of the membrane with the tip of an AFM cantilever to cause a deflection of the membrane δ, as shown in Fig. 9.1b. The force applied to the centre of the membrane, F, is proportional to the stiffness k_c of the cantilever used and its deflection, Δz_c. Using cantilevers with calibrated stiffnesses of $k_c = 8.87 \pm 0.08$ Nm^{-1} and $k_c = 18.90 \pm 0.11$ Nm^{-1}, we record the force versus membrane deflection curves of this membrane, as depicted in Fig. 9.1c with filled blue circles. The observed trend can be described by the point-force deflection model for a circular membrane, assuming negligible tip radius compared to the membrane diameter [12, 129]:

$$F = \left(\frac{4\pi E}{3(1-\nu^2)}\frac{h^3}{r^2}\right)\delta + (n_0\pi)\,\delta + \left(\frac{q^3 E h}{r^2}\right)\delta^3, \tag{9.1}$$

where E is the Young's modulus of the membrane, h the membrane thickness, $\nu = 0.22$ the Poisson ratio of CGT [284], n_0 the pre-tension and $q = 1/(1.05 - 0.15\nu - 0.16\nu^2)$ is a dimensionless geometrical parameter. To our knowledge, the Young's modulus of CGT has not been experimentally studied. We therefore extract its Young's modulus E_{CGT} from the experimental data using Eq. 9.1, as shown in Fig. 9.1c by the solid magenta line. To obtain a more reliable estimate of E_{CGT}, we measure 18 different membranes of varying thicknesses ($h = 9.5$ - 30.1 nm) and radii ($r = 1$ - 2.5 μm). We find a mean value,

$E_{\mathrm{CGT}} = 56.2 \pm 8.2$ GPa, as shown in the inset of Fig. 9.1c. The obtained value of E_{CGT} is consistent with the calculated [48] 2D Young's modulus of CGT, $E_{2\mathrm{D}} = 41.8\ \mathrm{Nm}^{-1}$, which yields to $E = E_{2\mathrm{D}}/h_{2\mathrm{D}} = 61.0$ GPa, in which $h_{2\mathrm{D}}$ is the single-layer thickness, taken as a third of that of the unit cell of CGT [266]: $h_{2\mathrm{D}} = 2.056\ \mathrm{nm}/3 \approx 0.685$ nm.

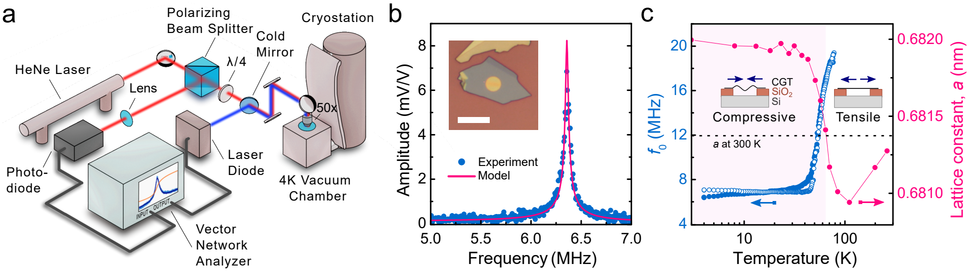

Figure 9.2: CGT membrane characterization using laser interferometry. **a** Schematic diagram of the laser interferometry setup. All measurements were performed at incident laser powers of $P_{\mathrm{red}} \leq 8\ \mu$W and $P_{\mathrm{blue}} \leq 1\ \mu$W. **b** Filled blue circles - measured amplitude of the fundamental resonance peak at $T = 4$ K. Solid magenta line - fit to a linear harmonic oscillator model. The inset shows an optical image of a 17.4 ± 0.3 nm thin CGT membrane of 2 μm radius. Scale bar: 8 μm. **c** The comparison of the measured resonance frequency f_0 of the thin film shown in (b) and the lattice constant of bulk CGT as a function of temperature. The filled and open blue circles represent the measured data during heating and cooling cycles respectively. The connected magenta circles represent the lattice constant a of bulk CGT as measured by Carteaux et al [266]. The dashed black horizontal line represents a at $T = 300$ K. The insets show schematics of membrane stretching or buckling at tensile or compressive strain, on the left and right respectively. The pink region indicates the temperature range where compressive strain is dominant and is a guide to an eye.

9.1.2. MEMBRANES IN MOTION

In order to study the coupling between magnetic phase and mechanical motion, we further investigate the dynamic nanomechanical properties of these membranes as a function of temperature. The temperature dependence of mechanical resonances of magnetic membranes is sensitive to changes in the magnetisation of the 2D layers [57] and the magnetic phase, via a mechanism that couples the specific heat to the membrane tension via the thermal expansion coefficient [67]. Thus, by observing changes in motion of the membrane at T_{C} it is possible to probe the ferromagnetic to paramagnetic transition via the mechanical resonance frequency of the membrane [67]. To do this, we use a laser interferometry technique [67, 136] (Fig. 9.2a). A CGT membrane (see the inset of Fig. 9.2b) is placed in the chamber of an optical cryostation. We use a power-modulated blue laser to opto-thermally excite a fundamental resonance mode of the membrane, and a red laser to measure the change in the reflected signal due to the subsequent displacement of the membrane.

We first measure the resonance peak of the fundamental membrane mode at $T = 4$ K (blue circles in Fig. 9.2b). We fit the experimental data to a harmonic oscillator model (solid magenta line in Fig. 9.2b) to determine the frequency of the fundamental membrane mode, f_0. Subsequently, while recording $f_0(T)$ we heat the sample to $T = 78$ K, above the expected T_{C} of 66 K [47, 266], and cool it down to $T = 4$ K. We plot the experimental data for the heating (filled blue circles) and the cooling (open blue circles) cycle in Fig. 9.2c. As the CGT membrane is cooled through the T_C, its resonance frequency f_0 reduces from 19.3 MHz at 78 K to 6.3 MHz at 4 K. To describe the $f_0(T)$ behaviour of CGT, we model the resonance frequency of a circular membrane as:

$$f_0(T) = \sqrt{\left(\frac{2.4048}{2\pi r}\right)^2 \frac{n_{\text{th}}(T)}{\rho h} + f_0^2(T_0)}, \tag{9.2}$$

where $f_0(T_0)$ is the resonance frequency at a reference temperature T_0 (e.g. room temperature) due to the contribution of the pre-tension and the bending rigidity, ρ the mass density, $n_{\text{th}}(T) = \frac{Eh}{(1-\nu)}\epsilon_{\text{th}}$ the thermally accumulated tension, and the thermal strain $\epsilon_{\text{th}} = -\int_{T_0}^{T_i} (\alpha_{\text{CGT}}(T) - \alpha_{\text{Si}}(T))\,\text{d}T$ at an arbitrary temperature T_{i} [67, 140], $\alpha_{\text{Si}}(T)$ the literature values for thermal expansion coefficient of Si substrate [142], and $\alpha_{\text{CGT}}(T)$ the temperature dependent thermal expansion coefficient of CGT. Thus, we attribute the observed $f_0(T)$ trend to a large change in the in-plane lattice constants of the unit cell and the resulting negative $\alpha_{\text{CGT}}(T)$ near the phase transition, which was also previously reported for bulk CGT [266]. This anomalous lattice expansion, when cooling down from the paramagnetic to the ferromagnetic state, is related to the strong magnetostriction effect at the ferromagnetic ordering temperature T_C in CGT [266, 275] that causes a substantial drop in strain $\epsilon_{\text{th}}(T)$ and a corresponding reduction of the membrane tension near T_C.

In Fig. 9.2c we also plot the change of the in-plane lattice constant, a, of bulk CGT, experimentally obtained by Carteaux et al. [266], as a function of temperature and compare it with the observed resonance frequency. The lattice constant a is shown to be smaller at room temperature (indicated by the black horizontal dashed line) in comparison to temperatures below the paramagnetic to ferromagnetic phase transition (~ 66 K). Since the lattice constant increases, the suspended part of the flake effectively has a larger volume at $T < T_C$ than at room temperature, indicating a switch from tensile to compressive strain, as indicated by the pink region in Fig. 9.2c. In this temperature range, the compressively strained suspended flake is likely to sag, irreproducibly wrinkle or buckle, which possibly explains a different warming and cooling trend for the resonance frequency $f_0(T)$. Buckling of magnetic layers itself is interesting for the development of reprogrammable mechanical memory devices at nano- and micro-scale [285] utilizing the bi-stable states of a buckled flake [75, 286]. However, due to the changing resonance mode shape in the compressive strain regime, and the potential wrinkling, Eq. 9.2 is not reliable for $T < T_C$. Thus, a comprehensive analysis of $f_0(T)$ near and below the phase transition [67] cannot be applied to resonators made of bare CGT.

9.1.3. HETEROSTRUCTURE MEMBRANES

To prevent the compressive strain that can lead to wrinkling in CGT membranes, and controllably probe $f_0(T)$ near and below its phase transition temperature, we fabricate a suspended membrane heterostructure composed of CGT and WSe_2 flakes, shown in Fig. 9.3. WSe_2 is a material with well-known mechanical properties [118, 123, 140] that does not undergo a phase transition from 4 to 300 K [118]. In the heterostructure, its positive thermal expansion coefficient $\alpha_{\text{WSe}_2}(T)$ counteracts the negative $\alpha_{\text{CGT}}(T)$ near T_C

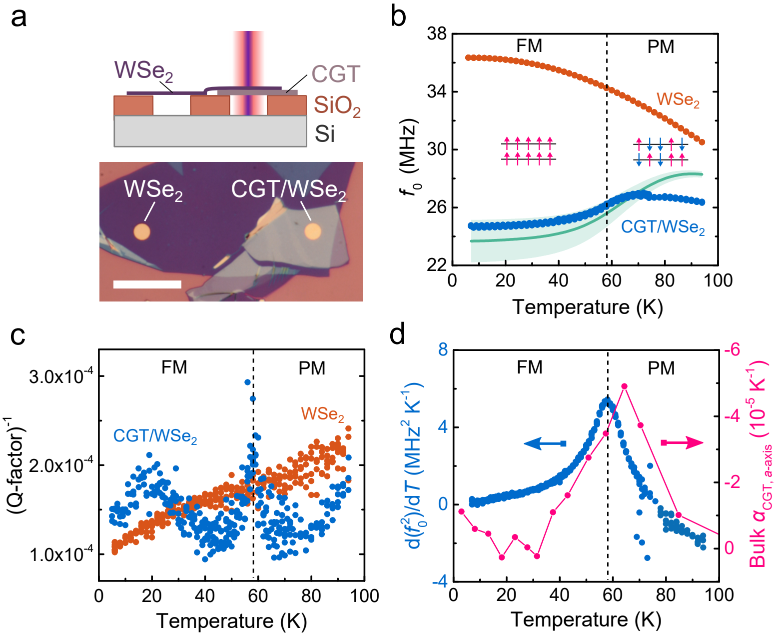

Figure 9.3: Mechanical properties of a suspended CGT/WSe$_2$ (16.7±0.3 nm/6.9±0.1 nm) heterostructure membrane with a radius $r = 2\ \mu$m. **a** Top panel: Schematic cross-section of the sample consisting of the suspended CGT/WSe$_2$ heterostructure membrane and the reference WSe$_2$ membrane of the same flake. Bottom panel: Optical image of the sample with specific membranes indicated. Scale bar: 16 μm. **b** Measured resonance frequencies f_0 of the membranes in (a). Solid green line - the fitted model of the resonance frequency of the CGT/WSe$_2$ heterostructure (Eq. 9.4). Light green region - the allowed higher and lower boundary of the model due to the uncertainties in $h_{1,2}$, $E_{1,2}$ and $f_0^2(T_0)$. Insets: Schematic of the collinear and random magnetic spin arrangement in a bilayer of CGT in the ferromagnetic (FM) and the paramagnetic (PM) phases respectively. **c** Mechanical damping Q^{-1} as a function temperature. **d** Filled blue circles - $\frac{\mathrm{d}\left(f_0^2\right)}{\mathrm{d}T}$ of the CGT/WSe$_2$ heterostructure as a function of temperature. Connected magenta circles - the thermal expansion coefficient of bulk CGT [266]. The black vertical dashed lines in (b-d) indicate the measured $T_\mathrm{C}^* = 58 \pm 0.5$ K as determined from the peak position of $\frac{\mathrm{d}\left(f_0^2\right)}{\mathrm{d}T}$.

of CGT, such that the total membrane stress remains tensile and f_0 can be used to probe $\alpha(T)$ even below T_C. We stack WSe$_2$ flakes on top of a suspended CGT layer to minimise the exposure time of CGT to air. Subsequently, samples were kept in an oxygen-free environment to avoid degradation.

We measure $f_0(T)$ of the suspended CGT/WSe$_2$ heterostructure together with a reference drum of the same WSe$_2$ flake (Fig. 9.3b). The $f_{0,\mathrm{WSe_2}}(T)$ follows a monotonous increase trend with decreasing temperature (filled orange circles), as expected from its positive $\alpha_{\mathrm{WSe_2}}(T)$ [118, 140]. In contrast, $f_{0,\mathrm{CGT/WSe_2}}(T)$ has a downturn with decreasing temperature near the transition temperature (filled blue circles). This behaviour is distinct from the bare CGT resonator (Fig. 9.2c) and is due to the positive thermal expansion coefficient of the WSe$_2$ layer, which maintains a tensile total strain of the heterostructure. We also plot the mechanical dissipation, the inverse of a quality factor $Q^{-1}(T)$, of both the WSe_2 and CGT/WSe_2 resonators in Fig. 9.3c. A notable peak in $Q_{\mathrm{CGT/WSe_2}}(T)$ is visible at $T = 58$ K. We attribute this observation to an increase of the thermoelastic damping [229, 287] expected near T_C in magnetic resonators [67]. This observation is supported by the measured maximum in $\frac{\mathrm{d}(f_0^2)}{\mathrm{d}T}$ (filled blue circles) [67] at 58 ± 0.5 K, the temperature which we define as T_C^* and indicate by the black vertical dashed lines in Fig. 9.3d. The observed maximum at T_C^* relates to the peak in the thermal expansion coefficient of CGT at T_C (filled magenta circles) that is shifted to lower temperatures in comparison to its bulk values of 60 – 66 K [47, 266].

We model the resonance frequency of a heterostructure $f_{0,\mathrm{h}}(T)$ by modifying Eq. 9.2 to describe the observations in Fig. 9.3b. We describe the total thermally accumulated tension of the CGT/WSe_2 heterostructure as a sum of individual tensions in each layer [280, 283]:

$$n_{\mathrm{th}}(T) = n_{\mathrm{th},1}(T) + n_{\mathrm{th},2}(T) = \frac{E_1 h_1}{(1-\nu_1)}\epsilon_{\mathrm{th},1}(T) + \frac{E_2 h_2}{(1-\nu_2)}\epsilon_{\mathrm{th},2}(T). \tag{9.3}$$

We assume that the slippage between the layers is negligible. Therefore, we obtain the final equation for the resonance frequency of the heterostructure as [*]:

$$f_{0,\mathrm{h}}(T) = \sqrt{\left(\frac{2.4048}{2\pi r}\right)^2 \frac{1}{\rho_1 h_1 + \rho_2 h_2}\left[\frac{E_1 h_1}{(1-\nu_1)}\epsilon_{\mathrm{th},1}(T) + \frac{E_2 h_2}{(1-\nu_2)}\epsilon_{\mathrm{th},2}(T)\right] + f_0^2(T_0)}. \tag{9.4}$$

We plot the model of Eq. 9.4 for the CGT/WSe_2 heterostructure in Fig. 9.3b (solid green line). In doing so, we use the bulk $\alpha_{\mathrm{CGT}}(T)$ values [266], $\rho_{\mathrm{CGT}} = 6091$ kg m^{-3} [266], $\nu_{\mathrm{CGT}} = 0.22$ [284], and $E_{\mathrm{CGT}} = 56.2 \pm 8.2$ GPa for CGT; $\epsilon_{\mathrm{th,WSe_2}}(T)$ extracted from the measured $f_{0,\mathrm{WSe_2}}(T)$ of the reference drum using Eq. 9.2, $\rho_{\mathrm{WSe_2}} = 9320$ kg m^{-3} [123, 289], $\nu_{\mathrm{WSe_2}} = 0.19$ [123, 290] and $E_{\mathrm{WSe_2}} = 167.1 \pm 0.7$ GPa (measured for this membrane using the nanoindentation method described above, which is consistent which previous studies [123]) for WSe_2; and $f_0(94\,\mathrm{K}) = 27.2 \pm 0.4$ MHz. The resulting model reproduces the experiment qualitatively, yet lacks quantitative agreement above T_C, most likely due to the overestimation of $\alpha_{\mathrm{CGT}}(T)$ for thin layers of CGT in contrast to its bulk value [266].

9.1.4. FERROMAGNET AND ANTIFERROMAGNET STACK

The presented methodology is not limited exclusively to the use of WSe_2, given that the thermal expansion coefficient of the added material is large and positive. To explore the possibility of detecting two magnetic phase transitions in the same membrane and also the possibility of having emergent properties arising from a coupling between the two flakes, we fabricate a heterostructure membrane made of a ferromagnetic CGT covered by an antiferromagnetic $FePS_3$ layer, as shown in Fig. 9.4a. Using the methods described above, we measure the resonance frequency of this suspended structure as a function of temperature. In Fig. 9.4b, we plot experimental $f_0(T)$ (filled blue circles) together with its $\frac{\mathrm{d}(f_0^2(T))}{\mathrm{d}T}$ (filled grey circles). The temperature derivative of f_0^2 shows two clear extrema, indicated by black vertical dashed lines: the first one at $T_C^* = 62 \pm 1$ K we attribute to

---

[*] As derived and discussed in detail in the BSc thesis of Slotboom, B.J.M. [288]

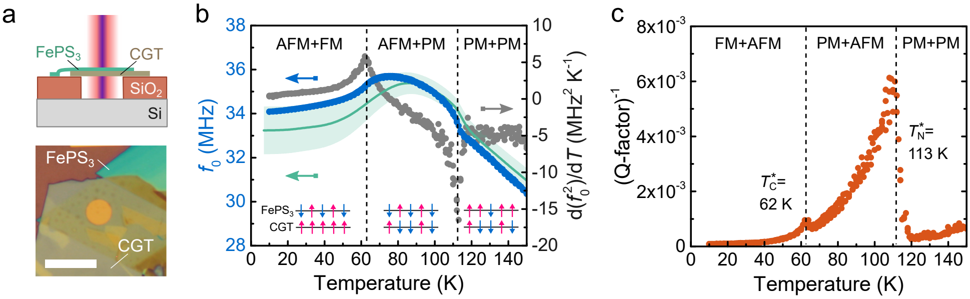

Figure 9.4: Mechanical properties of a CGT/FePS$_3$ (19.8 ± 0.2 nm/18.0 ± 0.1 nm) heterostructure membrane with a radius $r = 2.5\ \mu$m. **a** Top panel: A schematic cross-section of the suspended heterostructure membrane. Bottom panel: The optical image of the sample with the CGT/FePS$_3$ heterostructure. Scale bar: 10 μm. **b** Filled blue circles - the measured resonance frequency as a function of temperature. Filled grey circles — the temperature derivative of f_0^2. Solid green line - the heterostructure resonance frequency model as described by Eq. 9.4. The light green region indicates the higher and lower boundary of the model allowed due to the uncertainties in $h_{1,2}$, E_{CGT} and $f_0^2(T_0)$. The insets: Schematic pictures of a magnetic spin configuration in FePS$_3$ and CGT layers in corresponding combinations of antiferromagnetic (AFM), ferromagnetic (FM) and paramagnetic (PM) phases. **c** The mechanical damping Q^{-1} as a function temperature, in which the filled orange circles represent the measured data of the CGT/FePS$_3$ heterostructure. The black vertical dashed lines in (b) and (c) represent the measured $T_C^* = 62 \pm 1$ K of CGT and $T_N^* = 113 \pm 1$ K of FePS$_3$ as determined from positions of extrema in $\frac{\mathrm{d}\left(f_0^2\right)}{\mathrm{d}T}$ in (b).

the T_C of CGT [47, 266]; the second one at $T_N^* = 113 \pm 1$ K corresponds to the Néel temperature, T_N, of FePS$_3$ [45, 67]. We plot the model of Eq. 9.4 in Fig. 9.4b (solid green line) for the CGT/FePS$_3$ heterostructure using material parameters of CGT from literature [67, 266, 284] and E_{CGT} as determined from Fig. 9.1; $E_{\mathrm{FePS_3}} = 103$ GPa, $\rho_{\mathrm{FePS_3}} = 3375$ kg m^{-3}, $\nu_{\mathrm{FePS_3}} = 0.304$ [59, 67] for FePS$_3$; and $f_0(150\,\mathrm{K}) = 30.9 \pm 0.7$ MHz. The model describes the experiment well with some deviations at low temperatures similar to the ones described above in Fig. 9.3c. In addition, we observe two peaks in $Q^{-1}(T)$, displayed in Fig. 9.4c, that we attribute to increased thermoelastic damping near the phase transition [67, 229, 287]. The temperatures of these peaks coincide with the extrema from Fig. 9.4b, confirming the phase transitions in CGT and FePS$_3$.

9.1.5. TUNING CURIE TEMPERATURE

Since strong magnetostriction is responsible for the large anomalies in the mechanical response of CGT membranes at T_C [266, 275] (Fig. 9.1), we expect that the inverse effect should also be present allowing us to tune the T_C via strain [57, 67]. To study this effect, we fabricate another CGT/WSe$_2$ heterostructure membrane contacted to Pd electrodes, as shown in Fig. 9.5a-c. To realize electrical contact to some samples for electrostatic experiments, Pd electrodes are pre-patterned on top of Si/SiO$_2$ chips by a lift-off technique. We apply a gate voltage V_g between the heterostructure membrane and the bottom Si substrate electrode to induce an electrostatic force, F_{el}, that pulls the membrane down and thus strains the CGT/WSe$_2$ stack. In Fig. 9.5d, we show the measured f_0 of the heterostructure membrane as a function of temperature for six different values of V_g. A notable increase of f_0 as a function of V_g is evident which is attributed to the electrostatic strain introduced. To describe the gate dependence of the resonance frequency, we show the $f_0(V_g)$ relationship near the phase transition temperature at $T_0 = 60$ K in Fig. 9.5e. We fit the measurement data to a continuum mechanics model of a circular membrane resonator [143, 145] (see Appendix A1 and 9.5), which describes the experiment well. We thus estimate the added electrostatic strain [57, 145] as $\Delta\epsilon \approx \frac{2}{3}\left(\frac{\varepsilon_0 r}{8 g_0^2 n(T_0)}\right)^2 V_g^4$, where ε_0 is the dielectric permittivity of vacuum, and $n(T_0) = 2.538 \pm 0.003$ Nm^{-1} the total tension in the suspended heterostructure at $T_0 = 60$ K (extracted from the fit in Fig. 9.5e).

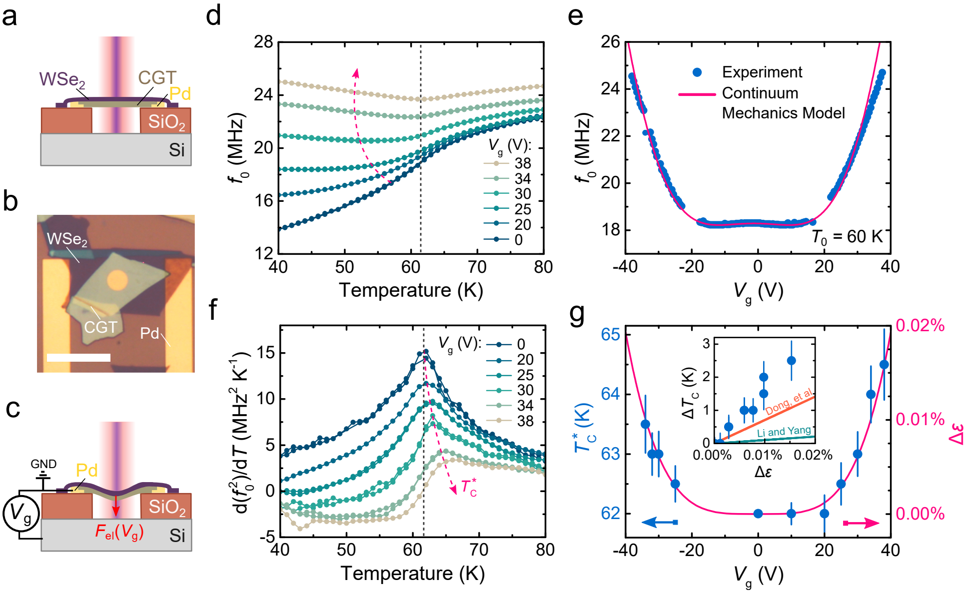

Figure 9.5: Curie temperature enhancement as a function of strain in a suspended CGT/WSe$_2$ heterostructure (19.7±0.1 nm/8.5±0.2 nm). **a** The schematic cross-section of the suspended CGT/WSe$_2$ heterostructure membrane. **b** The optical image of the heterostructure with materials indicated. Membrane radius: $r = 4$ μm. Scale bar: 12 μm. **c** The schematics of the electrostatic strain-tuning principle. **d** Measured resonance frequencies f_0 of the heterostructure membrane as a function of temperature for different gate voltages V_g. **e** Filled blue circles - the measured resonance frequency as a function of V_g at 60 K. Solid magenta line - the continuum model mechanics model fit [143, 145]. **f** The temperature derivative of f_0^2 as a function of temperature for different V_g. The black vertical dashed lines in (d) and (e) show the peak position in $\frac{\mathrm{d}\left(f_0^2\right)}{\mathrm{d}T}$ at $V_g = 0$ V. **g** Filled blue circles — the shift in measured T_C^* as a function of V_g extracted from the peak position in (e). Solid magenta line - the estimate of electrostatically induced strain $\Delta\epsilon$ as a function of V_g. The inset shows $\Delta T_C = T_C^*(V_g) - T_C^*(0\text{V})$ as a function of added voltage induced strain $\Delta\epsilon$ in addition to calculations from Li and Yang [48] (solid green line) and from Dong et al [291] (solid orange line). The vertical error bars in T_C^* were estimated from determining the peak position in (e) within 2% accuracy in the measured maximum.

Apart from the effect of electrostatically induced strain on $f_0(V_g)$ in Fig. 9.5d, the characteristic feature in the $f_0(T)$ curve, that we attribute to the Curie temperature of CGT [67], shifts to higher temperatures. This trend becomes even more apparent in Fig. 9.5f, where we plot $\frac{\mathrm{d}(f_0^2)}{\mathrm{d}T}$ for six different V_g. We extract T_C^* from the peak positions in $\frac{\mathrm{d}(f_0^2)}{\mathrm{d}T}$ for multiple V_g and plot it against the gate-induced strain, $\Delta\epsilon$, in Fig. 9.5g. The observed enhancement in T_C^* qualitatively agrees with the added tensile strain dependence symmetrically both for positive and negative V_g as shown in Fig. 9.5g. This indicates that the gate-induced strain has a dominant contribution to the change in the $T_\mathrm{C}^*(V_\mathrm{g})$ instead of a field effect [267, 268]. In the inset of Fig. 9.5g, we plot the experimental $\Delta T_\mathrm{C} = T_\mathrm{C}^*(V_\mathrm{g}) - T_\mathrm{C}^*(0\,\mathrm{V})$ versus the estimated strain $\Delta\epsilon$, together with predictions from density-functional theory calculations for 2D CGT by Li and Yang [48], considering the direct exchange interaction (solid green line), and by Dong et al [291], attributing the enhancement of T_C to the super-exchange interaction via Cr-Te-Cr bonds (solid orange line). The closer experimental agreement with the results of Dong et al. [291] suggests that it is the decreasing energy difference between $3d$ orbitals of Cr and $5p$ orbitals of Te in nearly $\sim 90°$ Cr-Te-Cr bonds of CGT that is likely to contribute to the enhancement of T_C^* as a function of strain [291]. Interestingly, we observed that the maximal T_C^* increase by mechanical strain was as much as 2.5 ± 0.6 K at $\Delta\epsilon \approx 0.016\%$. This is comparable to what was previously achieved in bulk CGT by applying an out-of-plane magnetic field of $0.7-1$ T [47, 269], proving that strain-based nanomechanical methods provide a compelling route for controlling and probing magneto-elastic coupling in ferromagnetic 2D layers and heterostructures.

9.2. CONCLUSIONS

In conclusion, we have probed the mechanical properties of CGT membranes by both static and dynamic nanomechanical means. We demonstrated that due to CGT's strong magnetostriction [266, 275] and large negative thermal expansion near T_C, bare CGT membranes experience strong resonance frequency reductions near their ferromagnetic Curie temperature and an accumulation of compressive strain. The compressive strain can produce buckling, wrinkling or sagging of the CGT layers, that significantly complicates the analysis for nanomechanical measurements of T_C [67]. We showed that this issue can be solved by integrating CGT in heterostructures with other materials with positive thermal expansion coefficients. This methodology can also be applied using materials that have phase transitions themselves, which we demonstrate by probing both T_N of $FePS_3$ and T_C of CGT within a single measurement of a CGT/$FePS_3$ heterostructure. The presented measurements and methodologies for nanomechanical characterisation of magnetic heterostructures open up possibilities to investigate magnetic properties that are the result of interfacial magnetic interactions in 2D magnetic heterostructures membranes [292], allowing novel magnetic properties to be discovered near the monolayer limit while also excluding substrate interactions. In addition, we expect that focused studies of the mechanical dissipation in such heterostructures as a function of temperature and strain could in the future provide more insights to thermodynamics and heat transport in 2D materials involved [67, 78, 79]. Finally, we showed that T_C of CGT can be enhanced by gate-induced electrostatic straining, showing that it is not only possible to probe, but also control the magnetic order in these ferromagnetic heterostructures. We anticipate that these studies in the future will lead to the development of membrane devices with gate-controlled magnetic actuation [293] and low-power spintronic implementations.

9.3. APPENDIX

A1: CONTINUUM MECHANICS MODEL OF ELECTROSTATICALLY STRAINED CIRCULAR MEMBRANE

A membrane suspended over a circular cavity forms a capacitor with a bottom gate electrode underneath. The change in gate voltage causes the membrane to deflect, tuning the tension and producing a shift in the resonance frequency. The resonance frequency of the fundamental vibration mode of the drum as a function of gate voltage is described as [143]:

$$f_0(V_\mathrm{g}) = \frac{1}{2\pi}\sqrt{\frac{1}{m_\mathrm{eff}}\left[\frac{2\pi E h \epsilon_0}{1-\nu^2} + \frac{8\pi E h}{\left(1-\nu^2\right) r^2} z_\mathrm{g}^2 - \frac{1}{2}\frac{\partial^2 C_\mathrm{g}}{\partial z^2} V_\mathrm{g}^2\right]}, \tag{9.5}$$

where $z_\mathrm{g} \approx \frac{\varepsilon_0 r^2}{8 g_0^2 n(T_0)} V_\mathrm{g}^2$ is the maximal deflection at the membrane centre [145], $\frac{\partial^2 C_\mathrm{g}}{\partial z^2} \approx \frac{0.542\varepsilon_0 \pi r^2}{g_0^3}$ the second derivative of capacitance [128, 145], and $m_\mathrm{eff} = 0.27\rho h \pi r^2$ the effective mass. In the case of a heterostructure membrane, material parameters are substituted for the heterostructure analogues [280]: $E = \frac{E_1 h_1 + E_2 h_2}{h_1 + h_2}$, $\rho = \frac{\rho_1 h_1 + \rho_2 h_2}{h_1 + h_2}$, $\nu = \frac{\nu_1 h_1 + \nu_2 h_2}{h_1 + h_2}$, and $h = h_1 + h_2$. For the CGT/WSe$_2$ heterostructure (19.7±0.1 nm/8.5±0.2 nm) in Fig. 9.5 we use the following material parameters: $E = 89.6$ GPa, $h = 28.2$ nm, $\nu = 0.21$, $\rho = 7064$ kg m^{-3}. We extract $\epsilon = 0.079 \pm 0.004\%$, $\frac{\partial^2 C_\mathrm{g}}{\partial z^2} = 3.46 \pm 0.11$ mFm^{-2} and $m_\mathrm{eff} = 996.45$ fg from the fit in Fig. 9.5e, that are close to the expected values [128, 145] of $\frac{\partial^2 C_\mathrm{g}}{\partial z^2} = 2.61$ mFm^{-2} and $m_\mathrm{eff} = 675.9$ fg.

IV

Part Four

Outlook

Chapters 10, 11 and 12

10

MAGNETICALLY-INDUCED ANISOTROPY IN ANTIFERROMAGNETIC MEMBRANES

Magnetostriction in two-dimensional (2D) materials is promising for effective control of magnetic order in (anti-)ferromagnets and their heterostructures using tension. This chapter will discuss and provide an outlook on the relationship between magnetostriction and nanomechanical resonance in membranes of multilayer 2D materials. We show that using the star-shaped array of rectangular membranes from Chapter 5 can help to investigate critical phenomena near the phase transition in antiferromagnetic MPS_3 *(M = Fe, Co, Ni) compounds. By analyzing the angle-resolved stress in the membrane resonators, while cooling them below their Néel temperature* T_N*, we obtain critical beta exponents for materials with strong and weak spontaneous magnetostriction. We anticipate that in the future this method can help in studying the critical exponent for atomically thin membranes made of 2D materials, in particular in antiferromagnets, where it is difficult to obtain information about the order parameter by other methods.*

THE magnetostriction effect in membranes of van der Waals materials is a measure of magneto-elastic coupling and thus can enable effective control of magnetic ordering through strain [90]. We show that it also could be used to access the order parameter of magnetic materials by solely nanomechanical means. For some materials, magnetostrictive strain near the transition temperature can distort the crystal lattice to facilitate an easy magnetic axis. This spontaneous lattice deformation is a consequence of the combination of the magnetostrictive coupling in the material and the spontaneous magnetic ordering of atomic moments that emerges below the magnetic transition temperature [294]. In transition metal phosphorus trisulfide (MPS_3) compounds this is often viewed as a contraction of one axis of the crystal and expansion of another within the van der Waals plane upon cooling below T_N [61, 295, 296]. As temperature dependence of in-plane lattice constants a and b is well-known only for $FePS_3$ [295, 296], we further label in-plane crystalline axes of MPS_3 compounds as x and y, where y is the expanding and x is the contracting axis. This behavior can even change the symmetry of the compound from paramagnetic D_{3d} point group towards antiferromagnetic C_{2h} [61], as shown in Fig. 10.1a. This also results in different strain $\epsilon_{x,y}$ accumulated along each crystalline axis in either x or y direction below T_N.

10.1. RESULTS AND DISCUSSION

10.1.1. SPONTANEOUS MAGNETOSTRICTIVE STRAIN

To study this phenomenon, we fabricate an array of rectangular cavities rotated at 30° with respect to each other, similar to those used in Chapter 5. We suspend single thin flakes of MPS_3 over these cavities to create arrays of rectangular membrane resonators. In contrast to experiments in Chapter 5, we fabricate thinner membranes of $h = 20-40$ nm in order to be more sensitive to the membrane term in Eq. 3.6.

The resonance frequency of the fundamental rectangular membrane mode is given by [297]:

$$f_0 = \frac{1}{2}\sqrt{\frac{E}{\rho}\left[\frac{1}{w^2}\epsilon_w + \frac{1}{l^2}\epsilon_l\right]}, \tag{10.1}$$

where ρ is the mass density, E the Young's modulus, w the width and l the length of the membrane, and $\epsilon_{w,l}$ the corresponding strain along these dimensions. The anisotropy in E (see Chapter 5) and its temperature dependence is expected to be much smaller than that in $\epsilon_{w,l}$, and thus we neglect it. At an arbitrary angle θ to the crystalline direction, $\epsilon_{w,l}$ will have the contribution from both ϵ_y and ϵ_x. When cavities are aligned with the flakes crystal axes x and y, and $w \ll l$, equation for f_θ will reduce to:

$$\begin{aligned} f_{0^\circ} &\approx \frac{1}{2}\sqrt{\frac{E}{\rho w^2}\epsilon_x}, \\ f_{90^\circ} &\approx \frac{1}{2}\sqrt{\frac{E}{\rho w^2}\epsilon_y}. \end{aligned} \tag{10.2}$$

Above T_N, under the assumption that the membrane is isotropic in the absence of magnetostrictive strains, $\epsilon_x = \epsilon_y = \epsilon_{th}(T) + \epsilon_0(T_0)$ and has a temperature dependence as

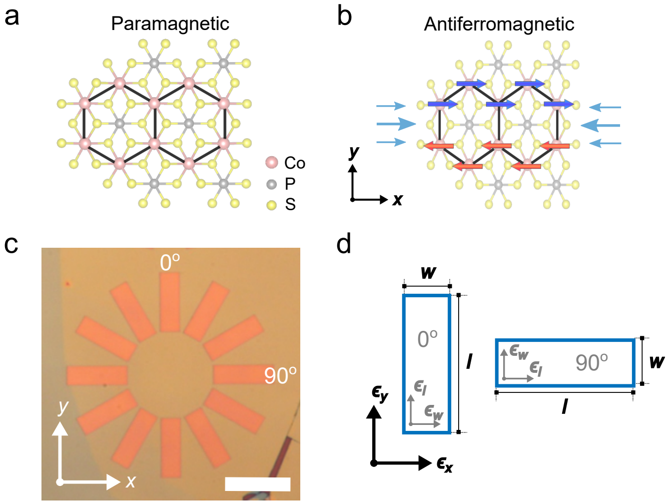

Figure 10.1: Magnetostriction effect on rectangular membranes. **a** Crystalline structure of $CoPS_3$ at the paramagnetic phase. Black hexagons indicate the organisation of Co atoms in the lattice. **b** The same crystalline structure as it elongates in the y direction and contracts in x. Red and dark blue arrows indicate the in-plane magnetic moment arrangement of Co atoms. Light blue arrows indicate the axial lattice distortion. **c** Optical image of the membrane array. Angle θ is indicated for w-direction with respect to x axis. Scale bar: 12 μm. **d** Schematic of 0° and 90° membranes from (c). w is the width of the membrane, l the length, $\epsilon_{x,y}$ the strain along x and y, $\epsilon_{w,l}$ the strain along w and l.

described in Chapter 6. Below T_{N}, strain in the membrane builds up due to three main contributions:

$$\begin{aligned}\epsilon_x(T) &= \epsilon_{\mathrm{th}}(T) + \epsilon_{0,x}(T_0) + \epsilon_{\mathrm{ms,x}}(T),\\ \epsilon_y(T) &= \epsilon_{\mathrm{th}}(T) + \epsilon_{0,y}(T_0) + \epsilon_{\mathrm{ms,y}}(T),\end{aligned} \tag{10.3}$$

where $\epsilon_{\mathrm{th}}(T)$ is the direction-independent thermodynamic contribution that is related to specific heat of the material (see Chapter 6), T the temperature, $\epsilon_{0,x}(T_0)$ and $\epsilon_{0,y}(T_0)$ the pre-strain contribution in x and y direction at a reference temperature T_0, and $\epsilon_{\mathrm{ms,y}}$ and $\epsilon_{\mathrm{ms,y}}$ the magnetostriction term in x and y direction.

10.1.2. ANISOTROPIC RESONANCE FREQUENCY

In the absence of magnetic order, and in the absence of anisotropies in the pre-strain due to manufacturing imperfections, at $T > T_{\mathrm{N}}$ membranes of MPS_3 would behave as isotropic nanomechanical membrane resonators for which the resonance frequency does not depend on the orientation of the membrane with respect to the crystalline axis. However, when the magnetic order appears at $T < T_{\mathrm{N}}$, magnetostrictive straining along x and y direction is expected to be uneven [61, 295, 296], that implies $\epsilon_{\mathrm{ms,x}} \neq \epsilon_{\mathrm{ms,y}}$ and thus the same membranes would show anisotropic features, such as the resonance frequency decrease of f_{0° and increase of f_{90°.

We investigate this by suspending $CoPS_3$ flake over two arrays of rectangular cavities, shown in Fig. 10.2. We then use the laser interferometry technique to measure the resonance frequency and quality factor of each membrane as a function of temperature. The arrangement of the cavities gives the angular resolution of 15° for the measured mechanical properties of the membranes. As the membranes are cooled through the transition temperature at $T_N \sim 118$ K [45], the resonance frequency shows a characteristic "dumbbell"-shaped trend as a function of angle to the x axis, when plotted in polar coordinates as shown in Fig. 10.2b.

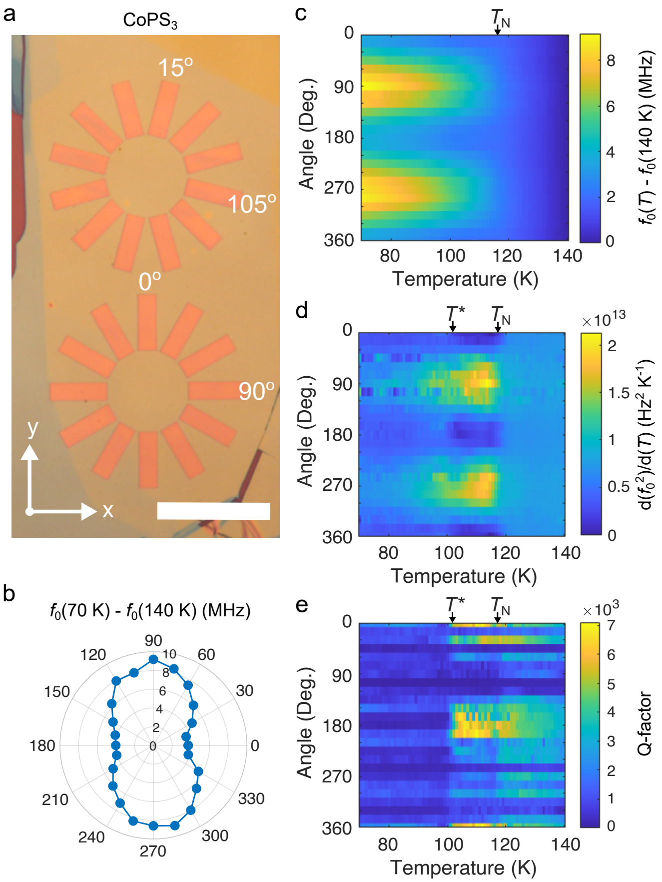

Figure 10.2: Array of rectangular membrane resonators of $CoPS_3$. **a** Optical image of the membrane array. Angle θ is indicated with respect to x axis. Scale bar: 24 μm. **b** Anisotropy in fundamental resonance frequency $f_0(T)$ difference between 70 K ($T < T_N$) and 140 K ($T > T_N$). **c** Resonance frequency difference, $f_0(T) - f_0(140\,\mathrm{K})$, as a function of angle of the membrane's w-direction with respect to the x axis, θ, and temperature. **d** $\frac{\mathrm{d}f_0^2}{\mathrm{d}T}$ as a function of angle and temperature. **e** Mechanical quality factor of membranes as a function of angle and temperature.

The fact that the anisotropic behavior arises at the T_N is more apparent in Fig. 10.2c, where f_0 is plotted as a function of θ and temperature. This suggests a correlation between magnetic order and anisotropic strain, which indicates the relevance of magnetostriction to account for this behaviour. Interestingly, by taking a temperature derivative of the frequency squared $\frac{\mathrm{d}f_0^2}{\mathrm{d}T}$, the thermal expansion coefficient related term (see Chapter 6), a substantial difference is observed between 0° and 90° at the temperature range from $T^* = 101$ K to $T_\mathrm{N} = 118$ K. We attribute this to a predominant contribution of ϵ_ms to f_0 in this temperature range, which will be analysed later.

Interestingly, as shown in Fig. 10.2e the quality factor also exhibits two anomalies at T^* and T_N, indicating abruptly increased mechanical dissipation near these temperatures. In addition to that, some possible angle-dependent structure is visible with larger Q-factor values at 0°/180° in comparison to that of 90°/270°. The reason behind this behavior remains unclear and requires more detailed investigation.

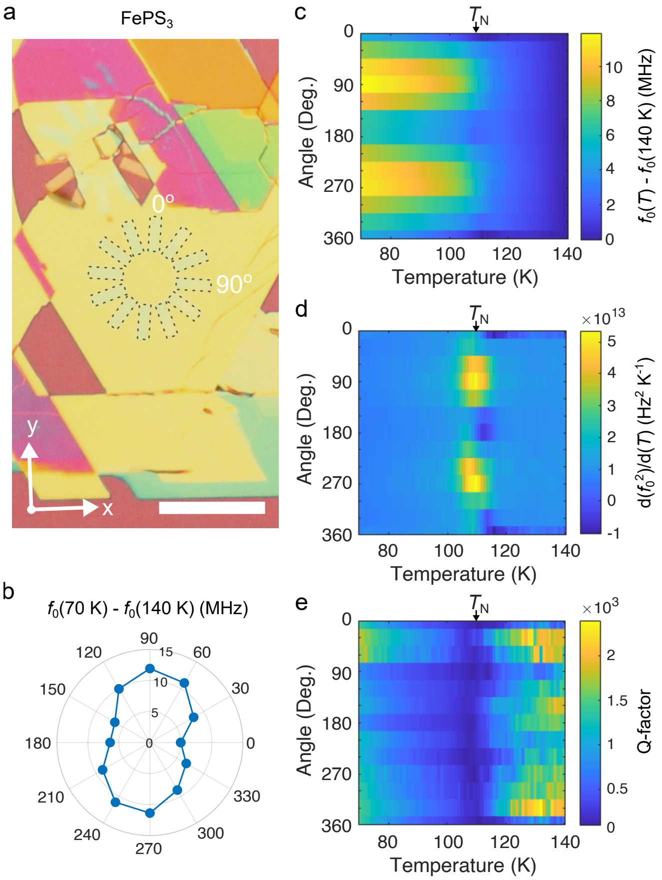

Figure 10.3: Array of rectangular membrane resonators of FePS$_3$. **a** Optical image of the membrane array. Angle is indicated with respect to x axis. Dashed lines highlight the resonators. Scale bar: 36 μm. **b** Anisotropy in $f_0(70\,\mathrm{K}) - f_0(140\,\mathrm{K})$ between antiferromagnetic ($T < T_\mathrm{N}$) and paramagnetic ($T > T_\mathrm{N}$) phase. **c** Resonance frequency difference, $f_0(T) - f_0(140\,\mathrm{K})$, as a function of angle and temperature. **d** $\frac{\mathrm{d}f_0^2}{\mathrm{d}T}$ as a function of angle and temperature. **d** Mechanical q-factor as a function of angle and temperature.

In previous studies, magnetostriction in CoPS$_3$ was attributed to 3d^7 electronic configuration of Co^{2+}, which implies spin-orbit coupling in CoPS$_3$ that accounts for the magnetic anisotropy and induces the structural change under a magnetic phase transition [61]. In order to confirm that the observed effect is indeed related to spin-orbit coupling induced magnetostriction, we also fabricate an array of $\mathrm{FePS_3}$ rectangular membranes, as shown in Fig. 10.3a. $\mathrm{Fe^{2+}}$ in $\mathrm{FePS_3}$ has $3\mathrm{d}^6$ electronic configuration, that would also produce similar effect [296].

As shown in Fig. 10.3b, a similar "dumbbell"-shaped trend is observed as the membranes of $\mathrm{FePS_3}$ are cooled trough its $T_\mathrm{N} = 115$ K. This also corresponds to a hardening of f_0 as a function of angle with a period of 180°, as visualised in Fig. 10.3c. The angular dependence of $\frac{\mathrm{d}f_0^2}{\mathrm{d}T}$ is also well-visible in Fig. 10.3d with the most prominent features confined in a small region of temperatures near the T_N. In contrast to $\mathrm{CoPS_3}$, no angle-dependent features were observed in the quality factor of these membranes at the T_N, as shown in Fig. 10.3e.

10.1.3. RELATION TO THE ORDER PARAMETER

The magnetostriction-related strain, that is responsible for the observed behaviour, is quadratic in antiferromagnetic order parameter along the easy axis L (see Chapter 6) as $\epsilon_\mathrm{ms,x} = \lambda_x L^2$ and $\epsilon_\mathrm{ms,y} = \lambda_y L^2$, where $\lambda_{x,y}$ are the phenomenological magnetostriction coefficients in x and y direction [294, 298]. Thus, by substituting Eq. 10.3 into 10.2 and taking the difference between $f_{0°}^2$ and $f_{90°}^2$, the final relation between $f_{0°}^2 - f_{90°}^2$ and order parameter L is given by:

$$f_{0°}^2 - f_{90°}^2 = f_{0°}^2(140K) - f_{90°}^2(140K) + \frac{1}{4}\frac{E}{\rho w^2}\lambda_x L^2 - \frac{1}{4}\frac{E}{\rho w^2}\lambda_y L^2, \tag{10.4}$$

which is rewritten in terms of $f_{x,y}^2(T) = f_0^2(T) - f_0^2(140K)$:

$$f_x^2 - f_y^2 = \frac{1}{4}\frac{E}{\rho w^2}\left[\lambda_x - \lambda_y\right] L^2. \tag{10.5}$$

We first note that from Eq. 10.5 it is possible to estimate the magnetostrictive product $(\lambda_x - \lambda_y)L^2(T)$. We use Eq. 10.5 to access the critical behaviour of the antiferromagnetic order parameter below T_N for $\mathrm{CoPS_3}$. In doing that we first measure $f_{0°}$ and $f_{90°}$ of this compound, as shown in Fig. 10.4a. We then plot corresponding $f_x^2 - f_y^2$ as a function of temperature in Fig. 10.4b. The trend shows a classical critical behaviour with a non-zero order parameter appearing in the ordered state at $T < T_\mathrm{N}$. We fit the region near T_N using a power-law $L^2 \propto (1 - \frac{T}{T_\mathrm{N}})^{2\beta}$ to extract the critical exponent β. For $\mathrm{CoPS_3}$, we extract $2\beta = 0.64 \pm 0.02$ for $T > 0.83T_\mathrm{N}$. The extracted 2β is also consisted with $2\beta = 0.60$ for $T > 0.9T_\mathrm{N}$ previously measured on bulk $\mathrm{CoPS_3}$ using neutron diffraction [62].

We have also applied the same analysis to $\mathrm{FePS_3}$ which we show in Fig. 10.4d-f. We have obtained $2\beta = 0.76 \pm 0.06$ for $T > 0.92T_\mathrm{N}$ which is higher than expected for 2D or 3D Ising model and is closer to that of 3D Heisenberg critical behaviour [42, 299, 300]. However, this value is consisted with the critical exponent of 0.37 measured in $\mathrm{FePS_3}$ near T_N using Raman spectroscopy [45].

10.1.4. MATERIALS WITH WEAK MAGNETOSTRICTION

Materials studied thus far in this work are compounds with large spin-orbit coupling induced magnetostriction [61, 294, 298]. It is informative to also apply the method to ma-

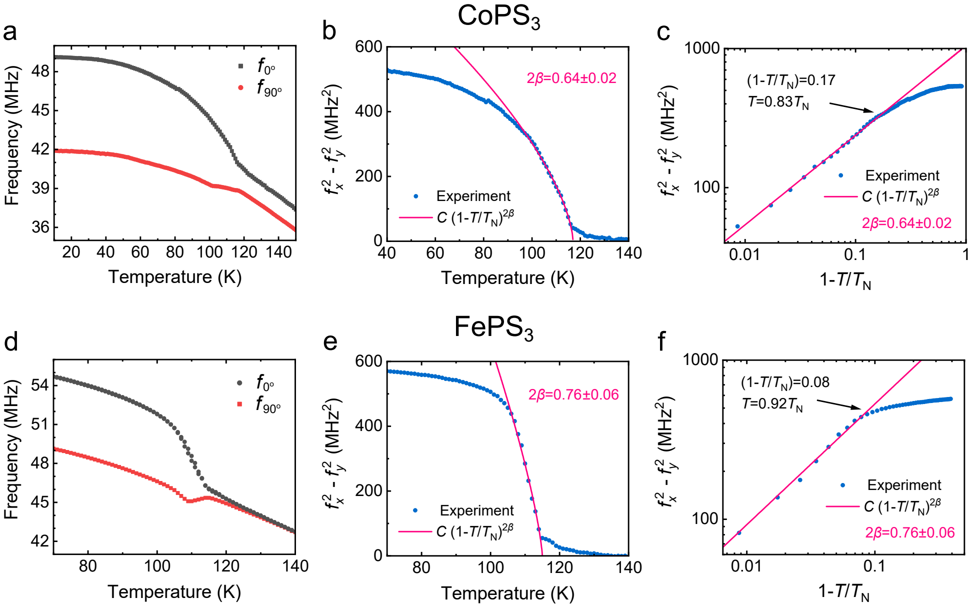

Figure 10.4: Critical behaviour in resonance frequency of CoPS$_3$ and FePS$_3$ membranes. **a** Resonance frequency of 0° and 90° membranes from Fig. 10.2. **b** Order parameter related difference of the frequency squared from Eq. 10.5. Magenta line is the fit to the power-law. Critical exponent 2β extracted from the fit indicated. **c** Difference of the frequency squared from Eq. 10.5 and the fit from (b) as a function of the reduced temperature $(1-\frac{T}{T_N})$. Black arrow indicates the deviation from the fit at $T \ll T_N$. **d-f** follows the same structure as (a-c) for FePS$_3$ membrane resonators in Fig. 10.3.

terials with weak magnetostriction effect. To accomplish this we use the Ni^{2+} compound of the MPS$_3$ family. We fabricate membranes of NiPS$_3$ of similar dimensions to those reported above, as shown in Appendix Fig. 10.6a. The difference between $f_{0°}$ and $f_{90°}$, that we plot in Fig. 10.5b, is substantially smaller than that of Fe/CoPS$_3$ membranes. In fact, the weakly anisotropic mechanical behaviour produces only small angular dependence for all studied mechanical parameters, as displayed in Appendix Fig. 10.6c-f. Nevertheless, we measure $f_{0°}$ and $f_{90°}$ of NiPS$_3$ compound, as shown in Fig. 10.5a, and then plot corresponding $f_x^2 - f_y^2$ as a function of temperature in Fig. 10.5b, following the analysis from above. Because even for the small magnetostriction effect the relation between the squared-frequency difference and order parameter given by the Eq. 10.5 holds, using the analysis described above we extract the critical exponent $2\beta = 0.62 \pm 0.08$, as shown in Fig. 10.5b,c. This is larger than $\beta = 0.22 \pm 0.02$ that was previously found from softening of the magnon modes in NiPS$_3$ [65] but consistent with $2\beta = 0.60 \pm 0.01$ reported from the neutron powder diffraction experiments [301]. Interestingly, when compared to CoPS$_3$ and FePS$_3$, NiPS$_3$ exhibits the effect which is more than an order of magnitude smaller, as we show in Fig. 10.5d.

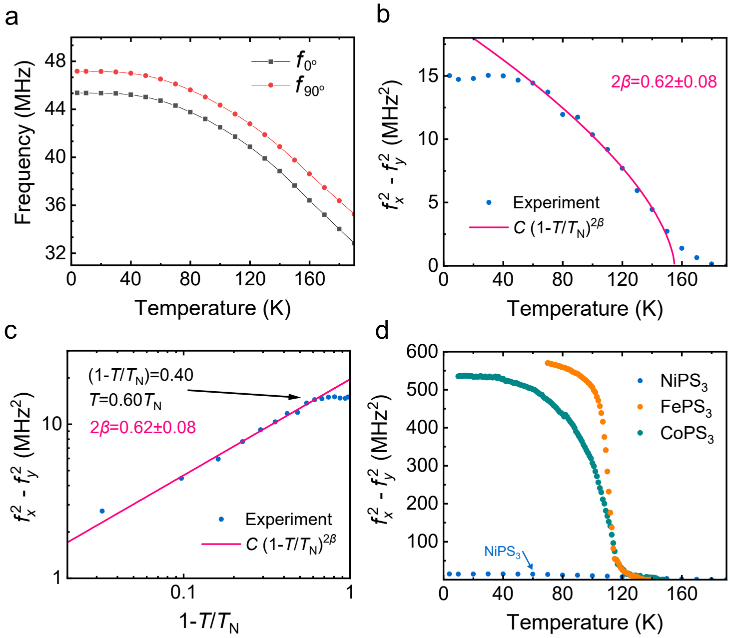

Figure 10.5: Critical behaviour in resonance frequency of NiPS$_3$ membranes. **a** Resonance frequency of 0° and 90° membranes from Appendix Fig. 10.6. **b** Order parameter related difference of the frequency squared from Eq. 10.5. Magenta line is the fit to the power-law. Critical exponent 2β extracted from the fit indicated. **c** Difference of the frequency squared from Eq. 10.5 and the fit from (b) as a function of the reduced temperature $(1-\frac{T}{T_N})$. Black arrow indicates the deviation from the fit at $T \ll T_N$. **d** Comparison of $f_x^2 - f_y^2$ in CoPS$_3$, FePS$_3$ and NiPS$_3$ samples from Fig. 10.2, 10.3 and 10.6, respectively.

10.2. OUTLOOK

The approach presented in this chapter allows access to the order parameter through purely nanomechanical methods even in the absence of a magnetic field. This can be useful for studies of 2D materials with high magnetostriction, in which the critical behavior is hard to study since the transition temperature and magnetisation is strongly dependent on the magnetic field [42, 47, 302]. In addition, this result is essential since it can provide an alternative to optical methods for studying the critical phenomenon near magnetic phase transitions in two-dimensional systems [45, 61]. This becomes especially applicable for studying 2D XY systems where, strictly speaking, long-range magnetic order cannot exist at finite temperature without the presence of magnetic anisotropy [42, 303]. For instance, in 2D CoPS$_3$, the KT transition is expected at lower temperatures [61]. Raman spectroscopy studies show that the transition is visible through Raman modes, which indicates a robust magnetoelastic coupling [61]. Yet, it was challenging to obtain a critical exponent from these data. The method presented in this work might help in understanding the KT phase in CoPS$_3$ material and ordering of spins in 2D.

The study of magnetostriction is interesting for a better understanding of magnetoelastic interactions in 2D crystals. It may open up more possibilities for controlling and tuning the spin ordering [281, 302]. In addition to that, this method, together with the method for detecting the transition temperature presented in Chapter 6, can also be applied to materials with electrical phases (in part discussed in Chapter 12). Thus, it is anticipated that this can also help in the study of the analogous phenomenon of electrostriction in ferroelectric van der Waals materials of the reduced dimensionality, like $CuInP_2S_6$ [304].

10.3. APPENDIX

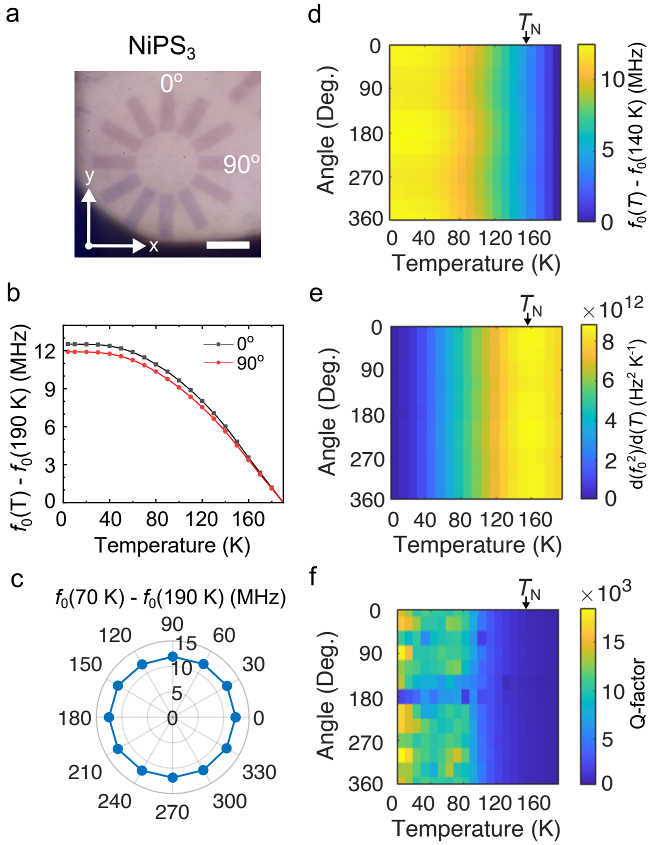

Figure 10.6: Array of rectangular NiPS$_3$ membrane resonators. **a** Optical image of the membrane array. Angle is indicated with respect to x axis. Scale bar: 12 μm. **b** $f_0(T) - f_0(190\,\mathrm{K})$ for 0° and 90° membrane as a function of temperature. **c** Anisotropy in $f_0(70\,\mathrm{K}) - f_0(190\,\mathrm{K})$ between antiferromagnetic ($T < T_\mathrm{N}$) and paramagnetic ($T > T_\mathrm{N}$) phase. **d** Resonance frequency difference, $f_0(T) - f_0(140\,\mathrm{K})$, as a function of angle and temperature. **e** $\frac{\mathrm{d}f_0^2}{\mathrm{d}T}$ as a function of angle and temperature. **f** Mechanical q-factor as a function of angle and temperature.

11

THERMOELASTIC PROPERTIES OF ANTIFERROMAGNETIC MEMBRANES

In the previous chapters we have shown that the resonance frequency of two-dimensional (2D) layered compounds can be used to characterize the magnetoelastic properties of 2D layered compounds. In antiferromagnetic resonators made out of $FePS_3$ *the mechanical damping was observed to increase dramatically near the magnetic transition temperature, showing a peak at the Néel temperature* T_N*. This chapter investigates and discusses the mechanical damping effect in these membranes in more detail, and in addition measures the thermal time constant, providing more insight in the membrane's thermodynamics near* T_N*. We propose a thermoelastic mechanism, which can account for the observed anomalous trend in the quality factor. We measure the quality factor and characteristic thermal relaxation time constant of the* $FePS_3$ *membrane using two different experimental methods. We confirm that the thermal time constant of the membrane plays an important role in explaining the mechanical damping trend. The results suggest that understanding the relationship between magnetism and thermoelastic properties is essential in the studies of magnetic 2D materials, as it can find new applications in the future, like the realization of the control over damping, thermal conductance and other thermodynamic properties using magnetic field or strain.*

MECHANICAL strain, thermodynamics and magnetism are inextricably coupled phenomena in layered van der Waals crystals. This coupling makes it possible to probe and tune the magnetic order in two-dimensional materials using strain [57, 67]. Perhaps, nanomechanical membrane resonators represent one of the most convenient ways to measure and control membrane tension through their resonance frequency on the device level [5]. However, resonant vibrations of these membranes are damped via the loss of mechanical energy via various processes [135].

One of the key processes that dictates the loss of mechanical energy in membrane resonators is heat generation and diffusion [67, 127, 135]. Studies of dissipation and thermal conductivity in 2D materials are an ongoing research topic [305], which also entails some unparalleled thermal management applications [306]. Currently, only the thermal conductivity of ultrathin layers and membranes of conventional 2D materials, such as graphene, hBN, MoS_2, or $MoSe_2$, has been studied [16, 78, 79, 127]. As a consequence, there is little knowledge available on the effect of phase transitions, like those in the magnetic metal phosphorus trisulfides (e.g., $FePS_3$), on thermal transport[67].

In this chapter we argue that a thermoelastic damping mechanism [229, 307] couples mechanical dissipation to magnetism-related features in thermodynamic quantities [67]. The analysis of the Q^{-1} presented in Chapter 6 describes the appearance of the peak near T_N. However, it lacks both qualitative and quantitative agreement with the experiment over a wider temperature range. In this work, we use nanomechanical methods [67, 127] to study simultaneously both thermal relaxation time and thermoelastic damping. Thus, the further detailed explanation for the phenomenon and inclusion of thermal conductivity effect to the thermoelastic damping is examined and discussed.

11.1. RESULTS AND DISCUSSION

11.1.1. $FePS_3$ MEMBRANE RESONATORS

We fabricate the $FePS_3$ membrane resonator, shown in Fig. 11.1a, using an approach similar to that described in Chapter 2 and 6. We measure the resonance frequency of the membrane f_0 using the laser interferometry technique. As shown in Fig. 11.1b (filled blue dots), f_0 builds up with decreasing temperature T revealing the region of highest slope in proximity of T_N. This is well-visible also in a derivative of f_0^2, as displayed with filled dark grey dots in Fig. 11.1b. The peak in $\frac{\mathrm{d}(f_0^2(T))}{\mathrm{d}T}$, produced by the discontinuity in c_v (see Eq. 6.2 in Chapter 6) indicates the phase change from paramagnetic to antiferromagnetic state at the T_N. At the same time, the measured inverse quality factor Q^{-1}, the mechanical energy dissipation term, also shows a maximum at T_N, as indicated in Fig. 11.1c. This behaviour is similar to that described and analyzed in Chapter 6, and in this chapter we will study it in more detail.

11.1.2. THERMOELASTIC DAMPING IN $FePS_3$ RESONATORS

We proposed that the mechanical damping in $FePS_3$ membrane resonators is dictated by a thermoelastic damping mechanism [67]. The thermoelastic damping Q_{TED}^{-1} is best

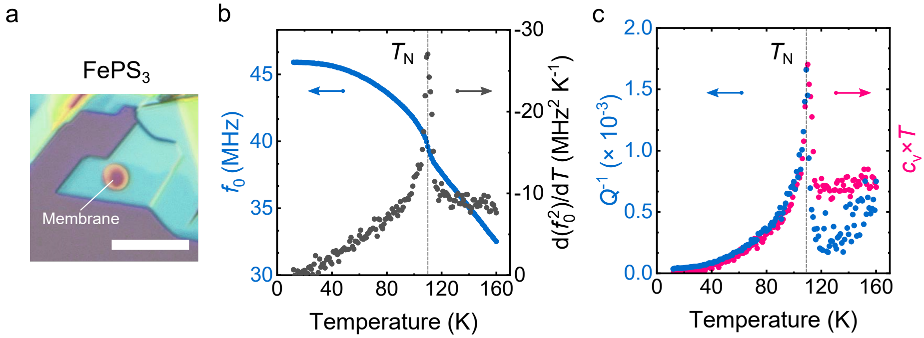

Figure 11.1: Membrane resonator of FePS$_3$. **a** Optical image of the sample. Suspended membrane is indicated. Scale bar: 18 μm. **b** Mechanical properties of the membrane. Filled blue dots - measured resonance frequency of the fundamental membrane mode f_0. Filled dark grey dots - temperature derivative of f_0^2. **c** Mechanical damping. Filled blue dots - measured inversed quality factor Q^{-1}. Filled magenta dots - thermoelastic damping related term $c_v \times T$ [229] (see Chapter 6). Vertical lines in (b) and (c) indicate the detected T_N.

described by the modified Lifshitz-Roukes formulation Q^{-1}_{LR} as [229, 307–309]:

$$
\begin{aligned}
Q^{-1}_{TED} &= \mu Q^{-1}_{LR} = \mu \Delta_E \Gamma(\omega, \tau) \\
&= \mu \left[\frac{E \alpha_L^2 T}{c_v \rho} \right] \left[\frac{6}{\xi^2} - \frac{6}{\xi^3} \frac{\sinh \xi + \sin \xi}{\cosh \xi + \cos \xi} \right],
\end{aligned}
\tag{11.1}
$$

where $\xi = \frac{\pi}{\sqrt{2}} \sqrt{\omega \tau}$, $\omega = 2\pi f_0$ is the resonance frequency, μ the correction pre-factor, Δ_E the relaxation strength, Γ the dissipation peak function, E the Young's modulus, α_L the linear thermal expansion coefficient, ρ the mass density, and τ the thermal time constant. The pre-factor μ varies depending on the geometry of the resonator [229, 307], type of vibration [309], heat conduction [308], and pre-tension [310]. For the circular plate resonator with axisymmetric out-of-plane vibration it is expected to be $\mu = \frac{1+\nu}{1-2\nu}$, where ν is the Poisson's ratio [307].

In the analysis described in Chapter 6, with the approximation $\alpha_L \propto c_v$, it was assumed that Γ is independent of temperature such that $\Delta_E \propto c_v \times T$ term has a predominant contribution near T_N and can indeed describe the appearance of the corresponding peak in Q^{-1}, as shown in Fig. 11.1c. However, this simplification leads to a poor description of Q^{-1} just above and, in some samples (e.g. Fig. 6.2), also below the T_N. This indicates a significant contribution of $\Gamma(\omega, \tau)$ to $Q^{-1}(T)$, that originates from the strong temperature dependence of thermal relaxation time constant $\tau(T)$ of FePS$_3$ near T_N.

11.1.3. THERMAL TIME CONSTANT

Lifshitz-Roukes and Sun-Saka derivations of thermoelastic damping [229, 307] considered an out-of-plane heat conduction and corresponding heat gradient that develops across the thickness of a plate resonator, which damps its motion. However, for nanometer-scale membrane thicknesses the characteristic thermal relaxation time is on the order of tens of picosecond [307], which would produce only a negligible Q^{-1} contribution. In-

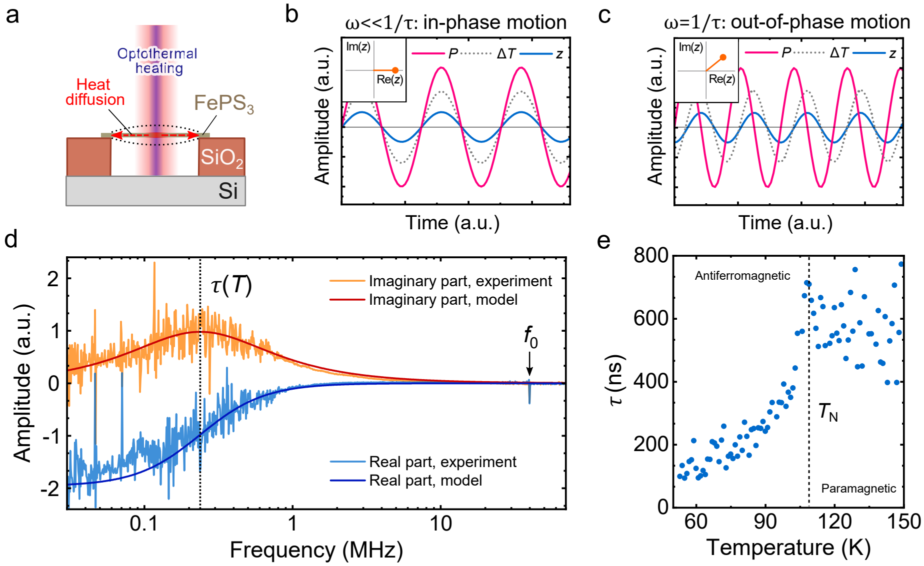

Figure 11.2: Thermomechanical characterization of the $FePS_3$ membrane. **a** Schematic of the radial heat diffusion in the membrane during the motion. **b** Schematic plot of in-phase amplitude of the optothermal heat flux P, the thermal gradient ΔT, and the membrane motion z at frequency $\omega = 2\pi f \ll \frac{1}{\tau}$. **c** Schematic plot of out-of-phase amplitude of P, ΔT, and z at $\omega = \frac{1}{\tau}$. **d** Measured real and imaginary component of z as a function of frequency at $T = 108$ K, together with the corresponding fit to the model of Eq. 11.3. Vertical line indicates the extracted thermal time constant τ at a cut-off frequency $\omega_c = \frac{1}{\tau}$. **e** Thermal time constants extracted from the measured data similar to the one shown in (d) as a function of temperature. Vertical line indicates the T_N from Fig. 11.1b and c.

stead, the dominant damping results from the heat conduction caused by the temperature gradient ΔT along the radial direction of the circular membrane [308], as schematically depicted in Fig. 11.2a. A characteristic thermal relaxation time is required to raise the temperature of the membrane. When τ is fairly short, $\omega \ll \frac{1}{\tau}$ and thus the membrane motion is in phase with the temperature gradient and the optothermal expansion force that drives the resonator, as shown in Fig. 11.2b. However, then τ is sufficiently long, it produces a delay between the optical power $P(t)$ and the temperature ΔT. (see Fig. 11.2c).

At this point, an independent method to study the thermal time constant τ is required in order to quantitatively explain thermoelastic damping-dominated Q^{-1} in the $FePS_3$ membrane from Fig. 11.1 using the model of Eq. 11.1. Several methods exist to experimentally measure τ in ultrathin membranes of 2D layered materials [78, 79, 127]. In this work, we follow the technique developed by Dolleman et al [78, 127]. We do so by optothermally exciting the membrane motion using a power-modulated blue laser and interferometrically measuring the resulting amplitude of its vibration using the red laser (see Chapter 3). In contrast to most of the experiments reported in previous chapters of this thesis, we measure the motion far below the fundamental resonance frequency f_0, in order to ensure that the position z is in phase with ΔT, such that all phase lag between

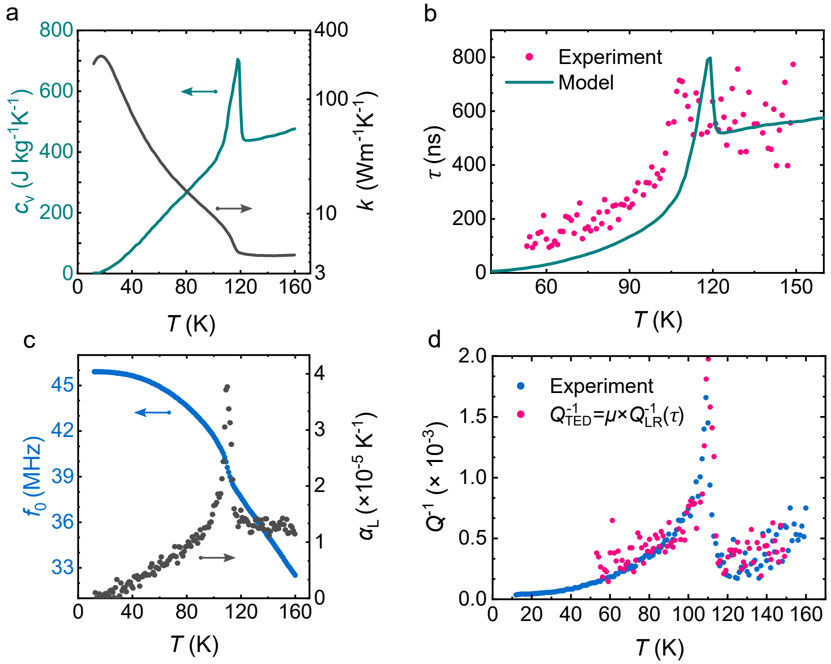

Figure 11.3: Thermal time constant and thermoelastic damping. **a** Literature values for specific heat c_V [227] and thermal conductivity k [311] of bulk FePS$_3$. **b** Measured τ from Fig. 11.2e compared to the model of Eq. 11.4 using bulk values from (a). **c** Mechanical properties of the membrane. Filled blue dots - resonance frequency f_0. Filled dark grey dots - thermal expansion coefficient α_L extracted from f_0 using Eq. 6.1. **d** Measured Q^{-1} compared to calculated Q^{-1}_{TED} from Eq. 11.1 as a function of temperature using $\mu = 8.4\left(\frac{1+\nu}{1-2\nu}\right)$.

$P(t)$ and $z(t)$ is due to thermal delay τ. Since the delay between the amplitude of membrane motion and the optothermal drive is mostly due to the heat conduction in FePS$_3$, the system can be described by the heat equation [78, 127]:

$$C\frac{\mathrm{d}\Delta T}{\mathrm{d}t} + \frac{1}{R}\Delta T = P_\omega e^{i\omega t}, \tag{11.2}$$

where C is the heat capacity, R the thermal resistance, t the time, and P_ω the heat flux. Far below the resonance frequency $\omega = 2\pi f_0$, the amplitude of the membrane motion $z = z_\omega e^{i\omega t}$ is directly related to the temperature change $z = A\Delta T$, such that:

$$z_\omega = AP_\omega R\frac{1 - i\omega t}{1+\omega^2\tau^2}, \tag{11.3}$$

where A is the proportionality constant related to the thermal expansion coefficient, and $\tau = RC$ the thermal time constant.

We measure z_ω of the FePS$_3$ membrane as a function of frequency and temperature from 52 to 150 K, that is well below and above the phase transition temperature T_N. In Fig. 11.2d, we plot the measured real and imaginary component of z_ω at $T = 108$ K as the example of typical experimental data. All parasitic electrical and optical phase shifts are measured by directly pointing the blue laser at the photodetector and are eliminated by correcting the experimental results using the measured transmission function [78, 127]. We then fit the measured data to the model of Eq. 11.3. A notable peak in imaginary amplitude is observed at $\omega_c = 2\pi \times 240$ kHz. This observation is a consequence of Eq. 11.3, that has a maximum in its imaginary part at a cut-off frequency $\omega_c = \frac{1}{\tau}$. Thus, from ω_c of the measured peak in imaginary amplitude z_ω we extract the corresponding $\tau(T)$. We plot the experimentally measured $\tau(T)$ in Fig. 11.2e. A drastic increase in τ of nearly an order of magnitude is visible as the membrane is heated across the T_N. Since many of the thermodynamic properties of $FePS_3$ abruptly change at T_N, it is of interest to investigate how these changes can account for the large change in τ.

As derived by Aubin [19, 312] and later experimentally verified for different 2D material membranes by Dolleman et al [78, 127], the thermal time constant for a uniformly heated circular membrane is given by:

$$\tau = \frac{r^2 \rho c_v}{2.4048^2 k}, \tag{11.4}$$

where $r = 3$ μm is the membrane radius, and k the thermal conductivity of the material. To validate our experimental observation, we take literature values $c_v(T)$ and $k(T)$ measured for bulk $FePS_3$ [227, 311], as shown in Fig. 11.3a, and plot the model of Eq. 11.4 together with the measured $\tau(T)$ in Fig. 11.3b. We obtain a remarkable quantitative correspondence between the model and the experiment. We also note that the experimental peak in τ of the thin membrane is somewhat lower than the model value based on bulk properties. The most likely explanation for this discrepancy is the effect of thermal strain accumulated in the membrane, as T_N shifts to lower values as a function of strain in $FePS_3$ (see Chapter 6). Another less probable reason for this observation can be the thickness dependence of T_N that is disputed in this compound [45, 313].

The observed large change in τ confirms the hypothesis that $\Gamma(\omega,\tau)$ has a strong temperature dependence and a significant effect on the Q^{-1}_{TED}. We thus use $E = 103$ GPa, $\nu = 0.304$ and $\rho = 3375$ kg m^{-3} [59], literature values for $c_v(T)$ and $k(T)$ [227, 311] from Fig. 11.3a, together with measured $\omega = 2\pi f_0(T)$ and $\alpha_L(T)$ of the $FePS_3$ membrane from Fig. 11.3c (see Chapter 6 for methods) and the experimentally measured $\tau(T)$ from Fig 11.3b to calculate $Q^{-1}_{\text{TED}}(T)$ using Eq. 11.1. The resulting calculation fits the experimental data well with the pre-factor $\mu = 8.4\left(\frac{1+\nu}{1-2\nu}\right)$, as shown by the magenta points in Fig. 11.3d. The good correspondence in Fig. 11.3d provides qualitative evidence that thermodynamic damping, and its dependence on the thermal time constant, plays a significant role in determining the Q-factor of magnetic membranes near the phase transition. The proportionality coefficient of 8.4 to μ from the circular plate model of Sun and Saka [307] suggests that the obtained values are reasonable, although more elaborate models to derive Eq. 11.1 in the membrane limit will be needed for further quantitative interpretation of the value of the pre-factor μ [308–310].

11.2. OUTLOOK

The strong relation of the quality factor of magnetic membranes to their thermodynamic material properties opens up interesting directions for further study. In future, when the full equation for Q_{TED}^{-1}, including the exact solution for pre-factor μ, is established for circular membranes under tension, a comprehensive thermal characterisation of the measured material can be carried out using a single type of measurement by analysing $f_0(T)$ and $Q^{-1}(T)$. This contrasts to other methods that are currently available where thermal and mechanical characterisation is usually performed by two separate experiments [78, 79, 127].

In addition to that, the relation of τ to the the thermal conductivity k may bring new knowledge about coupling between magnetic and thermal properties of layered ultrathin van der Waals magnets. This is particularly interesting in materials that become anisotropic in the magnetic state, like FePS_3 and CoPS_3 (see Chapter 10). Due to the structural distortion and resulting anisotropy at $T < T_\text{N}$ these materials may also exhibit anisotropic in-plane k, that may affect the τ of rectangular membranes and bridges as a function of angle to crystalline axes, consequently also affecting the measured Q.

Finally, an important factor is that all the presented methods are applicable to ultrathin membrane thicknesses and thus can be applied to thermally characterise thin 2D materials down to the single atom limit [78, 127], including those that exhibit various phase transitions. Understanding the thermal transport in 2D compounds is important as it may lead to high-performance applications [305, 306]. By utilizing 2D materials with specific properties one can establish new heat management and control options. In particular, the use of magnetic ultrathin 2D membranes may in the future lead to magnetic field control of thermal properties and mechanical dissipation in membranes and resonators of this kind. Also, since 2D materials can be stacked to form heterostructures [30, 42], in the future this could be utilized to artificially create materials of desired thermal and functional properties [314]. Thus, we anticipate that the presented methods can help to understand complex thermal transport in 2D material heterostructures [314] for various electronic device concepts, nanoelectromechanical systems and sensors.

12

ELECTRONIC SECOND-ORDER PHASE TRANSITIONS PROBED BY NANOMECHANICS

The relation between resonance frequency of membrane resonators and its specific heat has a general thermodynamic nature. The nanomechanical detection scheme presented in Chapter 6 is thus not limited to magnetic materials, and can therefore also be applied to electronic second-order phase transition systems, such as the charge density wave (CDW) materials. The CDW state in van der Waals systems shows interesting scaling phenomena as the number of layers can significantly affect the CDW transition temperature, T_{CDW}*. However, it is often difficult to use conventional methods to study the phase transition in these systems due to their small size and sensitivity to degradation. In this chapter, we probe the CDW phase transition by the mechanical resonances of suspended* $2H$-TaS_2 *and* $2H$-$TaSe_2$ *membranes. Materials show the transition near the reported literature values of 75 K and 122 K, respectively. We discuss the potential of using nanomechanical resonance to characterize the CDW and other electronic phase transitions in suspended 2D materials.*

Parts of this chapter have been published in *Applied Physics Letters* **118**, 19, 193105 (2021) and *Nature Communications* **11**, 2698 (2020) by Makars Šiškins, Martin Lee, Samuel Mañas-Valero, Eugenio Coronado, Yaroslav M. Blanter, Herre S. J. van der Zant and Peter G. Steeneken

The charge density wave (CDW) state in van der Waals (vdW) materials has recently become a resurgent area of research. Recent works on surprising and unexpected layer dependence and degradation effects on superconductivity (SC) and CDW in systems such as 2H-NbSe$_2$, 2H-TaS$_2$, and 2H-TaSe$_2$ have revived interest in studying their phase transitions [36, 315, 316]. For example, the superconducting transition temperature T_{SC} of 2H-NbSe$_2$ is decreased from 7.2 K in the bulk to 3 K in the monolayer limit, while the CDW transition temperature T_{CDW} is increased [317] from 33 K to 145 K. More surprisingly, the 2H-TaS$_2$ has a T_{SC} of 0.6 K in the bulk which increases to 3 K in a monolayer [36, 315] and a T_{CDW} of 75 K which also increases to 140 K [318]. Similar scaling is seen for T_{SC} in 2H-TaSe$_2$ [319]. It is an ongoing challenge to clarify these contradicting layer dependencies in order to shine light on the competition between CDW and SC in these materials.

The CDW transition, like other first and second order phase transitions, can be described by Landau's theory of phase transitions [105, 106], where the emergence of charge order gives rise to a sudden change in the specific heat. Measurement of the specific heat anomaly to probe the phase transition, however, is challenging for ultrathin exfoliated 2D material flakes using traditional methods. Recent works on using nanomechanical resonance to extract various phase transitions including structural, magnetic (also see Chapter 6), and electronic phase transitions have shown to provide a promising alternative [2, 41, 57, 67].

In this work, we study the CDW transitions of suspended 2H-TaS$_2$ and 2H-TaSe$_2$ flakes by tracking the temperature dependence of their nanomechanical resonance frequency. The resonance frequency of suspended pristine 2H-TaS$_2$ and 2H-TaSe$_2$ flakes shows an anomaly at the phase transition temperatures of 75 K and 122 K, respectively. We then discuss the results and provide the outlook for this technique as a probe to study the effect of degradation on the T_{CDW} in these compounds.

12.1. RESULTS AND DISCUSSION

12.1.1. RELATION OF RESONANCE FREQUENCY TO ELECTRONIC ORDER

The anomalous discontinuity in specific heat at the second-order phase transition temperature and its relation to the resonance frequency is a consequence of thermodynamic relations and thus can be described also for a specific case of the normal—CDW phase transition by applying Landau theory of second-order phase transitions [105, 106]. The Landau free energy can be written for CDW transitions as:

$$F = F_0 + a(T - T_{\mathrm{CDW}})\psi^2 + B\psi^4, \tag{12.1}$$

where F_0 is the temperature-dependent free energy of the normal state, ψ is the order parameter, and a and B are phenomenological positive constants. Minimizing the above equation with respect to ψ (i.e., $\partial F/\partial\psi = 0$) gives the CDW order parameter,

$$\psi = \sqrt{\frac{-a(T - T_{\mathrm{CDW}})}{2B}}, \tag{12.2}$$

and a minimum free energy $F_{\mathrm{min}} = F_0 - \frac{a^2}{4B}(T - T_{\mathrm{CDW}})^2$. Using the relation for the specific heat at constant pressure, $c_{\mathrm{p}}(T) = -T[\frac{\partial^2 F}{\partial T^2}]_p$ and by substituting the expression for

F_{min} into Eq. 12.1, the magnitude of the jump in the specific heat at the phase transition can be derived as $\Delta c_{\text{p}} = \frac{a^2 T_{\text{CDW}}}{2B}$. The relationship between the membrane resonance frequency $f_0(T)$ of a circular membrane under thermal strain, with $c_{\text{p}}(T) \simeq c_{\text{v}}(T)$, can be described by

$$f_0(T) = \frac{2.4048}{\pi d}\sqrt{\frac{E}{\rho}\frac{\epsilon(T)}{(1-\nu)}}, \tag{12.3}$$

where d is the membrane diameter, E is the Young's modulus, ρ is the density, ν is the Poisson's ratio, and $\epsilon(T)$ is the temperature-dependent biaxial strain. The thermal strain accumulated in the membrane is a result of the linear thermal expansion coefficient of the membrane α, that is related to specific heat as: $-\frac{\mathrm{d}\epsilon(T)}{\mathrm{d}T} \propto \alpha(T) \propto c_{\text{v}}(T)$. Thus the abrupt change in the specific heat results in a jump in a derivative of the square of the frequency in Eq. 12.3: $\Delta\frac{\mathrm{d}(f_0^2(T))}{\mathrm{d}T} \propto \Delta c_{\text{v}}(T)$. Detailed discussion on this relation can be found in Chapter 6. Through this relation, we can probe the T_{CDW} from determining the discontinuity in $\frac{\mathrm{d}(f_0^2(T))}{\mathrm{d}T}$.

12.1.2. PROBING CHARGE DENSITY WAVE TRANSITION IN 2H-TaS$_2$

In order to demonstrate the detection of a charge density wave transition, we now discuss results for 2H-TaS$_2$ that in bulk exhibits a CDW transition at $T_{\text{CDW}} \sim 77$ K [320]. Figure 12.1a shows a transition-related anomaly in both $f_0(T)$ (solid blue line) and the temperature derivative of $f_0^2(T)$ (solid magenta line) that peaks at 75 ± 3 K. We convert $\frac{\mathrm{d}(f_0^2(T))}{\mathrm{d}T}$ to the corresponding $c_{\text{v}}(T)$ using the same approach as discussed before in Chapter 6 (see Eq. 6.2). We use reported values of $E_{\text{2D}} = 87$ N m^{-1} and $\nu = 0.27$ for a monolayer of 1H-TaS$_2$ obtained from molecular dynamics simulations [122] and mass density $\rho = 6110$ kg m^{-3}. We find the corresponding $E = E_{\text{2D}}/t = 149$ GPa, taking the interlayer spacing $t = 0.58$ nm.

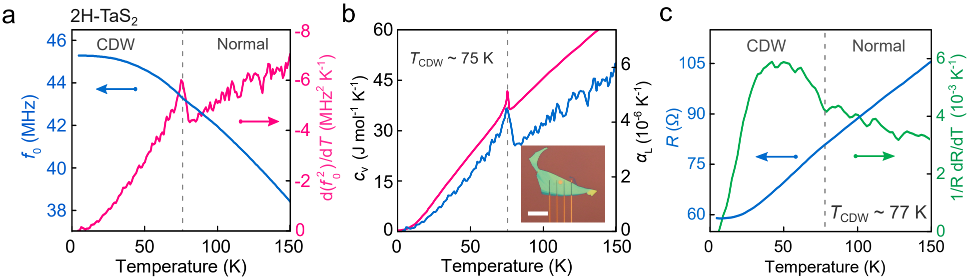

Figure 12.1: Mechanical properties of a 2H-TaS$_2$ resonator with membrane thickness of 31.2 ± 0.6 nm and $d = 4$ μm. **a** Solid blue line - resonance frequency as a function of temperature. Solid magenta line - temperature derivative of f_0^2. **b** Solid blue line - experimentally derived c_{v} and thermal expansion coefficient as a function of temperature. Solid magenta line - specific heat of bulk 2H-TaS$_2$ as reported in Abdel-Hafiez et al. [320]. Inset: optical image of the sample. Scale bar: 20 μm. Dashed vertical line in (a) and (b) indicates the detected T_{CDW}, that is defined by the peak in $\frac{\mathrm{d}(f_0^2(T))}{\mathrm{d}T}$. **c** Solid blue line - four-point resistance of the same sample. Solid green line - $\frac{1}{R}\frac{dR}{dT}$ plot showing the CDW related feature at T_{CDW} (dashed vertical line).

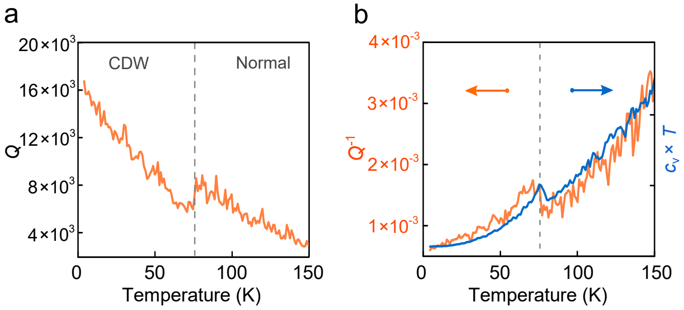

Figure 12.2: Mechanical dissipation of a 2H-TaS$_2$ resonator. Dashed vertical lines in the panels indicate the transition temperature, T_{CDW}. **a** Quality factor $Q(T)$ as a function of temperature. **b** Solid orange line - measured mechanical damping $Q^{-1}(T)$ as a function of temperature. Solid blue line - curve proportional to the term $c_{\mathrm{v}}(T)\,T$ [228, 229] (see Chapter 6), with $c_{\mathrm{v}}(T)$ taken from the experimental data in Fig. 12.1b.

The estimated specific heat of the 2H-TaS$_2$ membrane is depicted in Fig. 12.1b (solid blue line). Figure 12.1b shows a downward step in the specific heat at 75 K (solid blue line), indicative of a phase transition from the CDW to the disordered high-temperature state [106, 119] with a good correspondence to c_{v} measured in a bulk crystal [320] (drawn magenta line). It indicates that it is the anomaly in c_{v} of 2H-TaS$_2$ which produces the most dominant of the observed changes in resonance frequency and the large peak in $\frac{\mathrm{d}(f_0^2)}{\mathrm{d}T}$ visible in Fig. 6.2a. The changes in the Young's modulus near the CDW phase transition can be of the order of a couple of percent [40, 41] but they alone cannot explain the observed trend and thus are less significant [67, 124].

The four-probe resistance was measured on the same flake to confirm the existence of a CDW transition using a conventional electronic based method as shown in Fig. 12.1c. A small kink in $\frac{1}{R}\frac{dR}{dT}$ is observed in the electrical data shown in Fig. 12.1c at ~ 77 K. The anomaly in c_{v} occurs near the electrically determined phase transition temperature of ~ 77 K on the same flake and is also consistent with the CDW transition temperature previously reported in 2H-TaS$_2$ [320].

The Q-factor also shows a local minimum with a drop next to the transition temperature, as we shown in Fig. 12.2a. Due to the thermoelastic damping [228, 229] (see Chapters 6 and 11), $Q^{-1}(T)$ is expected to follow the same trend as $c_{\mathrm{v}}(T)\,T$ if the material's thermal conductivity contribution is either negligible or weakly temperature dependent. Both these quantities are displayed in Fig. 12.2b and indeed show a good qualitative correspondence.

12.1.3. CHARGE DENSITY WAVE TRANSITION IN 2H-TASE$_2$

We also demonstrate that the nanomechanical detection scheme is applicable to other CDW materials [41, 101] by probing T_{CDW} of 2H-TaSe$_2$. We fabricated a membrane of 2H-TaSe$_2$ that is also contacted electrically, as displayed in Fig 12.3a. The solid green line in Fig. 12.3b shows the specific heat-related temperature derivative of f_0^2 that reveals a clear peak at T_{CDW} ~ 122 K. We also have measured the four-probe resistance on the same flake and confirm the existence of a CDW transition as shown in Fig. 12.3c. The expected characteristic kink in the resistance is visible at ~ 124 K, consistent with the

CDW transition temperature previously reported in 2H-$TaSe_2$ [319].

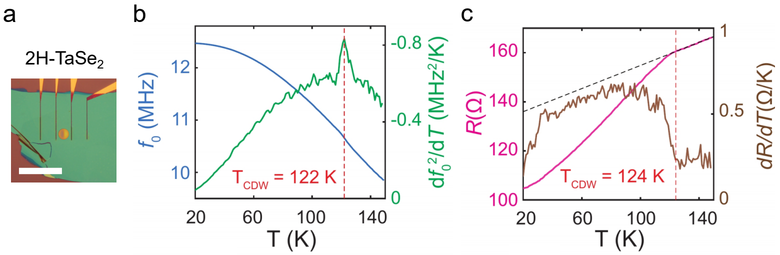

Figure 12.3: Mechanical properties of a 2H-$TaSe_2$ resonator with membrane thickness of 23.3 ± 0.5 nm, $d = 10$ μm.**a** Optical image of the sample. Scale bar: 40 μm. **b** Solid blue line - resonance frequency as a function of temperature. Solid green line - temperature derivative of f_0^2. **c** Solid magenta line - four-point resistance of the same sample. Solid brown line - $\frac{dR}{dT}$ plot showing the CDW related feature near T_{CDW}. Dashed vertical lines in panels (b) and (c) indicate the corresponding detected transition temperatures, T_{CDW}.

12.2. OUTLOOK

In this work, we studied the effect of electronic second-order phase transitions on nanomechanics. We have probed CDW transitions in the archetypal vdW systems 2H-TaS_2 and 2H-$TaSe_2$, by using the resonance frequency of suspended membranes. The temperature dependence of the resonance frequency can be translated into the specific heat, which shows an anomaly at the phase transition temperature. As the CDW state in van der Waals systems shows interesting scaling phenomena with the number of layers, we anticipate that the nanomechanical resonance is a powerful tool to study the CDW transitions in ultrathin-suspended vdW materials complementary to the temperature-dependent electronic transport [315].

Another matter is that the degradation in air is an important parameter, which has been shown to greatly influence the superconductivity in layered systems [316]. Since the CDW state competes with the onset of superconductivity, it is expected that T_{CDW} will also be affected by the degradation. In other published work of ours [124], we studied the effect of degradation on 2H-TaS_2 using the mechanical resonance. We observed a significant enhancement of T_{CDW} up to 129 K after degradation in ambient air. We also studied a sample with local degradation and observe that multiple phase transitions occur with a hysteresis in temperature in the same membrane[*] [124]. We note that it shows the potential of using nanomechanical resonance to characterize the CDW in suspended 2D materials even in the degraded state and demonstrates that the degradation can have a large effect on transition temperatures. Compared to electrical transport methods, the advantage of nanomechanical probing of phase transitions is that they probe a weighted average of the material properties over the suspended area of the membrane. In contrast, electrical methods measure the properties over the path along current flows, which in the case of material non-uniformities (e.g. low resistance areas, or high contact resistances) might not reflect the average material properties as well.

---

[*] This work will be discussed in details in the Ph.D. thesis of Lee, M., TU Delft.

Furthermore, we believe that the method described in this chapter is applicable also to other types of electric phase transitions in ultra-thin layers, such as ferroelectricity and superconductivity as both of these exhibit discontinuities in c_v at the T_c [2, 320, 321]. It is particularly attractive for 2D superconductors of extreme sensitivity in air, like BSCCO [322], where the degradation of the crystal in air has an effect on the transition temperature [316, 322]. Detecting the change in the resonance frequency could be an alternative non-invasive way to probe superconductivity by utilizing the specific heat and thermal expansion coefficient anomalies in these compounds [323, 324].

13

CONCLUSION

In this thesis we discussed a wide variety of topics, including nanomechanical characterisation methods, material properties and applications of 2D material membranes. This concluding chapter provides a summary of the results with final remarks and interpretation. Here, we share our vision for the results obtained, the feasibility of their technical implications for society, and impact on the research community.

THIS work gave an overview of the studies I carried out in the period of four years to elucidate the properties of two-dimensional materials (2D) and enable a wide range of electronic and mechanical devices. First, we described novel methods for studies of 2D material membranes that can be used as probes for various material and thermodynamic effects. Next, we discussed the mechanical properties of membranes ranging from graphene layers, notable for their properties, to more complex anisotropic membranes of As_2S_3 to the complex dynamics of membranes influenced by physical phenomena. We now reflect on the information we have gained from the experiments and present our vision of how it might affect valorization and commercial applications of these membranes, and discuss the role of dynamics and its potential impact on future nanomechanical experiments.

Intuitively, out of all 2D material membranes considered in this thesis, graphene-based membranes are the simplest from a mechanical perspective but, as a consequence, the most well-understood and thus also the closest to realize commercialization. In Chapter 4, we showed that CVD-grown graphene sheets could be used to fabricate arrays of freestanding 2D material membranes in mm^2 scales. The high flexibility, impermeability, and strength of graphene membranes are key properties that facilitated such fabrication and enabled us to use these as nanomechanical sensors. We realized highly sensitive capacitive pressure sensors out of nearly ten thousand stacked double-layer graphene membranes. These sensors have shown to outperform commercial sensors with state-of-the-art responsivity while readout using a low-cost battery-powered circuit board, which is beneficial for further integration of such chips to smart devices [6].

Interesting implementations arise also for structurally anisotropic membranes. In Chapter 5, we for the first time isolated anisotropic 2D layers of As_2S_3. We showed that the anisotropy in Young's modulus of As_2S_3 is close to that of black phosphorus, which is currently known to have the largest in-plane stiffness ratio among 2D crystals [25]. These mechanical properties make As_2S_3 an interesting alternative to black phosphorus for applications in flexible strain-dependent optoelectronic devices [185], as well as for the research of anisotropic nonlinear mechanics in the 2D limit [5]. We also believe that, due to its high flexibility [117, 211, 212, 325], promising piezoelectic [326], thermoelectric [327] and optoelectronic properties [201, 209], As_2S_3 has perspectives to become an interesting candidate material for applications in flexible electronics [187, 188, 326, 327].

Perhaps, the most central matters risen in this work revolve around the idea that nanomechanical resonators can be used as a useful tool to probe condensed matter physics. Chapter 6 presented initial evidence of the detection of second-order phase transitions and thermodynamic phenomena in van der Waals material membranes. We have demonstrated a strong coupling between mechanical motion and order in ultrathin membranes of 2D materials. This interrelation is of universal thermodynamic nature and is not limited to specific materials only, as we demonstrated by studying different phases of magnetic systems in Chapters 7, 8 and 9, and electronic charge density wave transitions in Chapter 12. We derived an analytical equation for the relation between the specific heat of the material and the temperature-dependent resonance frequency. This shows the potential of membrane resonators for probing non-mechanical effects in a large range of van der Waals materials and correlated systems [30, 42, 124], such as 2D ferromagnets [57], thin 2D complex oxide sheets [2, 234] and organic antiferromagnets

[64].

First and foremost, the presented measurements and methodologies open up possibilities to investigate magnetic and electronic properties near the monolayer 2D limit. Membranes made of a single 2D material would exclude interlayer interactions, allowing to study 2D Ising antiferromagnets [45] and ferromagnetism in 2D atomic layers [46, 47]. In addition to that, the approach presented in Chapter 10 allows to access to the magnetic order parameter through purely nanomechanical methods even in the absence of an external magnetic field. Since only a few methods are available to study critical phenomena in magnetic 2D materials [42, 45–47], mechanical resonance methods can serve as a powerful noninvasive tool to probe condensed matter phenomena related to ordering mechanisms in 2D even in materials that couple weakly to conventional magnetic, electronic, or optical probes. In addition, preliminary results in Chapter 11 show that focused studies of the mechanical dissipation in such 2D material membranes as a function of temperature, accessible with the same measurement technique, could provide insights into thermodynamics and heat transport in these layers [67, 78, 79].

Secondly, we showed that the transition temperatures in magnetic 2D material membranes could be tuned by applying the electrostatic force with the gate electrode voltage, thus straining the membranes. In Chapter 6, we demonstrated that by following this approach T_N in $\mathrm{FePS_3}$ could be reduced by at least 6 K. At the same time, T_C of ferromagnetic CGT can be enhanced using the same method. Nanomechanical strain thus offers a compelling degree of freedom to control magnetic ordering in 2D layered compounds [90]. We anticipate that these studies in the future will lead to the development of membrane devices with gate-controlled magnetic actuation [293] and low-power spintronic implementations.

Fundamental studies of this kind are essential to identify material systems and physical phenomena, that can serve people by being utilized for new data processing concepts. For instance, in Chapter 7 we have demonstrated a gate voltage dependent mechanism that mediates strong coupling between spatially separated membranes made of antiferromagnetic $\mathrm{FePS_3}$ and $\mathrm{MnPS_3}$. This coupling mechanism can enable bit-by-bit communication as well as switched on and tuned by an electrostatic gate. In addition, mechanical dissipation near the phase transition of antiferromagnetic material membranes can affect the coupling strength of such a mechanism. All these parameters, that can be tuned by temperature, electrostatic gate or other mechanical means, provide control advantages that can find use in the development of new device concepts, such as nanomechanical logic gates [74–76].

Finally, new functionalities and phenomena will become available in unique types of magnetic and electronic phases in these layers, including those produced by interlayer magnetic interactions in 2D magnetic heterostructures [42, 57, 292, 328–330] and exotic electronic phases, like magic-angle induced superconductivity and ferromagnetism in twisted-bilayer graphene [225, 226]. As shown in Chapter 9, the presented methodologies are sensitive even to multiple phase transitions that occur in different layers that compose a heterostructure, that we demonstrated by simultaneous probing both T_N of $\mathrm{FePS_3}$ and T_C of CGT a single CGT/$\mathrm{FePS_3}$ device. Thus, we anticipate that mechanical resonance could be specifically sensitive to the manifestation of strongly correlated phenomena due to the interlayer coupling of different nature in twistronics [90, 331].

Another promising direction for the nanomechanical community to follow is to direct attention to the electrostatic capacitive softening contribution to the resonance frequency at small gate voltages, described in Chapters 3, 6, 7 and 8. At the premature assessment, this dependence of resonance frequency on the capacitance of the membrane device seems not too useful. However, in many low-dimensional systems, such as graphene, the membrane electrode cannot effectively screen the electric field due to its low density of states. Instead, quantum capacitance, which is directly related to the density of states of the material, manifests itself as an additional capacitance component in series with geometrical device capacitance [174]. This establishes a crucial relation between the resonance frequency of a resonator and the density of states of the material [86, 104]. Such relation allows studies of condensed matter physics and quantum phenomena in low-dimensional systems using nanomechanical resonators [86, 104]. Moreover, this principle is not limited only to charge carrier transport phenomena. The ability of graphene to hybridize its electronic state with that from other 2D materials allows to study, for instance, magnetic states in 2D ferromagnets [332].

Eventually, the bridge between nanomechanics and condensed matter physics should be established much more capaciously and thoroughly. Mechanics is not so much a classic branch of physics and engineering as is commonly believed. Yes, many nanomechanical resonators made of 2D materials behave like membranes made of ordinary, conventional materials and differ little from membranes used, for example, in a musical instrument. However, this presumption is not universally valid. Many other 2D material membranes **are not** classical and intuitive resonators. In many ways, their movement and tension depend on physical processes and phenomena of a higher complexity occurring at a more fundamental level. Therefore, we should cease thinking of freestanding 2D materials as purely mechanical systems and question from the perspective of condensed matter physics. What happens to the dissipation of energy in low dimensions [80]? How do the distinctive thermodynamic properties of 2D materials affect the movement of membranes [78, 79, 127]? Can we couple complex strongly correlated phases to the resonant mechanical motion [225, 226]? Is strain really a versatile knob to control various magnetic and electronic phases [57, 67, 124]? How about generating spin currents [251] from dynamic strain modulation [83]? Can we also tweak the quantum effects utilizing tension [86, 104]? And what about pseudo-magnetic fields at critically high tensions [333]? Each of these questions can establish a separate research direction that may lead to a better understanding of thermodynamics, quantum phenomena, and ordering mechanisms in two dimensions. One important step toward studying the deviations between classical membrane physics and nanomechanics will also lie into reproducible fabrication of highly uniform 2D material membranes. Of course, it may also lead to novel device concepts. Thus, working on this frontier we can contribute to society by foreseeing future challenges of technological advances and proposing concepts that could help to timely solve these.

ACKNOWLEDGEMENTS

I hope you enjoyed reading this thesis. About 200 pages, eh? Seems like this size of a dissertation becomes a new norm in the Quantum Nanoscience department*. If you did enjoy reading it, then all the effort I put in it was worth it. However, I was not alone throughout these years in preparing the content of this book. Now, it is time to say thank you to everyone who contributed to this thesis either directly or indirectly. It is not without the help and support from my colleagues, friends, and family that this work became possible.

First and foremost, I would like to thank my promoters. **Peter**, you have been the first person that I met in TU Delft on my arrival for the job interview. Even without meeting Herre yet, I instantly knew that if I accept the offer I will be in good hands. Thank you for our research. We saw our group growing from a small lab to a department-scale entity in 3mE. Your research interests spread starting from NEMS and now studying so many exciting topics, like bacterial motion to making antennas out of plants – it is impressive to observe how all this comes together so organically in a single research group. I am happy to be a part of that from the very beginning. Also, thank you for your support. In pretty much the absence of postdocs (at first), for these whole 4 years you have always been there for Martin and me in case we run into any kind of problems. Yes, sometimes you and I could think out-of-phase, debating over work-related nuances and strategies, but I find that without discussions of this kind there would have never been a good improvement. Looking around I can surely say that we were extremely lucky with the supervisor in this sense.

Herre, I believe you are the kind of person that can inspire people. It was always a pleasure to talk to you – independent on the matter of the talk. I truly learned a lot from you – both about science and how exactly the world of academic research works. It is your guidance and sharp, right-on-point advice that helped me to get through the shock-barrier of understanding how strategic decision-making and interpersonal relationships exactly operate in an academic environment. From time to time, when I am telling you about the work of some random guy, hearing "Oh yes, ..., I know him/her very well" gives me the impression that you know absolutely every single decent researcher on this planet. After hearing your stories, I want to believe that now I understand where do I want to go with my career, how I am planning to get there, and most importantly I understand *why* would I want that. And I thank you for that. Also, it is a pity we never organized that sailing group outing. Now, especially after I got my bareboat skipper license and had proper training, aye aye Captain, I will be waiting for the invitation!

It was a great time at QN with both of you. I never did even question my decision to accept a job offer from both of you in 2017 and come to Delft. I believe I have made the correct choice. I am grateful and proud to be your student. I wish you both all the

---

[*] Hope not really.

success and really hope to stay in touch with you in the future.

Secondly, I would like to thank people on the committee of my PhD defence. **Artem**, thank you for everything. Really. Not only for your time to join the committee and read the thesis but also for my time in the Condensed Matter Physics group in Manchester. I have to say, I often look up the “News” section on the website of your group[†]. It is always nice to see how your lab grows and how the exciting research that you do in Manchester is properly recognized at the highest level. I wish you all the best and hope to have a chance to do science together again at some time in the future.

Eugenio, even though we never met in person (does Zoom count in 2021?), thank you for your continuous support and scientific contribution to my work. Without our collaboration with your lab and the top-quality materials that you grow in Valencia this thesis would look totally different. I would be delighted to continue our collaboration with you and your lab in the future, hopefully even after my graduation.

Kirill, thank you for joining my committee and for your time to read my work. Many research articles that come from you and your group are very highly appreciated in our lab. It is a pleasure to have you on the committee and I hope you will find the presented work interesting and useful for your own research in Berlin, the same way as we find yours.

Fai, I find amazing the work that you and your lab did on magnetic resonators and even more exciting that you are doing now on twisted layers. I am grateful that you have joined the committee and I hope Delft and Cornell will stay in touch after the defence as I truly believe that our labs should start to collaborate in the future.

Yaroslav, большое спасибо for your attendance to the committee, your theoretical contribution to our work, support and all the time spend chatting with me next to the coffee machine. I am grateful that you are genuinely interested in my work. Your insights helped me enormously to understand and valorize my experiments, including many of those that I present in this thesis.

Gary, thank you for joining the committee as a reserve member. Your lab has some data and knowledge management practices that I believe the whole department shall adapt. I wish you all the best in your research.

And now the people of TU Delft. I would like to thank everyone who made my stay pleasant and memorable. First, the warmest regards go to Steeneken lab. I will start with the TNW part of our team. **Martin**, my brother-in-arms and the closest collaborator for these 4 years. We joined the group practically on the same day and instantly realized that we shall work our way through this together. It was genuinely pleasant to share the legendary F178 office[‡] with you and work on all these crazy Friday-night ideas that we had. I remember how we were worried about making enough papers to graduate in the beginning and now your thesis lists 32! (!!!) I think we totally nailed it. I wish you the best possible scientific career to happen and I will be waiting for a lab of prof. Lee to be established to collaborate further.

Dejan, благодарам многу to you, man. It was always so refreshing to talk to you about science, life or anything else really. I wish you very good luck with your start-up idea and hope for a free version of your tool for myself one day. **Robin**, we have always

---

[†] Congratulations on the discovery of “room temperature superconductivity”!

[‡] R.I.P. F178.

wondered how you managed to have SO many projects and SO many papers. Martin somehow managed to pull off 32 (!?!) papers, but the first impression will always stay with me. Hope your academic career is blooming and I wish you the best of it. **Santiago**, we only exchanged virtually a few sentences before you left Delft after defending your PhD, but I wish you good luck with your Graphene GIMOD start-up in Estonia and for the sake of economics of Baltic states I hope it will grow into a true "Unicorn".

Dong Hoon, seeing your posters around the department is a prime reminder to all of us, young PhD students, to never miss an opportunity to apply for grants and scholarships despite how hard-to-get these seem. **Maurits**, a combination of theoretical background and passion to do experimental science is exactly the formula that shall lead to success in projects that you inherited from Martin and me. I am also glad to see that you keep in touch with Valencia. **Gabriele**, you have a very nice touch on how you do science. I hope to record some podcasts on a graphene microphone of yours one day, right - so you keep it up! With you guys, my heart is calm for the continuation of our work. I wish you to have the most of your time as a PhD/postdoc, grow even further as experimental scientists and finally get our first Nature Nature of the group – something we tried to do with Martin (sorry Dejan, we really tried) but as with many other crazy ideas that we had "just never got 'round to it", I suppose.

Now, to my students. **Katya**, first of all, thank you for surviving and tolerating me as your daily supervisor. You are, in fact, a key person of my time in Delft both because of how you changed my perspective on supervision and, of course, because you introduced me to Mari. It is a pleasure to have you now as my true friend. Thank you for everything and I wish you the best in your life and career. **Hugo**, even though technically you have been a student of Martin, I could have never left you out of this list. We have a beautiful paper together, but most importantly it was a really nice time when both you and Katya were a part of our team. And I still remember your competent instructions on how to drink tequila the true Mexican way! My BSc students, **Mark**, **Thijmen**, **Roderick**, **Berend**, **Otman**, **Benjamin** and **Willemijn**, you all were decent researchers even at this early stage. I am sure I can be proud of my students[§]. As proof of that, you can find your personal contribution to my own work all around this thesis. I thank you for that and wish you keep doing good science!

Reflecting on it, our internal collaborators had a lot of positive influence on this work that needs to be acknowledged. I will start with Caviglia lab and van der Sar lab, because between our labs there have always been some good vibes, especially in recent years[¶]. People of Caviglia lab, **Dima**, **Thierry**, **Jorrit**, **Ulderico**, **Mattias**, **Victoria**, **Andrea** and others, your group have been a close collaborator to us for as long as I can remember. Frankly, the collaboration is so close that at some point it felt that the borderline was basically nominal. **Dima**, thanks for our time together. It's both the friendship and fruitful research collaboration that we have built during these years. Let's not get lost and it's good that I know where to find you. I wish you luck and endurance in Nijmegen! **Thierry**, it is a pleasure to know you, man. I still feel a pity I could not join you for your APS US trip. Good luck with your soon-to-happen defence and, also, do not tell anyone how to open old doors (and the roof). This is a sacred knowledge of the ancients. **Jorrit** and

---

[§] Read: "I really am." Is it that I am so lucky, that I only have good people being my students?

[¶] "Why is it when something happens, it's always you three?", McGonagall

Mattias, I absolutely love your research and I wish both of you all the best of luck in your further career. **Victoria**, I find it very important that you are doing with the "QN Culture and Community" team. I believe we as the department shall go even further, assigning a Keeper of Traditions. **Ulderico**, you started off as a half-Steeneken lab master student and I am glad that you stayed for science. Persistence is the way to go and trust me it will pay off. **Andrea**, thank you for your contribution to our work and I wish you all the best in Geneva!

People of van der Sar lab, **Samer**, **Edouard**, **Brecht**, **Michael**, **Iacopo**, **Toeno** and others, we started to collaborate relatively recently but I have no idea why we would wait so long to start. It feels like many research interests naturally go in line for our groups. **Samer**, over a relatively short period of time, you became a true friend for me. It is heartbreaking to go now. I wish you the best of luck with grant applications, your further career and of course all the best to you and Fran. You both are always welcome to visit me anytime at whichever place on this planet I will end up at. I will always be happy to see you! **Edouard**, I thought about it long enough and I think you are right: science does not answer the question "what is the purpose" or even "why" – it only tells you "how". But I think it may be for us, human beings, to use more available tools than only blunt mathematical methods to answer the "why". I wish you good luck in Germany and stay in touch. **Brecht**, thank you for your contribution to our work (I still think you should have been on that paper, even though you disagree) and I wish you a successful PhD! **Michael**, I want that German techno playlist, cannot get it out of my head. **Iacopo**, was always nice to talk to you, good luck with your research. **Toeno**, thank you for your interest in my work and that you bridged me with beautiful people from your lab, which resulted in such a fruitful collaboration!

People of van der Zant lab, **Pascal**, **Damian**, **Chunwei**, **Jacqueline**, **Sergeii**, **Jasper** and others, it was always interesting to observe things that you do in your lab from the perspective of an uninvolved person. **Pascal**, we never collaborated, unfortunately, but it was always impressive to see what you and your students did with graphene devices. I wish you good luck now as a PI. **Damian**, I am not sure if you are aware of that, but Chapter 7 of this thesis was inspired by the work you did with Dejan back in your BSc times. Thank you for that. **Chunwei**, **Jacqueline**, **Tristan**, **Sebastian** and others involved, thanks for creating the nice atmosphere at our new office. Take good care of it as now it is truly nice because of your input! **Sergeii**, unfortunately, we had too little of a chance to properly talk about life, but we have a common friend from your Skolkovo times that was of a very good opinion of you. Now, after knowing you in person, I tend to fully agree with him. **Jasper**, I still wonder what we can do with these magic cable-bacteria. Hope to see some exciting results published by you in the future!

I am also thankful to the rest of the department for making my research possible and my stay so pleasant. It is people from **Groeblacher lab**, **Steele lab**, **Blanter Group** (especially **Xiang**), **Conesa Boj lab**, **Vollebregt lab** (especially **Sten** and **Roberto**), **Kuipers lab** (and **Kobus** himself) and many others that I would like to thank. Some special thanks go also to ex-colleagues. **Nikos**, you were the man who gave me a good kick-start at the QN. Thank you for taking care of me in my first days and I wish you all the best in your career! **Marc**, the German Legend, it was a pleasure to share our office with you! (Or rather, thanks for sharing your office with us.) I miss your sense of humour and our small talks, but I also heard about your new job at Grünecker, so I am very happy for you, man. Also, hope your laptop is all safe and sound once you left Delft as it is out of my jurisdiction now. **Wayne**, even though neither our DNA project ever was finished nor a friend of mine joined you as a student, it was a pleasure to work with you. Hope someday our research paths cross again. Other special thanks go to **Allard**, the AFM guru. Thank you for all these hours spent teaching me how to properly do AFM measurements and showing true research capabilities of this, falsely at first sight simple, elegant technique.

Management staff, **Maria**, **Etty**, **Dorine**, thank you for making our work easier. Technicians, **Tino**, **Ronald** and **Mark**, thank you for helping us out with the heavy work. Especially, for the times then our main cryo-setup broke down and we risked staying without our working-horse for the last year of our PhD. It is your help that made it possible to fix it in no time and save our work. People at Kavli Nanolab Delft, **Charles**, **Marco**, **Anja**, **Eugene** and all others, thank you for making the cleanroom such a pleasant place.

People of 3mE are up next. Many in QN do not realise that in a building just across the road "small" Steeneken lab has its own secret department-scale army of colleagues. It's many wonderful people and excellent researchers I had the pleasure to work with in the past years. **Farbod**, we collaborated quite closely during my first year in Delft. That resulted in several nice papers that we have together. I enjoy working with you and would be happy to collaborate more in the future! **Irek**, dziękuję bardzo for everything and also particularly for translating my summary and propositions to Dutch. We worked together from the days of your masters' project and I can say with all the responsibility - 3mE is lucky to have you! Guys, I am so confident that the bacteria project of yours will be accepted to a journal with extremely high impact, that I already know which champagne I will open *le sabrage* for the celebration. Even if I will be away from Delft already - I do not care, I celebrate on Zoom!

Ata, I always liked your projects: from levitating plates to non-linear dynamics. I see that you have everything to succeed with them so I do wish you to succeed indeed! **Abhilash**, thank you for teaching me in my first steps of AFM characterisation. I wish you good luck with your defence this year! **Cury**, I really like the figures that you make for your papers. You have a very nice touch to visuals. Also, thank you for involving me in your projects - I hope to be useful for you and your research! Some special salute also goes to **Alkisti**, technically you were never officially part of our lab but let's be honest - it always felt like you were one of us! I wish you luck, persistence, even more luck, and love for what you do in your current work. **Vincent**, **Andrea**, **Matthijs**, **Ali**, **Minxing**, **Inge**, and many other PhD students of DMN, also to you I wish the best of the rest of your PhD and the following successful career!

Our postdocs, **Satadal**, **Dongil**, **Hadi**, **Tomas** and many others, interaction with you was always pleasant. Our PhDs should be happy to have such a competent team of senior research peers. Young assistant professors of our group, **Richard**, **Gerard**, **Sabina** and **Wouter**. You show a lot of solid knowledge, commitment and enthusiasm in your work. I see a big future for the DMN group with PIs like you. **Murali**, thank you for involving me in multiple interesting projects of yours and I am glad I was helpful. **Masoud**, it is impressive how you voluntarily choose to do more international postdocs while already having a PI position back at home. Your research group in Iran shall be proud of their supervisor.

Both the QN department and 3mE was a warm welcome. Please, do not be frustrated if you miss your name on this list. My memory can be like a Dutch cheese with a lot of holes in it[‖], but be sure my heart remembers **every one of you**.

Now, the next "thank you" goes to our key collaborators outside TU Delft. People of the University of Valencia, **Javi** and **Samuel**, we have several beautiful papers together and I think this collaboration was one of the most fruitful I ever had. It was a pleasure to meet you in person when you visited Delft and it is a pity I never did make it to Valencia myself. **Samuel**, when I am writing this your PhD defence shall happen in three days, but I suspect that by the time you will be reading this you are already Dr. Mañas-Valero. On which I (take courage to) congratulate you (in advance)!

People of Applied Nanolayers, **Dominique**, **Richard**, **Paul** and others, we truly pushed the limits with how commercially competitive graphene devices can be. Our pressure sensors are a prime development of our collaboration, and let it be only the first of many in the future.

People at SRON and NASA, **Henk**, **Johannes**, **Nicholas**, **Simon** and others, it was my pleasure to be useful for your project. I always found the space industry to be so attractive. I thank you for the opportunity to take a small part in it and I hope that the space mission will be more than successful.

Graphene Flagship, my acknowledgements for sponsoring my research. Also, particularly people of WP6 Sensors, it was always a pleasure to attend our progress meetings. Special salute and thanks go to **Marko** at IHTM in Belgrade. I wish you all the luck in continuing to do frontier science in Serbia, as you are doing the very right thing.

Thank you to the people at Peking University, **Wenyu**, **Shuang** and **Wei**, for the top quality CGT crystals and your enthusiasm for our work. People in Duisburg, Germany, **Lukas** and **Marika**, thank you for your contribution to the gas effusion project that converged to our nice Nature Communications paper in the end. Thanks to our collaborators in Leiden, **Peter** and **Sense Jan**, and Groningen, **Marcos** and **Freddie**, for your interest in my work and the ongoing research that we do together. And lastly, **Alexei** from CFI, University of Latvia, thank you for your interest in my current work and for my time under your supervision in Riga.

And this is my word to other enormously important collaborators to my life - my friends. People of ДК "У Ребят" [**], **Arturs**, **Vassili**, **Polina**, **Iurie**, **Elena**, **Egor**, **Vladimir**, **Margo**, **Katya D.**, and **Katya S.** – this is to you. My time in Delft would never be the same if it hadn't been for our gang. You helped me to keep my work-life balance: real hard work being balanced by partying real hard, of course. And it was also so much easier to survive the COVID-19 pandemic together [††]. You all reserved a special place in my heart. We have no other option now but to stay in touch. That was a beautiful and fun time for us all. Always remember ДК.

Denis and **Rauan**, my Manchester lads. I am very grateful for your support throughout these last 4 years and I am happy we are maintaining our long-distance friendship. **Denis**, I wish you the best of luck at your PhD defence in Zurich and I want you to know

---

[‖] "More cheese – more holes. More holes – less cheese.", Arturs Blinovs.

[**] DK "U Rebyat", House of Culture "At folks'"

[††] Помните переходящую корону короля шуток про коронавирус? Remember the carry-over crown of the king of coronavirus jokes?

that I will be there for you. **Rauan**, good luck with your career in London (you are doing so great!), and all the best to your young family! My Riga guys, **Antons**, **Konstantins** and **Arturs**, thank you for your support and for making Riga feel like home every time I travel back even after 10 years living abroad.

Last but not least is a thank you to my family. Beloved **Mari**, you inspire me. You are a wonderful person and you charge me and everyone around with your *joie de vivre*. I am grateful for your support in any life situation (truly of any kind, COVID-19 proves it), as well as for your patience and acceptance of who I am and what I want to do with my life. With your reliance and trust, I can confidently move forward. You were always by my side all these years, as I was by yours, and so be it in the future. There is so much I want to say that likely I will need another 200-page book to write, yet even better I will tell you all that sentence by sentence in person in time to come! **Porto the Dog**, you contributed to the writing process of many research articles of mine by trying to involve me in “discussions” every 15 minutes during long COVID-19 working-from-home hours. Also, increasing the preparation time three-folds. You are the goodest boi and do not tell Mari that I am secretly giving you chorizo that you love so much.

And finally, the very last words are dedicated to my parents. Любимые **мама**, **папа**, бабушка **Женя** и сестра **Даша**, эти слова для Вас. Вы никогда не ограничивали меня в занятии тем, что мне нравится и посмотрите к чему это привело! (Смеюсь.) А если серьезно. Папа, спасибо тебе за все жизненные уроки - я многому у тебя научился. То, что ты сейчас изучаешь историю нашей семьи это титанический труд, но я считаю его крайне важным – успехов и удач тебе в этом нелегком деле! Мама, спасибо тебе за заботу, понимание в любой жизненной ситуации и за то, что мне всегда приятно возвращатся домой! Я желаю тебе успехов в твоей работе и счастья в жизни. Бабушка **Женя**, я до сих пор стараюсь найти хороший ответ на твой вопрос: “А после того, как ты станешь физиком, чем ты собираешься заниматься в жизни?” (Смеюсь.) Видимо пока что я буду становится физиком дальше. Спасибо тебе за твое чувство юмора и любовь к жизни, а так же здоровья тебе и долгих лет! **Даша**, спасибо тебе - самой лучшей в мире сестре! Я желаю тебе получить магистерскую степень, удачи в твоих начинаниях в бизнесе, а так же счастья и успехов вместе с Сашей.

Спасибо всем Вам за Вашу выдержку, любовь и заботу. Эта книга и весь мой труд не был бы возможен без Вашей поддержки и напутствий. Эту диссертацию я посвящаю Вам и всей нашей семье.

Makars Šiškins
Riga, September 2021

BIBLIOGRAPHY

[1] U. Delić, M. Reisenbauer, K. Dare, D. Grass, V. Vuletić, N. Kiesel, and M. Aspelmeyer, "Cooling of a levitated nanoparticle to the motional quantum ground state", Science **367**, 892–895 (2020).

[2] D. Davidovikj, D. J. Groenendijk, A. M. R. V. L. Monteiro, A. Dijkhoff, D. Afanasiev, M. Šiškins, M. Lee, Y. Huang, E. van Heumen, H. S. J. van der Zant, A. D. Caviglia, and P. G. Steeneken, "Ultrathin complex oxide nanomechanical resonators", Commun. Phys. **3**, 163 (2020).

[3] S. Stassi, M. Marini, M. Allione, S. Lopatin, D. Marson, E. Laurini, S. Pricl, C. F. Pirri, C. Ricciardi, and E. D. Fabrizio, "Nanomechanical DNA resonators for sensing and structural analysis of DNA-ligand complexes", Nat. Commun. **10**, 1690 (2019).

[4] J. C. Meyer, A. K. Geim, M. I. Katsnelson, K. S. Novoselov, T. J. Booth, and S. Roth, "The structure of suspended graphene sheets", Nature **446**, 60–63 (2007).

[5] P. G. Steeneken, R. J. Dolleman, D. Davidovikj, F. Alijani, and H. S. J. van der Zant, "Dynamics of 2D material membranes", 2D Mater. **8**, 042001 (2021).

[6] M. C. Lemme, S. Wagner, K. Lee, X. Fan, G. J. Verbiest, S. Wittmann, S. Lukas, R. J. Dolleman, F. Niklaus, H. S. J. van der Zant, G. S. Duesberg, and P. G. Steeneken, "Nanoelectromechanical sensors based on suspended 2D materials", Research **2020**, 8748602 (2020).

[7] K. S. Novoselov, A. K. Geim, S. V. Morozov, D. Jiang, Y. Zhang, S. V. Dubonos, I. V. Grigorieva, and A. A. Firsov, "Electric field effect in atomically thin carbon films", Science **306**, 666–669 (2004).

[8] A. K. Geim and K. S. Novoselov, "The rise of graphene", Nat. Mater. **6**, 183–191 (2007).

[9] K. Bolotin, K. Sikes, Z. Jiang, M. Klima, G. Fudenberg, J. Hone, P. Kim, and H. Stormer, "Ultrahigh electron mobility in suspended graphene", Solid State Commun. **146**, 351–355 (2008).

[10] K. S. Novoselov, Z. Jiang, Y. Zhang, S. V. Morozov, H. L. Stormer, U. Zeitler, J. C. Maan, G. S. Boebinger, P. Kim, and A. K. Geim, "Room-temperature quantum Hall effect in graphene", Science **315**, 1379–1379 (2007).

[11] K. Momma and F. Izumi, "VESTA 3 for three-dimensional visualization of crystal, volumetric and morphology data", J. Appl. Crystallogr. **44**, 1272–1276 (2011).

[12] C. Lee, X. Wei, J. W. Kysar, and J. Hone, "Measurement of the elastic properties and intrinsic strength of monolayer graphene", Science **321**, 385–388 (2008).

[13] E. Ganz, A. B. Ganz, L.-M. Yang, and M. Dornfeld, "The initial stages of melting of graphene between 4000 K and 6000 K", Phys. Chem. Chem. Phys. **19**, 3756–3762 (2017).

[14] Z. Zhang, Y. Yang, E. S. Penev, and B. I. Yakobson, “Elasticity, flexibility, and ideal strength of borophenes”, Adv. Funct. Mater. **27**, 1605059 (2017).

[15] A. J. Mannix, Z. Zhang, N. P. GuIsinger, B. I. Yakobson, and M. C. Hersam, “Borophene as a prototype for synthetic 2D materials development”, Nat. Nanotechnol. **13**, 444–450 (2018).

[16] X. Xu, L. F. C. Pereira, Y. Wang, J. Wu, K. Zhang, X. Zhao, S. Bae, C. T. Bui, R. Xie, J. T. L. Thong, B. H. Hong, K. P. Loh, D. Donadio, B. Li, and B. Özyilmaz, “Length-dependent thermal conductivity in suspended single-layer graphene”, Nat. Commun. **5**, 3689 (2014).

[17] L. Liao and X. Duan, “Graphene for radio frequency electronics”, Mater. Today **15**, 328–338 (2012).

[18] M. F. El-Kady, Y. Shao, and R. B. Kaner, “Graphene for batteries, supercapacitors and beyond”, Nat. Rev. Mater. **1**, 16033 (2016).

[19] J. S. Bunch, *Mechanical and electrical properties of graphene sheets* (Ph.D. thesis, Cornell University Ithaca, NY, 2008).

[20] J. Abraham, K. S. Vasu, C. D. Williams, K. Gopinadhan, Y. Su, C. T. Cherian, J. Dix, E. Prestat, S. J. Haigh, I. V. Grigorieva, P. Carbone, A. K. Geim, and R. R. Nair, “Tunable sieving of ions using graphene oxide membranes”, Nat. Nanotechnol. **12**, 546–550 (2017).

[21] M. Šiškins, C. Mullan, S.-K. Son, J. Yin, K. Watanabe, T. Taniguchi, D. Ghazaryan, K. S. Novoselov, and A. Mishchenko, “High-temperature electronic devices enabled by hBN-encapsulated graphene”, Appl. Phys. Lett. **114**, 123104 (2019).

[22] S.-K. Son, M. Šiškins, C. Mullan, J. Yin, V. G. Kravets, A. Kozikov, S. Ozdemir, M. Alhazmi, M. Holwill, K. Watanabe, T. Taniguchi, D. Ghazaryan, K. S. Novoselov, V. I. Fal’ko, and A. Mishchenko, “Graphene hot-electron light bulb: incandescence from hBN-encapsulated graphene in air”, 2D Mater. **5**, 011006 (2017).

[23] J. S. Bunch, S. S. Verbridge, J. S. Alden, A. M. van der Zande, J. M. Parpia, H. G. Craighead, and P. L. McEuen, “Impermeable atomic membranes from graphene sheets”, Nano Lett. **8**, 2458–2462 (2008).

[24] J. S. Bunch, A. M. van der Zande, S. S. Verbridge, I. W. Frank, D. M. Tanenbaum, J. M. Parpia, H. G. Craighead, and P. L. McEuen, “Electromechanical resonators from graphene sheets”, Science **315**, 490–493 (2007).

[25] J. Tao, W. Shen, S. Wu, L. Liu, Z. Feng, C. Wang, C. Hu, P. Yao, H. Zhang, W. Pang, X. Duan, J. Liu, C. Zhou, and D. Zhang, “Mechanical and electrical anisotropy of few-layer black phosphorus”, ACS Nano **9**, 11362–11370 (2015).

[26] Z. Wang and P. X.-L. Feng, “Design of black phosphorus 2D nanomechanical resonators by exploiting the intrinsic mechanical anisotropy”, 2D Mater. **2**, 021001 (2015).

[27] M. Buscema, D. J. Groenendijk, S. I. Blanter, G. A. Steele, H. S. J. van der Zant, and A. Castellanos-Gomez, “Fast and broadband photoresponse of few-layer black phosphorus field-effect transistors”, Nano Lett. **14**, 3347–3352 (2014).

[28] W. Zhu, S. Park, M. N. Yogeesh, K. M. McNicholas, S. R. Bank, and D. Akinwande, “Black phosphorus flexible thin film transistors at gighertz frequencies”, Nano Lett. **16**, 2301–2306 (2016).

[29] Z. Wang, H. Jia, X. Zheng, R. Yang, Z. Wang, G. J. Ye, X. H. Chen, J. Shan, and P. X.-L. Feng, “Black phosphorus nanoelectromechanical resonators vibrating at very high frequencies”, Nanoscale **7**, 877–884 (2015).

[30] K. S. Novoselov, A. Mishchenko, A. Carvalho, and A. H. C. Neto, “2D materials and van der Waals heterostructures”, Science **353**, aac9439 (2016).

[31] S. Manzeli, D. Ovchinnikov, D. Pasquier, O. V. Yazyev, and A. Kis, “2D transition metal dichalcogenides”, Nat. Rev. Mater. **2**, 17033 (2017).

[32] B. Radisavljevic, A. Radenovic, J. Brivio, V. Giacometti, and A. Kis, “Single-layer MoS_2 transistors”, Nat. Nanotechnol. **6**, 147–150 (2011).

[33] O. Lopez-Sanchez, D. Lembke, M. Kayci, A. Radenovic, and A. Kis, “Ultrasensitive photodetectors based on monolayer MoS_2”, Nat. Nanotechnol. **8**, 497–501 (2013).

[34] P. Tonndorf, R. Schmidt, P. Böttger, X. Zhang, J. Börner, A. Liebig, M. Albrecht, C. Kloc, O. Gordan, D. R. T. Zahn, S. M. de Vasconcellos, and R. Bratschitsch, “Photoluminescence emission and Raman response of monolayer MoS_2, $MoSe_2$, and WSe_2”, Opt. Express **21**, 4908 (2013).

[35] R. A. Craven and S. F. Meyer, “Specific heat and resistivity near the charge-density-wave phase transitions in 2H-$TaSe_2$ and 2H-TaS_2”, Phys. Rev. B **16**, 4583–4593 (1977).

[36] E. Navarro-Moratalla, J. O. Island, S. Mañas-Valero, E. Pinilla-Cienfuegos, A. Castellanos-Gomez, J. Quereda, G. Rubio-Bollinger, L. Chirolli, J. A. Silva-Guillén, N. Agraït, G. A. Steele, F. Guinea, H. S. J. van der Zant, and E. Coronado, “Enhanced superconductivity in atomically thin TaS_2”, Nat. Commun. **7**, 11043 (2016).

[37] A. Castellanos-Gomez, V. Singh, H. S. J. van der Zant, and G. A. Steele, “Mechanics of freely-suspended ultrathin layered materials”, Ann. Phys. (Berlin, Ger.) **527**, 27–44 (2014).

[38] C. Androulidakis, K. Zhang, M. Robertson, and S. Tawfick, “Tailoring the mechanical properties of 2D materials and heterostructures”, 2D Mater. **5**, 032005 (2018).

[39] D. Akinwande, C. J. Brennan, J. S. Bunch, P. Egberts, J. R. Felts, H. Gao, R. Huang, J.-S. Kim, T. Li, Y. Li, K. M. Liechti, N. Lu, H. S. Park, E. J. Reed, P. Wang, B. I. Yakobson, T. Zhang, Y.-W. Zhang, Y. Zhou, and Y. Zhu, “A review on mechanics and mechanical properties of 2D materials – graphene and beyond”, Extreme Mech. Lett. **13**, 42–77 (2017).

[40] M. Barmatz, L. R. Testardi, and F. J. D. Salvo, “Elasticity measurements in the layered dichalcogenides $TaSe_2$ and $NbSe_2$”, Phys. Rev. B **12**, 4367–4376 (1975).

[41] S. Sengupta, H. S. Solanki, V. Singh, S. Dhara, and M. M. Deshmukh, “Electromechanical resonators as probes of the charge density wave transition at the nanoscale in $NbSe_2$”, Phys. Rev. B **82**, 155432 (2010).

[42] M. Gibertini, M. Koperski, A. F. Morpurgo, and K. S. Novoselov, “Magnetic 2D materials and heterostructures”, Nat. Nanotechnol. **14**, 408–419 (2019).

[43] M.-C. Wang, C.-C. Huang, C.-H. Cheung, C.-Y. Chen, S. G. Tan, T.-W. Huang, Y. Zhao, Y. Zhao, G. Wu, Y.-P. Feng, H.-C. Wu, and C.-R. Chang, “Prospects and opportunities of 2D van der Waals magnetic systems”, Ann. Phys. **532**, 1900452 (2020).

[44] Y. Khan, S. M. Obaidulla, M. R. Habib, A. Gayen, T. Liang, X. Wang, and M. Xu, “Recent breakthroughs in two-dimensional van der Waals magnetic materials and emerging applications”, Nano Today **34**, 100902 (2020).

[45] J.-U. Lee, S. Lee, J. H. Ryoo, S. Kang, T. Y. Kim, P. Kim, C.-H. Park, J.-G. Park, and H. Cheong, “Ising-type magnetic ordering in atomically thin $FePS_3$”, Nano Lett. **16**, 7433–7438 (2016).

[46] B. Huang, G. Clark, E. Navarro-Moratalla, D. R. Klein, R. Cheng, K. L. Seyler, D. Zhong, E. Schmidgall, M. A. McGuire, D. H. Cobden, W. Yao, D. Xiao, P. Jarillo-Herrero, and X. Xu, “Layer-dependent ferromagnetism in a van der Waals crystal down to the monolayer limit”, Nature **546**, 270–273 (2017).

[47] C. Gong, L. Li, Z. Li, H. Ji, A. Stern, Y. Xia, T. Cao, W. Bao, C. Wang, Y. Wang, Z. Q. Qiu, R. J. Cava, S. G. Louie, J. Xia, and X. Zhang, “Discovery of intrinsic ferromagnetism in two-dimensional van der Waals crystals”, Nature **546**, 265–269 (2017).

[48] X. Li and J. Yang, “$CrXTe_3$ ($X = Si, Ge$) nanosheets: two dimensional intrinsic ferromagnetic semiconductors”, J. Mater. Chem. C **2**, 7071 (2014).

[49] Y. Deng, Y. Yu, Y. Song, J. Zhang, N. Z. Wang, Z. Sun, Y. Yi, Y. Z. Wu, S. Wu, J. Zhu, J. Wang, X. H. Chen, and Y. Zhang, “Gate-tunable room-temperature ferromagnetism in two-dimensional Fe_3GeTe_2”, Nature **563**, 94–99 (2018).

[50] Z. Fei, B. Huang, P. Malinowski, W. Wang, T. Song, J. Sanchez, W. Yao, D. Xiao, X. Zhu, A. F. May, W. Wu, D. H. Cobden, J.-H. Chu, and X. Xu, “Two-dimensional itinerant ferromagnetism in atomically thin Fe_3GeTe_2”, Nat. Mater. **17**, 778–782 (2018).

[51] H. L. Zhuang, P. R. C. Kent, and R. G. Hennig, “Strong anisotropy and magnetostriction in the two-dimensional Stoner ferromagnet Fe_3GeTe_2”, Phys. Rev. B **93**, 134407 (2016).

[52] D. Ghazaryan, M. T. Greenaway, Z. Wang, V. H. Guarochico-Moreira, I. J. Vera-Marun, J. Yin, Y. Liao, S. V. Morozov, O. Kristanovski, A. I. Lichtenstein, M. I. Katsnelson, F. Withers, A. Mishchenko, L. Eaves, A. K. Geim, K. S. Novoselov, and A. Misra, “Magnon-assisted tunnelling in van der Waals heterostructures based on $CrBr_3$”, Nat. Electron. **1**, 344–349 (2018).

[53] J. Liu, Q. Sun, Y. Kawazoe, and P. Jena, “Exfoliating biocompatible ferromagnetic Cr-trihalide monolayers”, Phys. Chem. Chem. Phys. **18**, 8777–8784 (2016).

[54] X. Cai, T. Song, N. P. Wilson, G. Clark, M. He, X. Zhang, T. Taniguchi, K. Watanabe, W. Yao, D. Xiao, M. A. McGuire, D. H. Cobden, and X. Xu, “Atomically thin $CrCl_3$: an in-plane layered antiferromagnetic insulator”, Nano Lett. **19**, 3993–3998 (2019).

[55] F. Cantos-Prieto, A. Falin, M. Alliati, D. Qian, R. Zhang, T. Tao, M. R. Barnett, E. J. G. Santos, L. H. Li, and E. Navarro-Moratalla, “Layer-dependent mechanical properties and enhanced plasticity in the van der Waals chromium trihalide magnets”, Nano Lett. **21**, 3379–3385 (2021).

[56] F. Zheng, J. Zhao, Z. Liu, M. Li, M. Zhou, S. Zhang, and P. Zhang, “Tunable spin states in the two-dimensional magnet CrI_3”, Nanoscale **10**, 14298–14303 (2018).

[57] S. Jiang, H. Xie, J. Shan, and K. F. Mak, "Exchange magnetostriction in two-dimensional antiferromagnets", Nat. Mater. **19**, 1295–1299 (2020).

[58] P. A. Joy and S. Vasudevan, "Magnetism in the layered transition-metal thiophosphates MPS_3 (M=Mn, Fe, and Ni)", Phys. Rev. B **46**, 5425–5433 (1992).

[59] A. Hashemi, H.-P. Komsa, M. Puska, and A. V. Krasheninnikov, "Vibrational properties of metal phosphorus trichalcogenides from first-principles calculations", J. Phys. Chem. C **121**, 27207–27217 (2017).

[60] X. Zhang, X. Zhao, D. Wu, Y. Jing, and Z. Zhou, "$MnPSe_3$ monolayer: a promising 2D visible-light photohydrolytic catalyst with high carrier mobility", Adv. Sci. **3**, 1600062 (2016).

[61] Q. Liu, L. Wang, Y. Fu, X. Zhang, L. Huang, H. Su, J. Lin, X. Chen, D. Yu, X. Cui, J.-W. Mei, and J.-F. Dai, "Magnetic order in XY-type antiferromagnetic monolayer $CoPS_3$ revealed by Raman spectroscopy", Phys. Rev. B **103**, 235411 (2021).

[62] A. R. Wildes, V. Simonet, E. Ressouche, R. Ballou, and G. J. McIntyre, "The magnetic properties and structure of the quasi-two-dimensional antiferromagnet $CoPS_3$", J. Phys. Condens. Matter. **29**, 455801 (2017).

[63] Q. Gui, Y. Feng, B. Chen, F. Gu, L. Chen, S. Meng, M. Xu, M. Xia, C. Zhang, and J. Yang, "Extrinsic-structured bimetallic-phase ternary metal phosphorus trisulfides coupled with n-doped graphitized carbon for superior electrochemical lithium storage", Adv. Energy Mater. **11**, 2003553 (2021).

[64] J. López-Cabrelles, S. Manas-Valero, I. J. Vitórica-Yrezábal, P. J. Bereciartua, J. A. Rodríguez-Velamazán, J. C. Waerenborgh, B. J. C. Vieira, D. Davidovikj, P. G. Steeneken, H. S. J. van der Zant, G. M. Espallargas, and E. Coronado, "Isoreticular two-dimensional magnetic coordination polymers prepared through pre-synthetic ligand functionalization", Nat. Chem. **10**, 1001–1007 (2018).

[65] D. Afanasiev, J. R. Hortensius, M. Matthiesen, S. Mañas-Valero, M. Šiškins, M. Lee, E. Lesne, H. S. J. van der Zant, P. G. Steeneken, B. A. Ivanov, E. Coronado, and A. D. Caviglia, "Controlling the anisotropy of a van der Waals antiferromagnet with light", Sci. Adv. **7**, eabf3096 (2021).

[66] J. L. Lado and J. Fernández-Rossier, "On the origin of magnetic anisotropy in two dimensional CrI_3", 2D Mater. **4**, 035002 (2017).

[67] M. Šiškins, M. Lee, S. Mañas-Valero, E. Coronado, Y. M. Blanter, H. S. J. van der Zant, and P. G. Steeneken, "Magnetic and electronic phase transitions probed by nanomechanical resonators", Nat. Commun. **11**, 2698 (2020).

[68] K. L. Ekinci and M. L. Roukes, "Nanoelectromechanical systems", Rev. Sci. Instrum. **76**, 061101 (2005).

[69] M. Aspelmeyer, P. Meystre, and K. Schwab, "Quantum optomechanics", Phys. Today **65**, 29–35 (2012).

[70] M. Aspelmeyer, T. J. Kippenberg, and F. Marquardt, "Cavity optomechanics", Rev. Mod. Phys. **86**, 1391–1452 (2014).

[71] M. Spletzer, A. Raman, H. Sumali, and J. P. Sullivan, “Highly sensitive mass detection and identification using vibration localization in coupled microcantilever arrays”, Appl. Phys. Lett. **92**, 114102 (2008).

[72] E. Gil-Santos, D. Ramos, A. Jana, M. Calleja, A. Raman, and J. Tamayo, “Mass sensing based on deterministic and stochastic responses of elastically coupled nanocantilevers”, Nano Lett. **9**, 4122–4127 (2009).

[73] F. Bannon, J. Clark, and C.-C. Nguyen, “High-Q HF microelectromechanical filters”, IEEE J. Solid-State Circuits **35**, 512–526 (2000).

[74] C.-Y. Tsai, W.-T. Kuo, C.-B. Lin, and T.-L. Chen, “Design and fabrication of MEMS logic gates”, J. Micromech. Microeng. **18**, 045001 (2008).

[75] I. Mahboob and H. Yamaguchi, “Bit storage and bit flip operations in an electromechanical oscillator”, Nat. Nanotechnol. **3**, 275–279 (2008).

[76] S. C. Masmanidis, R. B. Karabalin, I. D. Vlaminck, G. Borghs, M. R. Freeman, and M. L. Roukes, “Multifunctional nanomechanical systems via tunably coupled piezoelectric actuation”, Science **317**, 780–783 (2007).

[77] R. B. Karabalin, R. Lifshitz, M. C. Cross, M. H. Matheny, S. C. Masmanidis, and M. L. Roukes, “Signal amplification by sensitive control of bifurcation topology”, Phys. Rev. Lett. **106**, 094102 (2011).

[78] R. J. Dolleman, S. Houri, D. Davidovikj, S. J. Cartamil-Bueno, Y. M. Blanter, H. S. J. van der Zant, and P. G. Steeneken, “Optomechanics for thermal characterization of suspended graphene”, Phys. Rev. B **96**, 165421 (2017).

[79] N. Morell, S. Tepsic, A. Reserbat-Plantey, A. Cepellotti, M. Manca, I. Epstein, A. Isacsson, X. Marie, F. Mauri, and A. Bachtold, “Optomechanical measurement of thermal transport in two-dimensional $\mathrm{MoSe_2}$ lattices”, Nano Lett. **19**, 3143–3150 (2019).

[80] R. J. Dolleman, Y. M. Blanter, H. S. J. van der Zant, P. G. Steeneken, and G. J. Verbiest, “Phonon scattering at kinks in suspended graphene”, Phys. Rev. B **101**, 115411 (2020).

[81] D. Davidovikj, F. Alijani, S. J. Cartamil-Bueno, H. S. J. van der Zant, M. Amabili, and P. G. Steeneken, “Nonlinear dynamic characterization of two-dimensional materials”, Nat. Commun. **8**, 1253 (2017).

[82] R. J. Dolleman, D. Davidovikj, H. S. J. van der Zant, and P. G. Steeneken, “Amplitude calibration of 2D mechanical resonators by nonlinear optical transduction”, Appl. Phys. Lett. **111**, 253104 (2017).

[83] X. Zhang, K. Makles, L. Colombier, D. Metten, H. Majjad, P. Verlot, and S. Berciaud, “Dynamically-enhanced strain in atomically thin resonators”, Nat. Commun. **11**, 5526 (2020).

[84] V. Singh, O. Shevchuk, Y. M. Blanter, and G. A. Steele, “Negative nonlinear damping of a multilayer graphene mechanical resonator”, Phys. Rev. B **93**, 245407 (2016).

[85] A. Keşkekler, O. Shoshani, M. Lee, H. S. J. van der Zant, P. G. Steeneken, and F. Alijani, “Tuning nonlinear damping in graphene nanoresonators by parametric–direct internal resonance”, Nat. Commun. **12**, 1099 (2021).

[86]C. Chen, V. V. Deshpande, M. Koshino, S. Lee, A. Gondarenko, A. H. MacDonald, P. Kim, and J. Hone, "Modulation of mechanical resonance by chemical potential oscillation in graphene", Nat. Phys. **12**, 240–244 (2015).

[87]R. J. Dolleman, *Dynamics of interacting graphene membranes* (Ph.D. thesis, Delft University of Technology, Delft, 2018).

[88]D. Davidovikj, *Two-dimensional membranes in motion* (Ph.D. thesis, Delft University of Technology, Delft, 2018).

[89]C. Chen, S. Rosenblatt, K. I. Bolotin, W. Kalb, P. Kim, I. Kymissis, H. L. Stormer, T. F. Heinz, and J. Hone, "Performance of monolayer graphene nanomechanical resonators with electrical readout", Nat. Nanotechnol. **4**, 861–867 (2009).

[90]F. Miao, S.-J. Liang, and B. Cheng, "Straintronics with van der Waals materials", npj Quantum Mater. **6**, 59 (2021).

[91]I. E. Rosłoń, R. J. Dolleman, H. Licona, M. Lee, M. Šiškins, H. Lebius, L. Madauß, M. Schleberger, F. Alijani, H. S. J. van der Zant, and P. G. Steeneken, "High-frequency gas effusion through nanopores in suspended graphene", Nat. Commun. **11**, 6025 (2020).

[92]M. Lee, D. Davidovikj, B. Sajadi, M. Šiškins, F. Alijani, H. S. J. van der Zant, and P. G. Steeneken, "Sealing graphene nanodrums", Nano Lett. **19**, 5313–5318 (2019).

[93]P. Z. Sun, Q. Yang, W. J. Kuang, Y. V. Stebunov, W. Q. Xiong, J. Yu, R. R. Nair, M. I. Katsnelson, S. J. Yuan, I. V. Grigorieva, M. Lozada-Hidalgo, F. C. Wang, and A. K. Geim, "Limits on gas impermeability of graphene", Nature **579**, 229–232 (2020).

[94]R. J. Dolleman, D. Davidovikj, S. J. Cartamil-Bueno, H. S. J. van der Zant, and P. G. Steeneken, "Graphene squeeze-film pressure sensors", Nano Lett. **16**, 568–571 (2015).

[95]C. Berger, R. Phillips, I. Pasternak, J. Sobieski, W. Strupinski, and A. Vijayaraghavan, "Touch-mode capacitive pressure sensor with graphene-polymer heterostructure membrane", 2D Mater. **5**, 015025 (2017).

[96]Y.-M. Chen, S.-M. He, C.-H. Huang, C.-C. Huang, W.-P. Shih, C.-L. Chu, J. Kong, J. Li, and C.-Y. Su, "Ultra-large suspended graphene as a highly elastic membrane for capacitive pressure sensors", Nanoscale **8**, 3555–3564 (2016).

[97]D. Davidovikj, P. H. Scheepers, H. S. J. van der Zant, and P. G. Steeneken, "Static capacitive pressure sensing using a single graphene drum", ACS Appl. Mater. Interfaces **9**, 43205–43210 (2017).

[98]A. Noury, J. Vergara-Cruz, P. Morfin, B. Plaçais, M. C. Gordillo, J. Boronat, S. Balibar, and A. Bachtold, "Layering transition in superfluid Helium adsorbed on a carbon nanotube mechanical resonator", Phys. Rev. Lett. **122**, 165301 (2019).

[99]D. Lee, K. W. Lee, J. V. Cady, P. Ovartchaiyapong, and A. C. B. Jayich, "Topical review: spins and mechanics in diamond", J. Opt. **19**, 033001 (2017).

[100]R. Norte, M. Forsch, A. Wallucks, I. Marinković, and S. Gröblacher, "Platform for measurements of the Casimir force between two superconductors", Phys. Rev. Lett. **121**, 030405 (2018).

[101] S. Sengupta, N. Samudrala, V. Singh, A. Thamizhavel, P. B. Littlewood, V. Tripathi, and M. M. Deshmukh, "Plasmon mode modifies the elastic response of a nanoscale charge density wave system", Phys. Rev. Lett. **110**, 166403 (2013).

[102] J. Brill, "Elastic anomalies at the charge density wave transition in TaS_3", Solid State Commun. **41**, 925–929 (1982).

[103] W. A. Aiello, C. R. Wolfe, and W. A. Little, "Simplified vibrating-reed technique for the measurement of the temperature dependence of Young's modulus of small samples", Rev. Sci. Instrum. **54**, 594–596 (1983).

[104] M. Kim, J. Kim, Y. Hou, D. Yu, Y.-J. Doh, B. Kim, K. W. Kim, and J. Suh, "Nanomechanical characterization of quantum interference in a topological insulator nanowire", Nat. Commun. **10**, 4522 (2019).

[105] L. D. Landau, "On the theory of phase transitions", Zh. Eksp. Teor. Fiz. **7**, [*Ukr. J. Phys.* **53**, 25 (2008)], 19–32 (1937).

[106] L. D. Landau, L. P. Pitaevskii, and E. M. Lifshitz, *Electrodynamics of continuous media*, 2nd ed., Vol. 8 (Butterworth, New York, 1984).

[107] A. Castellanos-Gomez, L. Vicarelli, E. Prada, J. O. Island, K. L. Narasimha-Acharya, S. I. Blanter, D. J. Groenendijk, M. Buscema, G. A. Steele, J. V. Alvarez, H. W. Zandbergen, J. J. Palacios, and H. S. J. van der Zant, "Isolation and characterization of few-layer black phosphorus", 2D Mater. **1**, 025001 (2014).

[108] M. Šiškins, M. Lee, F. Alijani, M. R. van Blankenstein, D. Davidovikj, H. S. J. van der Zant, and P. G. Steeneken, "Highly anisotropic mechanical and optical properties of 2D layered As_2S_3 membranes", ACS Nano **13**, 10845–10851 (2019).

[109] Q. Yang, Y. Su, C. Chi, C. T. Cherian, K. Huang, V. G. Kravets, F. C. Wang, J. C. Zhang, A. Pratt, A. N. Grigorenko, F. Guinea, A. K. Geim, and R. R. Nair, "Ultrathin graphene-based membrane with precise molecular sieving and ultrafast solvent permeation", Nat. Mater. **16**, 1198–1202 (2017).

[110] M. Šiškins, M. Lee, D. Wehenkel, R. van Rijn, T. W. de Jong, J. R. Renshof, B. C. Hopman, W. S. J. M. Peters, D. Davidovikj, H. S. J. van der Zant, and P. G. Steeneken, "Sensitive capacitive pressure sensors based on graphene membrane arrays", Microsyst. Nanoeng. **6**, 102 (2020).

[111] F. Pizzocchero, L. Gammelgaard, B. S. Jessen, J. M. Caridad, L. Wang, J. Hone, P. Bøggild, and T. J. Booth, "The hot pick-up technique for batch assembly of van der Waals heterostructures", Nat. Commun. **7**, 11894 (2016).

[112] A. Castellanos-Gomez, M. Buscema, R. Molenaar, V. Singh, L. Janssen, H. S. J. van der Zant, and G. A. Steele, "Deterministic transfer of two-dimensional materials by all-dry viscoelastic stamping", 2D Mater. **1**, 011002 (2014).

[113] D. Davidovikj, D. Bouwmeester, H. S. J. van der Zant, and P. G. Steeneken, "Graphene gas pumps", 2D Mater. **5**, 031009 (2018).

[114] K. S. Novoselov, D. Jiang, F. Schedin, T. J. Booth, V. V. Khotkevich, S. V. Morozov, and A. K. Geim, "Two-dimensional atomic crystals", Proc. Natl. Acad. Sci. U.S.A. **102**, 10451–10453 (2005).

[115] A. Jain, P. Bharadwaj, S. Heeg, M. Parzefall, T. Taniguchi, K. Watanabe, and L. Novotny, "Minimizing residues and strain in 2D materials transferred from PDMS", Nanotechnology **29**, 265203 (2018).

[116] G.-H. Lee, R. C. Cooper, S. J. An, S. Lee, A. van der Zande, N. Petrone, A. G. Hammerberg, C. Lee, B. Crawford, W. Oliver, J. W. Kysar, and J. Hone, "High-strength chemical-vapor-deposited graphene and grain boundaries", Science **340**, 1073–1076 (2013).

[117] L. E. McNeil and M. Grimsditch, "Elastic constants of As_2S_3", Phys. Rev. B **44**, 4174–4177 (1991).

[118] D. Çakır, F. M. Peeters, and C. Sevik, "Mechanical and thermal properties of h-MX_2 (M=Cr, Mo, W; X = O, S, Se, Te) monolayers: a comparative study", Appl. Phys. Lett. **104**, 203110 (2014).

[119] M. Saint-Paul and P. Monceau, "Survey of the thermodynamic properties of the charge density wave systems", Adv. Condens. Matter Phys. **2019**, 1–14 (2019).

[120] R. Muñoz and C. Gómez-Aleixandre, "Review of CVD synthesis of graphene", Chem. Vap. Deposition **19**, 297–322 (2013).

[121] M. Šiškins, S. Kurdi, M. Lee, B. J. M. Slotboom, W. Xing, S. M. Valero, E. Coronado, S. Jia, W. Han, T. van der Sar, H. S. J. van der Zant, and P. G. Steeneken, "Nanomechanical probing and strain tuning of the Curie temperature in suspended $Cr_2Ge_2Te_6$ heterostructures", Preprint at arXiv:2104.09614 (2021).

[122] J.-W. Jiang and Y.-P. Zhou, "Parameterization of stillinger-weber potential for two-dimensional atomic crystals", in *Handbook of stillinger-weber potential parameters for two-dimensional atomic crystals* (IntechOpen, 2017).

[123] R. Zhang, V. Koutsos, and R. Cheung, "Elastic properties of suspended multilayer WSe_2", Appl. Phys. Lett. **108**, 042104 (2016).

[124] M. Lee, M. Šiškins, S. Mañas-Valero, E. Coronado, P. G. Steeneken, and H. S. J. van der Zant, "Study of charge density waves in suspended 2H-TaS_2 and 2H-$TaSe_2$ by nanomechanical resonance", Appl. Phys. Lett. **118**, 193105 (2021).

[125] T. Natsuki, J.-X. Shi, and Q.-Q. Ni, "Vibration analysis of nanomechanical mass sensor using double-layered graphene sheets resonators", J. Appl. Phys. **114**, 094307 (2013).

[126] H.-L. Lee, Y.-C. Yang, and W.-J. Chang, "Mass detection using a graphene-based nanomechanical resonator", Japanese J. Appl. Phys. **52**, 025101 (2013).

[127] R. J. Dolleman, D. Lloyd, M. Lee, J. S. Bunch, H. S. J. van der Zant, and P. G. Steeneken, "Transient thermal characterization of suspended monolayer MoS_2", Phys. Rev. Mater. **2**, 114008 (2018).

[128] M. Will, M. Hamer, M. Müller, A. Noury, P. Weber, A. Bachtold, R. V. Gorbachev, C. Stampfer, and J. Güttinger, "High quality factor graphene-based two-dimensional heterostructure mechanical resonator", Nano Lett. **17**, 5950–5955 (2017).

[129] A. Castellanos-Gomez, M. Poot, G. A. Steele, H. S. J. van der Zant, N. Agraït, and G. Rubio-Bollinger, "Elastic properties of freely suspended MoS_2 nanosheets", Adv. Mater. **24**, 772–775 (2012).

[130] E. J. Miller, W. Trewby, A. F. Payam, L. Piantanida, C. Cafolla, and K. Voïtchovsky, "Subnanometer resolution imaging with amplitude-modulation atomic force microscopy in liquid", J. Vis. Exp., e54924 (2016).

[131] P. Martins, P. Delobelle, C. Malhaire, S. Brida, and D. Barbier, "Bulge test and AFM point deflection method, two technics for the mechanical characterisation of very low stiffness freestanding films", Eur. Phys. J. Appl. Phys. **45**, 10501 (2009).

[132] C. Berger, R. Phillips, A. Centeno, A. Zurutuza, and A. Vijayaraghavan, "Capacitive pressure sensing with suspended graphene–polymer heterostructure membranes", Nanoscale **9**, 17439–17449 (2017).

[133] L. D. Landau and E. M. Lifshitz, *Theory of elasticity*, 3rd ed. (Elsevier, 1986).

[134] D. Davidovikj, J. J. Slim, S. J. Cartamil-Bueno, H. S. J. van der Zant, P. G. Steeneken, and W. J. Venstra, "Visualizing the motion of graphene nanodrums", Nano Lett. **16**, 2768–2773 (2016).

[135] S. Schmid, L. G. Villanueva, and M. L. Roukes, *Fundamentals of nanomechanical resonators* (Springer International Publishing, 2016).

[136] A. Castellanos-Gomez, R. van Leeuwen, M. Buscema, H. S. J. van der Zant, G. A. Steele, and W. J. Venstra, "Single-layer MoS_2 mechanical resonators", Adv. Mater. **25**, 6719–6723 (2013).

[137] T. Wah, "Vibration of circular plates", J. Acoust. Soc. Am. **34**, 275–281 (1962).

[138] S. Timoshenko, D. H. Young, and W. Weaver, *Vibration problems in engineering*, 4th ed. (Wiley, New York, 1974).

[139] V. Singh, S. Sengupta, H. S. Solanki, R. Dhall, A. Allain, S. Dhara, P. Pant, and M. M. Deshmukh, "Probing thermal expansion of graphene and modal dispersion at low-temperature using graphene nanoelectromechanical systems resonators", Nanotechnology **21**, 165204 (2010).

[140] N. Morell, A. Reserbat-Plantey, I. Tsioutsios, K. G. Schädler, F. Dubin, F. H. L. Koppens, and A. Bachtold, "High quality factor mechanical resonators based on WSe_2 monolayers", Nano Lett. **16**, 5102–5108 (2016).

[141] G. White, J. Birch, and M. H. Manghnani, "Thermal properties of sodium silicate glasses at low temperatures", J. Non-Cryst. Solids **23**, 99–110 (1977).

[142] K. G. Lyon, G. L. Salinger, C. A. Swenson, and G. K. White, "Linear thermal expansion measurements on silicon from 6 to 340 K", J. Appl. Phys. **48**, 865–868 (1977).

[143] C. Chen, *Graphene nanoelectromechanical resonators and oscillators* (Ph.D. thesis, Columbia University, NY, 2013).

[144] S. P. Timoshenko, *Theory of plates and shells*, 2nd ed. (McGraw Hill, New York, 1959).

[145] P. Weber, J. Güttinger, I. Tsioutsios, D. E. Chang, and A. Bachtold, "Coupling graphene mechanical resonators to superconducting microwave cavities", Nano Lett. **14**, 2854–2860 (2014).

[146] M. K. Small and W. Nix, "Analysis of the accuracy of the bulge test in determining the mechanical properties of thin films", J. Mater. Res. Technol. **7**, 1553–1563 (1992).

[147]A. Zurutuza and C. Marinelli, “Challenges and opportunities in graphene commercialization”, Nat. Nanotechnol. **9**, 730–734 (2014).

[148]T. Cui, S. Mukherjee, P. M. Sudeep, G. Colas, F. Najafi, J. Tam, P. M. Ajayan, C. V. Singh, Y. Sun, and T. Filleter, “Fatigue of graphene”, Nature Mater. **19**, 405–411 (2020).

[149]J.-H. Chen, C. Jang, S. Xiao, M. Ishigami, and M. S. Fuhrer, “Intrinsic and extrinsic performance limits of graphene devices on SiO_2”, Nat. Nanotechnol. **3**, 206–209 (2008).

[150]S.-E. Zhu, M. K. Ghatkesar, C. Zhang, and G. C. A. M. Janssen, “Graphene based piezoresistive pressure sensor”, Appl. Phys. Lett. **102**, 161904 (2013).

[151]A. D. Smith, F. Niklaus, A. Paussa, S. Vaziri, A. C. Fischer, M. Sterner, F. Forsberg, A. Delin, D. Esseni, P. Palestri, M. Östling, and M. C. Lemme, “Electromechanical piezoresistive sensing in suspended graphene membranes”, Nano Lett. **13**, 3237–3242 (2013).

[152]A. D. Smith, F. Niklaus, A. Paussa, S. Schröder, A. C. Fischer, M. Sterner, S. Wagner, S. Vaziri, F. Forsberg, D. Esseni, M. Östling, and M. C. Lemme, “Piezoresistive properties of suspended graphene membranes under uniaxial and biaxial strain in nanoelectromechanical pressure sensors”, ACS Nano **10**, 9879–9886 (2016).

[153]R. N. Patel, J. P. Mathew, A. Borah, and M. M. Deshmukh, “Low tension graphene drums for electromechanical pressure sensing”, 2D Mater. **3**, 011003 (2016).

[154]J. Romijn, S. Vollebregt, R. J. Dolleman, M. Singh, H. S. van der Zant, P. G. Steeneken, and P. M. Sarro, “A miniaturized low power Pirani pressure sensor based on suspended graphene”, in 2018 IEEE 13th annual international conference on nano/micro engineered and molecular systems (NEMS) (Apr. 2018).

[155]R. J. Dolleman, S. J. Cartamil-Bueno, H. S. J. van der Zant, and P. G. Steeneken, “Graphene gas osmometers”, 2D Mater. **4**, 011002 (2016).

[156]S. J. Cartamil-Bueno, A. Centeno, A. Zurutuza, P. G. Steeneken, H. S. J. van der Zant, and S. Houri, “Very large scale characterization of graphene mechanical devices using a colorimetry technique”, Nanoscale **9**, 7559–7564 (2017).

[157]R. A. Barton, B. Ilic, A. M. van der Zande, W. S. Whitney, P. L. McEuen, J. M. Parpia, and H. G. Craighead, “High, size-dependent quality factor in an array of graphene mechanical resonators”, Nano Lett. **11**, 1232–1236 (2011).

[158]S. J. Cartamil-Bueno, P. G. Steeneken, A. Centeno, A. Zurutuza, H. S. J. van der Zant, and S. Houri, “Colorimetry technique for scalable characterization of suspended graphene”, Nano Lett. **16**, 6792–6796 (2016).

[159]C. N. Berger, M. Dirschka, and A. Vijayaraghavan, “Ultra-thin graphene–polymer heterostructure membranes”, Nanoscale **8**, 17928–17939 (2016).

[160]Y.-C. Lin, C.-C. Lu, C.-H. Yeh, C. Jin, K. Suenaga, and P.-W. Chiu, “Graphene annealing: how clean can it be?”, Nano Lett. **12**, 414–419 (2011).

[161]Y. Ahn, J. Kim, S. Ganorkar, Y.-H. Kim, and S.-I. Kim, “Thermal annealing of graphene to remove polymer residues”, Mater. Express **6**, 69–76 (2016).

[162]L.-W. Huang, C.-K. Chang, F.-C. Chien, K.-H. Chen, P. Chen, F.-R. Chen, and C.-S. Chang, “Characterization of the cleaning process on a transferred graphene”, J. Vac. Sci. Technol. **32**, 050601 (2014).

[163] L. Gammelgaard, J. M. Caridad, A. Cagliani, D. M. A. Mackenzie, D. H. Petersen, T. J. Booth, and P. Bøggild, "Graphene transport properties upon exposure to PMMA processing and heat treatments", 2D Mater. **1**, 035005 (2014).

[164] C. S. Ruiz-Vargas, H. L. Zhuang, P. Y. Huang, A. M. van der Zande, S. Garg, P. L. McEuen, D. A. Muller, R. G. Hennig, and J. Park, "Softened elastic response and unzipping in chemical vapor deposition graphene membranes", Nano Lett. **11**, 2259–2263 (2011).

[165] R. J. Nicholl, H. J. Conley, N. V. Lavrik, I. Vlassiouk, Y. S. Puzyrev, V. P. Sreenivas, S. T. Pantelides, and K. I. Bolotin, "The effect of intrinsic crumpling on the mechanics of free-standing graphene", Nat. Commun. **6**, 8789 (2015).

[166] Z. Li, I. A. Kinloch, R. J. Young, K. S. Novoselov, G. Anagnostopoulos, J. Parthenios, C. Galiotis, K. Papagelis, C.-Y. Lu, and L. Britnell, "Deformation of wrinkled graphene", ACS Nano **9**, 3917–3925 (2015).

[167] J. W. Suk, R. D. Piner, J. An, and R. S. Ruoff, "Mechanical properties of monolayer graphene oxide", ACS Nano **4**, 6557–6564 (2010).

[168] C. Gómez-Navarro, M. Burghard, and K. Kern, "Elastic properties of chemically derived single graphene sheets", Nano Lett. **8**, 2045–2049 (2008).

[169] A. C. Ferrari, "Raman spectroscopy of graphene and graphite: disorder, electron–phonon coupling, doping and nonadiabatic effects", Solid State Commun. **143**, 47–57 (2007).

[170] K. Kim, S. Coh, L. Z. Tan, W. Regan, J. M. Yuk, E. Chatterjee, M. F. Crommie, M. L. Cohen, S. G. Louie, and A. Zettl, "Raman spectroscopy study of rotated double-layer graphene: misorientation-angle dependence of electronic structure", Phys. Rev. Lett. **108**, 246103 (2012).

[171] Z. H. Ni, H. M. Wang, Y. Ma, J. Kasim, Y. H. Wu, and Z. X. Shen, "Tunable stress and controlled thickness modification in graphene by annealing", ACS Nano **2**, 1033–1039 (2008).

[172] A. Eckmann, A. Felten, A. Mishchenko, L. Britnell, R. Krupke, K. S. Novoselov, and C. Casiraghi, "Probing the nature of defects in graphene by Raman spectroscopy", Nano Lett. **12**, 3925–3930 (2012).

[173] L. A. Ponomarenko, R. Yang, R. V. Gorbachev, P. Blake, A. S. Mayorov, K. S. Novoselov, M. I. Katsnelson, and A. K. Geim, "Density of states and zero Landau level probed through capacitance of graphene", Phys. Rev. Lett. **105**, 136801 (2010).

[174] J. Xia, F. Chen, J. Li, and N. Tao, "Measurement of the quantum capacitance of graphene", Nat. Nanotechnol. **4**, 505–509 (2009).

[175] A. Harzheim, F. Könemann, B. Gotsmann, H. S. J. van der Zant, and P. Gehring, "Single-material graphene thermocouples", Adv. Funct. Mater. **30**, 2000574 (2020).

[176] B. Sa, J. Chen, X. Yang, H. Yang, J. Zheng, C. Xu, J. Li, B. Wu, and H. Zhan, "Elastic anisotropy and optic isotropy in black phosphorene/transition-metal trisulfide van der Waals heterostructures", ACS Omega **4**, 4101–4108 (2019).

[177] W. Shen, C. Hu, J. Tao, J. Liu, S. Fan, Y. Wei, C. An, J. Chen, S. Wu, Y. Li, J. Liu, D. Zhang, L. Sun, and X. Hu, "Resolving the optical anisotropy of low-symmetry 2D materials", Nanoscale **10**, 8329–8337 (2018).

[178] H. Tian, J. Tice, R. Fei, V. Tran, X. Yan, L. Yang, and H. Wang, “Low-symmetry two-dimensional materials for electronic and photonic applications”, Nano Today **11**, 763–777 (2016).

[179] H. Yang, H. Jussila, A. Autere, H.-P. Komsa, G. Ye, X. Chen, T. Hasan, and Z. Sun, “Optical waveplates based on birefringence of anisotropic two-dimensional layered materials”, ACS Photonics **4**, 3023–3030 (2017).

[180] S. Yang, C. Hu, M. Wu, W. Shen, S. Tongay, K. Wu, B. Wei, Z. Sun, C. Jiang, L. Huang, and Z. Wang, “In-plane optical anisotropy and linear dichroism in low-symmetry layered TlSe”, ACS Nano **12**, 8798–8807 (2018).

[181] X. Zhou, X. Hu, B. Jin, J. Yu, K. Liu, H. Li, and T. Zhai, “Highly anisotropic GeSe nanosheets for phototransistors with ultrahigh photoresponsivity”, Adv. Sci. **5**, 1800478 (2018).

[182] Q. Wei and X. Peng, “Superior mechanical flexibility of phosphorene and few-layer black phosphorus”, Appl. Phys. Lett. **104**, 251915 (2014).

[183] M. Moreno-Moreno, G. Lopez-Polin, A. Castellanos-Gomez, C. Gomez-Navarro, and J. Gomez-Herrero, “Environmental effects in mechanical properties of few-layer black phosphorus”, 2D Mater. **3**, 031007 (2016).

[184] R. Frerichs, “New optical glasses with good transparency in the infrared”, J. Opt. Soc. Am. **43**, 1153 (1953).

[185] N. Miao, J. Zhou, B. Sa, B. Xu, and Z. Sun, “Few-layer arsenic trichalcogenides: emerging two-dimensional semiconductors with tunable indirect-direct band-gaps”, J. Alloys Compd. **699**, 554–560 (2017).

[186] L. Debbichi, H. Kim, T. Björkman, O. Eriksson, and S. Lebègue, “First-principles investigation of two-dimensional trichalcogenide and sesquichalcogenide monolayers”, Phys. Rev. B **93**, 245307 (2016).

[187] D. F. Blossey, “Iodine quenching of the surface photoresponse of crystalline As_2S_3”, Chem. Phys. Lett. **25**, 593–595 (1974).

[188] D. F. Blossey and R. Zallen, “Surface and bulk photoresponse of crystalline As_2S_3”, Phys. Rev. B **9**, 4306–4313 (1974).

[189] J. M. Rouvaen, E. Bridoux, M. Moriamez, and R. Torguet, “Acoustic anharmonic properties of arsenic trisulfide glass”, Appl. Phys. Lett. **25**, 97–99 (1974).

[190] M. Khan, A. Mahmoud, L. Cai, M. Mahmoud, T. Mukherjee, J. A. Bain, and G. Piazza, “Acousto-optic modulator based on the integration of arsenic trisulfide photonic components with lithium niobate surface acoustic waves”, in Proceedings of 2019 conference on lasers and electro-optics (cleo), Vol. 8750211 (2019), pp. 1–2.

[191] D. J. E. Mullen and W. Nowacki, “Refinement of the crystal structures of realgar, AsS and orpiment, As_2S_3”, Z. Kristallogr. Cryst. Mater. **136**, 48–65 (1972).

[192] G. V. Gibbs, A. F. Wallace, R. Zallen, R. T. Downs, N. L. Ross, D. F. Cox, and K. M. Rosso, “Bond paths and van der Waals interactions in orpiment, As_2S_3”, J. Phys. Chem. A **114**, 6550–6557 (2010).

[193] E. Ozakin, R. Can, F. Kaya, N. Acar, and A. A. Cevik, “Arsenic poisoning due to the intake of orpiment”, J. Clin. Toxicol. **3**, 176 (2013).

[194] J. A. Buchanan, A. Eberhardt, Z. D. Tebb, K. Heard, R. F. Wendlandt, and M. J. Kosnett, "Massive human ingestion of orpiment (arsenic trisulfide)", J. Emerg. Med. **44**, 367–372 (2013).

[195] J. Liu, Y. Lu, Q. Wu, R. A. Goyer, and M. P. Waalkes, "Mineral arsenicals in traditional medicines: orpiment, realgar, and arsenolite", J. Pharmacol. Exp. Ther. **326**, 363–368 (2008).

[196] C. J. Shearer, A. D. Slattery, A. J. Stapleton, J. G. Shapter, and C. T. Gibson, "Accurate thickness measurement of graphene", Nanotechnology **27**, 125704 (2016).

[197] J. D. Wood, S. A. Wells, D. Jariwala, K.-S. Chen, E. Cho, V. K. Sangwan, X. Liu, L. J. Lauhon, T. J. Marks, and M. C. Hersam, "Effective passivation of exfoliated black phosphorus transistors against ambient degradation", Nano Lett. **14**, 6964–6970 (2014).

[198] B. A. Fowler, C.-H. S. J. Chou, R. L. Jones, and C.-J. Chen, in *Handbook on the toxicology of metals*, edited by G. F. Nordberg, B. A. Fowler, M. Nordberg, and L. T. Friberg, 3rd ed. (Elsevier, San Diego, 2007), pp. 367–406.

[199] P. J. Allen, B. R. Johnson, and B. J. Riley, "Photo-oxidation of thermally evaporated As_2S_3 thin films", J. Optoelectron. Adv. Mater. **7**, 3281–3291 (2005).

[200] M. F. Lengke and R. N. Tempel, "Reaction rates of natural orpiment oxidation at 25 to 40°C and pH 6.8 to 8.2 and comparison with amorphous As_2S_3 oxidation", Geochim. Cosmochim. Acta **66**, 3281–3291 (2002).

[201] R. Zallen and D. F. Blossey, in *Optical and electrical properties*, edited by P. A. Lee (Springer, Dordrecht, 1976), pp. 231–272.

[202] R. Zallen, M. L. Slade, and A. T. Ward, "Lattice vibrations and interlayer interactions in crystalline As_2S_3 and As_2Se_3", Phys. Rev. B **3**, 4257–4273 (1971).

[203] C. Razzetti and P. Lottici, "Polarization analysis of the Raman spectrum of As_2S_3 crystals", Solid State Commun. **29**, 361–364 (1979).

[204] R. J. Kobliska and S. A. Solin, "Temperature dependence of the Raman spectrum and the depolarization spectrum of amorphous As_2S_3", Phys. Rev. B **8**, 756–768 (1973).

[205] P. B. Klein, P. C. Taylor, and D. J. Treacy, "Two-phonon vibrational spectra of As_2S_3. I. Crystalline phase", Phys. Rev. B **16**, 4501–4510 (1977).

[206] S. Mamedov and N. Drichko, "Characterization of 2D As_2S_3 crystal by Raman spectroscopy", MRS Adv. **3**, 385–390 (2018).

[207] A. P. DeFonzo and J. Tauc, "Network dynamics of 3:2 coordinated compounds", Phys. Rev. B **18**, 6957–6972 (1978).

[208] W. Zhu, L. Liang, R. H. Roberts, J.-F. Lin, and D. Akinwande, "Anisotropic electron-phonon interactions in angle-resolved Raman study of strained black phosphorus", ACS Nano **12**, 12512–12522 (2018).

[209] R. Drews, R. Emerald, M. Slade, and R. Zallen, "Interband spectra of As_2S_3 and As_2Se_3 crystals and glasses", Solid State Commun. **10**, 293–296 (1972).

[210] M. Frumar, A. Firth, and A. Owen, "Optically induced crystal-to-amorphous-state transition in As_2S_3", J. Non-Cryst. Solids **192-193**, 447–450 (1995).

[211] F. Glaze, D. Blackburn, J. Osmalov, D. Hubbard, and M. Black, “Properties of arsenic sulfide glass”, J. Res. Natl. Bur. Stand. **59**, 83 (1957).

[212] G. N. Greaves, A. L. Greer, R. S. Lakes, and T. Rouxel, “Poisson’s ratio and modern materials”, Nat. Mater. **10**, 823–837 (2011).

[213] S. I. Chang, A. K. Bajaj, and C. M. Krousgrill, “Non-linear vibrations and chaos in harmonically excited rectangular plates with one-to-one internal resonance”, Nonlinear Dyn. **4**, 433–460 (1993).

[214] A. Avsar, I. J. Vera-Marun, J. Y. Tan, K. Watanabe, T. Taniguchi, A. H. C. Neto, and B. Özyilmaz, “Air-stable transport in graphene-contacted, fully encapsulated ultrathin black phosphorus-based field-effect transistors”, ACS Nano **9**, 4138–4145 (2015).

[215] V. M. Bermudez, “Vibrations of glasslike disordered systems. II. The A_2B_3 network in two dimensions-application to vitreous As_2Se_3 and As_2S_3”, J. Chem. Phys. **57**, 2793–2799 (1972).

[216] G. Lucovsky, “Optic modes in amorphous As_2S_3 and As_2Se_3”, Phys. Rev. B **6**, 1480–1489 (1972).

[217] R. Zallen and M. Slade, “Rigid-layer modes in chalcogenide crystals”, Phys. Rev. B **9**, 1627–1637 (1974).

[218] R. Loudon, “The Raman effect in crystals”, Adv. Phys. **13**, 423–482 (1964).

[219] M. Amabili, *Nonlinear vibrations and stability of shells and plates* (Cambridge University Press, Cambridge, 2008).

[220] B. Merle, K. S. Nicholson, E. G. Herbert, and M. Göken, “An improved method for point deflection measurements on rectangular membranes”, Mater. Des. **109**, 485–491 (2016).

[221] S. G. Lekhnitski, “Anisotropic plates”, in, 2nd ed. (Gordon and Breach, New York, 1968).

[222] M. Kim, S. Han, J. H. Kim, J.-U. Lee, Z. Lee, and H. Cheong, “Determination of the thickness and orientation of few-layer tungsten ditelluride using polarized Raman spectroscopy”, 2D Mater. **3**, 034004 (2016).

[223] Q. Song, H. Wang, X. Xu, X. Pan, Y. Wang, F. Song, X. Wan, and L. Dai, “The polarization-dependent anisotropic Raman response of few-layer and bulk WTe_2 under different excitation wavelengths”, RSC Adv. **6**, 103830–103837 (2016).

[224] C. Chen, S. Lee, V. V. Deshpande, G.-H. Lee, M. Lekas, K. Shepard, and J. Hone, “Graphene mechanical oscillators with tunable frequency”, Nat. Nanotechnol. **8**, 923–927 (2013).

[225] Y. Cao, V. Fatemi, S. Fang, K. Watanabe, T. Taniguchi, E. Kaxiras, and P. Jarillo-Herrero, “Unconventional superconductivity in magic-angle graphene superlattices”, Nature **556**, 43–50 (2018).

[226] A. L. Sharpe, E. J. Fox, A. W. Barnard, J. Finney, K. Watanabe, T. Taniguchi, M. A. Kastner, and D. Goldhaber-Gordon, “Emergent ferromagnetism near three-quarters filling in twisted bilayer graphene”, Science **365**, 605–608 (2019).

[227] Y. Takano, N. Arai, A. Arai, Y. Takahashi, K. Takase, and K. Sekizawa, “Magnetic properties and specific heat of MPS_3 (M=Mn, Fe, Zn)”, J. Magn. Magn. Mat. **272-276**, E593–E595 (2004).

[228] C. Zener, “Internal friction in solids I. Theory of internal friction in reeds”, Phys. Rev. **52**, 230–235 (1937).

[229] R. Lifshitz and M. L. Roukes, “Thermoelastic damping in micro- and nanomechanical systems”, Phys. Rev. B **61**, 5600–5609 (2000).

[230] D. S. Sanditov and V. N. Belomestnykh, “Relation between the parameters of the elasticity theory and averaged bulk modulus of solids”, Tech. Phys. **56**, 1619–1623 (2011).

[231] V. N. Belomestnykh and E. P. Tesleva, “Interrelation between anharmonicity and lateral strain in quasi-isotropic polycrystalline solids”, Tech. Phys. **49**, 1098–1100 (2004).

[232] K. Leont’ev, “On connection between elastic and thermal properties of substances”, Akusticheskij Zhurnal **27**, 554–561 (1981).

[233] J. Lee, Z. Wang, K. He, R. Yang, J. Shan, and P. X.-L. Feng, “Electrically tunable single- and few-layer MoS_2 nanoelectromechanical systems with broad dynamic range”, Sci. Adv.. **4**, eaao6653 (2018).

[234] D. Ji, S. Cai, T. R. Paudel, H. Sun, C. Zhang, L. Han, Y. Wei, Y. Zang, M. Gu, Y. Zhang, W. Gao, H. Huyan, W. Guo, D. Wu, Z. Gu, E. Y. Tsymbal, P. Wang, Y. Nie, and X. Pan, “Freestanding crystalline oxide perovskites down to the monolayer limit”, Nature **570**, 87–90 (2019).

[235] C. Zener, “Internal friction in solids II. General theory of thermoelastic internal friction”, Phys. Rev. **53**, 90–99 (1938).

[236] K. Kim, S. Y. Lim, J.-U. Lee, S. Lee, T. Y. Kim, K. Park, G. S. Jeon, C.-H. Park, J.-G. Park, and H. Cheong, “Suppression of magnetic ordering in XXZ-type antiferromagnetic monolayer $NiPS_3$”, Nat. Commun. **10**, 345 (2019).

[237] D. S. Sanditov, A. A. Mashanov, M. V. Darmaev, B. D. Sanditov, and V. V. Mantatov, “Grüneisen parameter and elastic constants of crystals and vitreous bodies”, Russ. Phys. J. **52**, 221–230 (2009).

[238] H. Okamoto, A. Gourgout, C.-Y. Chang, K. Onomitsu, I. Mahboob, E. Y. Chang, and H. Yamaguchi, “Coherent phonon manipulation in coupled mechanical resonators”, Nat. Phys. **9**, 480–484 (2013).

[239] T. Faust, J. Rieger, M. J. Seitner, J. P. Kotthaus, and E. M. Weig, “Coherent control of a classical nanomechanical two-level system”, Nat. Phys. **9**, 485–488 (2013).

[240] D. Zhu, X.-H. Wang, W.-C. Kong, G.-W. Deng, J.-T. Wang, H.-O. Li, G. Cao, M. Xiao, K.-L. Jiang, X.-C. Dai, G.-C. Guo, F. Nori, and G.-P. Guo, “Coherent phonon Rabi oscillations with a high-frequency carbon nanotube phonon cavity”, Nano Lett. **17**, 915–921 (2017).

[241] S.-B. Shim, M. Imboden, and P. Mohanty, “Synchronized oscillation in coupled nanomechanical oscillators”, Science **316**, 95–99 (2007).

[242] J. P. Mathew, R. N. Patel, A. Borah, R. Vijay, and M. M. Deshmukh, “Dynamical strong coupling and parametric amplification of mechanical modes of graphene drums”, Nat. Nanotechnol. **11**, 747–751 (2016).

[243] C.-H. Liu, I. S. Kim, and L. J. Lauhon, “Optical control of mechanical mode-coupling within a MoS_2 resonator in the strong-coupling regime”, Nano Lett. **15**, 6727–6731 (2015).

[244] P. Prasad, N. Arora, and A. K. Naik, “Gate tunable cooperativity between vibrational modes”, Nano Lett. **19**, 5862–5867 (2019).

[245] G. Luo, Z.-Z. Zhang, G.-W. Deng, H.-O. Li, G. Cao, M. Xiao, G.-C. Guo, L. Tian, and G.-P. Guo, “Strong indirect coupling between graphene-based mechanical resonators via a phonon cavity”, Nat. Commun. **9**, 383 (2018).

[246] Z.-Z. Zhang, X.-X. Song, G. Luo, Z.-J. Su, K.-L. Wang, G. Cao, H.-O. Li, M. Xiao, G.-C. Guo, L. Tian, G.-W. Deng, and G.-P. Guo, “Coherent phonon dynamics in spatially separated graphene mechanical resonators”, Proc. Natl. Acad. Sci. U.S.A **117**, 5582–5587 (2020).

[247] X. Song, M. Oksanen, M. A. Sillanpää, H. G. Craighead, J. M. Parpia, and P. J. Hakonen, “Stamp transferred suspended graphene mechanical resonators for radio frequency electrical readout”, Nano Lett. **12**, 198–202 (2011).

[248] D. H. Zanette, “Energy exchange between coupled mechanical oscillators: linear regimes”, J. Phys. Commun. **2**, 095015 (2018).

[249] C. R. S. Haines, M. J. Coak, A. R. Wildes, G. I. Lampronti, C. Liu, P. Nahai-Williamson, H. Hamidov, D. Daisenberger, and S. S. Saxena, “Pressure-induced electronic and structural phase evolution in the van der Waals compound $FePS_3$”, Phys. Rev. Lett. **121**, 266801 (2018).

[250] R. A. Evarestov and A. Kuzmin, “Origin of pressure-induced insulator-to-metal transition in the van der Waals compound $FePS_3$ from first-principles calculations”, J. Comput. Chem. **41**, 1337–1344 (2020).

[251] C. Ulloa, R. E. Troncoso, S. A. Bender, R. A. Duine, and A. S. Nunez, “Piezospintronic effect in honeycomb antiferromagnets”, Phys. Rev. B **96**, 104419 (2017).

[252] M. Rajapakse, B. Karki, U. O. Abu, S. Pishgar, M. R. K. Musa, S. M. S. Riyadh, M. Yu, G. Sumanasekera, and J. B. Jasinski, “Intercalation as a versatile tool for fabrication, property tuning, and phase transitions in 2D materials”, npj 2D Mater. Appl. **5**, 30 (2021).

[253] J. Dugay, M. Aarts, M. Giménez-Marqués, T. Kozlova, H. W. Zandbergen, E. Coronado, and H. S. J. van der Zant, “Phase transitions in spin-crossover thin films probed by graphene transport measurements”, Nano Lett. **17**, 186–193 (2016).

[254] M. Gobbi, E. Orgiu, and P. Samorì, “When 2D materials meet molecules: opportunities and challenges of hybrid organic/inorganic van der Waals heterostructures”, Adv. Mater. **30**, 1706103 (2018).

[255] Y. Peng, Y. Li, Y. Ban, H. Jin, W. Jiao, X. Liu, and W. Yang, “Metal-organic framework nanosheets as building blocks for molecular sieving membranes”, Science **346**, 1356–1359 (2014).

[256] C. Hermosa, B. R. Horrocks, J. I. Martínez, F. Liscio, J. Gómez-Herrero, and F. Zamora, “Mechanical and optical properties of ultralarge flakes of a metal–organic framework with molecular thickness”, Chem. Sci. **6**, 2553–2558 (2015).

[257] T. Rodenas, I. Luz, G. Prieto, B. Seoane, H. Miro, A. Corma, F. Kapteijn, F. X. L. i Xamena, and J. Gascon, “Metal–organic framework nanosheets in polymer composite materials for gas separation”, Nat. Mater. **14**, 48–55 (2014).

[258] J. C. Tan, T. D. Bennett, and A. K. Cheetham, “Chemical structure, network topology, and porosity effects on the mechanical properties of zeolitic imidazolate frameworks”, Proc. Natl. Acad. Sci. U.S.A. **107**, 9938–9943 (2010).

[259] J.-C. Tan, B. Civalleri, C.-C. Lin, L. Valenzano, R. Galvelis, P.-F. Chen, T. D. Bennett, C. Mellot-Draznieks, C. M. Zicovich-Wilson, and A. K. Cheetham, “Exceptionally low shear modulus in a prototypical imidazole-based metal-organic framework”, Phys. Rev. Lett. **108**, 095502 (2012).

[260] J. C. Tan and A. K. Cheetham, “Mechanical properties of hybrid inorganic–organic framework materials: establishing fundamental structure–property relationships”, Chem. Soc. Rev. **40**, 1059 (2011).

[261] A. L. Goodwin, M. Calleja, M. J. Conterio, M. T. Dove, J. S. O. Evans, D. A. Keen, L. Peters, and M. G. Tucker, “Colossal positive and negative thermal expansion in the framework material $Ag_3[Co(CN)_6]$”, Science **319**, 794–797 (2008).

[262] M. J. Cliffe, J. A. Hill, C. A. Murray, F.-X. Coudert, and A. L. Goodwin, “Defect-dependent colossal negative thermal expansion in UiO-66(Hf) metal–organic framework”, Phys. Chem. Chem. Phys. **17**, 11586–11592 (2015).

[263] M. T. Dove and H. Fang, “Negative thermal expansion and associated anomalous physical properties: review of the lattice dynamics theoretical foundation”, Rep. Prog. Phys. **79**, 066503 (2016).

[264] J. D. Evans, J. P. Dürholt, S. Kaskel, and R. Schmid, “Assessing negative thermal expansion in mesoporous metal–organic frameworks by molecular simulation”, J. Mater. Chem. A **7**, 24019–24026 (2019).

[265] W. Miller, C. W. Smith, D. S. Mackenzie, and K. E. Evans, “Negative thermal expansion: a review”, J. Mater. Sci. **44**, 5441–5451 (2009).

[266] V. Carteaux, D. Brunet, G. Ouvrard, and G. Andre, “Crystallographic, magnetic and electronic structures of a new layered ferromagnetic compound $Cr_2Ge_2Te_6$”, J. Phys. Condens. Matter. **7**, 69–87 (1995).

[267] I. A. Verzhbitskiy, H. Kurebayashi, H. Cheng, J. Zhou, S. Khan, Y. P. Feng, and G. Eda, “Controlling the magnetic anisotropy in $Cr_2Ge_2Te_6$ by electrostatic gating”, Nat. Electron. **3**, 460–465 (2020).

[268] Z. Wang, T. Zhang, M. Ding, B. Dong, Y. Li, M. Chen, X. Li, J. Huang, H. Wang, X. Zhao, Y. Li, D. Li, C. Jia, L. Sun, H. Guo, Y. Ye, D. Sun, Y. Chen, T. Yang, J. Zhang, S. Ono, Z. Han, and Z. Zhang, “Electric-field control of magnetism in a few-layered van der Waals ferromagnetic semiconductor”, Nat. Nanotechnol. **13**, 554–559 (2018).

[269] S. Selter, G. Bastien, A. U. B. Wolter, S. Aswartham, and B. Büchner, “Magnetic anisotropy and low-field magnetic phase diagram of the quasi-two-dimensional ferromagnet $Cr_2Ge_2Te_6$”, Phys. Rev. B **101**, 014440 (2020).

[270] Y. Sun, R. C. Xiao, G. T. Lin, R. R. Zhang, L. S. Ling, Z. W. Ma, X. Luo, W. J. Lu, Y. P. Sun, and Z. G. Sheng, “Effects of hydrostatic pressure on spin-lattice coupling in two-dimensional ferromagnetic $Cr_2Ge_2Te_6$”, Appl. Phys. Lett. **112**, 072409 (2018).

[271] T. Sakurai, B. Rubrecht, L. T. Corredor, R. Takehara, M. Yasutani, J. Zeisner, A. Alfonsov, S. Selter, S. Aswartham, A. U. B. Wolter, B. Büchner, H. Ohta, and V. Kataev, “Pressure control of the magnetic anisotropy of the quasi-two-dimensional van der Waals ferromagnet $Cr_2Ge_2Te_6$”, Phys. Rev. B **103**, 024404 (2021).

[272] N. Wang, H. Tang, M. Shi, H. Zhang, W. Zhuo, D. Liu, F. Meng, L. Ma, J. Ying, L. Zou, Z. Sun, and X. Chen, “Transition from ferromagnetic semiconductor to ferromagnetic metal with enhanced Curie temperature in $Cr_2Ge_2Te_6$ via organic ion intercalation”, J. Am. Chem. Soc. **141**, 17166–17173 (2019).

[273] V. Gupta, T. M. Cham, G. M. Stiehl, A. Bose, J. A. Mittelstaedt, K. Kang, S. Jiang, K. F. Mak, J. Shan, R. A. Buhrman, and D. C. Ralph, “Manipulation of the van der Waals magnet $Cr_2Ge_2Te_6$ by spin–orbit torques”, Nano Lett. **20**, 7482–7488 (2020).

[274] V. Ostwal, T. Shen, and J. Appenzeller, “Efficient spin-orbit torque switching of the semiconducting van der Waals ferromagnet $Cr_2Ge_2Te_6$”, Adv. Mater. **32**, 1906021 (2020).

[275] Y. Tian, M. J. Gray, H. Ji, R. J. Cava, and K. S. Burch, “Magneto-elastic coupling in a potential ferromagnetic 2D atomic crystal”, 2D Mater. **3**, 025035 (2016).

[276] D. P. Kozlenko, O. N. Lis, S. E. Kichanov, E. V. Lukin, N. M. Belozerova, and B. N. Savenko, “Spin-induced negative thermal expansion and spin–phonon coupling in van der Waals material $CrBr_3$”, npj Quantum Mater. **6**, 19 (2021).

[277] L. D. Casto, A. J. Clune, M. O. Yokosuk, J. L. Musfeldt, T. J. Williams, H. L. Zhuang, M.-W. Lin, K. Xiao, R. G. Hennig, B. C. Sales, J.-Q. Yan, and D. Mandrus, “Strong spin-lattice coupling in $CrSiTe_3$”, APL Mater. **3**, 041515 (2015).

[278] M. A. McGuire, H. Dixit, V. R. Cooper, and B. C. Sales, “Coupling of crystal structure and magnetism in the layered, ferromagnetic insulator CrI_3”, Chem. Mater. **27**, 612–620 (2015).

[279] S. Yang, Y. Chen, and C. Jiang, “Strain engineering of two-dimensional materials: methods, properties, and applications”, InfoMat **3**, 397–420 (2021).

[280] F. Ye, J. Lee, and P. X.-L. Feng, “Atomic layer MoS_2-graphene van der Waals heterostructure nanomechanical resonators”, Nanoscale **9**, 18208–18215 (2017).

[281] Z. Ni, A. V. Haglund, H. Wang, B. Xu, C. Bernhard, D. G. Mandrus, X. Qian, E. J. Mele, C. L. Kane, and L. Wu, “Imaging the Néel vector switching in the monolayer antiferromagnet $MnPSe_3$ with strain-controlled Ising order”, Nat. Nanotechnol. **16**, 782–787 (2021).

[282] K. Liu, Q. Yan, M. Chen, W. Fan, Y. Sun, J. Suh, D. Fu, S. Lee, J. Zhou, S. Tongay, J. Ji, J. B. Neaton, and J. Wu, “Elastic properties of chemical-vapor-deposited monolayer MoS_2, WS_2, and their bilayer heterostructures”, Nano Lett. **14**, 5097–5103 (2014).

[283] S. Kim, J. Yu, and A. M. van der Zande, “Nano-electromechanical drumhead resonators from two-dimensional material bimorphs”, Nano Lett. **18**, 6686–6695 (2018).

[284] M. de Jong, W. Chen, T. Angsten, A. Jain, R. Notestine, A. Gamst, M. Sluiter, C. K. Ande, S. van der Zwaag, J. J. Plata, C. Toher, S. Curtarolo, G. Ceder, K. A. Persson, and M. Asta, “Charting the complete elastic properties of inorganic crystalline compounds”, Sci. Data **2**, 150009 (2015).

[285] T. Chen, M. Pauly, and P. M. Reis, “A reprogrammable mechanical metamaterial with stable memory”, Nature **589**, 386–390 (2021).

[286] D. Roodenburg, J. W. Spronck, H. S. J. van der Zant, and W. J. Venstra, “Buckling beam micromechanical memory with on-chip readout”, Appl. Phys. Lett. **94**, 183501 (2009).

[287] Y. Sun, D. Fang, and A. K. Soh, “Thermoelastic damping in micro-beam resonators”, Int. J. Solids. Struct. **43**, 3213–3229 (2006).

[288] B. J. M. Slotboom, *Temperature dependent high-frequency mechanics of stacked ultra-thin ferromagnetic nanoresonators* (BSc thesis, Delft University of Technology, Delft, 2020).

[289] M. Agarwal and P. Wani, “Growth conditions and crystal structure parameters of layer compounds in the series $Mo_{1-x}W_xSe_2$”, Mater. Res. Bull. **14**, 825–830 (1979).

[290] F. Zeng, W.-B. Zhang, and B.-Y. Tang, “Electronic structures and elastic properties of monolayer and bilayer transition metal dichalcogenides MX_2 (M= Mo, W; X= O, S, Se, Te): a comparative first-principles study”, Chin. Phys. B **24**, 097103 (2015).

[291] X.-J. Dong, J.-Y. You, Z. Zhang, B. Gu, and G. Su, “Great enhancement of Curie temperature and magnetic anisotropy in two-dimensional van der Waals magnetic semiconductor heterostructures”, Phys. Rev. B **102**, 144443 (2020).

[292] L. Zhang, X. Huang, H. Dai, M. Wang, H. Cheng, L. Tong, Z. Li, X. Han, X. Wang, L. Ye, and J. Han, “Proximity-coupling-induced significant enhancement of coercive field and Curie temperature in 2D van der Waals heterostructures”, Adv. Mater. **32**, 2002032 (2020).

[293] Y. Ben-Shimon and A. Ya’akobovitz, “Magnetic excitation and dissipation of multilayer two-dimensional resonators”, Appl. Phys. Lett. **118**, 063103 (2021).

[294] M. Doerr, M. Rotter, and A. Lindbaum, “Magnetostriction in rare-earth based antiferromagnets”, Adv. Phys. **54**, 1–66 (2005).

[295] P. Jernberg, S. Bjarman, and R. Wäppling, “$FePS_3$: a first-order phase transition in a 2D Ising antiferromagnet”, J. Magn. Magn. Mater. **46**, 178–190 (1984).

[296] C. Murayama, M. Okabe, D. Urushihara, T. Asaka, K. Fukuda, M. Isobe, K. Yamamoto, and Y. Matsushita, “Crystallographic features related to a van der Waals coupling in the layered chalcogenide $FePS_3$”, J. Appl. Phys. **120**, 142114 (2016).

[297] A. W. Leissa and M. S. Qatu, *Vibrations of continuous systems* (New York: McGraw-Hill, 2011).

[298] R. I. Thomson, T. Chatterji, and M. A. Carpenter, “CoF_2: a model system for magnetoelastic coupling and elastic softening mechanisms associated with paramagnetic-antiferromagnetic phase transitions”, J. Phys. Condens. Matter. **26**, 146001 (2014).

[299] T. Sekine, M. Jouanne, C. Julien, and M. Balkanski, “Light-scattering study of dynamical behavior of antiferromagnetic spins in the layered magnetic semiconductor $FePS_3$”, Phys. Rev. B **42**, 8382–8393 (1990).

[300] K. C. Rule, G. J. McIntyre, S. J. Kennedy, and T. J. Hicks, “Single-crystal and powder neutron diffraction experiments on $FePS_3$: search for the magnetic structure”, Phys. Rev. B **76**, 134402 (2007).

[301] A. R. Wildes, V. Simonet, E. Ressouche, G. J. McIntyre, M. Avdeev, E. Suard, S. A. J. Kimber, D. Lançon, G. Pepe, B. Moubaraki, and T. J. Hicks, “Magnetic structure of the quasi-two-dimensional antiferromagnet $NiPS_3$”, Phys. Rev. B **92**, 224408 (2015).

[302] S. Yang, T. Zhang, and C. Jiang, “Van der Waals magnets: material family, detection and modulation of magnetism, and perspective in spintronics”, Adv. Sci. **8**, 2002488 (2020).

[303] S. T. Bramwell and P. C. W. Holdsworth, “Magnetization and universal sub-critical behaviour in two-dimensional XY magnets”, J. Phys. Condens. Matter. **5**, L53–L59 (1993).

[304] F. Liu, L. You, K. L. Seyler, X. Li, P. Yu, J. Lin, X. Wang, J. Zhou, H. Wang, H. He, S. T. Pantelides, W. Zhou, P. Sharma, X. Xu, P. M. Ajayan, J. Wang, and Z. Liu, “Room-temperature ferroelectricity in $CuInP_2S_6$ ultrathin flakes”, Nat. Commun. **7**, 12357 (2016).

[305] Y. Wang, N. Xu, D. Li, and J. Zhu, “Thermal properties of two dimensional layered materials”, Adv. Funct. Mater. **27**, 1604134 (2017).

[306] H. Song, J. Liu, B. Liu, J. Wu, H.-M. Cheng, and F. Kang, “Two-dimensional materials for thermal management applications”, Joule **2**, 442–463 (2018).

[307] Y. Sun and M. Saka, “Thermoelastic damping in micro-scale circular plate resonators”, J. Sound Vib. **329**, 328–337 (2010).

[308] Y. Fang, P. Li, and Z. Wang, “Thermoelastic damping in the axisymmetric vibration of circular microplate resonators with two-dimensional heat conduction”, J. Therm. Stress. **36**, 830–850 (2013).

[309] R. Resmi, V. S. Babu, and M. R. Baiju, “Analysis of thermoelastic damping limited quality factor and critical dimensions of circular plate resonators based on axisymmetric and non-axisymmetric vibrations”, AIP Adv. **11**, 035108 (2021).

[310] C. Ma, S. Chen, and F. Guo, “Thermoelastic damping in micromechanical circular plate resonators with radial pre-tension”, J. Therm. Stress. **43**, 175–190 (2019).

[311] A. Haglund, *Thermal conductivity of* MXY_3 *magnetic layered trichalcogenides* (Ph.D. thesis, University of Tennessee, Knoxville, 2019).

[312] K. L. Aubin, *Radio frequency nano/microelectromechanical resonators: thermal and nonlinear dynamics studies* (Ph.D. thesis, Cornell University Ithaca, NY, 2004).

[313] X. Wang, K. Du, Y. Y. F. Liu, P. Hu, J. Zhang, Q. Zhang, M. H. S. Owen, X. Lu, C. K. Gan, P. Sengupta, C. Kloc, and Q. Xiong, “Raman spectroscopy of atomically thin two-dimensional magnetic iron phosphorus trisulfide ($FePS_3$) crystals”, 2D Mater. **3**, 031009 (2016).

[314] X.-K. Chen, Y.-J. Zeng, and K.-Q. Chen, “Thermal transport in two-dimensional heterostructures”, Front. Mater. **7**, 578791 (2020).

[315] S. C. de la Barrera, M. R. Sinko, D. P. Gopalan, N. Sivadas, K. L. Seyler, K. Watanabe, T. Taniguchi, A. W. Tsen, X. Xu, D. Xiao, and B. M. Hunt, "Tuning Ising superconductivity with layer and spin-orbit coupling in two-dimensional transition-metal dichalcogenides", Nat. Commun. **9**, 1427 (2018).

[316] J. Bekaert, E. Khestanova, D. G. Hopkinson, J. Birkbeck, N. Clark, M. Zhu, D. A. Bandurin, R. Gorbachev, S. Fairclough, Y. Zou, M. Hamer, D. J. Terry, J. J. P. Peters, A. M. Sanchez, B. Partoens, S. J. Haigh, M. V. Milošević, and I. V. Grigorieva, "Enhanced superconductivity in few-layer TaS_2 due to healing by oxygenation", Nano Lett. **20**, 3808–3818 (2020).

[317] X. Xi, L. Zhao, Z. Wang, H. Berger, L. Forró, J. Shan, and K. F. Mak, "Strongly enhanced charge-density-wave order in monolayer $NbSe_2$", Nat. Nanotechnol. **10**, 765–769 (2015).

[318] D. Zhang, Y. Wu, Y.-H. Su, M.-C. Hsu, C. Ó. Coileáin, J. Cho, M. Choi, B. S. Chun, Y. Guo, C.-R. Chang, and H.-C. Wu, "Charge density waves and degenerate modes in exfoliated monolayer 2H-TaS_2", IUCrJ **7**, 913–919 (2020).

[319] Y. Wu, J. He, J. Liu, H. Xing, Z. Mao, and Y. Liu, "Dimensional reduction and ionic gating induced enhancement of superconductivity in atomically thin crystals of 2H-$TaSe_2$", Nanotechnology **30**, 035702 (2018).

[320] M. Abdel-Hafiez, X.-M. Zhao, A. A. Kordyuk, Y.-W. Fang, B. Pan, Z. He, C.-G. Duan, J. Zhao, and X.-J. Chen, "Enhancement of superconductivity under pressure and the magnetic phase diagram of tantalum disulfide single crystals", Sci. Rep. **6**, 31824 (2016).

[321] S. T. Davitadze, S. N. Kravchun, B. A. Strukov, B. M. Goltzman, V. V. Lemanov, and S. G. Shulman, "Specific heat and thermal conductivity of $BaTiO_3$ polycrystalline thin films", Appl. Phys. Lett. **80**, 1631–1633 (2002).

[322] S. F. Zhao, N. Poccia, M. G. Panetta, C. Yu, J. W. Johnson, H. Yoo, R. Zhong, G. Gu, K. Watanabe, T. Taniguchi, S. V. Postolova, V. M. Vinokur, and P. Kim, "Sign-reversing Hall effect in atomically thin high-temperature $Bi_{2.1}Sr_{1.9}CaCu_{2.0}O_{8+\delta}$ superconductors", Phys. Rev. Lett. **122**, 247001 (2019).

[323] H. Kierspel, H. Winkelmann, T. Auweiler, W. Schlabitz, B. Büchner, V. Duijn, N. Hien, A. Menovsky, and J. Franse, "Thermal expansion, specific heat, and uniaxial pressure dependences of tc in $Bi_2Sr_2CaCu_2O_{8+\delta}$", Phys. C (Amsterdam, Neth.) **262**, 177–186 (1996).

[324] O. M. Nes, M. Castro, M. Slaski, T. Laegreid, K. Fossheim, N. Motohira, and K. Kitazawa, "Anomalies in elastic and thermal properties associated with the superconducting transition of single crystal $Bi_2Sr_2CaCu_2O_y$", Supercond. Sci. Technol. **4**, S388–S390 (1991).

[325] X. Liu, Z. Zhang, Z. Ding, B. Lv, Z. Luo, J.-S. Wang, and Z. Gao, "Highly anisotropic electronic and mechanical properties of monolayer and bilayer As_2S_3", Appl. Surf. Sci. **542**, 148665 (2021).

[326] W. Gao and J. R. Chelikowsky, "Prediction of intrinsic ferroelectricity and large piezoelectricity in monolayer arsenic chalcogenides", Nano Lett. **20**, 8346–8352 (2020).

[327] A. Patel, D. Singh, Y. Sonvane, P. Thakor, and R. Ahuja, “Bulk and monolayer As_2S_3 as promising thermoelectric material with high conversion performance”, Computational Materials Science **183**, 109913 (2020).

[328] K. Hejazi, Z.-X. Luo, and L. Balents, “Noncollinear phases in moiré magnets”, Proc. Natl. Acad. Sci. U.S.A. **117**, 10721–10726 (2020).

[329] J. Shang, X. Tang, X. Tan, A. Du, T. Liao, S. C. Smith, Y. Gu, C. Li, and L. Kou, “Stacking-dependent interlayer magnetic coupling in 2D $CrI_3/CrGeTe_3$ nanostructures for spintronics”, ACS Appl. Nano Mater. **3**, 1282–1288 (2019).

[330] Q. Tong, F. Liu, J. Xiao, and W. Yao, “Skyrmions in the moiré of van der Waals 2D magnets”, Nano Lett. **18**, 7194–7199 (2018).

[331] S. Carr, S. Fang, and E. Kaxiras, “Electronic-structure methods for twisted moiré layers”, Nat. Rev. Mater. **5**, 748–763 (2020).

[332] Z. Qiu, M. Holwill, T. Olsen, P. Lyu, J. Li, H. Fang, H. Yang, M. Kashchenko, K. S. Novoselov, and J. Lu, “Visualizing atomic structure and magnetism of 2D magnetic insulators via tunneling through graphene”, Nat. Commun. **12**, 70 (2021).

[333] T. Liu, D. I. Pikulin, and M. Franz, “Quantum oscillations without magnetic field”, Phys. Rev. B **95**, 041201 (2017).

CURRICULUM VITÆ

Makars ŠIŠKINS

03-09-1993	Born in Riga, Latvia.

EDUCATION

2000–2012	High School Secondary School #95 of Riga, Riga, Latvia
2012–2017	Master of Physics (Honours) The University of Manchester, Manchester, The United Kingdom
Thesis:	High-temperature electronics based on graphene and boron nitride heterostructures
Promotors:	Prof. dr. A. Mishchenko, Prof. dr. Sir K. S. Novoselov
2017–2021	Ph.D. in Physics Delft University of Technology, Delft, The Netherlands
Thesis:	Higher-order phenomena in nanomechanics of two-dimensional material membranes
Promotors:	Prof. dr. P. G. Steeneken, Prof. dr. ir. H. S. J. van der Zant

AWARDS

2017	Platt Prize in Physics for experimental work, The University of Manchester

LIST OF PUBLICATIONS

15. J. López-Cabrelles[*], S. Mañas-Valero[*], I. J. Vitórica-Yrezábal, **M. Šiškins**, M. Lee, P. G. Steeneken, H. S. J. van der Zant, G. M. Espallargas, E. Coronado, *Chemical design and magnetic ordering in thin layers of 2D MOFs*, Under Review, Preprint: arXiv:2107.11569 (2021).

14. **M. Šiškins**, S. Kurdi, M. Lee, B. J. M. Slotboom, W. Xing, S. Mañas-Valero, E. Coronado, S. Jia, W. Han, T. van der Sar, H. S. J. van der Zant, P. G. Steeneken, *Nanomechanical probing and strain tuning of the Curie temperature in suspended* $Cr_2Ge_2Te_6$ *heterostructures*, Under Review, Preprint: arXiv:2104.09614 (2021).

13. **M. Šiškins**[*], E. Sokolovskaya[*], M. Lee, S. Mañas-Valero, D. Davidovikj, E. Coronado, H. S. J. van der Zant, P. G. Steeneken, *Tunable strong coupling of mechanical resonance between spatially separated* $FePS_3$ *nanodrums*, Under Review, Preprint: arXiv:2107.01262 (2021).

12. M. Lee[*], **M. Šiškins**[*], S. Mañas-Valero, E. Coronado, P. G. Steeneken, H. S. J. van der Zant, *Study of charge density waves in suspended 2H-*TaS_2 *and 2H-*$TaSe_2$ *by nanomechanical resonance*, Applied Physics Letters **118** (19), 193105 (2021).

11. D. Afanasiev, J. R. Hortensius, M. Matthiesen, S. Mañas-Valero, **M. Šiškins**, M. Lee, E. Lesne, H. S. J. van der Zant, P. G. Steeneken, B. A. Ivanov, E. Coronado, A. D. Caviglia, *Controlling the anisotropy of a van der Waals antiferromagnet with light*, Science Advances **7** (23), eabf3096 (2021).

10. I. E. Rosłoń, R. J. Dolleman, H. Licona, M. Lee, **M. Šiškins**, H. Lebius, L. Madauß, M. Schleberger, F. Alijani, H. S. J. van der Zant, P. G. Steeneken, *High-frequency gas effusion through nanopores in suspended graphene*, Nature Communications **11** (1), 6025 (2020).

9. **M. Šiškins**, M. Lee, D. Wehenkel, R. van Rijn, T. W. de Jong, J. R. Renshof, B. C. Hopman, W. S. J. M. Peters, D. Davidovikj, H. S. J. van der Zant, P. G. Steeneken, *Sensitive capacitive pressure sensors based on graphene membrane arrays*, Microsystems & Nanoengineering **6** (1), 102 (2020).

8. D. Davidovikj, D. J. Groenendijk, A. M. R. V. L. Monteiro, A. Dijkhoff, D. Afanasiev, **M. Šiškins**, M. Lee, Y. Huang, E. van Heumen, H. S. J. van der Zant, A. D. Caviglia, P. G. Steeneken, *Ultrathin complex oxide nanomechanical resonators*, Communications Physics **3** (1), 163 (2020).

7. **M. Šiškins**[*], M. Lee[*], S. Mañas-Valero, E. Coronado, Y. M. Blanter, H. S. J. van der Zant, P. G. Steeneken, *Magnetic and electronic phase transitions probed by nanomechanical resonators*, Nature Communications **11** (1), 2698 (2020).

6. T. C. van Thiel, J. Fowlie, C. Autieri, N. Manca, **M. Šiškins**, D. Afanasiev, S. Gariglio, A. D. Caviglia, *Coupling lattice instabilities across the interface in ultrathin oxide heterostructures*, ACS Materials Letters **2** (4), 389–394 (2020).

---

[*] These authors contributed equally

5. **M. Šiškins**, M. Lee, F. Alijani, M. R. van Blankenstein, D. Davidovikj, H. S. J. van der Zant, and P. G. Steeneken, *Highly anisotropic mechanical and optical properties of 2D layered As_2S_3 membranes*, ACS Nano **13** (9), 10845–10851 (2019).

4. M. Lee, D. Davidovikj, B. Sajadi, **M. Šiškins**, F. Alijani, H. S. J. van der Zant, P. G. Steeneken, *Sealing graphene nanodrums*, Nano Letters **19** (8), 5313–5318 (2019).

3. **M. Šiškins***, C. Mullan*, S.-K. Son, J. Yin, K. Watanabe, T. Taniguchi, D. Ghazaryan, K. S. Novoselov, A. Mishchenko, *High-temperature electronic devices enabled by hBN-encapsulated graphene*, Applied Physics Letters **114** (12), 123104 (2019).

2. P. Belardinelli, L. M. F. R. Hauzer, **M. Šiškins**, M. K. Ghatkesar, F. Alijani, *Modal analysis for density and anisotropic elasticity identification of adsorbates on microcantilevers*, Applied Physics Letters **113** (14), 143102 (2018).

1. S.-K. Son*, **M. Šiškins***, C. Mullan*, J. Yin, V. G. Kravets, A. Kozikov, S. Ozdemir, M. Alhazmi, M. Holwill, K. Watanabe, T. Taniguchi, D. Ghazaryan, K. S. Novoselov, V. I. Fal'ko, A. Mishchenko, *Graphene hot-electron light bulb: incandescence from hBN-encapsulated graphene in air*, 2D Materials **5** (1), 011006 (2018).

---

*These authors contributed equally